CHALMERS
UNIVERSITY OF TECHNOLOGY

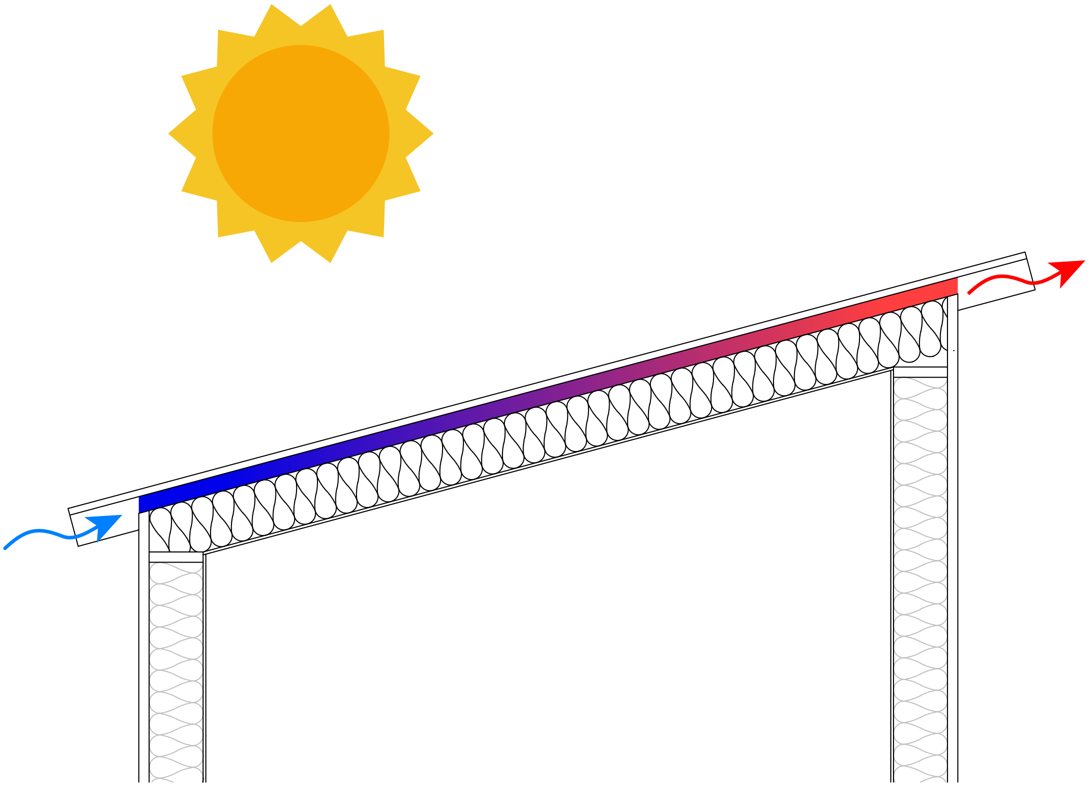

Ventilation by Thermal Buoyancy in the Air Cavity of Pitched Roofs

An Experimental and Numerical Study of Air Cavity Design and Natural Convection in Parallel Roof Constructions

Master's thesis in Structural Engineering and Building Technology

MARTINA SVANTESSON
TOIVO SÄWÉN

Master's thesis ACEX30-19-79
Department of Architecture and Civil Engineering
CHALMERS UNIVERSITY OF TECHNOLOGY
Gothenburg, Sweden 2019

MASTER'S THESIS ACEX30-19-79

Ventilation by Thermal Buoyancy in the Air Cavity of Pitched Roofs

An Experimental and Numerical Study of Air Cavity Design and Natural Convection in Parallel Roof Constructions

MARTINA SVANTESSON
TOIVO SÄWÉN

CHALMERS
UNIVERSITY OF TECHNOLOGY

Department of Architecture and Civil Engineering
Division of Building Technology
CHALMERS UNIVERSITY OF TECHNOLOGY
Gothenburg, Sweden 2019

Ventilation by Thermal Buoyancy in the Air Cavity of Pitched Roofs
An Experimental and Numerical Study of Air Cavity Design and Natural Convection in Parallel Roof Constructions

Ventilation med termisk drivkraft i luftspalter i lutande tak
MARTINA SVANTESSON, TOIVO SÄWÉN

Supervisors: Ken Hagrydh, Jörgen Wadman, Integra Engineering AB
Examiner: Paula Wahlgren, Department of Architecture and Civil Engineering

Master's Thesis ACEX30-19-79
Department of Architecture and Civil Engineering
Division of Building Technology
Chalmers University of Technology
SE-412 96 Gothenburg
Telephone +46 31 772 1000

Cover: Parallel roof ventilation driven by thermal buoyancy

Typeset in LaTeX
Gothenburg, Sweden 2019

Ventilation by Thermal Buoyancy in the Air Cavity of Pitched Roofs

An Experimental and Numerical Study of Air Cavity Design and Natural Convection in Parallel Roof Constructions

MARTINA SVANTESSON, TOIVO SÄWÉN
Department of Architecture and Civil Engineering
Chalmers University of Technology

Abstract

A parallel roof is a common roof type in Nordic countries, ventilated through an air cavity for the removal of heat and moisture. The air flow is driven by wind pressure and thermal buoyancy. A large amount of research has been performed on wind driven cavity ventilation for the purpose of heat removal. However, few studies have considered the thermal buoyancy as a driving force, or the perspective of moisture removal. Also, there is a lack of quantitative guidelines for the design of air cavities in roof constructions in Sweden, making it difficult to evaluate a proposed roof design.

This study investigates how the air cavity design affects the thermal buoyancy by experiments and by numerical simulations. The experimental tests were performed on a full-scale roof model, with a cavity length of 3.5 m, heated to simulate a solar heated roof. Cavity heights between 23 and 70 mm as well as roof inclinations between 5 and 45° were tested for different heat intensities applied to the system. Surface and air temperatures were measured and the air velocity in the cavity was determined by smoke tests.

Numerical CFD modelling of the same heated air cavity was also performed in COMSOL Multiphysics, aiming to replicate the experimental results. The experimental and numerical results were used to characterise the driving forces and the resistances for air flow by using the dimensionless Grashof number. To also include the thermal conditions of the cavity, the dimensionless Rayleigh number was used and a relationship between Rayleigh number and air flow rate was derived. An analytical model of the thermal and mechanical behaviour in the air cavity was created, as a basis for further studies of the moisture conditions in an air cavity.

The study shows that an increased heat intensity increases air and surface temperatures, which in turn causes larger air flow rates. An increased cavity height and a higher inclination cause larger air flow rates, while the air velocity has a maximum value. Higher flow rates cause decreased air and surface temperatures for a constant heat intensity. The results of the study imply that thermal buoyancy is of relevance when evaluating the performance of cavity ventilated roof constructions from a moisture perspective in Swedish climates. However, further research is required to ascertain the impact of these findings regarding moisture safety.

Keywords: parallel roof, cavity ventilation, natural convection, thermal buoyancy, CFD

Ventilation med termisk drivkraft i luftspalter i lutande tak

Experimentell och numerisk studie av luftspaltens utformning och naturlig konvektion i parallelltak

MARTINA SVANTESSON, TOIVO SÄWÉN
Institutionen för arkitektur och samhällsbyggnadsteknik
Chalmers Tekniska Högskola

Sammandrag

Ett paralleltak är en vanlig taktyp i Norden, som ventileras genom en luftspalt för att föra bort värme och fukt. Luftflödet drivs av vinden och skorstenseffekten. En rad studier har genomförts på vinddriven spaltventilation, främst i syfte att transportera värme. Dock är det få studier som undersökt skorstenseffekten som drivkraft, eller fukttransportperspektivet. Det saknas också kvantitativa riktlinjer för utformningen av luftspalter i takkonstruktioner i Sverige, vilket gör det svårt att utvärdera en föreslagen dimensionering.

Den här studien undersöker hur utformningen av luftspalten påverkar skorstenseffekten i spalten genom experiment och genom numeriska simuleringar. Experimenten genomfördes på ett uppvärmt tak (motsvarande soluppvärmning) i en fullskalemodell med längd $3,5$ meter. Spalthöjder mellan 23 och 70 mm undersöktes tillsammans med taklutningar mellan 5 och 45 °, med varierande värmeeffekt tillförd till systemet. Yt- och lufttemperaturer mättes upp, och lufthastigheten i spalten uppskattades genom rökförsök.

Numerisk CFD-modellering av samma uppvärmda spalt genomfördes i COMSOL Multiphysics, med mål att att återskapa de experimentella resultaten. De experimentella och numeriska resultaten användes för att karakterisera drivkrafter och flödesmotstånd genom det dimensionslösa Grashof-talet. För att också ta hänsyn till de termiska förhållandena i spalten användes Rayleigh-talet, och ett samband mellan Rayleigh-tal och luftflöde ställdes upp. En analytisk modell för de termiska och mekaniska förhållandena i spalten skapades som grund för vidare studier av fuktförhållandena i luftspalten.

Studien visar att en ökad värmeintensitet ökar luft- och yttemperaturer, vilket i sin tur ger ett ökat luftflöde. Högre spalthöjder och taklutningar leder till högre luftflöde och lägre temperaturer. Dock verkar lufthastigheten ha ett maxvärde för en viss värmeintensitet. Sammanfattningsvis tyder resultaten på att skorstenseffekten spelar en viktig roll vid utvärderingen av ventilerade takkonstruktioner ur ett fuktperspektiv vid svenska förhållanden. Dock krävs vidare forskning för att utvärdera konsekvenserna av detta för fuktsäkerheten.

Sökord: parallelltak, luftspalt, ventilation, naturlig konvektion, CFD, luftflöde

Preface & Acknowledgements

The present thesis is the result of a Master's thesis project at Chalmers University of Technology, Gothenburg, Sweden, performed by Martina Svantesson and Toivo Säwén for the degree of Master of Science in Structural Engineering and Building Technology. The work was performed in collaboration with supervisors at Integra Engineering AB.

As authors, we would firstly like to extend our warm thanks to our examiner and supervisor Paula Wahlgren at the division of Building Technology at Chalmers. She has been providing both excellent technical advice, enthusiastic encouragement from start to finish, and put us in touch with experienced researchers at Chalmers, including Fredrik Domhagen, Carl-Eric Hagentoft, Tommie Månsson, Vahid Nik, and Kaj Pettersson. We are thankful for their comments and useful input, always providing new angles from which we can approach our work. We have also been surrounded by helpful fellow students, especially our opponent Linda Wäppling and her project partner Ona Forss, who have been a great source for inspiration and feedback.

Secondly, we would like to thank our supervisors at Integra Engineering AB, Ken Hagrydh and Jörgen Wadman, who have been of great assistance both in providing useful experiences from real applications, in connecting us with various professionals in the field, and in helping us stay on track and always focus on the most important issues. We would also like to thank all our colleagues at Integra for generously providing office spaces and inspiring us with their curiosity and experience. Additionally, we received useful input from a number of professionals, working with construction and moisture safety, and would like to thank Johnny Kronvall, Strusoft, Lars Olsson and Thorbjörn Gustavsson, RISE, Eva Gustafsson, Conservator, and Ruth Strøm, Securo, for their time and assistance.

We were also lucky enough to be invited to NTNU in Trondheim, Norway, and get the possibility of conducting the experimental study. We have had a great collaboration with our fellow Master's thesis student Nora Schjøth Bunkholt, who has helped us shape the methodology, and with whom we have collaborated in the experiments and in the analysis of the results. We would also like to thank her supervisors Tore Kvande and Lars Gullbrekken for their assistance in understanding the theoretical framework and the experimental design, along with Øystein Holmberget, Egil Rognvik, Ole Aunrønning and Jardar Lohne who were helpful during the experimental study. We would also like to thank ÅForsk and Civ. Ing. Torsten Janssons Stipendiefond for kindly providing monetary support for our visit to Trondheim.

Martina Svantesson & Toivo Säwén
Gothenburg, June 2019

Contents

Nomenclature

Roman upper case letters

D_h	Hydraulic diameter	m
G_v	Moisture transport potential	kg/s
H	Total roof height	m
I	Current	A
I_{sol}	Irradiance normal to a surface	$\mathrm{W/m^2}$
L	Cavity length	m
L_0	Characteristic length	m
P	Pressure	Pa
Q	Heat	W
R	Thermal resistance	$\mathrm{m^2\,K/W}$
RH	Relative humidity	-
S	Air flow resistance	$\mathrm{Pa/(m^3/s)}$
T	Temperature	°C
T_0	Effective temperature	°C
U	Voltage	V
U_{10}	Wind speed	m/s
$\dot{V}$	Air flow rate	$\mathrm{m^3/s}$

Roman lower case letters

b	Cavity width	m
c_a	Specific heat capacity of air, at constant pressure	$\mathrm{J/(kg \cdot K)}$
c_p	Wind pressure coefficient	-
f_p	Pipe factor	-
g	Gravitational constant	$9.82\,\mathrm{m/s^2}$
g_v	Moisture flux	$\mathrm{kg/(m^2 \cdot s)}$
h	Cavity height	m
q	Heat flux	$\mathrm{W/m^2}$

t	Layer thickness	m
u	Air velocity	m/s
u_{max}	Maximum cavity air velocity	m/s
u_{mean}	Mean cavity air velocity	m/s
v	Absolute humidity	kg/m^3

Greek letters

Θ	Wind approach angle	$^\circ$
α	Heat transfer coefficient	$W/(m^2K)$
α_0	Effective heat transfer coefficient	$W/(m^2K)$
α_{sol}	Solar absorptivity	-
β	Coefficient of thermal expansion	1/K
ε	Emissivity	-
λ_f	Frictional loss coefficient	-
λ_m	Thermal conductivity	$W/m \cdot K$
μ	Dynamic viscosity	$Pa \cdot s$
ν	Kinematic viscosity	m^2/s
ϕ	Dimensional factor	-
ρ	Air density	kg/m^3
θ	Roof inclination	$^\circ$
ξ	Local loss coefficient	-

Dimensionless numbers

Gr	Grashof number
Pr	Prandtl number
Ra	Rayleigh number
Re	Reynolds number

The definitions of the geometric parameters and coordinates in this study are provided in Figure 0.1, where the origin is at the bottom surface of the inlet in the centre line of the cavity.

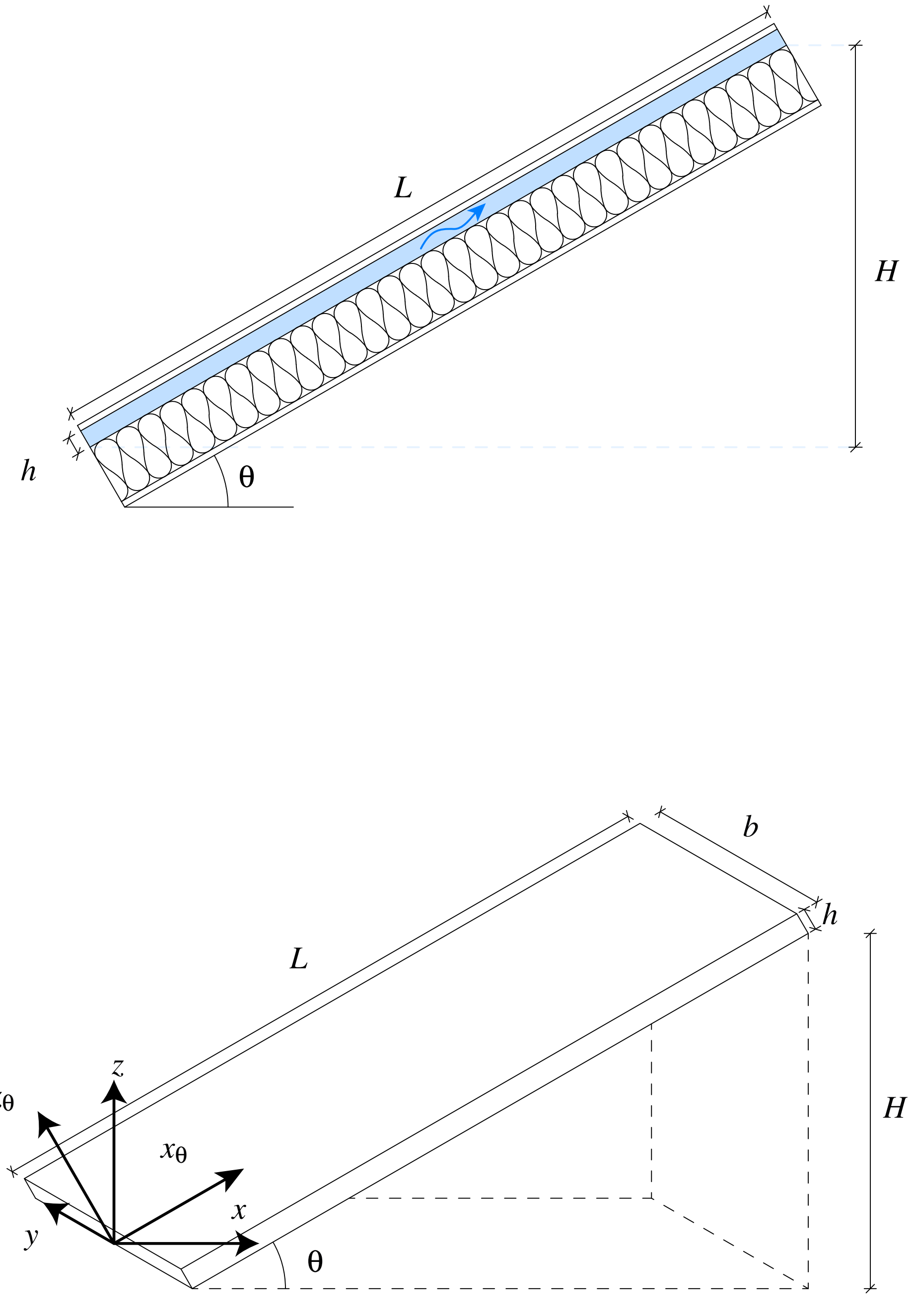

Figure 0.1. Geometric parameters and definition of coordinates of the air cavity.

1
Introduction

The main purpose of a roof is to act as a climate shelter to maintain good indoor climate in a building. This includes shelter from temperature, wind and precipitation, as shown in Figure 1.1. The roof is a part of the building envelope that is exposed to weather conditions with large variations. It can be exposed to very high temperatures during daytime, due to solar radiation, and very low temperatures during nighttime, due to long wave radiation to the sky. The roof is also exposed to rain and snow, as well as wind pressure of varying magnitude.

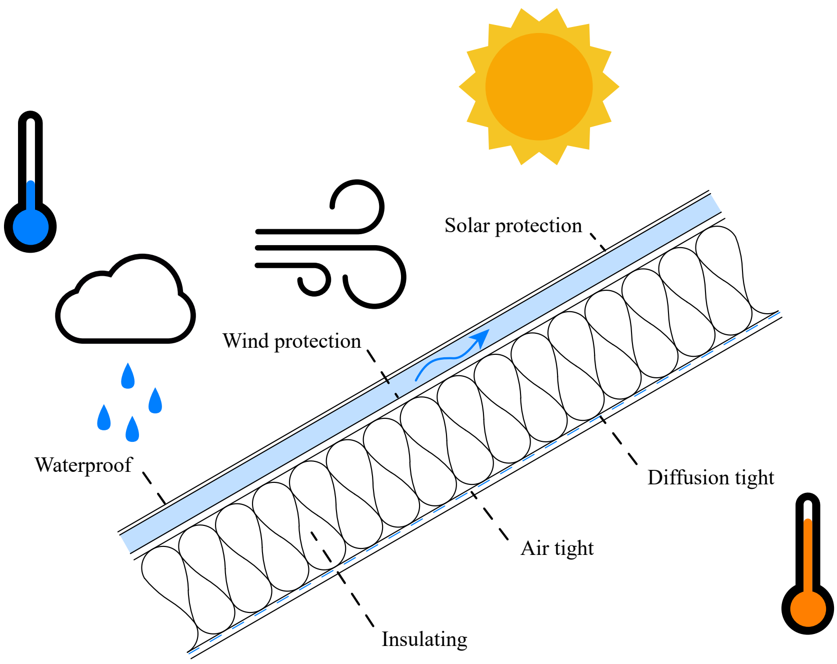

Figure 1.1. Climatic factors affecting the roof, and physical function of roof construction. Adapted from Liersch (1986).

For the roof to maintain its function during the full life time of the building and for all different weather conditions, it is important that it is designed properly and that moisture is handled in a way that prevents damage to the construction. Moisture damage to a building component includes mould growth, causing a risk for poor indoor air quality, or even rot, compromising the structural integrity of the component.

One way of removing moisture in order to prevent damage is ventilation of the roof construction. In parallel roofs the construction is ventilated through an air cavity layer between parallel surfaces, as further explained in Chapter 2. The ventilation of the cavity is driven by natural forces such as wind pressure and thermal buoyancy, which is further explained in Section 3.2.2.

While the climatic conditions govern the driving forces for flow, the air flow resistance in the cavity is largely affected by its design. This study investigates the magnitude of thermal buoyancy in air cavities characterised by design factors, such as cavity height and roof inclination, with regards to their impact on air flow.

1.1 Background

To face increasing demands on energy efficiency in the past decades, insulation layers of larger thickness are installed in roof constructions, reducing the heat transfer through the roof. The effect of increased insulation is a decrease in the thermal driving force for air flow in the cavity. At the same time, lower temperatures increase the relative humidity in the cavity, which increases the risk for condensation and moisture problems. These changing boundary conditions for air cavity ventilation have been the motivation for a number of experimental, numerical and analytical studies of the performance of parallel roof constructions.

In recent years, the hygrothermal function of the air cavity in a parallel roof has been studied at NTNU in Trondheim, Norway (Gullbrekken, 2018). The research has considered roof ventilation in order to reduce roof temperatures, avoiding snow melt problems and improving photovoltaic panel function, as well as to avoid moisture problems. In warmer climates the potential of roof cavity ventilation for reduction of solar heat gains has been the topic of several studies, e.g. Lee, Park, Yeo and Kim (2009). These studies have been performed both through laboratory and field experiments, and through numerical studies. However, to the authors' knowledge, the potential for thermal buoyancy to drive ventilation, and its impact on moisture conditions, have not been studied in a Nordic context, where both climatic conditions and and building tradition are different.

In Sweden, moisture safety is considered to be the main reason for air cavity ventilation (Petersson, 2009) and moisture problems in buildings have been shown to cause health issues (Bornehag et al., 2001). The prevalence of moisture problems in roof constructions has been confirmed for roofs with a cold attic (Arfvidsson, Harderup & Samuelson, 2017) and the problem is exacerbated by the increased insulation thickness of modern roof constructions. However, most studies, including building performance modelling and field studies, have been performed on cold attic constructions. Hence, more studies are needed on the prevalence of moisture issues in parallel roofs, as well as on the performance of chosen designs.

Design parameters such as roof inclination, roof length, insulation thickness and inlet design are often driven by architectural considerations or energy performance (Gullbrekken, 2018). Air cavity height, on the other hand, is typically selected based on ease of construction and the available materials. Thus, engineers need guidelines or tools to decide on an appropriate solution and dimensions of the air cavity for a given roof construction. However, there are no quantitative guidelines in Sweden besides experience-based "rules of thumb" for the design of air cavities in roof constructions given the purpose of ventilating moisture, as further explained in Section 2.2. Trends in building design, such as longer roofs, increased insulation thickness and novel eave design solutions accentuate the need for such a design framework. This calls for additional research to establish the effects of design choices on cavity ventilation, and provide tools for engineers to predict the air flow based on design parameters.

1.2 Aim and research questions

The aim of this study is firstly to evaluate how the design of modern parallel roof constructions affects the air flow in the air cavity, and secondly to quantify the thermal buoyancy as a driving force for air cavity air flow. The goal is to be able to predict the air flow caused by natural convection in the cavity for a given design in a certain climate. The airflow is to be evaluated in the context of moisture safety of the construction.

The aim of the study will be achieved by answering the following research questions:

1. What is the magnitude of the thermal driving force for cavity air flow in a Nordic context?
2. How do design parameters, such as cavity height and inclination, affect the air flow?
3. How would a useful model be formulated to predict the thermal buoyancy driven air flow based on climatic conditions and design parameters?

The questions can be summarised as presented in Figure 1.2.

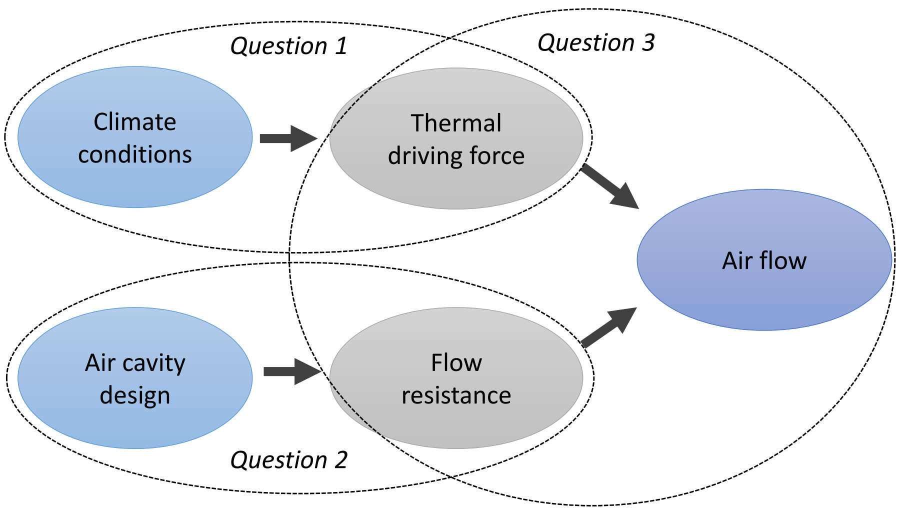

Figure 1.2. Schematic representation of the research questions.

1.3 Scope

This study is limited to parallel roof constructions. Consequently, roof solutions such as compact roofs and cold attics are not considered and mechanical ventilation is out of scope. No assessment is made of the economical and life cycle aspects of different roof construction types, and fire safety is not assessed.

The study investigates air cavities without direction changes and with openings at the bottom and top of the cavity, corresponding to a pent roof or ridge ventilated roof. Thus, other solutions such as gable roofs with eave-to-eave ventilation and more complex geometries are not considered. The air cavity is assumed to consist of two parallel planes, with no obstructions impeding the air flow. The influence of different cavity surface materials on the air flow is not studied. Further, the study does not directly study the effect of different design of the cavity inlet and outlet, but as a baseline for comparison, a reference roof construction is presented in Chapter 2.

Only the effect of overheating is studied, thus the effect of undercooling of the roof surface due to night long wave radiation is omitted. Further, the study is based on the assumption of steady-state conditions, not considering transient effects of changing climatic conditions. When evaluating the results, the effects of mixed convection are not studied. In the application of the results of the study, the considered climate is representative for the southwest of Sweden, disregarding the possible influence of snow cover on the roof.

During the study, the moisture safety of the roof construction is considered to be the main motivation for air cavity ventilation, as outlined in Section 2.1. Other potential functions, such as cooling of the roof construction, are not evaluated, thus the removal of heat from the roof construction is not directly quantified.

The study aims to present a relationship between given geometric parameters and climatic conditions, and the resulting air flow and thermal conditions. Thus, it provides a basis for the evaluation of moisture safety, while not thoroughly investigating the main factors influencing the moisture conditions in the cavity.

1.4 Methodology

As a starting point for the thesis project, a literature study was performed for an overview of previous research and different approaches to understanding the function of, and risks associated with, parallel roof constructions. The literature study was performed both starting from the sources of the work performed at NTNU as well as through a general keyword search through Google Scholar, using keywords including "air cavity", "ventilated roof", "CFD", and searches in the libraries at Chalmers University of Technology. The literature study was then expanded through a backward snowball search with the studies obtained as a starting point to find key research and identify knowledge gaps. Also, interviews were performed with professionals at the construction consultancy Integra Engineering AB and the research institute of Sweden; RISE, and with building technology researchers at Chalmers.

To respond to the research questions described in Section 1.2, two main methods were used in parallel as a foundation for this study with a clear connection to the theoretical framework. The choice of method was made based on the complexity of analytical solutions for non-isothermal air flow, even in simple geometries, calling for empirical results to support the validity of such methods. A representation of the methodology is presented in Figure 1.3.

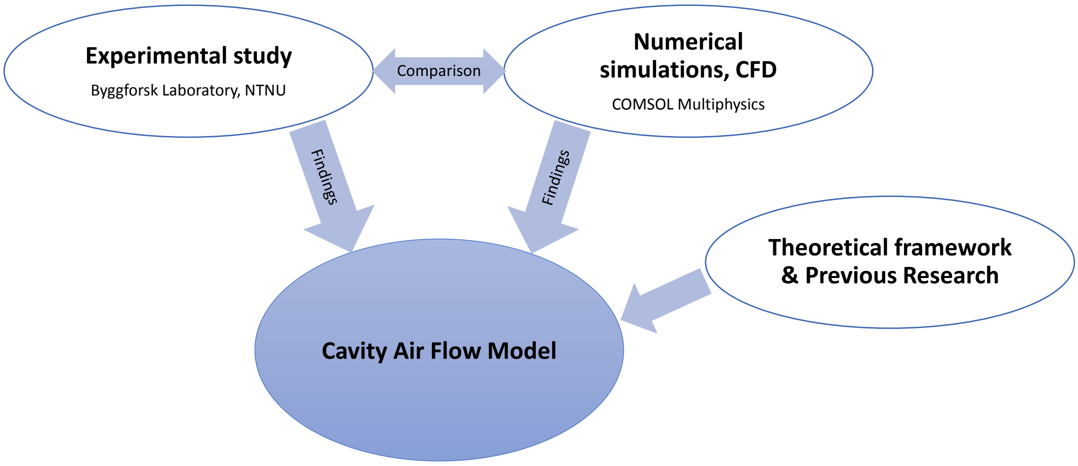

Figure 1.3. Representation of the methodology of the study.

Firstly, experimental tests were conducted on the thermal buoyancy in inclined air cavities. The experiments were performed at the SINTEF/Byggforsk laboratory at NTNU, Trondheim, where ongoing research on roof air cavities is being conducted. The experiments were performed on a full scale model, designed to represent a realistic roof construction. The geometric parameters studied were the air cavity height h, and the roof inclination θ. Due to practical limitations, the air cavity length and width were kept constant for all the tests. To represent heating caused by solar radiation, a heating foil was installed in the top of the cavity in the model.

The temperature conditions in the air cavity when applying different heating intensity were measured using thermocouples. The air velocity was measured using visual observation of smoke flowing through the air cavity. Analytical models were employed according to the theoretical framework to calculate the thermal driving force and the resulting air flow rate.

Secondly, in addition to the experimental tests, a numerical study was conducted through simulations using the CFD module of the Finite Element Method (FEM) implementation COMSOL Multiphysics, which uses a physics-based interface to solve coupled systems of partial differential equations. The geometrical and thermal conditions simulated were chosen to replicate the experimental results as closely as possible, in order to be able to compare the results and estimate the sources of error in the two studies. The simulations were performed assuming steady-state conditions, and using a two dimensional representation of the air cavity to reduce computational cost. Two dimensional temperature and velocity profiles as well as air flow rates were exported from the software, while the thermal driving force and air flow resistance were calculated according to the theoretical framework.

Thirdly, based on the experimental and numerical study, the thermal driving force and airflow resistance in the air cavity were characterised through the dimensionless Grashof number and Rayleigh number. The results from the experimental and numerical study were compared to existing analytical models for air cavity air flow, to estimate the reliability of such models in predicting the air flow for any given construction.

As a basis for risk assessment regarding moisture safety, a calculation model was created which provides an estimation for the airflow, for a given cavity design in a specific climate condition. The intention is to make a model that is compatible with a risk assessment model using climate data and air cavity geometry as an input. A schematic design of such a calculation model is provided in Figure 1.4. However, note that this study only covers a part of the model.

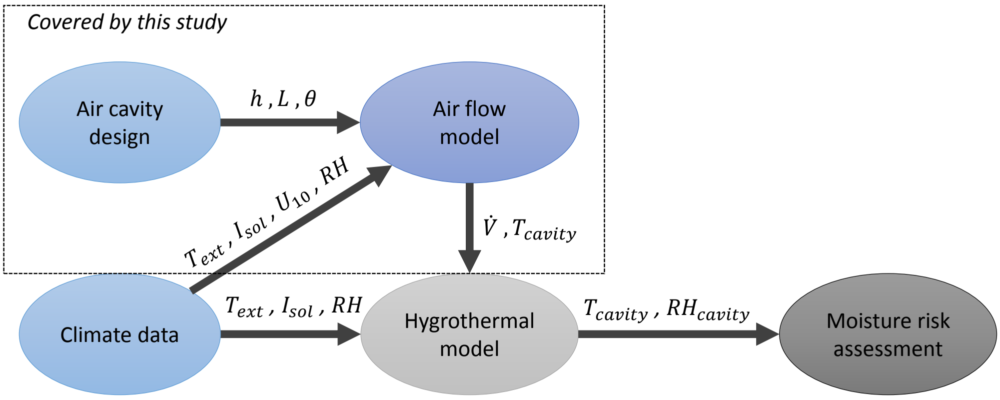

Figure 1.4. Flow chart depicting a schematic design of a risk assessment calculation model for a roof construction. The model takes climatic conditions and geometric parameters into account and predicts the hygrothermal conditions, forming the basis for moisture risk assessment.

1.5 Previous research

The hygrothermal function of the air cavity in ventilated walls was studied by Falk (2014), who experimentally tested the drying time for cavities of different dimensions. The study showed that there was little difference in drying time between air cavities with heights of 40 mm and 25 mm, but a significant prolongation of drying time between air cavities with heights of 10 mm and 5 mm. However, as air cavities in walls and in roofs function differently, the results of this study are not directly applicable for the research of this study.

The hygrothermal function of the air cavity in ventilated roofs has been studied in two Norwegian PhD theses (Blom, 1991, 2001; Gullbrekken, 2018), supported by several Master's theses (Hofseth, 2004; Hansen, 2016; Eggen & Røer, 2018). In Norway the main focus of research has been on the cooling potential of the air cavity to avoid snow melt problems, while the moisture safety of the air cavity has been the topic of debate for the last decades in other Nordic countries (Petersson, 1983; Korsgaard, Christensen, Prebensen & Bunch-Nielsen, 1985; Samuelson, 2000; Tobin, 2016). This has been investigated in various student theses, some focusing on numerical modelling (Latif & Ehsani, 2013; Lindgren, 2017; Eriksson, 2017), some on field measurements (Åström, 2017; Rikner & von Platen, 2015), and some on comparisons of both (Johansson & Larsson, 2016; Rada & Beto, 2016). Thermal buoyancy in roof constructions has been studied through CFD analyses performed at Chalmers (Bengtson & Fransson, 2014; Hellsvik, 2015), focusing on cold attics. These studies have been the basis for the formulation of the research questions and the choice of methodology.

The thermal buoyancy in the air cavity of inclined roofs has also been the topic of study in international studies, through numerical studies (Biwole, Woloszyn & Pompeo, 2008; Manca, Mangiacapra, Marino & Nardini, 2014) and laboratory experiments (Bunnag, Khedari, Hirunlabh & Zeghmati, 2004; Susanti, Homma, Matsumoto, Suzuki & Shimizu, 2008; Lee et al., 2009; Chami & Zoughaib, 2010). However, these studies have mostly focused on the cooling effect of the air cavity to reduce high summer temperatures. While this effect is considered secondary in Nordic climates today, it may be of increasing interest due to changing temperature extremes (Kjellström et al., 2007; Nikulin, Kjellström, Hansson, Strandberg & Ullerstig, 2011).

Thermal buoyancy as a driving force for cavity ventilation has also been studied experimentally from a moisture perspective by Nusser and Teibinger (2013), focussing on low-inclination roofs. These studies have been used to assess the relevance of the results of the present experimental and numerical study.

Biwole et al. (2008) performed a numerical study, investigating the heat transfer in parallel roofs ventilated by thermal buoyancy, and found that the radiative properties of the cavity internal materials, as well as the roof inclination, are the most relevant parameters governing the air flow.

Bunnag et al. (2004) performed an experimental study, investigating convection in an open-ended rectangular inclined channel heated from the top. By combining different heat fluxes, air cavity heights and roof inclinations, the study observed that increased roof inclination decreased cavity temperatures significantly, while the air velocity increased.

The air velocity in an air cavity model with various inclinations was later measured experimentally by Susanti et al. (2008). The study observed that a decreased inclination gave a reduction in velocity. The air velocity was also reduced when cavity temperatures decreased.

Temperature conditions in ventilated air channels were investigated by Chami and Zoughaib (2010). The study observed that a reduction in heat flux applied to the top surface of the cavity decreased the mean temperatures on the surfaces of the cavity and hence decreased the airflows through the cavity.

Thermal buoyancy driven airflow in the cavity of low-pitched roofs in particular was examined by Nusser and Teibinger (2013). A full-scale air cavity model was employed in the investigation of the relationship between roof inclination, air cavity height and resulting airflow in the cavity. The study included roof inclinations in the interval $3-7°$ and cavity heights between $50-100\,\mathrm{mm}$, and found that a larger temperature difference between the air cavity surfaces and the ambient air caused higher air velocities, but that a changed inclination had a limited effect on air flow.

Further results of the literature study on thermal buoyancy in inclined ventilated roofs are presented in Bunkholt et al. (2019).

1.6 Thesis outline

Chapter 2, Ventilated roof constructions, presents roof building traditions as well as the purpose and function of the air cavity in parallel roof constructions. The chapter also presents current Swedish design guidelines and the reference roof design considered in this study.

Chapter 3, Air cavity physics, presents the theoretical framework used for the study, focused on explaining the physical conditions of an air cavity. The theory serves as a foundation for the analysis conducted.

Chapter 4, Experimental study, presents the experimental study carried out as one of the main methods in this study. The chapter presents the set-up and procedure of experimental tests as well as the measurement results and the uncertainty analysis conducted.

Chapter 5, Numerical study, presents the numerical simulations conducted in the study. The chapter presents the basic theory of computational fluid dynamics, the modelling and assumptions behind the simulations, as well as the simulation results.

Chapter 6, Analysis and comparison, presents the analysis carried out in the study which origins from the results retrieved from both the experimental study and the numerical simulations. The analysis includes a comparison between the results as well as a comparison with the theory and with results of previous studies, as presented in Section 1.5.

Chapter 7, Discussion, presents an elaboration on the interpretation and implication of the experimental and numerical results, as well as on the analysis.

Chapter 8, Practical applications, presents the implications of the analysis in a realistic context, applying the results from the previous chapters to the reference roof construction presented in Chapter 2. The chapter also presents a foundation for how the results of this study could be used in future studies of the moisture safety of cavity ventilated roofs.

Chapter 9, Conclusions, summarises the study and presents the conclusions drawn. Suggestions for further studies on thermal buoyancy driven air flow in naturally ventilated roof constructions, and for studies on how air cavity design impacts the moisture safety of roof constructions, are provided.

2

Ventilated roof constructions

Timber constructions have a long-standing tradition in the Nordic countries and are commonly used for small buildings. The raw material wood is readily available in the Nordic region and with innovations in the timber construction industry, timber now constitutes a sustainable alternative to materials such as steel and concrete. Timber constructions are gaining interest even in larger scale building projects (Gullbrekken, 2018).

Buildings with a timber construction typically have a pitched roof, but there are various methods of ensuring the appropriate function of the roof from the perspective of building physics. Traditionally, a distinction has been made between warm and cold roof constructions, depending on the magnitude of the heat flux through the outer surface of the roof (Arfvidsson et al., 2017).

A cold roof construction has a large ventilated volume, causing most of the heat flux from the internal space to be removed with the ventilating air, thus providing a cooling effect on the external roof surface. Traditionally, cold roof structures with a ventilated attic have been employed in Nordic countries (Blom, 1991). As the demands for usable space have increased, parallel roofs have gained popularity (Björk, Nordling & Reppen, 2009). The attics are increasingly insulated and the ventilation potential is reduced, as can be seen in Figure 2.1. In parallel, particularly in industrial construction, roof inclinations are decreased, and larger roof elements with higher air tightness are employed (Liersch, 1986).

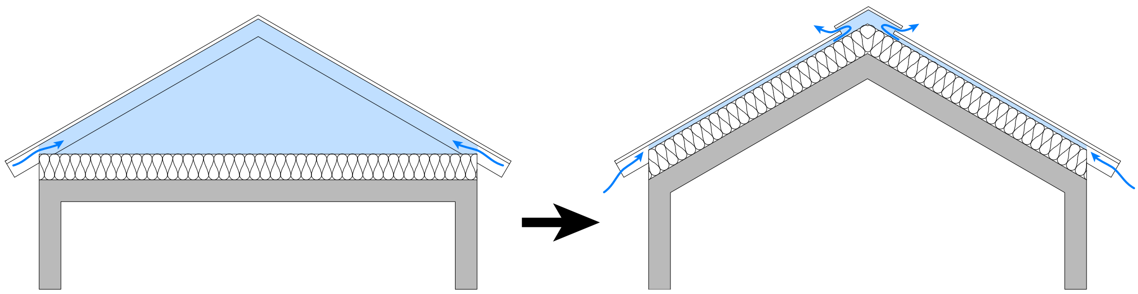

Figure 2.1. Historic development of ventilated roofs, from a "cold roof" with a large ventilated space, to a "warm roof" where the insulation is parallel to the roofing. The blue area represents the ventilated space. Adapted from Liersch (1986).

A warm roof construction (also referred to as a compact roof) has no ventilation which means the heat flux through the inner roof surface equals the one through the outer roof surface. This could in turn increase the temperature of the external roof surface, which could cause snow on the roof to melt and then refreeze at the eave as icicles, with risk to persons or building component damage as a consequence (Blom, 1991). In cold roof constructions, moisture is removed through ventilation. In compact roof constructions the aim is to prevent the moisture from entering the construction at all (Petersson, 2009).

With the large insulation thicknesses of today, commonly exceeding 400 mm, even a "warm" roof construction results in a rather cool roof surface similar to the surface of the "cold" roof. Arfvidsson et al. (2017) suggests a distinction between ventilated and non-ventilated roof constructions as more appropriate for modern constructions.

A parallel roof is a ventilated roof construction where the external and internal surfaces are parallel, with an air cavity between the water proof outer layer and the insulation. The volume of the air cavity is much smaller than that of the attic in a traditional cold roof, which makes this type of roof construction a moderately ventilated roof construction. According to Petersson (2009) the parallel roof could be regarded as a combination of a warm and a cold roof construction. The parallel roof is a construction type mainly used for timber roof constructions, both in gable roofs and pent roofs, with varying inclinations.

The design of the air cavity in parallel roof constructions varies between countries, as shown in Figure 2.2. In Sweden, the underlayer roof, responsible for the removal of rainwater, is placed above the air cavity, while the wind barrier, providing wind protection and air tightness, is placed below the cavity (Edvardsen & Torjussen, 2000). This reduces the available space of the air cavity, but also reduces the number of obstructions for air flow. In Norway, the layers for rainwater removal and wind protection are commonly combined, meaning the interior of the building can be quickly protected from climate factors during the construction process and saving on material cost. However, research on building integrated photovoltaics has sparked a renewed interest for the roof type with separate wind and rain protection layers (Gullbrekken, 2018).

2.1 Purpose and function of the air cavity

As outlined by Gullbrekken (2018), the purpose of air cavity ventilation is to transport heat and moisture away from the roof construction.

The initial purpose of the ventilation of a roof construction in Nordic climates was to cool the roof to avoid snow melt, which could cause ice formations at the eaves (Blom, 1991). In modern roof constructions, where the amount of thermal insulation is larger, the problem with snow melt is reduced due to less heat transmission, but the cooling of the roof surface remains an important concern.

In warm climates, cavity ventilation is employed to efficiently reduce solar heat gains through the roof (Lee et al., 2009). This effect may also be of increasing interest even in Nordic climates, due to climate change. Another important use for cavity ventilation may be cooling of solar photovoltaic panels applied to building envelopes (Gullbrekken, 2018).

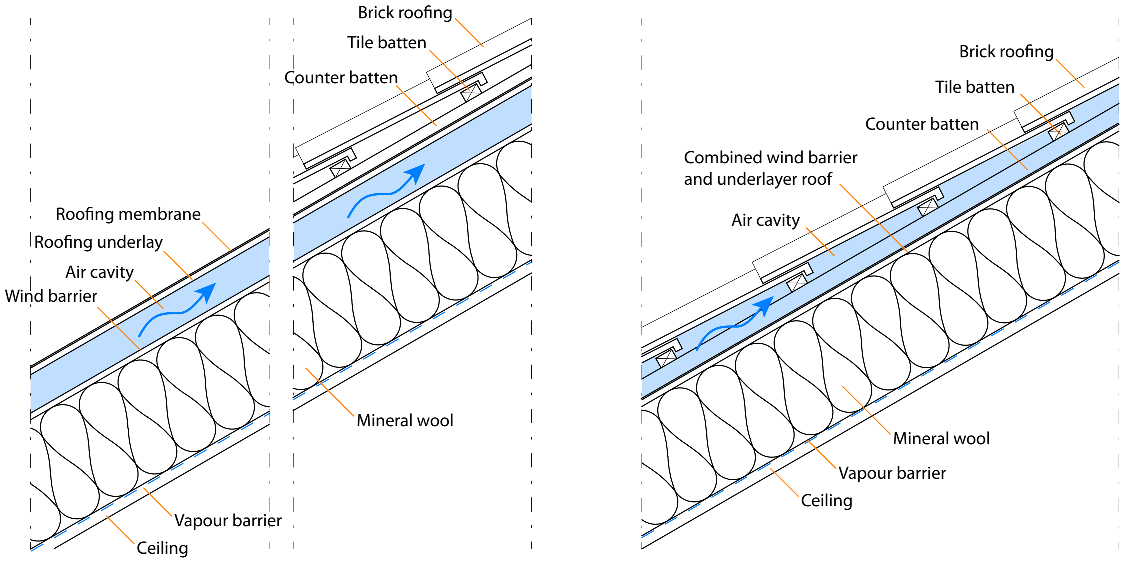

Figure 2.2. Two varieties in parallel roof constructions, typical in Sweden (left image) and in Norway (right image). The Swedish parallel roof has two separate layers for protection from rainwater and wind, while the Norwegian parallel roof combines them into one, providing a larger ventilation space (Gullbrekken, 2018).

On the other hand, the decreased temperature in the outer parts of the roof construction will increase the relative humidity in the air cavity. This increases the risk for moisture problems, and thus the ventilation demand for moisture control. Therefore, the modern purpose of the air cavity in roof constructions is mainly to ventilate and remove excessive moisture (Petersson, 2009).

According to Petersson (2009), the origin of moisture in the air cavity can be the following:

- Built in moisture from precipitation during construction work or moisture in delivered material
- Precipitation combined with leakages in the roof cladding
- Leakages through the internal vapor barrier in combination with internal over pressure
- Condensation inside the air cavity from moist inlet air and under-temperature in the cavity

Constructions with less insulation have a better function with regards to moisture safety due to higher temperatures in the air cavity. A larger insulation thickness also increases the risk for natural convection inside the insulation layer which may increase the transport of moisture if there is a leakage from inside (Gullbrekken, Uvsløkk, Geving & Kvande, 2017b).

For the air cavity ventilation to have a drying effect, a sufficient air flow is required. However, the critical factor for moisture removal is the drying potential of the ventilating air (Arfvidsson et al., 2017). The drying potential is dependent on the temperature and moisture content of the inlet air compared to the conditions in the cavity. Warm and humid air could enter the cavity in daytime, increasing the moisture content of the cavity materials, and when cooled during night the dew point of the air might be reached, causing condensation. This means that ventilation in the cavity can have an undesired effect of introducing excess moisture for some conditions and these conditions will vary over the year.

A constant high ventilation rate will cause hygrothermal conditions in the air cavity similar to the outdoor conditions. According to L. Olsson (personal communication, February 15, 2019) this would most likely cause moisture problems for the materials used in current parallel roofs constructions. However, a constant low ventilation rate might not be sufficient to handle the present moisture loads. Hence, the relationship between ventilation rate and moisture safety of the construction is complex and the design of the cavity needs to consider several phenomena with contradictory optimum solutions regarding the magnitude of ventilation in the cavity.

Additional insulation on the external side of the air cavity is one way of improving the thermal conditions in the air cavity. The insulation would reduce the impact of changes in the external conditions and generally keep the air cavity slightly warmer when the roof is exposed to longwave radiation, assuming a low ventilation rate. An increased temperature in the air cavity would increase the moisture safety of the construction, especially against the condensation potential of inlet air. On the other hand, the potential for daytime drying may be reduced and furthermore, high temperatures are favourable to mould growth.

2.2 Design guidelines

Current Swedish building guidelines state that roof constructions should be designed in such a way that no moisture could be damaging (Boverket, 2018). The guidelines also provide some suggestions on how this is achieved, such as recommendations regarding air tightness from the interior and diversion of rain water. For ventilated roofs, a recommended minimum inlet area (dependent on the area of the attic) can be found for roofs with a large ventilated volume (Boverket, 1988). Recommendations are also available regarding the dimensions of air cavities in ventilated walls (Svensk Byggtjänst, 2018). However, there is a lack of guidelines regarding the dimensions of the air cavity in parallel roofs.

In other countries, such as Norway, Finland and Germany, national guidelines for dimensions of the air cavity exist and these guidelines are dependent on roof length, roof inclination and different cavity inlet designs (Gullbrekken, 2018). Norway has the most detailed recommendations, suggesting cavity heights between 23 – 96 mm. The only guideline there is to be found in Sweden is from Arfvidsson et al. (2017), recommending an air cavity height of at least 50 mm for large roofs. This is a rather generalising recommendation since the impact from different inclinations, insulation thickness or inlet designs are neglected. Also, the definition of a "large roof" is not specified.

2.3 Reference roof construction

The roof design chosen as a reference roof construction for this study is a design common for parallel roofs in modern Sweden (Träguiden, 2019), as well as a design that might be critical with regards to moisture safety. A sketch of the roof construction and materials of the layers is presented in Figure 2.3.

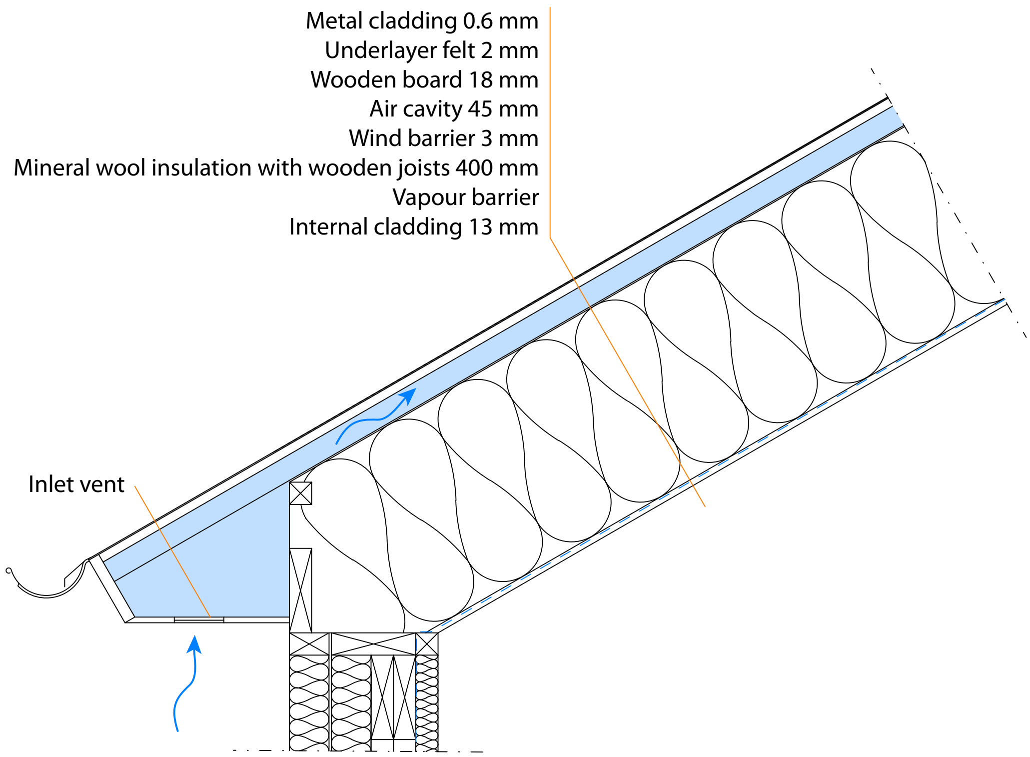

Figure 2.3. Sketch of the reference roof construction considered in this study, including the inlet design.

The load bearing structure is made of timber beams, between which mineral wool serves as thermal insulation. On the interior side of the roof there is a vapour tight plastic foil and internal cladding. On top of the timber beams there is a wind barrier made of a wooden board. The air cavity is built up by wooden battens on top of the wooden board, with a constant spacing of 600 mm. The top surface of the air cavity consists of a plywood board, onto which an underlayer felt is attached before the roofing made of folded sheet metal.

The timber construction was chosen for study due to the moisture sensitivity of wooden members. The metal sheet roofing was chosen due to the practical complications in combining this cladding with additional insulation on the external side of the air cavity (J. Wadman, personal communication, January 22, 2019).

The design parameters of interest are presented in Section 1.2. The studied values for these parameters are the following:

- Air cavity height: 28, 35, **45**, 70 mm
- Length of air cavity: 5, **10**, 20 m
- Inclination of the roof: 5, 15, **30**, 45 °
- Insulation thickness: 250, **350**, 450 mm

Dimensions in bold are chosen for the reference roof construction.

The air inlets considered are fire resistant vents placed in the eaves. The purpose of this type of vents is to prevent fire from reaching the air cavity, avoiding a rapid spread of fire through the whole roof. The outlet of the cavity is assumed to be similar to the inlet design out of simplicity for this study. The inlet and outlet of the cavity are important for the ventilation due to the large air flow resistances they constitute. However, air flow resistance from different inlet and outlet designs is the topic of other research and only representative values, as presented further in Section 3.2.3, will be used in this study.

The surfaces in the air cavity are considered to be smooth and no obstacles in the cavity, such as bends, turns or structural components perpendicular to the rafters, are considered. The dimensions as well as assumed material properties of the roof construction are presented in Table 2.1, ordered from the exterior to the interior of the roof.

Table 2.1. Materials, dimensions and assumed material properties for the reference roof construction.

Part	Material	t [mm]	λ_m [W/m·K]	ε [-]	α_{sol}
External cladding	Metal sheet	0.6	-	0.7	0.8
Under layer felt	-	2	-	-	-
Roofing underlay	Wooden board	18	0.13	0.9	-
Air cavity	-	45	-	-	-
Wind barrier	Wooden board	3	0.13	0.9	-
Insulation	Mineral wool	400	0.036	-	-
Vapour barrier	Plastic foil	-	-	-	-
Internal cladding	Gypsum	13	0.25	-	-

3

Air cavity physics

This chapter presents the theory behind the physics governing the function of the air cavity. The chapter works as a foundation for the study and the assumptions made in the analysis of the results.

The physics of the air cavity can be described through the heat, air and moisture flow conditions of the air and the surrounding surfaces. The thermal conditions, described in Section 3.1, are governed by convective heat transfer to the air as well as radiative heat transfer between the surfaces. The air flow dynamics, described in Section 3.2, can be described through the flow caused by pressure differences either induced by wind pressure or thermal buoyancy as the air is heated. Finally, the moisture transfer, described in Section 3.3, is a combination of diffusive and convective transfer of moisture in the flowing air.

The coupled nature of the various processes means analytical solutions to the partial differential equations involved are difficult to achieve, consequently, experimental and numerical studies are to prefer in order to fully understand the physical behaviour of the air cavity.

For reference, the dimensions and coordinates of the air cavity are defined in Figure 0.1 and presented in the nomenclature.

3.1 Thermal conditions

The temperature in the air cavity is mainly dependent on the external climate, as long as the air cavity is ventilated with outdoor air and the air cavity is positioned in the outer parts of the roof construction. However, the impact of the outdoor climate on the air temperature varies considerably, depending on the design of the roof structure. There is also some impact on the temperature from the interior conditions, the magnitude of which depends mainly on the insulation thickness.

This section aims to present the theory behind the thermal conditions in the cavity. Note that all equations and relations presented assume steady-state conditions and that the heat capacity of materials is neglected. According to Arfvidsson et al. (2017), this assumption can be made for most real cases when analysing air cavities.

The air temperature at the inlet of the cavity is equal to the external temperature, but along the air cavity, the temperature will be affected by heat exchange between the air and the surfaces in the cavity. The heat exchange will affect the air temperature along the length of the cavity according to Equation 3.1 and 3.2, where the characteristic length L_0 [m] is a measure of the magnitude of the heat exchange (Arfvidsson et al., 2017). Figure 3.1 presents the temperature along the length of cavities of different characteristic length. In the figure, L is the length of the cavity.

$$T_a = T_0 - (T_0 - T_{in}) \cdot e^{-x_\theta / L_0} \tag{3.1}$$

T_a	air temperature in the cavity [°C]
T_0	effective air temperature in the cavity [°C]
T_{in}	temperature of inlet air [°C]
x	distance from inlet [m]
L_0	characteristic length [m]

$$L_0 = \rho \cdot c_a \cdot h \cdot u \cdot \frac{1}{\alpha_0} \tag{3.2}$$

ρ	density of air [kg/m^3]
c_a	specific heat capacity of air [J/(kg·K)]
u	air velocity in the cavity [m/s]
α_0	effective heat transfer coefficient of the cavity [W/(m^{2}K)], see Equation D.8a

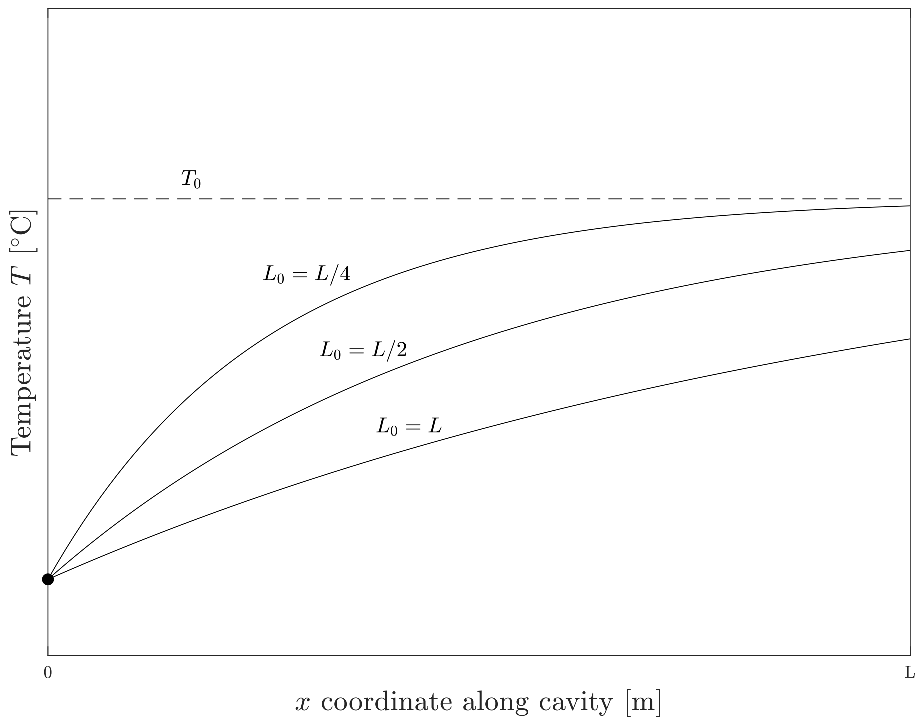

Figure 3.1. Theoretical air temperature variation along the cavity length.

The effective temperature T_0 [°C] represents the air temperature that would be reached if the length of the cavity was infinite, $x \to \infty$, or if the air flow was zero, $u = 0$. This temperature is dependent on the thermal conditions affecting the cavity, which are presented in the thermal network in Figure 3.2 (Arfvidsson et al., 2017).

As can be seen, the temperature in the cavity is affected by heat transmission to the internal air, heat transmission to the external air, direct solar radiation and long wave radiation. Inside the cavity there is convective heat transfer between the surfaces and the air as well as radiation between the two surfaces. All latent heat effects are neglected in this study.

The temperature T_0 can be found by reducing the thermal network. The reduced thermal network represent the same total heat flow to the air in the cavity as in the full network. The reduction of the network can be found in Appendix D.1 and the expression for the effective temperature T_0 is presented in Equation D.7c (Arfvidsson et al., 2017).

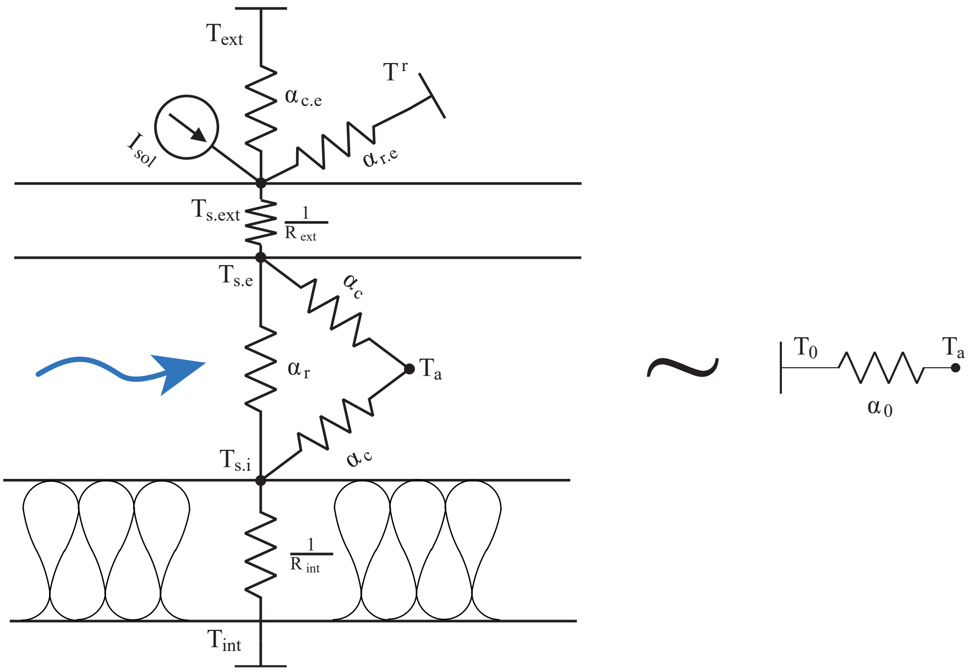

Figure 3.2. Thermal network of the air cavity.

T_a	air temperature in the cavity [°C]
T_{ext}	air temperature of external air [°C]
T_{int}	air temperature of internal air [°C]
T^r	temperature of surroundings facing the roof surface [°C]
I_{sol}	solar heat load, acting normal to the roof surface [W/m^2]
α_r	radiant surface heat transfer coefficient in the cavity [$W/m^2 \cdot K$]
α_c	convective surface heat transfer coefficient in the cavity [$W/m^2 \cdot K$]
$\alpha_{r.e}$	radiant surface heat transfer coefficient for the external roof surface [$W/m^2 \cdot K$]
$\alpha_{c.e}$	convective surface heat transfer coefficient for the external roof surface [$W/m^2 \cdot K$]
R_{ext}	thermal resistance of the external roof structure [$m^2 \cdot K/W$]

R_{int} thermal resistance of the internal roof structure $[\mathrm{m}^2 \cdot \mathrm{K/W}]$
T_0 effective temperature of the cavity [°C]
α_0 effective heat transfer coefficient of the cavity $[\mathrm{W/m}^2 \cdot \mathrm{K}]$

3.2 Air flow conditions

The air flow in an air cavity is dependent on the present driving forces and air flow resistances. Hagentoft (2001) presents the expression in Equation 3.3, where the air flow is proportional to the sum of driving forces and inversely proportional to the sum of flow resistances. Driving forces acting on the system are described further in Section 3.2.2 and flow resistances are described further in Section 3.2.3.

$$\dot{V} = \frac{\sum \Delta P}{\sum S} \tag{3.3}$$

$\dot{V}$ air flow rate $[\mathrm{m}^3/\mathrm{s}]$
ΔP driving force [Pa]
S air flow resistance $[\mathrm{Pa}/(\mathrm{m}^3/\mathrm{s})]$

The total air flow in a cavity can be calculated based on the mean air velocity u_{mean}, as presented in Equation 3.4.

$$\dot{V} = u_{mean} \cdot b \cdot h \tag{3.4}$$

3.2.1 Air flow characteristics

Depending on velocity and geometry of the cavity, the air flow behaves differently. Air flowing through an air cavity in a roof can generally be considered an incompressible fluid (Hansen, Stampe & Kjerulf-Jensen, 1992). For incompressible flows, the flow behaviour is described by the Reynolds number, Re [-], presented in Equation 3.5 (Hagentoft, 1991).

$$Re = \frac{\rho \cdot u_{mean} \cdot D_h}{\mu}, \tag{3.5}$$

ρ density $[\mathrm{kg/m}^3]$
u_{mean} mean velocity [m/s]
D_h hydraulic diameter [m]
μ dynamic viscosity $[\mathrm{Pa} \cdot \mathrm{s}]$

The hydraulic diameter for a rectangular duct can be expressed by Equation 3.6 (Kronvall, 1980).

$$D_h = \frac{2 \cdot h \cdot b}{h + b}, \tag{3.6}$$

Up until a critical value of Reynolds number, commonly defined as $Re_{crit} = 2000$ for air cavities (Hagentoft, 1991), the flow is described as laminar, with a parabolic velocity profile and limited interaction with the cavity edges. Above this value the flow enters a transitional regime, and above $Re = 4000$, the flow can be described as turbulent, with irregular motion causing a momentum exchange in the transversal direction of the flow (Kronvall, 1980). The influence on the flow pattern is depicted in Figure 3.3. The air velocity profiles for laminar and turbulent flow are shown in Figure 3.4.

Depending on the flow regime, the relation between the mean velocity, u_{mean}, and the maximum velocity, u_{max}, is different due to the differing velocity profile of the flow. For laminar flow the mean velocity can be calculated by Equation 3.7. For axisymmetric cavity cross sections the pipe factor is $f_p = 0.5$, while for a rectangular cavity of high aspect ratio has a pipe factor of $f_p \approx 0.67$ (ASHRAE, 2013).

$$u_{mean} = f_p \cdot u_{max} \tag{3.7}$$

f_p pipe factor [-]
u_{max} maximum air velocity [m/s]

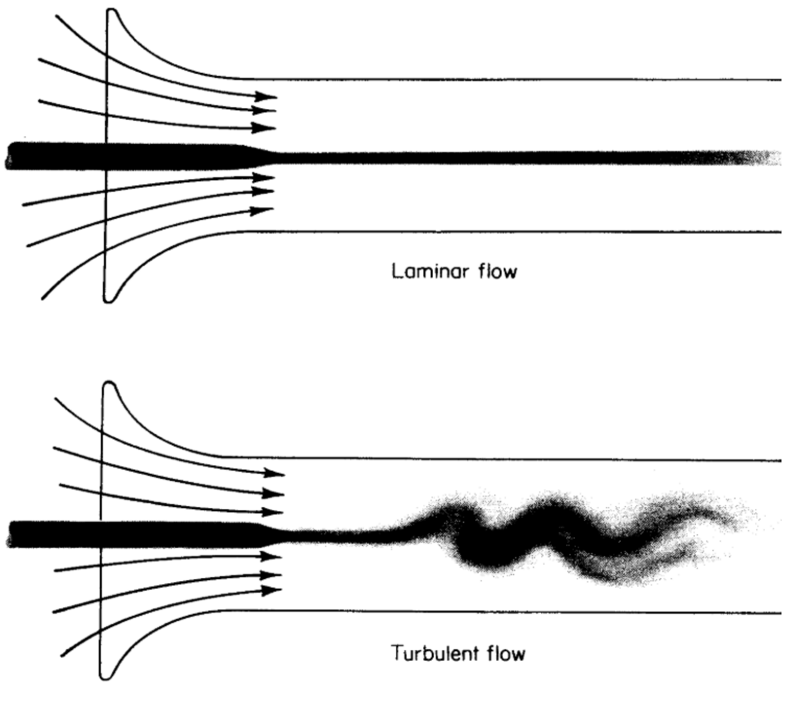

Figure 3.3. Visualisation of air flow behaviour for laminar and turbulent flow. Figure from Kronvall (1980) with permission.

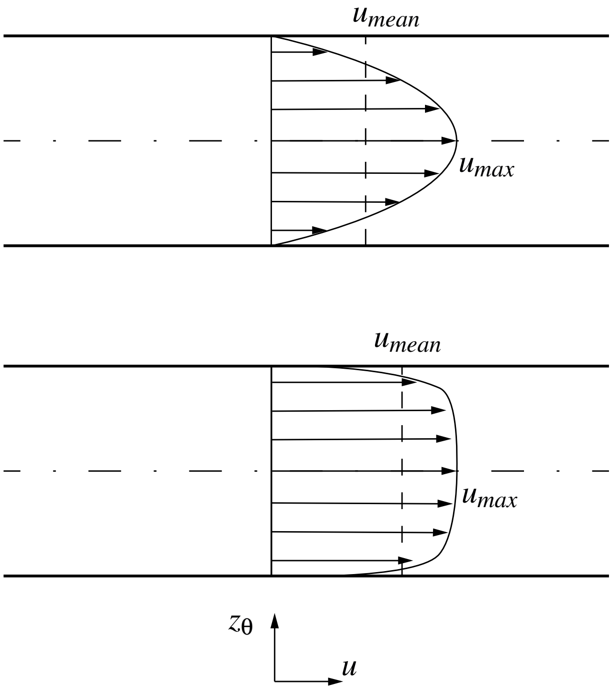

Figure 3.4. Velocity profiles for laminar and turbulent pipe flow. Adapted from Hansen, Stampe and Kjerulf-Jensen (1992).

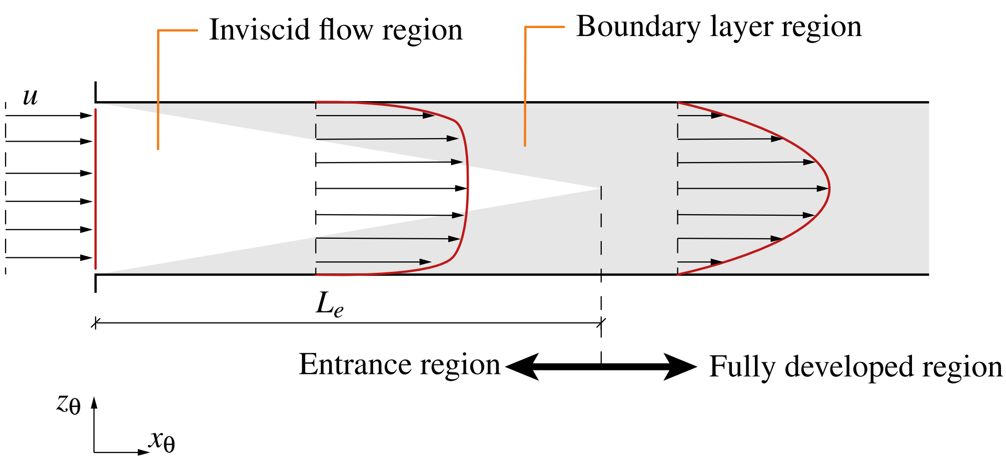

Figure 3.5. Development of laminar flow along entrance length L_e. Adapted from Incropera, DeWitt, Bergman and Lavine (2007).

When the air enters the inlet of the cavity, the flow contracts. The air enters with a near constant velocity and an abrupt velocity drop occurs near the edges. If no-slip conditions can be assumed in the cavity, air particles next to the wall are unable to move with the flow, causing friction. This friction causes the velocity profile to gradually change to a parabolic profile, as described in Figure 3.5. When this has been achieved, the flow is considered to be fully developed. The previous relations are only valid when fully developed flow can be assumed. The flow development is described through the entrance length L_e, which is calculated through Equation 3.8 (Incropera, DeWitt, Bergman & Lavine, 2007).

$$L_e = 0.05 \cdot Re \cdot D_h \tag{3.8}$$

Re	Reynolds number [-]
D_h	hydraulic diameter [m]

3.2.2 Driving forces

The air flow in a naturally ventilated air gap is driven by pressure differences between inlet and outlet. The pressure difference origins from two driving forces: *wind pressure* and *thermal buoyancy*. These two driving forces are the effect of external climatic conditions. Hence, they cannot be regulated in contrast with mechanical ventilation, but by changing the roof design, the impact they have on the air flow can be influenced.

According to Hagentoft (2001), the total pressure difference in the cavity can be expressed as the sum of the two driving forces, as presented in Equation 3.9.

$$\sum \Delta P = \Delta P_w + \Delta P_s \tag{3.9}$$

3.2.2.1 Wind pressure

Air flow in the air cavity driven by wind pressure is called forced convection. The forced convection is dependent on the dynamic pressure of the air and the wind pressure coefficients at inlet and outlet, schematically presented in Figure 3.6 and calculated according to Equation 3.10 (Hagentoft, 2001).

$$\Delta P_w = \frac{\rho \cdot U_{10}^2}{2} \cdot \Delta c_p \tag{3.10a}$$

$$\Delta c_p = c_{p1} - c_{p2} \tag{3.10b}$$

$$\Delta c_p(\Theta) = c_p(\Theta) - c_p(180 - \Theta) \tag{3.10c}$$

ρ_{ext}	density of the external air [kg/m^3]
U_{10}	wind speed at 10 m height, in the upstream undisturbed flow [m/s]
c_p	wind pressure coefficient [-]
Θ	wind approach angle to the inlet [°]

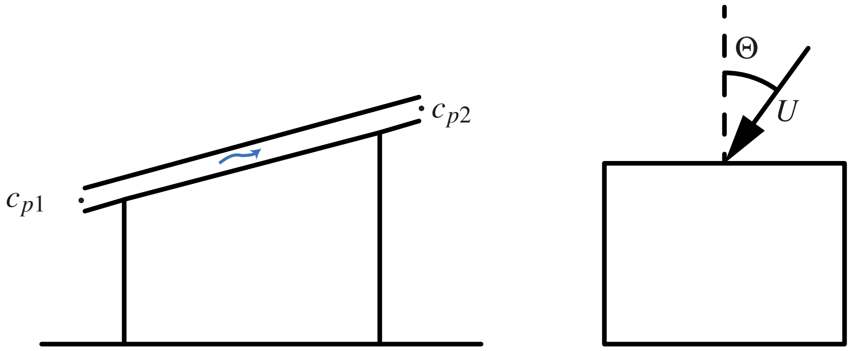

Figure 3.6. Schematic illustration of wind pressure coefficients.
To the left: Side view of the building showing the definition of c_{p1} and c_{p2}.
To the right: Top view of the building showing the wind angle of incidence Θ.

The value of Δc_p depends on many factors, including the shape and height of the building as well as the surroundings. Gullbrekken, Uvsløkk and Kvande (2018) found a Δc_p of 0.5-1.4 for one- to two-storey buildings with pitched roof and eaves-to-eaves ventilation. The same study also suggests that a Δc_p of 0.7 can be used for engineering evaluations of the wind-driven ventilation in the roof of such buildings. Arfvidsson et al. (2017) agrees that the value $\Delta c_p = 0.7$ can be used for estimations of wind driven ventilation in roof constructions.

3.2.2.2 Thermal buoyancy

Air flow driven by temperature differences is called thermal buoyancy or natural convection, sometimes referred to as free convection. Thermal buoyancy origins from differences in density of air with different temperature. Thermal buoyancy can also be expressed as a pressure difference, in that case called the stack effect (Hagentoft, 2001).

The air flow through the cavity driven by thermal buoyancy is dependent on the density differences between the air in the cavity and the ambient air. If the air in the cavity would have a constant temperature, the pressure difference between inlet and outlet of the cavity would increase with height, according to Equation 3.11 (Hagentoft, 2001).

$$\Delta P_s = (\rho_{amb} - \rho_{cavity}) \cdot g \cdot H \tag{3.11}$$

ρ_{amb} density of the surrounding air [kg/m^3]
ρ_{cavity} density of the air in the cavity [kg/m^3]
g gravity constant [m/s^2]

However, since the temperature in an air cavity will typically vary along the cavity length, according to the theory presented in Section 3.1, the density will vary accordingly, which means that the pressure difference will have a non-linear variation. The driving force is then best approximated by an integration of the density over the height from inlet of the cavity. This is presented in Equation 3.12 (Hansen et al., 1992). Note that this equation is based on the assumption of constant air temperature in each cross-section of the cavity.

$$\Delta P_s = g \cdot \int_0^H (\rho_{amb} - \rho_{cavity}) dz \tag{3.12}$$

Alternatively, the pressure difference can be described in terms of a temperature difference according to Equation 3.13 (Hagentoft, 1991).

$$\begin{aligned}\Delta P_s &= g \cdot \beta \cdot \rho_{amb} \int_0^H (T_a - T_{amb}) dz \\ &= g \cdot \beta \cdot \rho_{amb} \cdot \sin\theta \int_0^L (T_0 - (T_0 - T_{amb}) \cdot e^{-x_\theta / L_0} - T_{amb}) dx_\theta\end{aligned} \tag{3.13}$$

T_a	air temperature of the cavity [K], see Equation 3.1
T_{amb}	ambient air temperature [K]
T_0	effective temperature of the air cavity [K], see Appendix D.1
L_0	characteristic length of the channel [m], see Equation 3.2
g	gravity constant $[\mathrm{m/s^2}]$
ρ_{amb}	density of ambient air $[\mathrm{km^3}]$
β	coefficient of thermal expansion $[1/\mathrm{K}]$

A simplification of Equation 3.12, useful when the temperature is only known in few places along the cavity, would be to use the mean density of the cavity air to calculate the thermal driving force, which is presented in Equation 3.14a (Gullbrekken, 2018), or as a sum of mean densities multiplied with an assigned height, as presented in Equation 3.14b.

$$\Delta P_s = g \cdot \beta \cdot \rho_{amb} \cdot H \cdot (T_{a.mean} - T_{amb}) \tag{3.14a}$$

$$\Delta P_s = g \cdot \beta \cdot \rho_{amb} \cdot H \sum_{i=1}^{n} (T_{a.i-1,a.i} \cdot (z_i - z_{i-1}) - T_{amb}) \tag{3.14b}$$

The density of humid air is calculated through Equation 3.15 (Arfvidsson et al., 2017). The range of density of interest for this study is $1.092 - 1.394\ \mathrm{kg/m^3}$, corresponding to air temperatures from $-20\,^\circ\mathrm{C}$ to $50\,^\circ\mathrm{C}$ and relative humidity from 0% to 100%.

$$\rho = \frac{p_a}{R_a \cdot T_K} + \frac{p_v}{R_v \cdot T_K}$$
$$p_v = RH \cdot 6.1078 \cdot 10^{\frac{7.5 \cdot T}{T_K}} \tag{3.15}$$

p_a	partial pressure of dry air, 100325 Pa at ground level
R_a	specific gas constant for dry air, 287.0058 $J/(kg \cdot K)$
p_v	pressure for water vapor [Pa]
R_v	specific gas constant for water vapor, 461.4964 $J/(kg \cdot K)$
RH	relative humidity [-]
T_K	temperature [K]
T	temperature [°C]

3.2.3 Air flow resistances

Air flow resistance in a cavity is expressed as S [Pa/(m^3/s)] but can also be presented as a pressure loss, i.e. a difference in pressure ΔP_{loss} [Pa], which is the same as the driving force for a system in steady-state, see Equation 3.16.

$$\sum S = \frac{\Delta P_{loss}}{\dot{V}} \tag{3.16}$$

To calculate the total pressure loss for a system the pressure losses for each part has to be combined. For a cavity, the resistances are in series, which means that the total pressure loss can be calculated as the sum of the pressure losses for each part. Each part is either defined as pressure loss caused by friction over a length, or as local pressure losses, as presented in Equation 3.17a (Hagentoft, 2001). The same approach is applicable for flow resistances, as presented in Equation 3.17b.

$$\Delta P_{loss} = \sum \Delta P_f + \sum \Delta P_\xi \tag{3.17a}$$
$$\sum S = S_f + S_\xi = \frac{\sum \Delta P_f}{\dot{V}} + \frac{\sum \Delta P_\xi}{\dot{V}} \tag{3.17b}$$

ΔP_{loss}	total pressure loss of the cavity [Pa]
ΔP_f	frictional pressure loss [Pa]
ΔP_ξ	sum of local pressure losses [Pa]
$\sum S$	total flow resistance of the cavity [Pa/(m^3/s)]
S_f	flow resistance from frictional pressure loss [Pa/(m^3/s)]
S_ξ	flow resistance from local pressure losses [Pa/(m^3/s)]
$\dot{V}$	air flow rate [m^3/s]

3.2.3.1 Frictional pressure loss

The pressure loss in the cavity caused by friction is increased with increased cavity length and can be calculated with Equation 3.18, also called the general friction formula or Darcy-Weisbach formula (Kronvall, 1980).

$$\Delta P_f = \lambda_f \cdot \frac{P_d \cdot L}{D_h} \tag{3.18}$$

P_d dynamic pressure of the fluid [Pa], see Equation 3.19
D_h hydraulic diameter [m], see Equation 3.6
λ_f friction coefficient [-]

The dynamic pressure of the air flow P_d is calculated according to Equation 3.19.

$$P_d = \frac{\rho \cdot u_{mean}^2}{2} \tag{3.19}$$

ρ air density [kg/m^3]
u_{mean} mean velocity of the flow section [m/s]

For laminar flows, the friction coefficient λ_f is dependent on Reynolds number (*Re*) and a factor ϕ considering the dimensions of the cavity's cross-section, according to Equation 3.20a. The dimensional factor ϕ can be calculated approximately by Equation 3.20b (Kronvall, 1980), where *h* and *b* are defined as cavity height [*m*] and cavity width [*m*], respectively.

$$\lambda_f = \frac{64}{\phi \cdot Re} \tag{3.20a}$$

$$\phi = \frac{2}{3} + \frac{11}{24} \cdot \frac{h}{b}(2 - \frac{h}{b}) \tag{3.20b}$$

Re Reynolds number [-]

In addition to depending on the Reynolds number, the friction coefficient λ_f is also dependent on the factor ε/D_h for turbulent flows, where ε [-] is the absolute surface roughness and D_h the hydraulic diameter [m]. Kronvall (1980) presents a number of expressions for analytical determination of the friction coefficient for turbulent flow. Another way of finding the friction coefficient for turbulent flows is by the Moody diagram for pipe flow, which also covers the transition zone (Kronvall, 1980). However, turbulent flows will not be analysed in this study.

3.2.3.2 Local pressure losses

Local pressure losses can be expressed in various ways. According to Equation 3.21 (Hansen et al., 1992) the pressure loss is calculated from the dynamic pressure and the loss coefficient ξ, which is dependent on geometry and air velocity.

$$\Delta P_\xi = \xi \cdot P_d \tag{3.21}$$

Local pressure losses can also be expressed as a function of the flow rate, according to Equation 3.22a, dependent on the quadratic loss coefficient *qlc* [kg/m^7] (COMSOL

Inc., 2018). The relationship between the loss coefficients ξ and qlc is defined according to Equation 3.22b.

$$\Delta P_e = qlc \cdot \dot{V}^2 \tag{3.22a}$$

$$qlc = \frac{\xi \cdot \rho}{2 \cdot A^2} \tag{3.22b}$$

ρ air density [kg/m^3]
A is the cavity area perpendicular to the flow [m^2]

The local pressure losses considered in this study are those from inlet and outlet of the cavity. According to Hansen et al. (1992), $\xi = 0.44$ and $\xi = 1.0$ can be used for contraction of air at the inlet and expansion of air at the outlet of a channel with sharp edges, respectively. However, the design of inlet and outlet in a roof construction is often more complex and generates more pressure losses, compared to a single channel. Gullbrekken et al. (2017b) performed experimental tests on different eaves designs and found values in the range between $\xi = 0.7$ and $\xi = 17$ for a cavity width of 552 mm.

Alternatively, the pressure loss is calculated through the air flow resistance. This relationship is expressed in Equation 3.3. According to Hagentoft (1991), the flow resistance due to local losses at inlet and outlet for a cavity, can be calculated according to Equation 3.23, where the parameter K_c includes the flow rate dependency of the local pressure loss coefficients. Note that K_c has a very weak dependence on the Reynolds number.

$$\begin{aligned} S_\xi &= \mu \cdot \frac{Re}{b \cdot D_h^2} \cdot (1 + K_c(Re)) \\ K_c(Re) &= \begin{cases} 0.98 \cdot Re^{-0.03} & \text{if } Re < 1000 \\ 10.59 \cdot Re^{-0.374} & \text{if } 1000 < Re < 2000 \end{cases} \end{aligned} \tag{3.23}$$

μ the fluid dynamic viscosity [Pa $\cdot$ s]
Re Reynolds number [-]
D_h hydraulic diameter [m]

The reference roof construction includes inlet vents, as presented in Section 2.3, which also gives a flow resistance to the system. From experimental tests, one type of fire resistant inlet vent, with the dimensions 500x154 mm, was shown to have a pressure loss that could be approximated with Equation 3.24 (R. Strøm, personal communication, January 31, 2019).

$$\Delta P_{vent} \approx 1500 \cdot \dot{V}^{1.8} \tag{3.24}$$

3.2.4 Natural convection

Natural convection is the result of buoyant forces causing air of lower density to rise, creating a flow (Bejan, 2004). The other type of convection is called forced convection, which is when the flow is induced by external mechanical influence or wind (Bejan, 2004). Further, the situation where both types of convection are relevant is referred to as mixed convection. However, forced convection or mixed convection are not further investigated in this study.

To achieve a dimensionless representation of the ratio between driving forces and flow resistances for natural convection, described in Section 3.2.2 and 3.2.3 respectively , the Grashof number, *Gr*, is commonly used (Bejan, 2004) and can be calculated with Equation 3.25.

$$Gr = \frac{g\beta\Delta T H_c^3}{\nu^2} \tag{3.25}$$

g	gravitational constant [m/s^2]
β	coefficient of thermal expansion [1/K]
ΔT	driving temperature difference [°C]
H_c	characteristic vertical length [m]
ν	kinematic viscosity [m^2/s]

For air cavity flow, Hagentoft (1991) provides a definition of the cavity Grashof number, as presented in Equation 3.26. This formulation essentially combines the results of Equation 3.11 and 3.17b, removing the influence of all geometrical factors.

$$Gr_c = \frac{g\beta\rho H(T_0 - T_{in})}{\nu \cdot b \cdot \sum S} \tag{3.26}$$

T_0	effective temperature as defined in Equation D.7c [°C]
T_{in}	temperature of the air entering the cavity [°C]
$\sum S$	total flow resistance of the cavity [Pa/(m^3/s)]
ρ	air density [kg/m^3]

As evident from Section 3.1, the thermal conditions in the cavity are dependent on the material properties of the air and the thermal properties of the surrounding materials. This is characterised by the cavity Prandtl number Pr_c, as defined by Equation 3.27.

$$Pr_c = \frac{\nu\rho c_a}{\alpha_0} \tag{3.27}$$

c_a	specific heat capacity of air [J/(kg · K)]
α_0	effective heat transfer coefficient of the cavity [W/(m^2 · K)] see Equation D.8a

The air flow based on thermal conditions, cavity geometry and material properties can then be characterised through the cavity Rayleigh number Ra_c, as defined by Equation 3.28. This number can be used to predict the air flow rate assuming only thermal buoyancy as a driving force. The full derivation of this relationship is provided in Appendix E.

$$Ra_c = Pr_c \cdot Gr_c \tag{3.28}$$

3.3 Moisture conditions

As described in Chapter 2, one of the main purposes of the air cavity is the ventilation of excess moisture to avoid condensation and free water in the air cavity. The theory of this section is adapted from Arfvidsson et al. (2017).

The governing factor for whether the air cavity ventilation introduces or removes moisture from the construction at any given time is the relationship between the temperature of the cavity air, T_a, and the temperature of the air entering the cavity, T_{in}. If the air cavity is warmer than the entering air, drying typically occurs. Conversely, if the air cavity is cooler, moisture is absorbed in the cavity, and may cause condensation if the moisture buffering potential of the surface materials is low.

The potential for moisture transport is defined by Equation 3.29a. To calculate the average moisture exchange between the cavity air and the cavity walls, the moisture flux can be calculated according to Equation 3.29b. Note that the absolute humidity, v_{out}, of the air exiting the cavity cannot exceed the absolute humidity of saturation, v_s, for the present temperature of the flowing air, T_{out}.

$$G = \dot{V} \cdot (v_{out} - v_{in}) \tag{3.29a}$$

$$g = h \cdot \frac{u_{mean}}{L} \cdot (v_{out} - v_{in}) \tag{3.29b}$$

G	moisture flow [kg/s]
g	moisture flux [kg/(m^{2}s)]
$\dot{V}$	air flow rate [m^3/s]
v_{in}	absolute humidity of the air entering the cavity [kg/m^3]
v_{out}	absolute humidity of the air exiting the cavity [kg/m^3]
h	cavity height [m]
u_{mean}	mean air velocity [m/s]
L	cavity length [m]

This relationship implies that the potential for drying is dependent both on the air flow and the thermal conditions in the cavity. An increased air flow would improve drying only when the cavity air is also warmer in the roof cavity than in the outdoor air.

The risk for condensation is largely dependent on the potential for the surface materials in the cavity to buffer moisture when long-wave radiation causes low roofing temperatures during nighttime, and then to quickly dry out when the roof is heated by solar radiation during daytime.

4

Experimental study

The experimental study was performed at the Byggforsk laboratory at NTNU in Trondheim, Norway, in collaboration with SINTEF Byggforsk and the Master's thesis student Nora Bunkholt. The complete study is also described in detail in the article Bunkholt et al. (2019).

The experimental study was performed with the aim of finding an empirical relationship between air cavity design and air flow driven by thermal buoyancy. The design parameters of interest are presented in Section 2.3 but the experimental study was limited to only studying different cavity heights and roof inclinations due to limitations of the experimental rig, further described in Section 4.1.1.

The scope of the experimental study included testing of over-temperature on the roofing compared to the ambient air, i.e. heating of the roofing. Hence, under-temperature in the air cavity or heating due to thermal transmission through the roof construction from the internal conditions were not studied. The phenomenon tested corresponds to an external roof surface heated by solar radiation, further described in Chapter 8. The heated roofing was achieved by a heating foil installed on the top surface inside the air cavity, and temperatures and air velocities were measured during the tests.

4.1 Experimental set-up

The objective of the experimental study was to test various cavity heights alongside various inclinations and for different heat intensities applied to the heating foil. The geometric set-ups tested are presented in Table 4.1 and for each set-up, four heat intensities Q were applied to the heating foil: 9 W, 36 W, 81 W and 144 W.

Table 4.1. Studied cavity heights and roof inclinations in the experimental tests. For each set-up, four heat intensities Q were applied to the heating foil: 9 W, 36 W, 81 W and 144 W.

h [mm]	23	36	48	70
θ [°]	5/10/15/30/45	5/10/15/30/45	5/10/15/30/45	5/10/15/30/45

The studied cavity heights were chosen based on Norwegian standard heights of battens used for air cavities (Gullbrekken et al., 2017b), which differ slightly to the Swedish standard batten heights, as presented in Section 2.3. The studied inclinations were chosen with the aim of studying as wide of a range as possible in the laboratory, and of studying the difference between low- and high-inclination roofs.

The heat intensity on the heating foil was regulated by adjusting the voltage level, U [V], and combined with the electric current, I [A], the heat intensity Q [W] was calculated according to $Q = U \cdot I$. The maximum heat intensity tested was chosen based on the voltage limitation on heating foil (maximum 240V) and the other levels of heat intensity correspond to an evenly difference in the applied voltage level (180V, 120V and 60V, respectively).

4.1.1 Experimental rig

The laboratory model used for the experimental study was designed and built as part of the PhD thesis of Gullbrekken (2018), and modified for this study. The rig is shown in Figure 4.1a and consists of a wooden structure and an aluminium cover of length 3500 mm and width 552 mm, with a space in between representing the air cavity. The width corresponds to the typical Swedish and Norwegian construction method with the underlayer roof carried by 48 mm battens with a centre to centre distance of 600 mm. Hinges at the cavity inlet allow the cavity to be inclined, keeping the inlet height over the laboratory floor constant and varying the outlet height.

The cavity in the roof model is shaped as a rectangular duct as shown in Figure 4.1b, with an open inlet and outlet, and no obstructions within the cavity. This corresponds to the cavity type with a separate underlayer roof and wind barrier, as described in Figure 2.2. To achieve the different desired cavity heights (see Table 4.1), 30 mm wide battens made of XPS material were mounted to the inside walls of the aluminium box, amounting to a final cavity width of 492 mm.

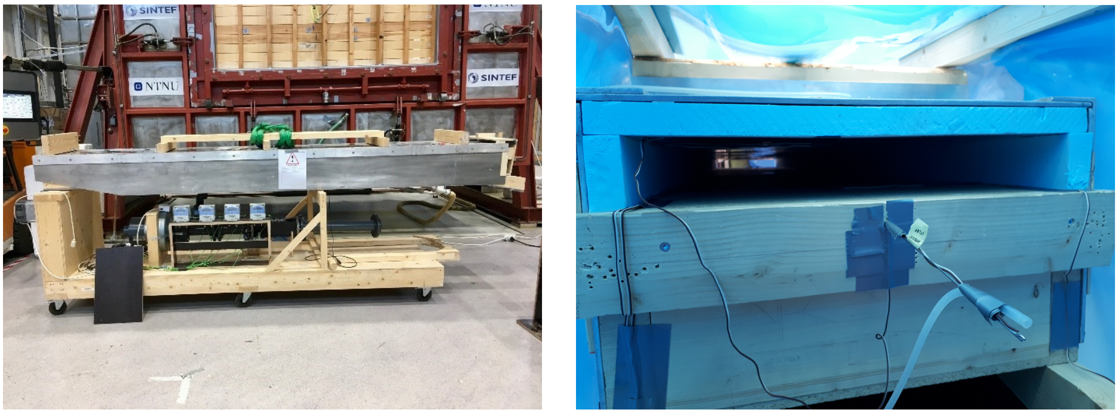

(a) The rig seen from the long side.

(b) The rig seen from the short side, looking through the cavity.

Figure 4.1. The rig used for the experimental study.

The roof model was initially built and used to study the local loss coefficients caused by different batten arrangements within the cavity (Gullbrekken, Kvande & Time, 2017a). To study the effects of thermal buoyancy, heating was achieved by mounting a heating foil

(Flexwatt F40-60W-230V (Flexwatt, 2019)) onto the upper surface of the cavity, separated from the aluminium box by an XPS-insulation to improve the effect of cavity heating, as can be seen in Figure 4.2c. The heating foil was controlled through two serially connected DC voltage controllers (PE 1648 DC Power supply 150V-3A), regulating the heat intensity.

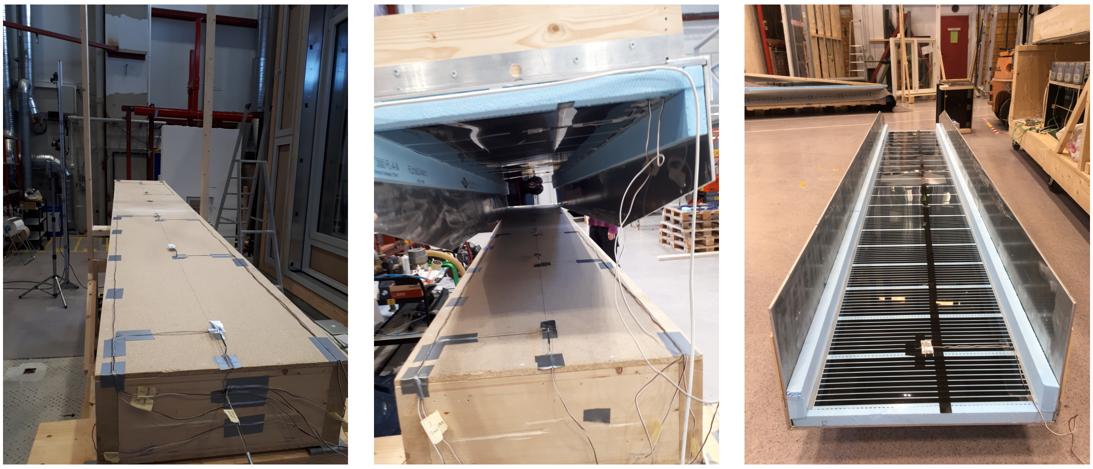

(a) Bottom part **(b)** Mounting of the top **(c)** Top part

Figure 4.2. The construction of the experimental rig before testing.

The estimated thicknesses and assumed material properties of the rig components are shown in Figure 4.3 and listed in Table 4.2 (Hagentoft, 2001; Arfvidsson et al., 2017), resulting in the thermal network presented in Figure 4.4. The heat intensity Q is assumed to spread evenly over the whole heating foil.

Table 4.2. Materials, dimensions and assumed material properties in the experimental rig.

Part	Material	t [mm]	λ_m [W/m·K]	ε [-]
External cover	Aluminium	6	200	0.9
Insulation above cavity	XPS	30	0.033	-
Top surface of cavity	Heating foil	-	-	0.9
Air cavity	-	h	-	-
Bottom surface of cavity	Fibre board	12	0.14	0.9
Insulation beneath cavity	Mineral wool	200	0.036	-
Lower board	Fibre board	12	0.14	-

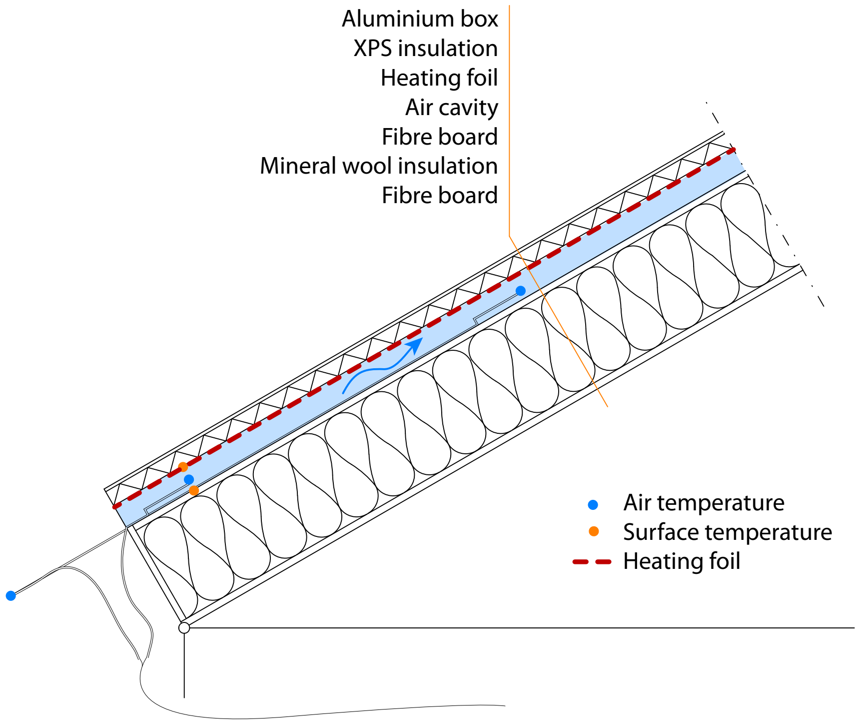

Figure 4.3. Detail of the experimental set-up near the inlet.

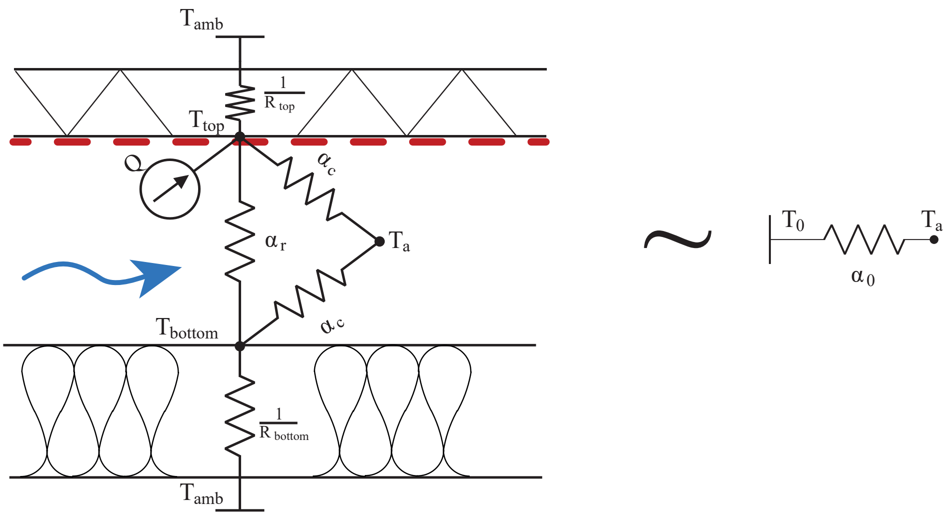

Figure 4.4. Thermal network of the experimental rig and test set-up.

Q	heat intensity on the heating foil [W]
T_a	air temperature in the cavity [°C]
T_{amb}	air temperature of surrounding air [°C]
α_r	radiant surface heat transfer coefficient in the cavity [$W/m^2 \cdot K$]

α_c convective surface heat transfer coefficient in the cavity $[\mathrm{W/m^2 \cdot K}]$
R_{top} thermal resistance of the top part of the roof structure $[\mathrm{m^2 \cdot K/W}]$ (including thermal surface resistances R_{si}, read more in Appendix D.1)
R_{bottom} thermal resistance of the bottom part of the roof structure $[\mathrm{m^2 \cdot K/W}]$ (including thermal surface resistances R_{si}, read more in Appendix D.1)

4.1.2 Measuring equipment

In the experimental tests, temperature and air velocity were measured. Temperatures were measured in the positions indicated by Figure 4.5, by using T-type thermocouples. The accuracy of the thermocouples is $\pm 0.5\,°\mathrm{C}$ and prior to installation in the experimental rig, they were immersed in a water bath which showed that the maximum difference was $\pm 0.5\,°\mathrm{C}$. The signals from these measurements were collected at a frequency of 1 Hz using a data-logger (Delphin Technology Expert Key 200L).

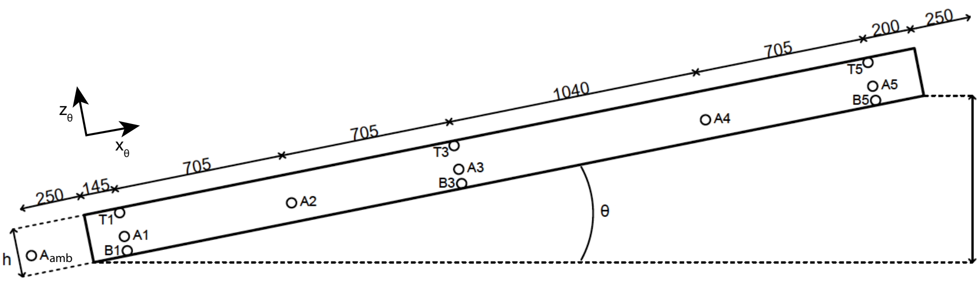

Figure 4.5. Positions [mm] of temperature measurements, in the experimental tests, for A - air temperature, T - top surface temperature and B - bottom surface temperature.

The thermocouples measuring air temperature in the cavity were fastened on metal wires, suspending the thermocouples at a distance of 15 mm from the bottom surface of the cavity and also ensuring the cord of the thermocouple to be at the same temperature for 100 mm, as shown in Figure 4.6a, which increases the accuracy of the measurement. Further, these thermocouples were sheathed from radiation from the heated top surface using a piece of aluminium tape, fastened horizontally on top of the thermocouples, as shown in Figure 4.6b. The ambient air temperature was measured with a thermocouple attached to a metal wire at a distance of 25 mm from the inlet of the cavity, as presented in Figure 4.5.

To measure surface temperatures, the thermocouples were attached to the surface using tape to ensure good contact, as shown in Figure 4.7. The aluminium tape was used here as well, with the intention of shielding the thermocouple from radiation, enabling measurements of only the temperature of the surface.

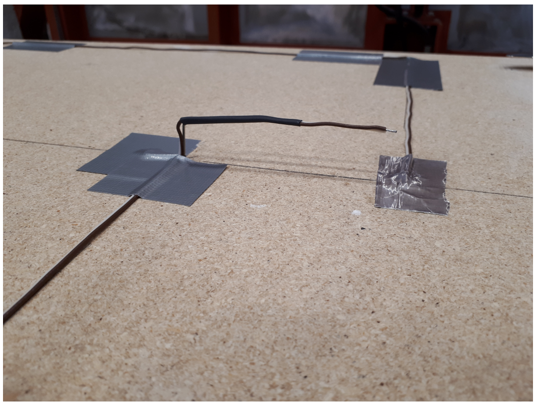

(a)

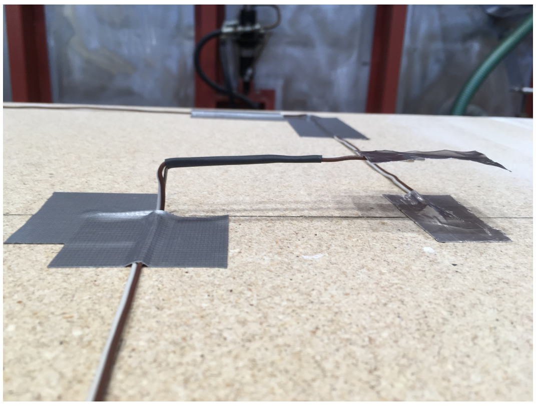

(b)

Figure 4.6. Thermocouple for air temperature measurements, before and after installing sheathing from radiation.

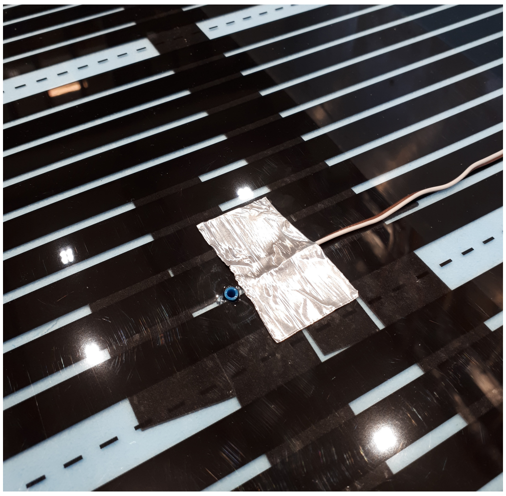

(a) Thermocouple at top surface.

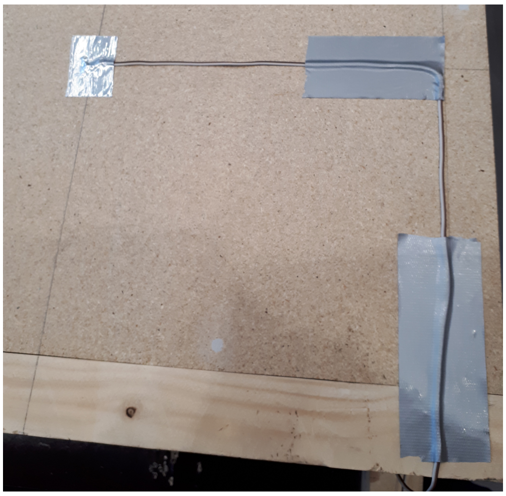

(b) Thermocouple at bottom surface.

Figure 4.7. Thermocouples measuring surface temperatures.

Velocity measurements were performed through two methods. Firstly, using an anemometer (SwemaAir 300) positioned at the centre-point of inlet and outlet, respectively. Secondly, smoke tests were performed, measuring the time required for smoke to pass from the inlet to the outlet by visual observation. Two different methods of smoke production were employed in the tests: 1) a smoke-pen with a lit wick (Figure 4.8a) and 2) a Dräger-tube involving a chemical reaction between air and fuming sulphuric acid (Figure 4.8b).

To perform the smoke tests, one person released the smoke at the cavity inlet, starting a stopwatch, while a second person observed the outlet, alerting the timekeeper when the first puff of smoke became visible upon exiting the cavity. As the smoke was quickly carried away by the flowing air, and the time was stopped upon the first smoke exiting the cavity, the measured time was assumed to correspond to the maximum velocity of the air.

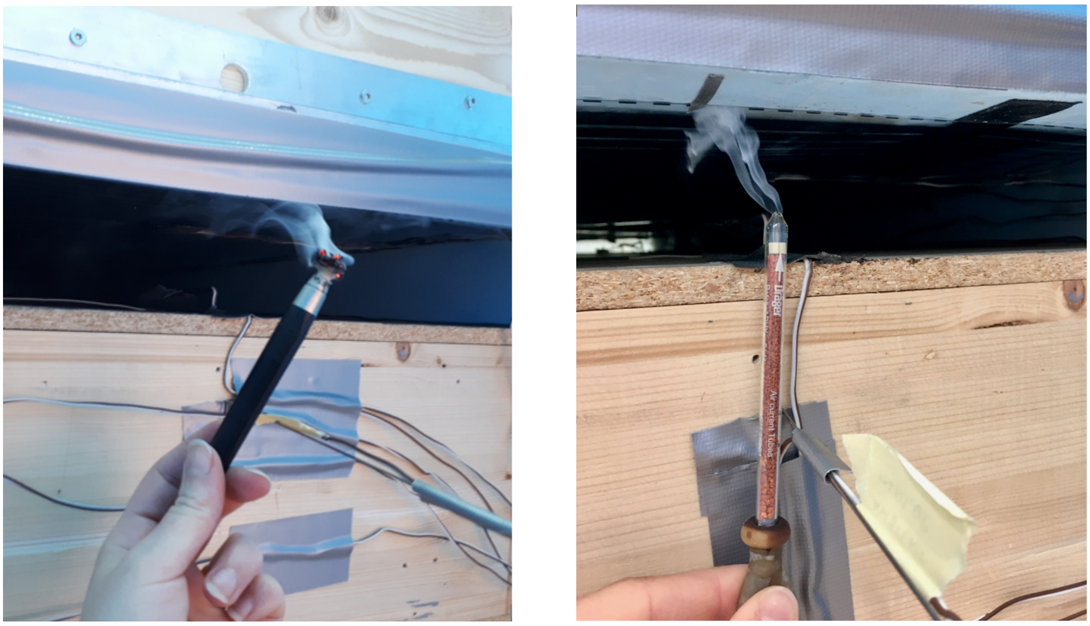

(a) Smoke-pen with a lit wick

(b) Dräger-tube

Figure 4.8. Smoke production methods used for velocity measurements.

4.1.3 Experimental procedure

In preparation of the measurements, battens of XPS were installed to achieve the desired cavity height. The aluminium box was lifted and screwed in place, and all joints and connections taped to ensure the air tightness of the cavity along the length (Eggen & Røer, 2018). To avoid the influence of air movements within the laboratory, the model was placed in a location far from the ceiling air outlets, and a plastic sheet was mounted above the in- and outlets to further shield the cavity and reduce forced air movements affecting the cavity flow. The cavity was then lifted to the desired inclination, and experiments were carried out for various heat intensity.

After setting the voltage controllers to the desired voltage, and allowing the temperature on the heating foil to stabilise, the measurements were started. Full steady-state conditions were not obtained due to time constraints. The relative humidity in the laboratory, as measured by a central hygrometer in the lab, was noted and for a period of 120 seconds, the model was left undisturbed. After this, the air velocity was measured using both anemometer and smoke tests. Five smoke releases were carried out for each test set-up and the final result was calculated as the mean of the five measured values, while the anemometer results were calculated as the mean between the measured values at inlet and outlet.

4.2 Experimental results

This section presents selected results from the experimental study, representative for the found phenomena. All measured results from the experimental study can be found in

Appendix A.

4.2.1 Measured thermal conditions

As presented in Section 4.1.2, temperatures were measured at 12 different positions during the tests. Figure 4.9 presents air temperature measurements, for different test configurations, along the cavity length x_θ. The results show that the air entering the cavity at ambient temperature is heated along the cavity length. The effect of an increased heat intensity applied to the heating foil, Q, is clearly higher air temperatures. An increased cavity height or inclination yield lower air temperatures which corresponds to higher air velocities (see results presented in Section 4.2.2).

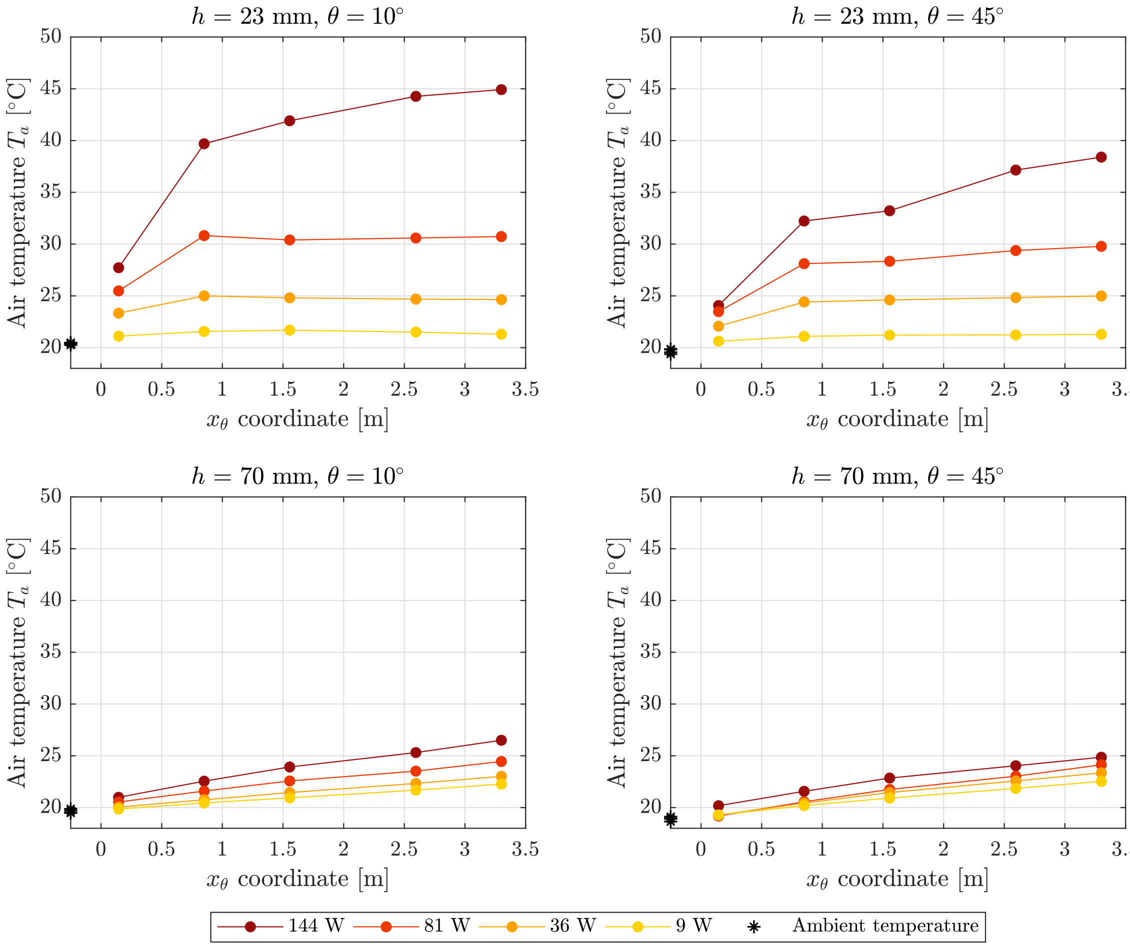

Figure 4.9. Measured air temperatures, T_a, along the cavity length, x_θ, for two different cavity heights and two different inclinations.

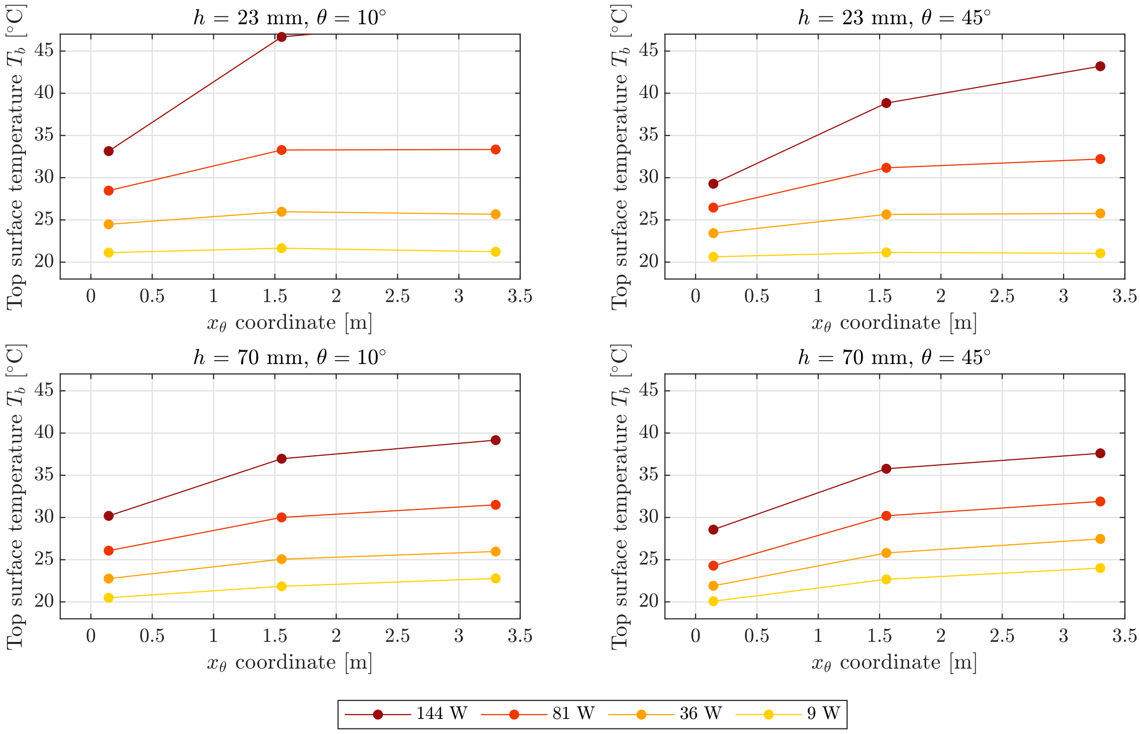

(a) Measured temperatures on top surface T_t along the cavity length x_θ, for two different cavity heights and two different inclinations.

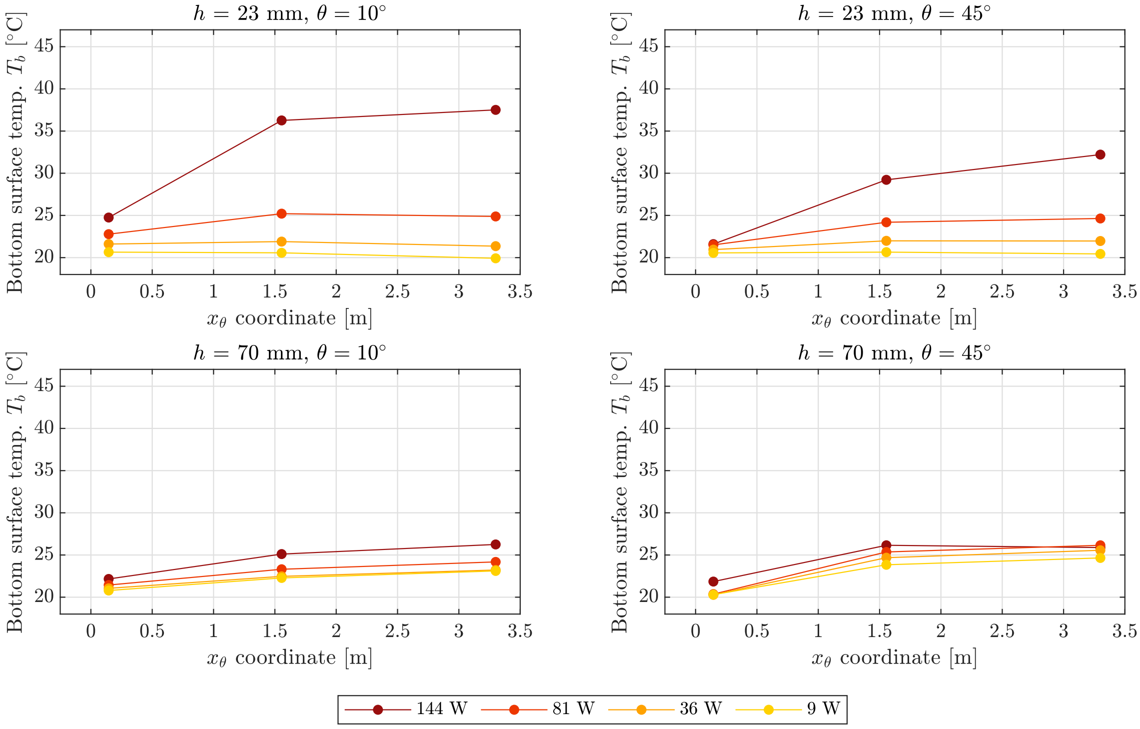

(b) Measured temperatures on bottom surface T_b along the cavity length x_θ, for two different cavity heights and two different inclinations.

Figure 4.10. Measured temperatures on the cavity surfaces along the cavity length x_θ, for two different cavity heights and two different inclinations.

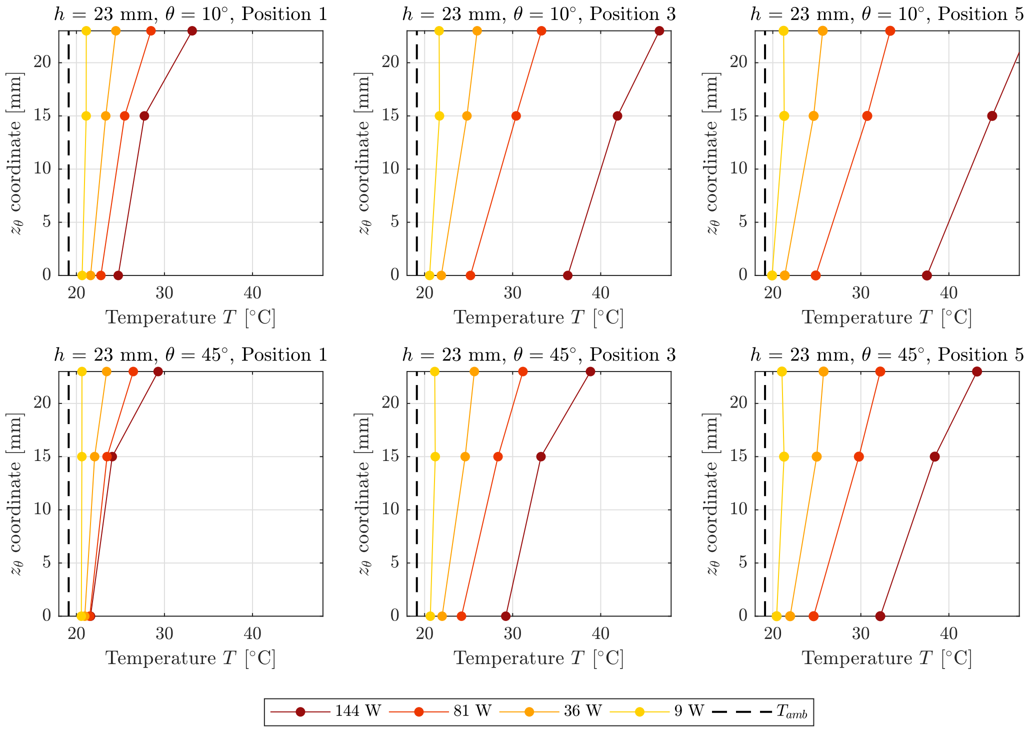

(a) Measured air and surface temperatures along the cavity height z_θ, in position 1, 3, and 5, for h= 23 mm and two different inclinations.

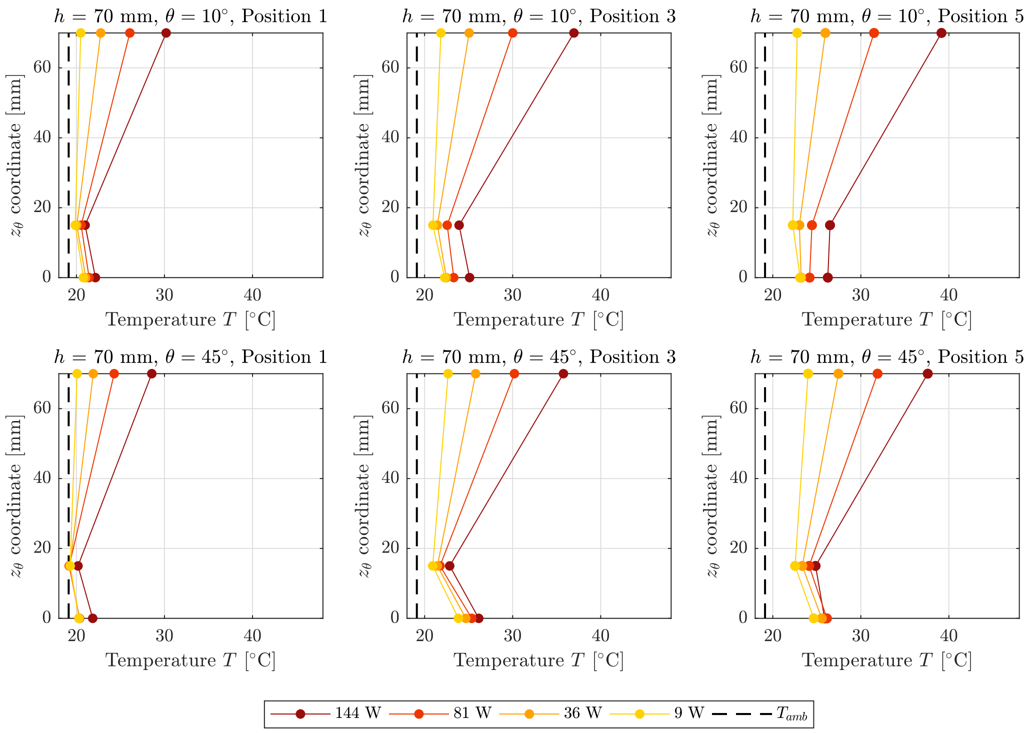

(b) Measured air and surface temperatures along the cavity height z_θ, in position 1, 3, and 5, for h= 70 mm and two different inclinations.

Figure 4.11. Measured air and surface temperatures along the cavity height z_θ, in three of the measuring sections of the cavity (see Figure 4.5), for two different cavity heights and two different inclinations.

Figure 4.10a and 4.10b present the measured results of temperatures on the top and bottom surfaces, respectively, along the cavity length, x_θ. The same pattern of temperature increase along the cavity length as for air temperature can be seen for the surface temperatures. For the top surface the measured temperatures show a clear dependence on the applied heating, Q, and a smaller difference when varying cavity height, h, and roof inclination, θ. For the bottom surface, the temperatures have the same dependency but with a slightly smaller impact of the applied heating.

Figure 4.11 presents the measured air and surface temperatures for the positions 1 ($x_\theta = 145\,\text{mm}$), 3 ($x_\theta = 1555\,\text{mm}$) and 5 ($x_\theta = 3300\,\text{mm}$) (i.e. measurements with the same x_θ-coordinate and shown in Figure 4.5), along the cavity height z_θ. Note that air temperatures were measured at a constant distance of 15 mm from the bottom surface of the cavity for all cavity heights h.

The results show that in general $T_{air} < T_{bottom} < T_{top}$ but for smaller cavities, where the air is heated more quickly, $T_{air} > T_{bottom}$ and the air temperature is approaching the temperature of the heated surface. The varying relation between the temperatures indicate the fact that steady-state conditions is not reached before the starting of the measurements. However, the relation between the air and surface temperatures is similar for the three measurement positions, for each test set-up, indicating the accuracy of the thermal network presented in Figure 4.4.

Considering the relationship between surface and air temperatures shown in Figure 4.11, the air is clearly heated between the measurement positions, but the shape of the transverse temperature profile $T_a(z_\theta)$ remains fairly constant. This implies that for the same air velocity, the convective heat transfer coefficient α_c is constant, which is consistent with theory (Hagentoft, 2001). The air temperatures are generally closer to the heated surface temperatures for smaller cavities, which may be explained both through a smaller L_0 for lower velocities, and through the fact that the air temperature was measured closer to the heated surface for lower cavity heights.

4.2.2 Measured air velocities

As presented in Section 4.1.2, air velocity through the cavity was measured by an anemometer at the inlet and outlet as well as with smoke tests of two different types. In Figure 4.12 the results from the anemometer measurements, $u_{anemometer}$, are presented in relation to the cavity height h, and roof inclination θ, for different heat intensities Q. The air velocities have an inconsistent pattern which correlates to the visual observation presented in Section 4.2.3 regarding difficulties in finding a stable value for the anemometer. While these results indicate that the smoke measurements are in the correct order of magnitude, they were deemed too unreliable to draw any further quantitative conclusions.

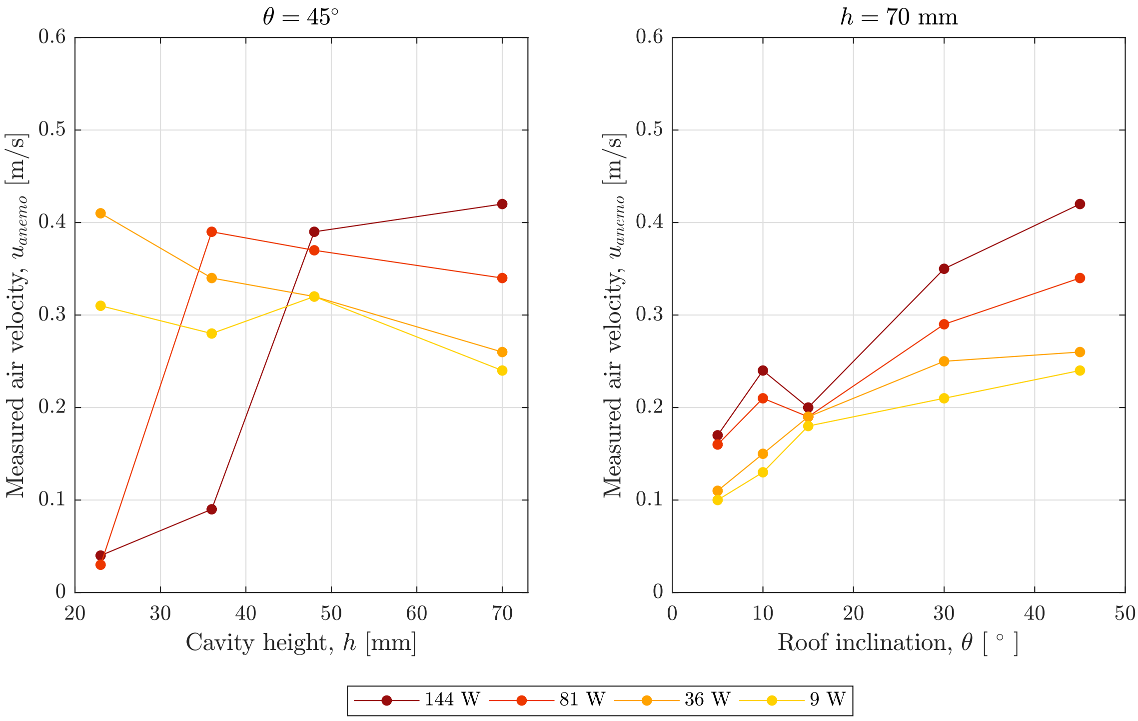

Figure 4.12. Air velocity, measured by anemometer, for $\theta = 45°$ and varying cavity height along with $h = 70$ mm and varying inclination.

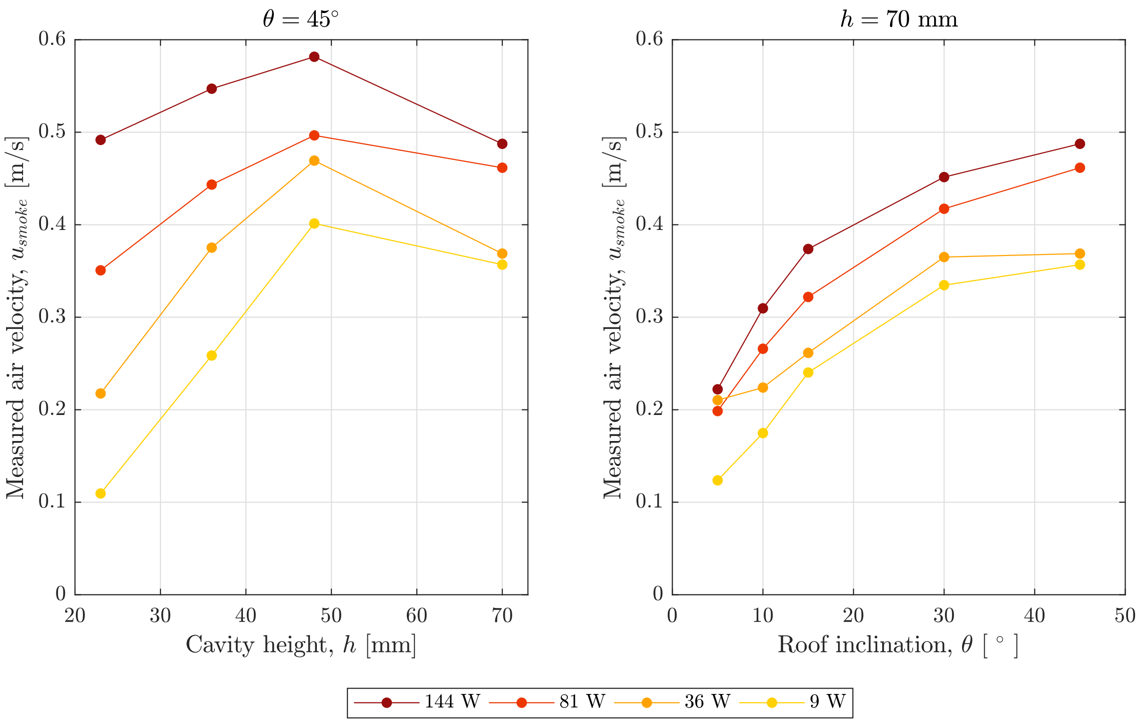

Figure 4.13. Air velocity, measured by smoke tests, for $\theta = 45°$ and varying cavity height along with $h = 70$ mm and varying inclination.

Figure 4.13 presents the measured air velocity from smoke tests, u_{smoke}, in relation to the cavity height h, and roof inclination θ, for different heat intensities Q. These results show a more consistent pattern for the velocity relative the other parameters compared to the anemometer measurements. The velocities measured in the smoke tests are higher than those measured by the anemometer.

The effect of an increased heat intensity, Q, is a clear increase in air velocity which is correlated to the increased temperatures (see the results presented in Section 4.2.1). An increased roof inclination also causes an increased air velocity, due to the increased driving force from the larger difference in height between inlet and outlet (described in Section 3.2.2.2). However, the relationship with an increased h is not as clear, as the velocity first increases and then decreases or shows a constant behaviour above $h = 48\,\text{mm}$, for high θ and low θ respectively. This will be further discussed in Chapter 7.

4.2.3 Visual observations

As the smoke measurements were performed using visual means, and the anemometer was held by hand and not fastened in a fixed position, the velocity results from both methods require scrutiny. The following observations were made during the velocity measurements:

- When using the anemometer, it was difficult to find a stable value for the air velocity, especially at the inlet.
- Generally for the smoke tests, a flow profile similar to the theoretical parabolic curve typical of laminar flow was observed.
- For lower air velocities, there was a tendency for the smoke to rise and move along the top surface of the cavity.
- For the highest inclinations, standing vortexes were observed near the sides of the cavity and some tendencies toward turbulent flow were present.
- For the lowest inclinations, there was some issues to see the smoke at all, as the low velocities caused the smoke to disperse, becoming difficult to observe.
- When smoke was released, a slight temperature increase was observed for the measurement points near the inlet.

4.3 Uncertainty analysis

This section presents measurement uncertainties and the supplementary measurements, performed with the aim of quantifying the uncertainties. The section also presents reasoning regarding the effect of complications during the experimental tests or factors which might affect the interpretation of the results.

Laboratory conditions

As presented in Section 4.1, the rig was covered by a plastic sheet to minimise the impact of air movements in the laboratory to the air flow in the cavity. Without any heating of the cavity, the air velocity beneath the plastic sheet, at the inlet and outlet of the cavity, was measured using an anemometer to be less than $0.01\,\mathrm{m/s}$. Hence, the air flow in the cavity can be considered undisturbed by air movements in the laboratory. However, the check of air velocity beneath the plastic sheet was performed only once and the movements in the laboratory could have varied due to external factors such as opening of doors.

The air temperature in the laboratory was kept relatively stable around $20\,^{\circ}\mathrm{C}$ while the relative humidity varied between 15 % and 25 %. Hence, the conditions of the air in the laboratory are considered to be stable, meaning that the results should not have been affected by changes in air properties dependent on humidity and temperature.

Radiation sheathing of thermocouples

Temperature was measured both in the air and at surfaces in the cavity using thermocouples, as explained in Section 4.1.2. The thermocouples measuring air temperature were shielded against radiation from the top surface, as was shown in Figure 4.6b. However, there was no shielding against radiation from the bottom surface or the sides of the air cavity. Hence, the measured air temperatures likely include the radiant heat exchange from the bottom surface and not only the air temperature in the position. The contribution from radiation from the bottom surface could have been in the range of $-5-2\,^{\circ}\mathrm{C}$ for the experimental tests, given conservative assumptions regarding the emissivity of the thermocouple. The calculation and assumptions for the radiative heat exchange can be found in Appendix D.3. The magnitude indicates that radiation from the bottom surface could have a large impact on the results for air temperature, compared to the accuracy of the thermocouples.

Additionally, the radiation sheathing of the thermocouples was performed without considering whether the aluminium tape was in contact with the measuring wires of the thermocouples. The effect of contact between the measuring wires and the tape is that the measuring wires measure the temperature of the aluminium tape as opposed to the air temperature in the section. The aluminium tape was intended to be horizontal, in the same height as the thermocouple, but during the experimental study the position of the tape might have changed. This would lead to measurements of the air temperature at a different height in the cavity than what was expected.

Regarding the air temperature profile along the cavity length, it can be seen in Figure 4.9 that the air temperature measured in position 1 is generally much higher than that of the ambient air. This implies that the air is heated very quickly when entering the channel, compared to the temperature rise in the remaining cavity. The magnitude of the measured temperature difference between inlet and position 1 indicates that the air temperature may be overestimated, possibly due to a radiative exchange with the hot surfaces or due to contact between the thermocouple and aluminium tape.

The thermocouples measuring surface temperatures were attached using aluminium tape in order to measure the temperature of the surface in contact only, and reducing the effect from radiation. Hence, as long as the aluminium tape was fastened properly, the thermocouples measuring surface temperatures should not have been influenced by radiation.

Steady-state thermal conditions without air flow

According to the theory presented in Section 3.1, the air temperature in the cavity should reach the temperature T_0 when no air movements are present, in steady-state conditions. A supplementary test was performed, aiming to find this temperature experimentally. The test was conducted on the experimental rig with an inclination of θ=0°, in order to have no air flow through the cavity, and for a cavity height of $h = 48$ mm. The test was performed for the heat intensities $Q = 9$ W, 36 W, 81 W and 144 W on the heating foil and during a time of 8 hours, aiming to find the steady-state thermal conditions for the system.

Figure 4.14 presents the measured temperatures at top surface, in the air and at the bottom surface from measurement position 3, where the influence of heat leakage to the inlet and outlet is the smallest. The results show that the temperatures increase rapidly in the beginning but then converges towards a value. However, none of the measurements seems to have reached steady-state conditions after 8 hours.

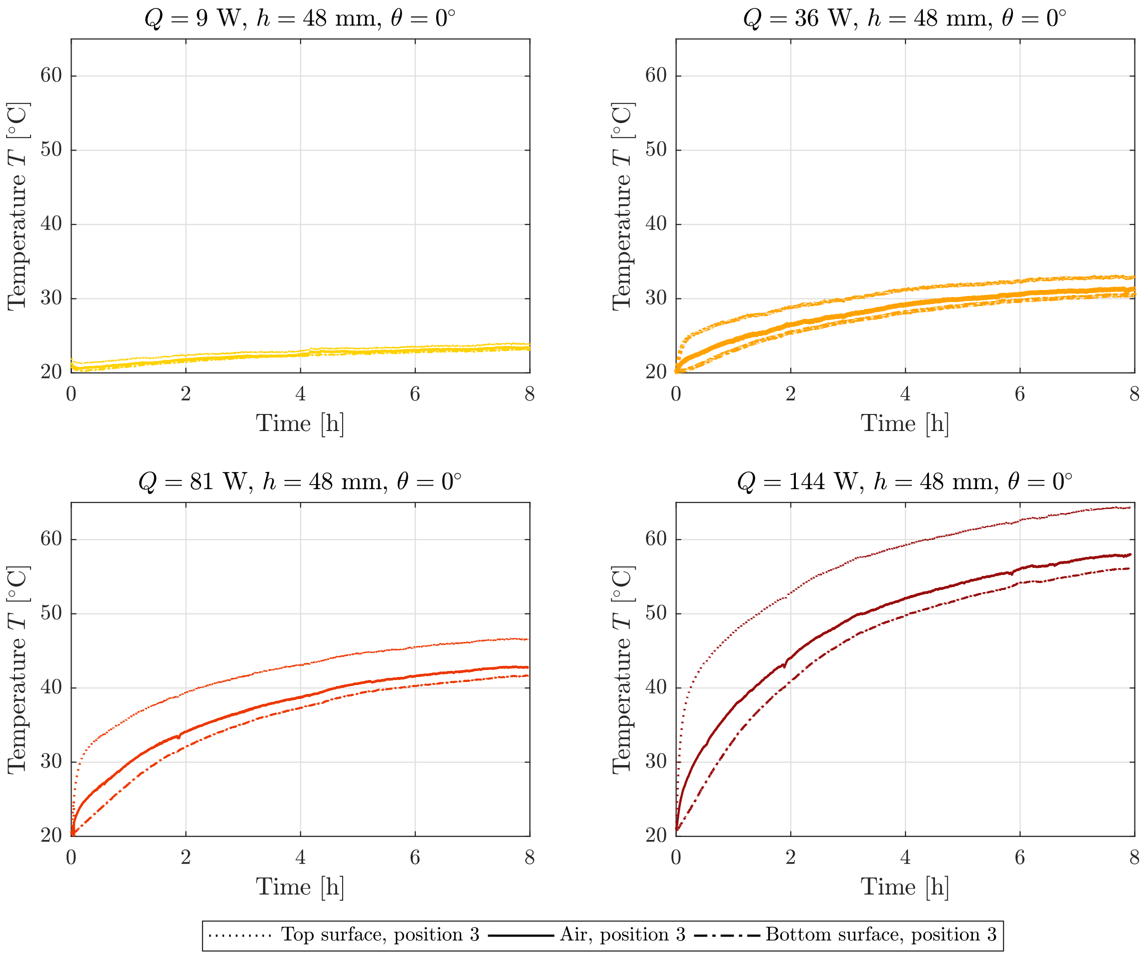

Figure 4.14. Temperature measurements in measurement position 3, during 8 hours, on the experimental model with no air flow ($\theta = 0$).

Surface contact between thermocouples and heating foil

As just mentioned, the thermocouples measuring surface temperatures were attached using aluminium tape to measure the surface in contact. This means that the surface in contact with the tape becomes significant for the measurements. The heating foil consisted of strips, where every second strip was an electrically conducting heating element (see Figure 4.15). The thermocouples were positioned on the heating foil without any consideration on how much of the tape was in contact with the heating elements or the strips between. This means that the top surface measurements could differ from each other, due to different contact surface of the electrically conducting heating elements.

To quantify the impact of different contact area between the tape and the current leading strips of the heating foil, a test was performed with thermocouples entirely on top of, partially on top of, and between the electrically conducting heating elements on the heating foil. Also, the test included thermocouples fastened with a different type of tape and measurements at the edges of the heating foil, near the sides of the cavity, see the positions of the thermocouples in Figure 4.15 and the results in Table 4.3.

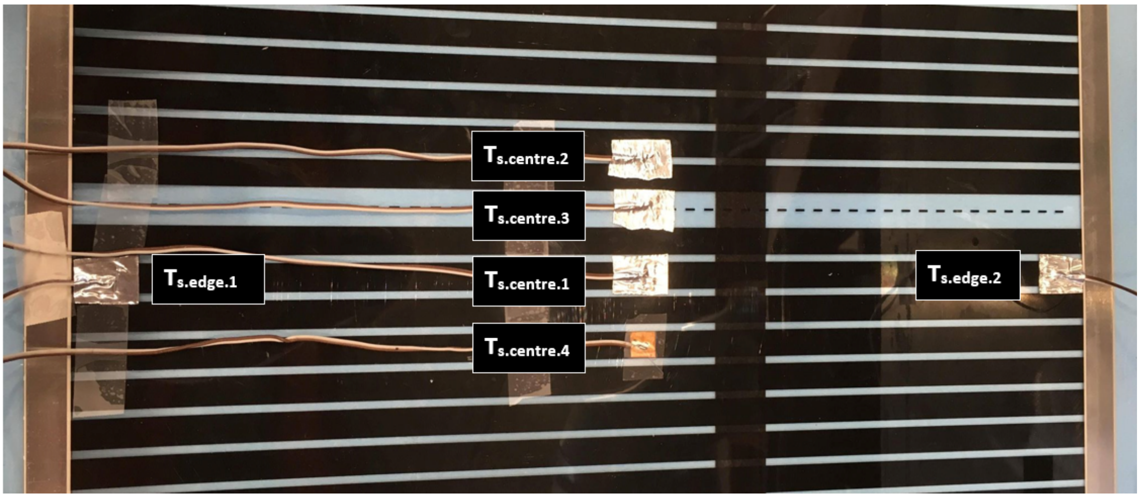

Figure 4.15. Positions of thermocouples during the uncertainty analysis of surface temperature measurements on the heating foil (i.e. the top surface).

Table 4.3. Uncertainty analysis of thermocouples measuring surface temperature on the heating foil (top surface).

	On heating el.	Partially on	Between	Different tape	Edge 1	Edge 2
Q [W]	$T_{s.c.1}$ [°C]	$T_{s.c.2}$ [°C]	$T_{s.c.3}$ [°C]	$T_{s.c.4}$ [°C]	$T_{s.e.1}$ [°C]	$T_{s.e.2}$ [°C]
9	21.07	20.93	20.54	21.20	20.78	20.79
36	23.73	23.51	22.30	23.49	22.40	22.06
81	27.36	27.03	24.52	26.72	24.61	24.06
144	32.00	31.47	27.19	30.88	27.52	26.68

The results show that the difference between the thermocouples fastened completely or partially on the electrically conducting heating elements ($T_{s.c.1}$ versus $T_{s.c.2}$) is small, especially for the low heat intensities, Q. The thermocouple fastened with no contact to the electrically conducting strips ($T_{s.c.3}$) and the thermocouple fastened with a different type of tape ($T_{s.c.4}$) show a larger difference from $T_{s.c.1}$, indicating that the positions of measurements are of importance. However, all the thermocouples measuring the top surface temperatures in the study ($T_{s.1}$, $T_{s.3}$ and $T_{s.5}$) were fastened with aluminum tape and at least partially on the electrically conducting strips. Hence, the results of top surface temperatures are considered to be trustworthy but small differences between them could be explained by differing areas of contact with the electrically conducting strips.

The temperatures measured at the edges of the cavity show a rather large difference from the results measured at the centre of the heating foil. This indicates that there are heat losses to the sides of the roof model and that the air passing through the cavity will be heated un-evenly from the top surface, meaning that the heat flux to the air in the cavity is likely to be smaller than what could be calculated theoretically, based on the applied heat intensity to the heating foil.

Human factors in air velocity measurements

The visual observations described in Section 4.2.3 indicate that the velocity measurements by smoke tests for higher velocities were performed with decent precision, while lower velocities caused the smoke to disperse and being difficult to observe. Other practical concerns such as higher cavity inclinations making measurements more difficult to perform may affect the integrity of these results.

The potential human errors involved in the time measurements may also affect the results and this error could affect the results in both ways (over- or underestimating the measured time). This since there was a human act in both the beginning and the end of the time measurements. Hence, the error due to the human factor is difficult to quantify or estimate. However, even though the results from using the anemometer gave very inconsistent results, and since this method of measuring air velocity was difficult, as described in Section 4.2.3, all measurements from the anemometer show lower air velocities than from the smoke tests. This may indicate that the smoke tests measured too high air velocities.

To validate the experimental method utilised for velocity measurements with smoke, one test set-up was reproduced 8 weeks after the initial tests. The test set-up with $h = 48\,\text{mm}$, $\theta = 15°$ was chosen, and tested for all heat intensities. Air velocity measurements were performed in the same way as carried out in the initial test run but with different people conducting the measurements from the initial tests. The results are presented in Table 4.4.

Table 4.4. Validation of the method used for velocity measurements.

Heat intensity Q [W]	Initial test u_{smoke} [m/s]	Control test u_{smoke} [m/s]
9	0.22	0.20
36	0.25	0.25
81	0.27	0.28
144	0.36	0.36

The results from the control test above appear to be in the same range as the results of the initial test run and the velocities which differ were measured to be both slightly higher and lower, compared to the initial results. This shows that the results from the initial tests are possible to replicate.

Characteristics of the smoke methods

To check for any differences between the two methods of smoke production, a supplementary test was performed for the two types of smoke. This test was performed for a cavity height of $h = 48\,\mathrm{mm}$, a roof inclination of $\theta = 15°$ and no heat applied to the heating foil, $Q = 0\,\mathrm{W}$. Five measurements were performed for each smoke type and the results are shown in Table 4.5.

The results show that the difference in velocity for the two smoke production methods is insignificant. However, the results also show that both types of smoke have a buoyancy force of their own, given that the results presented in Table 4.5 were obtained without any heat added to the system. This corresponds well to the visual observation of a temperature increase when smoke was released, as presented in Section 4.2.3.

Table 4.5. Uncertainty analysis of smoke production methods.

Test	Smoke pen [s]	Dräger-tube [s]
1	18.50	18.43
2	18.63	16.93
3	17.40	17.40
4	16.86	18.36
5	18.26	18.92
Mean value	17.93	18.01
Velocity [m/s]:	0.195	0.194

The assumption was made that the time for smoke to travel through the cavity corresponds to the maximum air velocity as driven by thermal buoyancy. This is likely to be true for higher air velocities as the smoke was clearly observed to quickly accelerate and follow the flow, exiting the outlet as a clear puff of smoke with a laminar profile. However, thermal buoyancy effects may have caused the smoke to rise within the cavity and follow a different path from the general air flow, thus moving with air which is more affected by friction losses. On the other hand, the buoyant effect of the smoke may have contributed to the velocity of the smoke, thus increasing the velocity of smoke compared to the air.

5

Numerical study

The numerical study was performed using the Finite Element Method implementation COMSOL Multiphysics. The aim of the numerical study was to replicate the experimental study and verify the empirical relations found. The same geometries and temperature conditions as in the experimental study were modelled, except that the cavity was modelled in two dimensions for the simulations to reduce the computational cost. Hence, assuming no influence from the cavity width on the air flow conditions or impact from heat losses to the sides. To simplify the calculations and assumptions involved, the simulations were performed for steady-state conditions.

5.1 Computational fluid dynamics

Computational fluid dynamics, CFD, is an umbrella term for a number of numerical solving methods for the Navier-Stokes equation, which describes the motion of viscous fluids (Pozrikidis, 2016). For an incompressible Newtonian fluid, the equation is written as presented in Equation 5.1.

$$\rho\left(\frac{\partial \mathbf{u}}{\partial t}+\mathbf{u}\cdot\nabla\mathbf{u}\right)=-\nabla p+\mu\nabla^2\mathbf{u}+\rho g \tag{5.1}$$

$\mathbf{u}$	fluid velocity [m/s]
g	gravitational constant [m/s^2]
p	fluid pressure [Pa]
ρ	fluid density [kg/m^3]
μ	fluid dynamic viscosity [Pa $\cdot$ s]

The equation is solved in conjunction with the continuity equation presented in Equation 5.2. The Navier-Stokes equation fulfils the thermodynamic law of conservation of momentum, while the continuity equation represents the conservation of mass (COMSOL, 2017).

$$\nabla\cdot\mathbf{u}=0 \tag{5.2}$$

The solution of these equations for particular boundary conditions is equivalent to predicting the fluid velocity and pressure within a specified geometry. However, the complexity of the equations makes finding analytical solutions impossible for many geometries. Instead, numerical solutions must be employed.

5.2 Simulation set-up

This section describes the numerical modelling and the settings used for the numerical modelling in COMSOL Multiphysics. To simulate natural convection, the Nonisothermal Flow multiphysics module from the CFD module was selected, including the Heat Transfer in Fluids as well as the Laminar Flow physics modules. The validity of the model and the results was corroborated through a convergence study and mesh refinement studies.

5.2.1 Geometry modelling

To reduce calculation times, a two dimensional representation of the air cavity was modelled. The length of the cavity was a constant 3.5 m, while the cavity height h and inclination θ were varied parametrically. The geometry was modelled using a simple rectangle to represent the cavity, as presented in Figure 5.1. Rather than modelling the actual geometry of the cavity inlet and outlet, which would require a far more complex mesh and the consideration of turbulence, Grille inflow and outflow boundary conditions were prescribed, further described in Section 5.2.2.

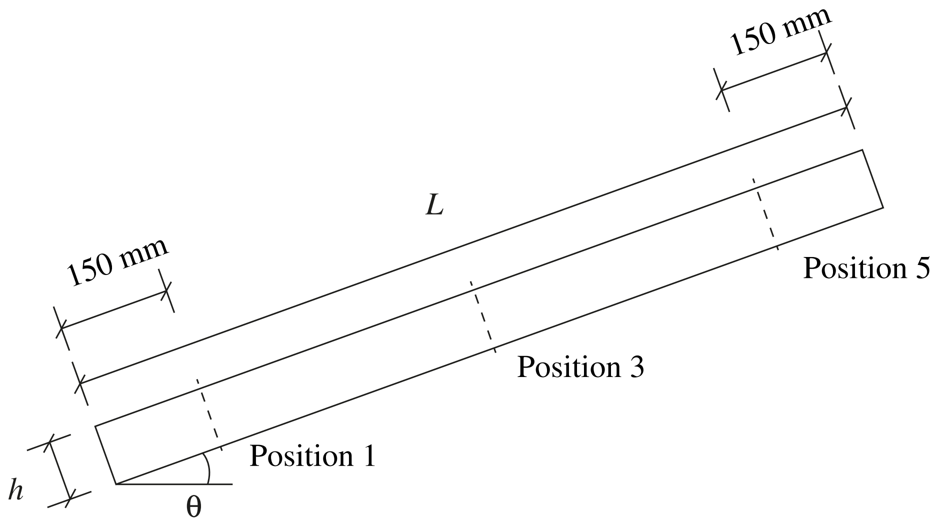

Figure 5.1. Geometry of the simulation model.

The mesh was constructed as a user-controlled mesh in COMSOL Multiphysics based off the "extremely fine" coarseness setting, and calibrated for fluid dynamics. The maximum element size was set to 0.01 m to achieve convergence at a reasonable computational cost. To improve convergence, the element aspect ratio was kept as low as possible. Different meshing methods such as a structured quad mesh were tested with limited impact on the result. Eventually, a free triangular mesh was selected for most of the domain, with a quad mesh used to represent the boundary layer of the top and bottom surface of the cavity. As laminar inflow and outflow was assumed, which is presented in Section 5.2.2, no edge refinement was done for the cavity inlet and outlet. An example of the resulting mesh can be seen in Figure 5.2.

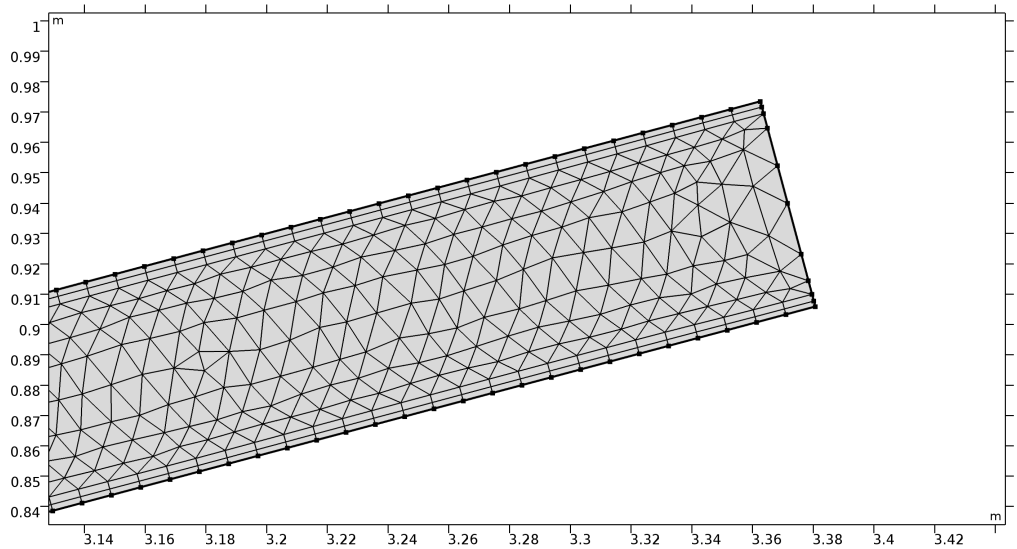

Figure 5.2. Example mesh used for the COMSOL Multiphysics simulations, for $h = 70\,\text{mm}$, $\theta = 15°$.

5.2.2 Non-isothermal flow modelling

The thermal boundary conditions are shown in Figure 5.3. The heat applied to of the heating foil was modelled through a heat flux q [W/m^2] corresponding to the experimental set-up, which was varied parametrically. The heat transmission losses through the cavity walls were modelled as convective heat flux boundary conditions, with the heat transfer coefficients $\alpha_{top} = \frac{1}{R_{top}}$ and $\alpha_{bottom} = \frac{1}{R_{bottom}}$, calculated through the thermal network shown in Figure 4.4 and the assumed material properties of the experimental rig, presented in Table 4.2. The temperature of the air entering the cavity was set to the ambient air temperature measured for each test. Radiation between the materials was modelled using diffuse surfaces with surface to surface radiation, and emissivity ε according to Table 4.2.

As a simplification, the air flow was assumed to be laminar for all the tests. The air flow was modelled using the boundary conditions described in Figure 5.4. For the inlet, a fully developed laminar flow is assumed, while for the outlet a free outflow is allowed. To model the effect of thermal buoyancy, gravity was active as a field condition. The assumed material properties of the fluid were chosen as the internal COMSOL Multiphysics settings for air. Due to software limitations, the air was considered to be dry.

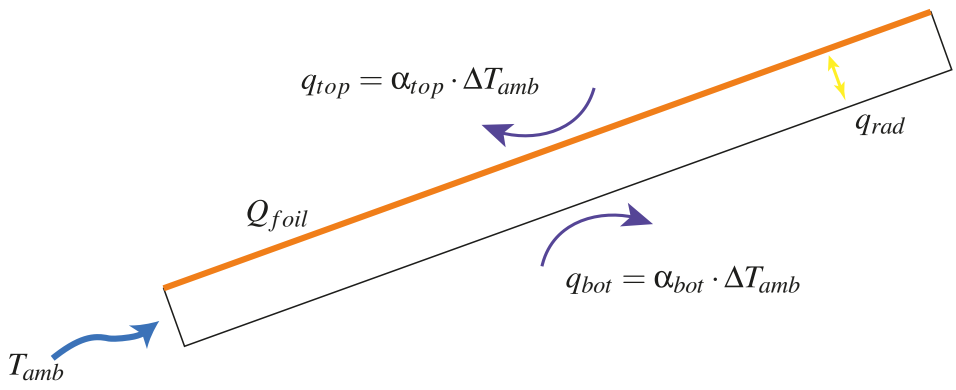

Figure 5.3. Boundary conditions for the Heat Transfer in Fluids (ht) physics module of COMSOL Multiphysics, used in the simulations.

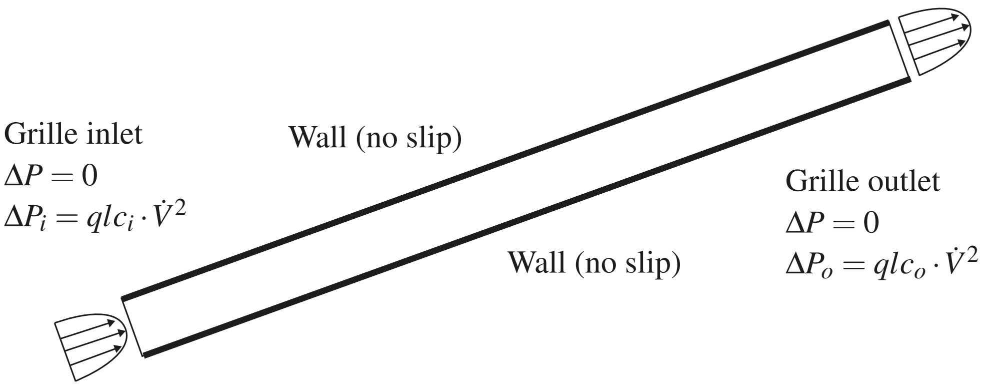

Figure 5.4. Boundary conditions for the Laminar Flow (spf) physics module of COMSOL Multiphysics, used in the simulations.

To represent the pressure losses caused by air contraction and expansion at the entrance and exits of the cavity, a Grille boundary condition was selected for the inlet and outlet. The Grille boundary condition imposes an entrance or exit pressure loss ΔP_e.

For the Grille boundaries, the pressure difference ΔP relative to the assumed ambient conditions ($P = 1\,\text{atm}$) was set to $0\,\text{Pa}$, corresponding to a case with no forced convection. The pressure loss ΔP_e was modelled using a quadratic loss coefficient qlc, calculated from Equation 3.22b with the recommended values of ξ from Hansen et al. (1992): $\xi = 0.44$ and $\xi = 1.0$ for inlet and outlet respectively.

The walls were modelled using a no slip condition, meaning the fluid velocity relative to the wall velocity is zero, i.e. $u = 0$ is prescribed at the fluid-solid interface (COMSOL Inc., 2018).

5.2.3 Solver configuration

The simulation was performed by solving the Navier-Stokes equations (Equation 5.1) for non-isothermal flow, calculating the field variables u, P and T. The initial values were set as $u_x = u_y = 0$, $P = 1\,\mathrm{atm} = 101.325\,\mathrm{kPa}$, $T = T_{amb}$, where T_{amb} was the ambient temperature of the corresponding experimental test.

In general the default settings of the Nonisothermal Flow multiphysics of COMSOL Multiphysics were used for the solver configurations. The simulations were performed for a steady-state solution. The relative tolerance for convergence was chosen to be 0.001.

A study of the mesh refinement was performed to establish an adequate mesh resolution. An element size of 0.01 m was shown to capture the thermal and fluidomechanic behaviour appropriately at a reasonable computational cost, with little improvement to the results upon further refining the mesh.

The following parameters were modified during the parametric sweep to model the thermal and geometric boundary conditions.

- Cavity height, h
- Roof inclination, θ
- Heat flux, q
- Ambient temperature, T_{amb}
- Entrance and exit loss coefficient, qlc_i and qlc_o
- Maximum mesh element size

5.3 Simulation results

This section presents the results of the numerical study. Selected representative results are shown, while the full results are presented in Appendix B.

From 80 configurations used in the parametric sweep, 58 solutions achieved convergence. Some of the divergent configurations were modified to improve convergence, with limited success, likely due to numerical issues with the boundary conditions. Nevertheless, the obtained solutions were found to be consistent with each other and with theory, allowing the results to be used with confidence.

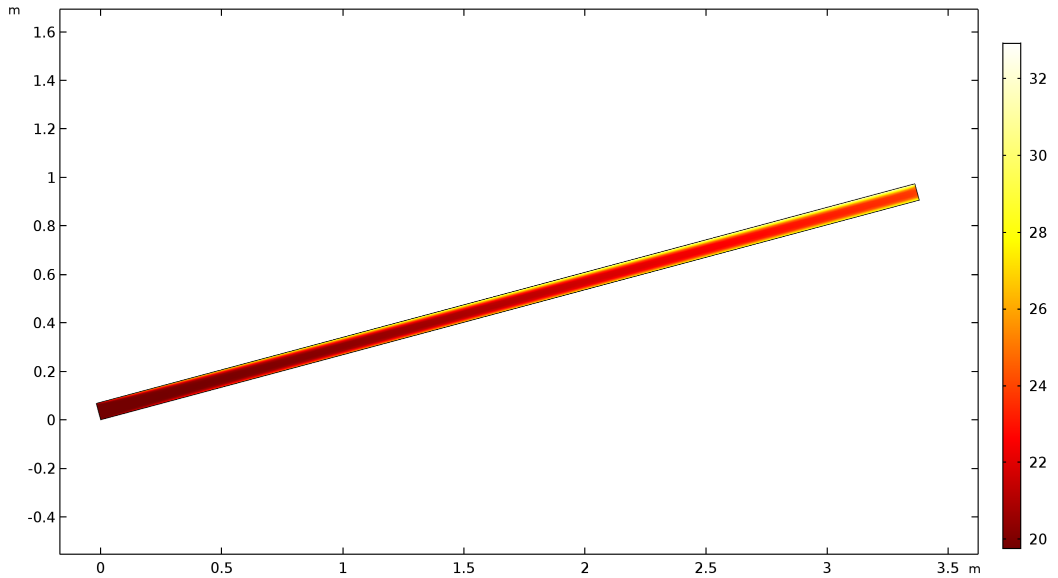

Figure 5.5. Simulated air temperatures [°C] in the cavity for $h = 70\,\text{mm}$, $\theta = 15°$ and q [W/m^2] corresponding to $Q = 144\,\text{W}$.

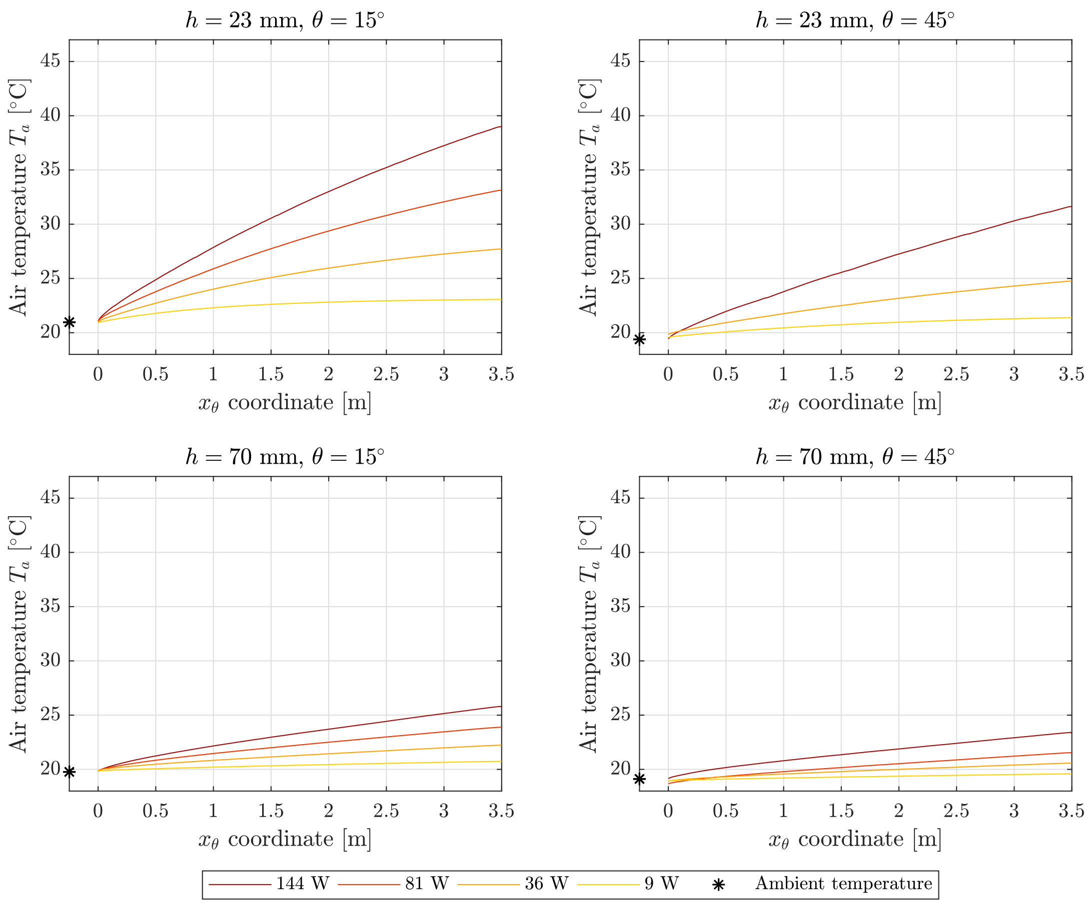

Figure 5.6. Simulated air temperatures, calculated as an average over each section along the cavity length x_θ.

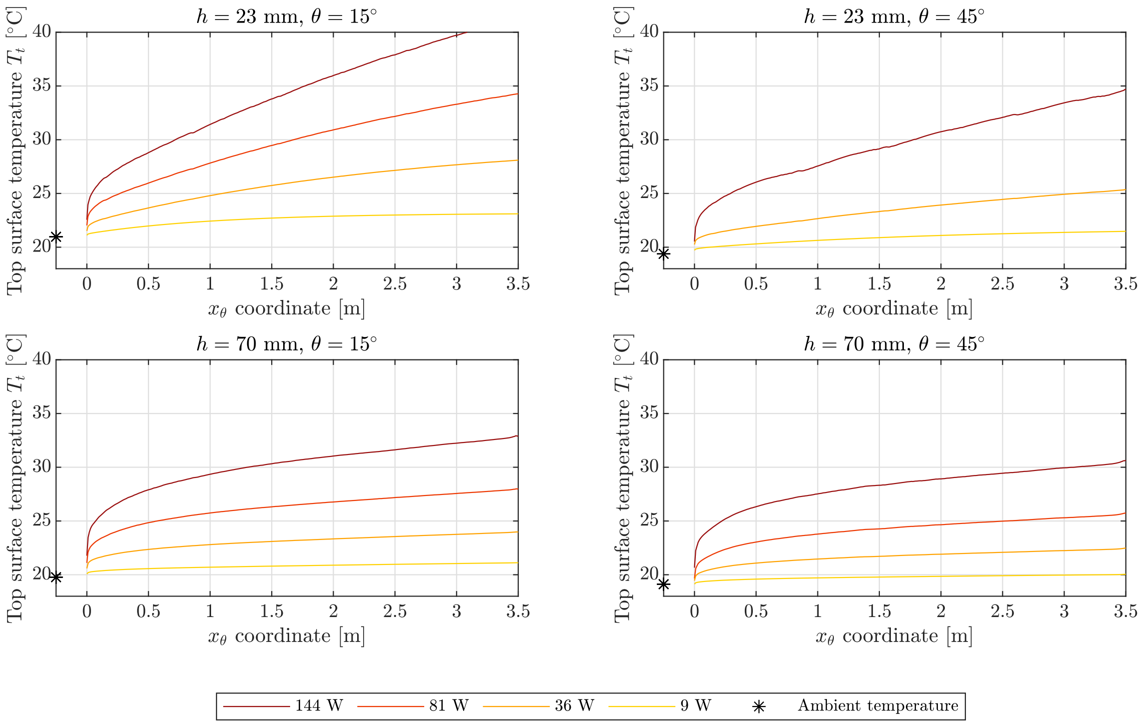

(a) Simulated temperatures on top surface, along the cavity length.

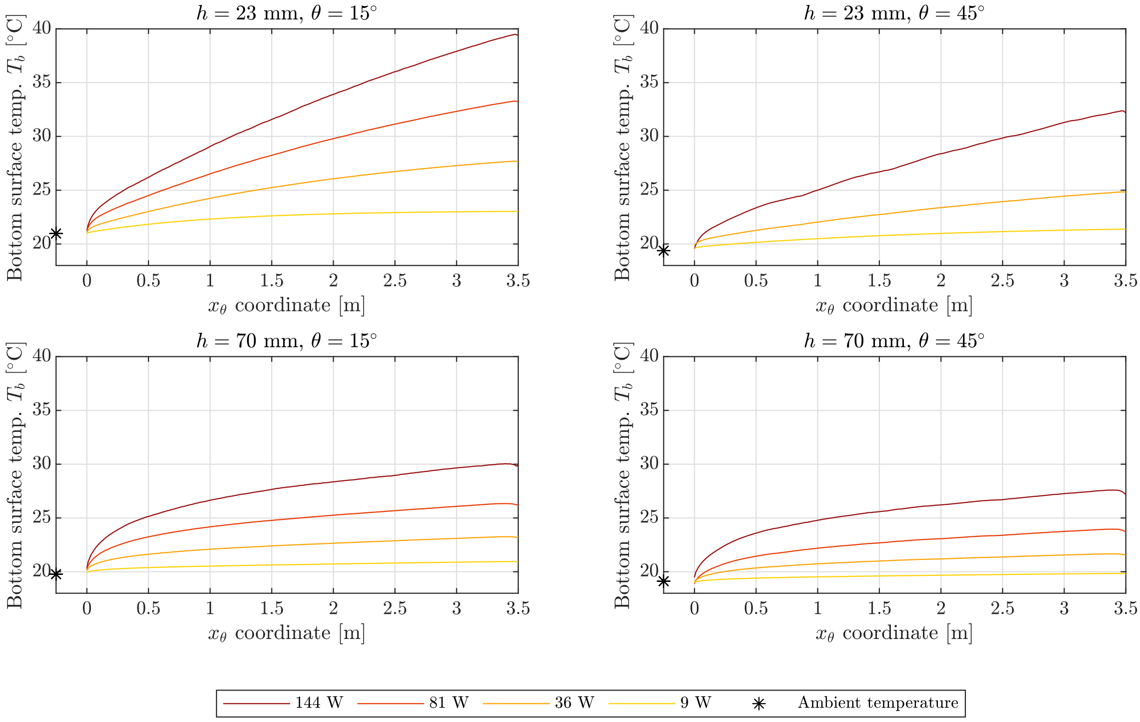

(b) Simulated temperatures on bottom surface, along the cavity length.

Figure 5.7. Simulated temperatures on the cavity surfaces along the cavity length x_θ, for two different cavity heights and two different inclinations.

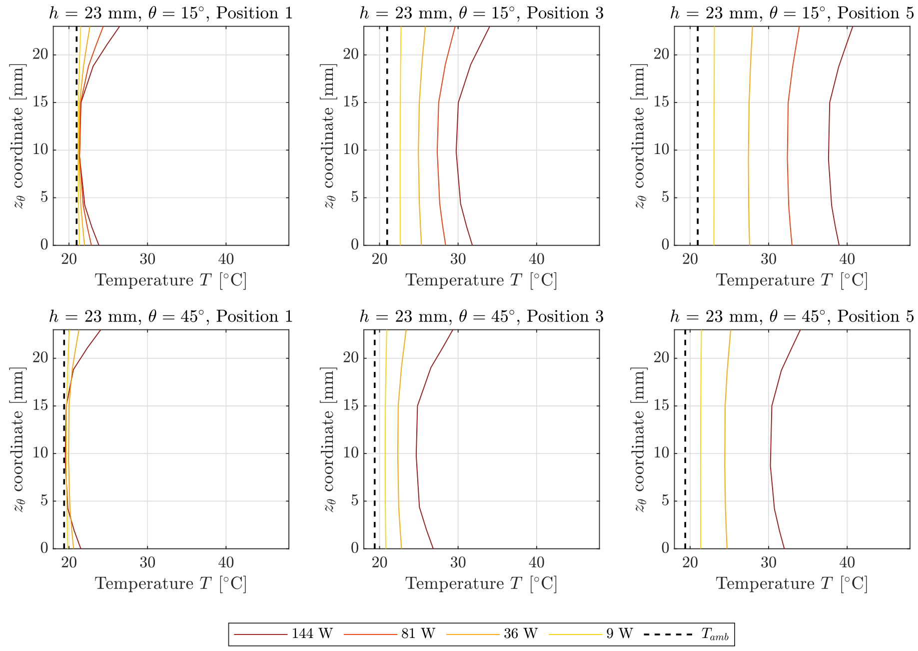

(a) Simulated air and surface temperatures along the cavity height z_θ, in position 1, 3, and 5, for $h = 23$ mm and two different inclinations.

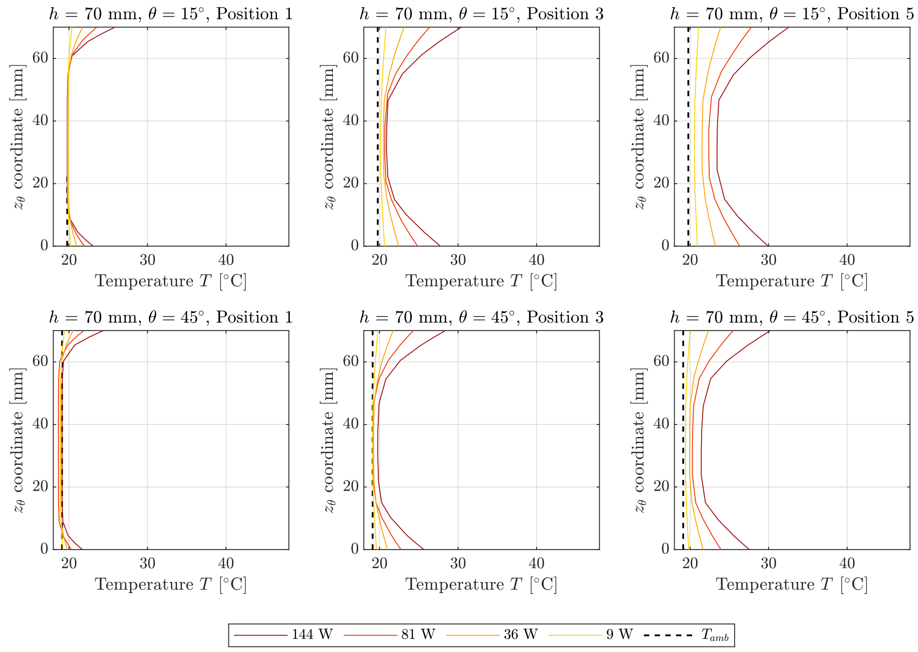

(b) Simulated air and surface temperatures along the cavity height z_θ, in position 1, 3, and 5, for $h = 70$ mm and two different inclinations.

Figure 5.8. Simulated air and surface temperatures along the cavity height z_θ, in three of the measuring sections of the cavity (see Figure 4.5), for two different cavity heights and two different inclinations.

5.3.1 Simulated thermal conditions

Figure 5.5 presents the temperature in the section of the cavity while Figure 5.6 presents the average air temperature in each section (i.e x_θ-coordinate) along the cavity length, for different cavity height h and inclination θ. The results show the air entering the cavity at ambient temperature and being heated along the cavity length, following a logarithmic growth curve. A higher heat production Q causes higher temperatures while an increased cavity height h and inclination θ yields lower air temperatures. The results also show increased temperatures near the cavity surfaces than in the middle of the cavity height.

Figure 5.7a and 5.7b present the temperatures along the cavity length of the top and bottom surfaces, respectively. The same temperature profile as for the air temperature can be seen for both the surfaces, with a clear dependence on heat intensity, Q. When increasing air cavity height h and roof inclination θ the temperature decreases, in the same way as for the air temperature but with smaller differences between different roof inclinations θ for higher air cavity heights h.

As the calculations are performed for steady-state, and the bottom surface is considered to be rather well insulated, the top and bottom surface temperatures are quite similar. The slight increase (for the top surface) and decline (for the bottom surface) in surface temperatures near the outlet of the cavity can likely be explained by simplifications in the radiation exchange modelling between the surfaces.

Figure 5.8a and 5.8b present the temperature profile across the cavity height for three different sections, i.e. x_θ-coordinate in the cavity. The sections correspond to the positions of measurement 1, 3 and 5 in the experimental study. In general, $T_{air} < T_{bottom} < T_{top}$ but for low heat intensities Q the temperature profile is nearly constant. For lower cavity heights h, the air temperature is close to the surface temperatures at the end of the cavity, especially for lower heat intensities Q and inclinations θ, while for higher air cavity heights h there is a larger difference in temperature across the section. For high cavities there is a large air volume in the centre of the cavity which remains rather unaffected by the surface temperatures along the cavity length. This effect is more pronounced for test set-ups with a higher air velocity u and a longer characteristic length L_0.

5.3.2 Simulated air flow conditions

Figure 5.9 presents the simulated air velocity in a part of the section of the cavity. The velocity vectors are seen to move parallel to the cavity walls but with a slight direction upwards along the cavity. A constant high velocity can be seen in the centre of the cavity, rapidly declining near the cavity edges.

Figure 5.10 presents the simulated velocity profile $u(z_\theta)$ near the cavity inlet and outlet (results from sections at x_θ-coordinate of position 1 and 5, respectively) for different cavity heights h and roof inclinations θ. Increasing θ, h and Q can be seen to cause increased velocities.

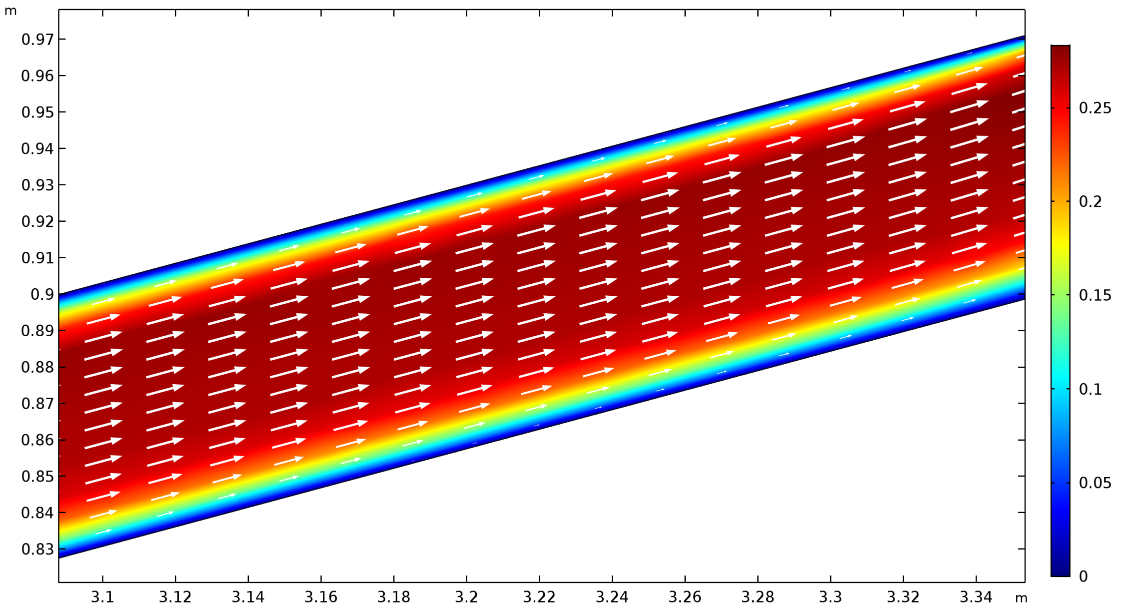

Figure 5.9. Zoomed in plot of simulated air velocity, with vectors representing the magnitude and direction of moving air for the set-up with air cavity height $h = 70\,\text{mm}$, roof inclination $\theta = 15°$ and heat intensity q [W/m^2] corresponding to $Q = 144\,\text{W}$.

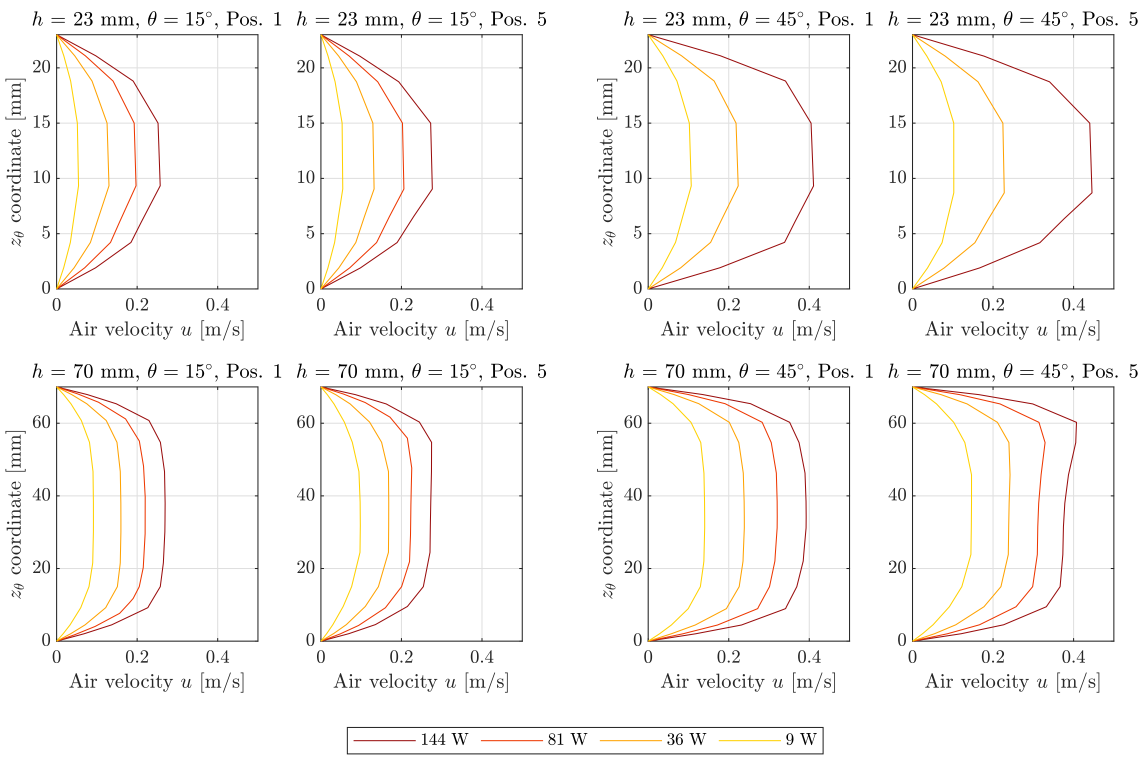

Figure 5.10. Simulated air velocity profile for measurement position 1 and 5 (shown in Figure 5.1), for two different cavity heights and two different inclinations.

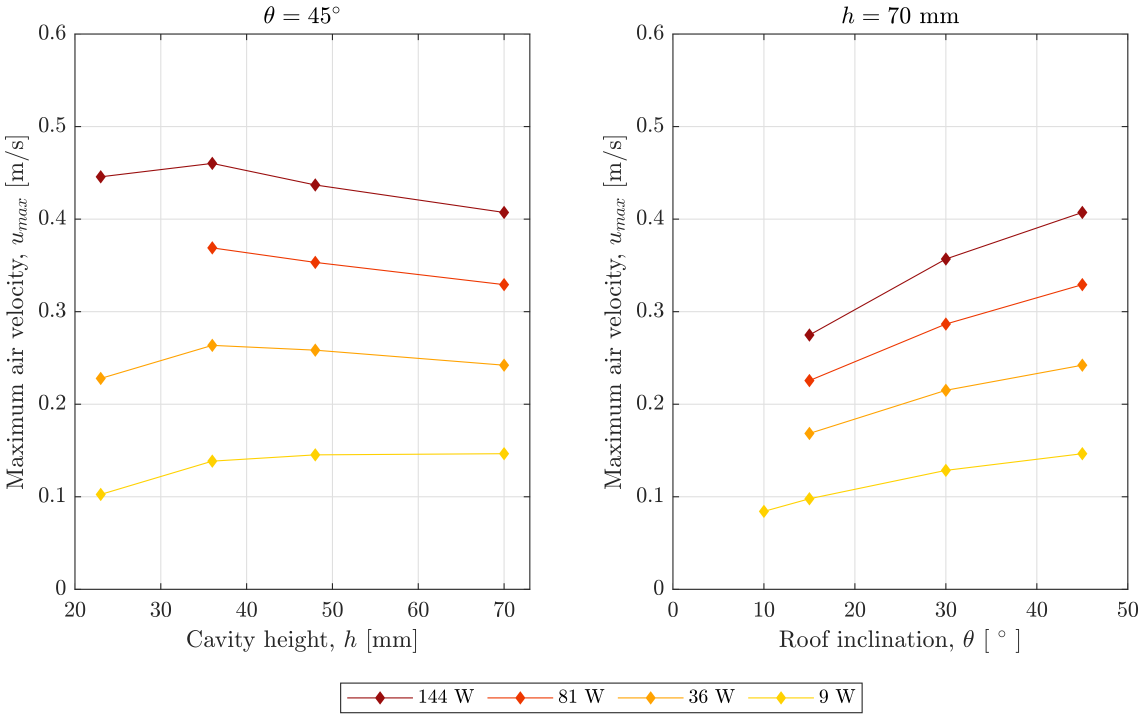

Figure 5.11. Simulated maximum air velocity u_{max} for $\theta = 45°$ and varying cavity height, along with $h = 70$ mm and varying inclination.

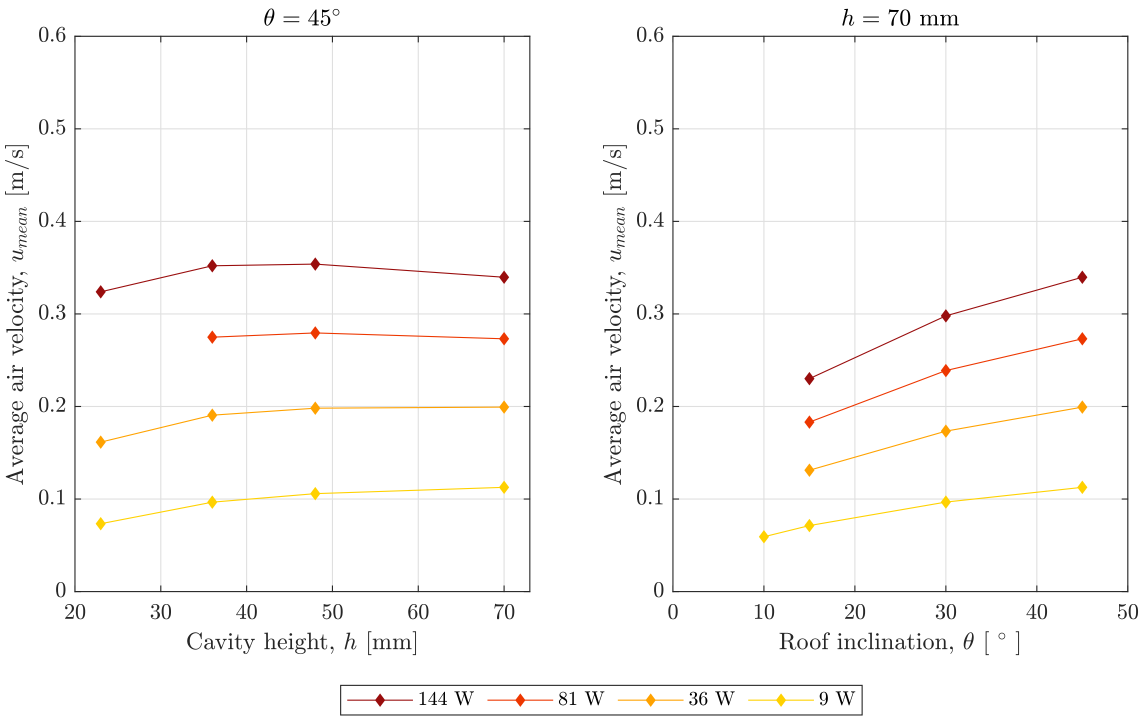

Figure 5.12. Simulated average air velocity u_{mean} for $\theta = 45°$ and varying cavity height, along with $h = 70$ mm and varying inclination.

For the 23 mm cavity, a near parabolic profile can be seen, while the 70 mm cavity exhibits a flatter profile. For higher inclinations, the higher cavity also exhibits a transition along the cavity length, where the velocity profile is symmetric near the inlet, while the max velocity is found closer to the top surface near the outlet. This can be explained by faster heating of the air near the warmer top surface, causing it to rising faster. A similar flow profile could be observed visually in the experimental tests, where the smoke appeared to move more quickly close to the heated top surface for high air cavity heights h.

Figure 5.11 and 5.12 show the simulated maximum and average air velocity, u_{max} and u_{mean} respectively, calculated in the cross-section at position 5 near the cavity outlet. The velocity is presented in relation to the cavity height, h, and roof inclination, θ, for different heat intensities Q. An increasing heat intensity Q and roof inclination θ clearly shows increasing velocities, while both max and mean velocities stay relatively constant with increasing air cavity heights h, even declining slightly for higher heat intensities Q.

5.4 Simplifications and assumptions

This section outlines the assumptions made when defining the boundary conditions for the CFD simulations. As discussed by Autodesk (2019), the Finite Element Method represents a more mathematical approach to the discretisation of the partial differential equation than other solution methods. This means that the steps involved in the solution may have less physical significance than when using e.g. Finite Difference Method. However, FEM provides the advantage of easily modelling of any geometry, and it has been shown that FEM and FDM produce the same matrix representations of the discretisied equation (Autodesk, 2019). Finite element modelling is also shown to be reliable for low velocity, laminar flows, as considered in this study. Furthermore, COMSOL Multiphysics provides the possibility of easily coupling heat transfer and air flow, further motivating the use for a FEM solution in this case.

To reduce computational cost, the cases studied were assumed to be in the laminar regime, and no turbulence modelling was performed. As further presented in Chapter 6, calculation of the Reynolds number Re indicates that this holds true for most simulations, but comparison with results using turbulence modelling would be useful to evaluate the effect of thermal buoyancy on the flow conditions. The mesh refinement was studied, and the chosen element size was deemed sufficient to capture the nonisothermal flow in the laminar regime. However, a higher mesh refinement may be required for simulations of turbulent flow.

One large assumption made early in the process was modelling a two-dimensional representation of the cavity. This choice was made for reasons of computational cost. However, further study of three-dimensional geometries would be needed to ascertain that the two-dimensional representation can be faithfully used for the relevant geometries.

Due to software limitations, the fluid modelled was considered to be dry air. This may affect the thermal and fluid conditions slightly, but should have no effect on the general trends shown in the results.

6

Analysis and comparison

In this chapter, the measured and simulated results are further analysed and compared. The figures presented are chosen as representative for the findings whereas analyses of all tests can be found in Appendix C. In the figures, the experimental measurements are represented by ∘ symbols, while the simulated results are represented by ⋄ symbols.

The results are also compared with the theory presented in Chapter 3 and with results from previous studies. An overview of the most relevant parameters and equations for the analysis is presented in Figure 6.1.

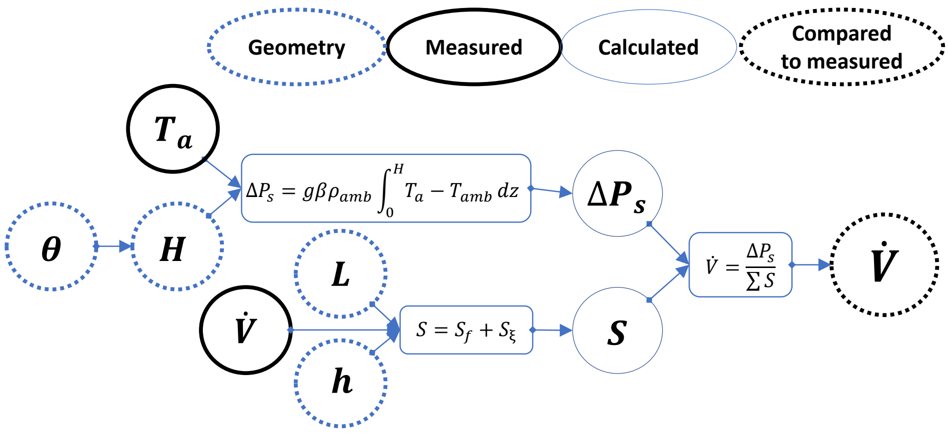

Figure 6.1. Overview of measured and geometrical parameters affecting the air flow according to the theory presented in Chapter 3, as well as the governing equations.

The analysis of the experimental results is based on the following assumptions, regarding the velocity measurements:

- The smoke tests are assumed to be more trustworthy than the measurements with the anemometer, regarding comparisons between tests.
- The smoke is assumed to flow through the cavity in the stream line representing the highest air velocity, u_{max}.

The assumptions are based on the visual observations presented in Section 4.2.3

and 4.2.2. Henceforth, measured (mean) air velocity refers to the results of smoke tests modified according to Equation 3.7 with a pipe factor $f_p = 0.67$.

6.1 Thermal conditions

The theoretical temperature profile along the cavity can be calculated for each test set-up using Equation 3.1 and 3.2. The effective cavity temperature T_0 can be calculated by reducing the thermal network of the experimental rig and set-up, presented in Figure 4.4. The full reduction and calculation of T_0 is presented in Appendix D.2.

Based on the results from the supplementary measurements during a longer time, as presented in Section 4.3, an estimation of the theoretical value T_0 has been made. When the air velocity is $0\,\mathrm{m/s}$, and the heat intensity Q is constant, the temperatures of the cavity materials will logarithmically converge to a constant value at $t \to \infty$. To find this value, a power law curve was fitted to the measured air temperature and the value to which the curve converges found through extrapolation. The curve fitting for $Q = 36\,\mathrm{W}$ is presented in Figure 6.2 and the results for all heat production levels are presented in Table 6.1. This test was done to find how well the effective cavity temperature calculated through reduction of the thermal network shown in Figure 4.4 corresponds to the actual thermal conditions.

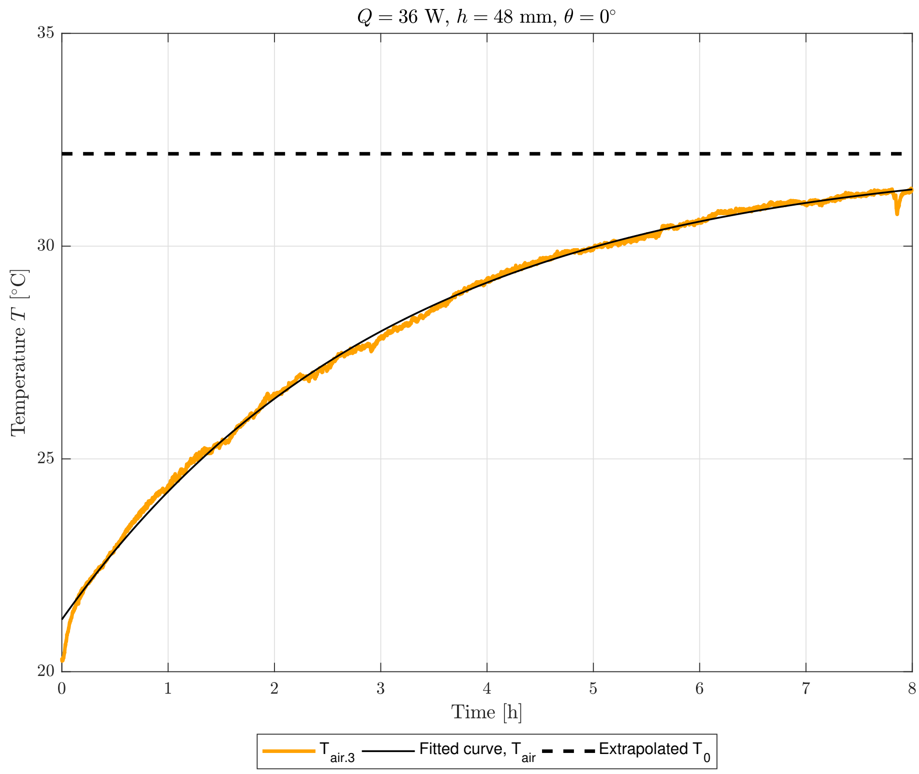

Figure 6.2. Measured air temperature in measurement position 3, during 8 hours, on the experimental model with no air flow (roof inclination $\theta = 0°$), along with a fitted curve and extrapolated effective cavity temperature T_0, for heat intensity $Q = 36\,\mathrm{W}$.

Table 6.1. Estimated effective cavity temperature T_0 from the long time measurements along with theoretically calculated T_0

Heat intensity, Q [W]	$T_{0.theory}$ [°C]	$T_{0.extrapolated}$ [°C]	$T_{0.extrapolated}/T_{0.theory}$ [%]
9	24.7	24.1	97.5
36	38.5	32.2	83.5
81	61.6	43.7	71.0
144	93.8	58.8	62.8

As can be seen from Table 6.1, the measured temperatures do not reach the theoretical values. This could be explained by the fact that the theoretical calculation is based on a two-dimensional heat flow, not considering the heat loss through the side walls of the cavity, i.e. heat flux in the y direction as defined in Figure 0.1. Further, the efficiency of the heating foil is assumed to be 100% in the theoretical calculations which might not be true. Bunnag et al. (2004) assumes an efficiency of 87.3% for a similar heating set-up. Additionally, as presented in Section 4.3, the temperature appears not to have reached steady-state even after 8 hours, which also could explain the difference.

However, the relative difference between the theoretically calculated T_0 and the extrapolated value from the long time measurements is very different in magnitude between the different heat intensities Q. Hence, the theoretically calculated T_0 is used when calculating the theoretical temperature profile for the tests. The characteristic length, L_0, is calculated using the mean air velocity from experimental results.

Figure 6.3 presents the measured thermal conditions for two cavity heights and a roof inclination of 45 degrees, together with the simulated results for the same set-ups and the corresponding calculated theoretical temperature profile, slightly differing based on different u. The shape of the theoretical profile correlates to the characteristic length, L_0, which is dependent on the air velocity, while the magnitude of the temperature increase is dependent on the effective temperature T_0.

The simulated temperatures seem to be underestimated compared to the theoretical profile. The variance may be explained by differences in convective heat transfer coefficient α_c, since it is assumed to be constant $= 3\,\mathrm{W}/(\mathrm{m}^2\mathrm{K})$ for calculation of the theoretical temperature profile (see Equation 3.1 and Appendix D.2). The theoretical profile also considers the temperature to be constant in each section of the cavity (i.e. constant $T(z_\theta)$ for each x_θ), which is a simplification compared to the simulation result.

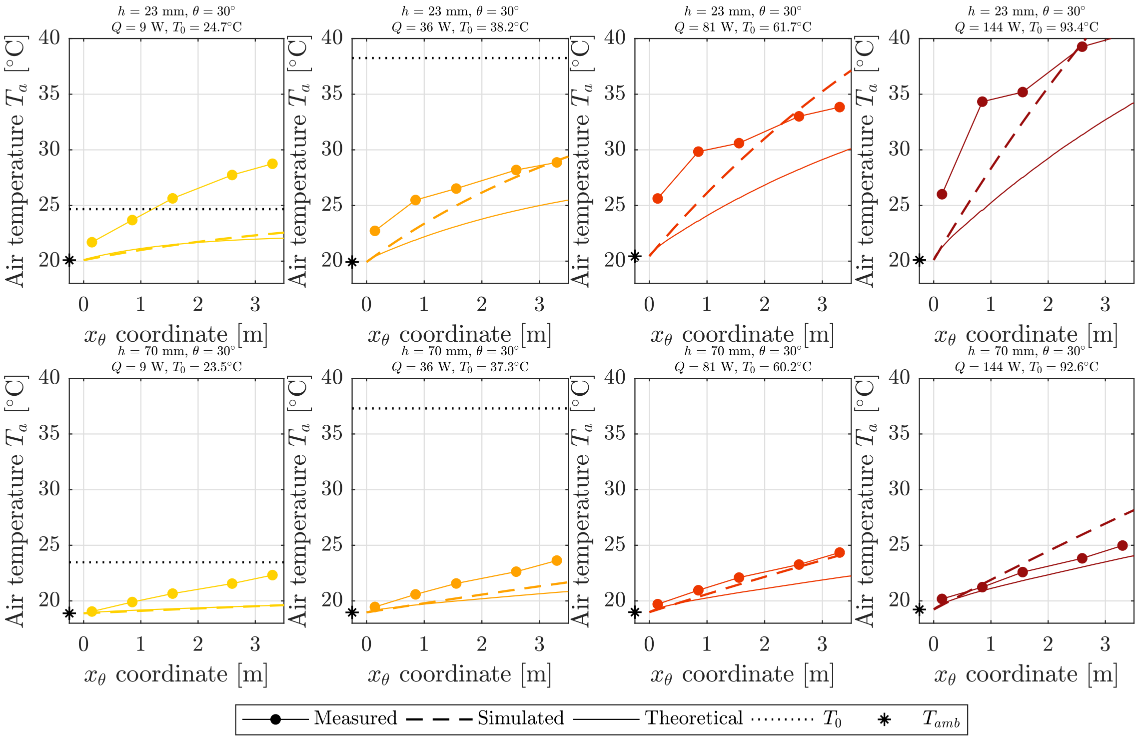

Figure 6.3. Comparison of measured, simulated and theoretical air temperature profiles for $\theta = 45°$ and two different cavity heights.

The measured air temperature profiles show to correspond rather well to the theoretical temperature profiles for some tests, but less for other. The higher cavities shows a more linear temperature increase while the lower cavities shows a more logarithmic-like increase. This corresponds well to the fact that lower air velocities were measured for the lower cavities, which gives a shorter characteristic length L_0. Irregularities in the measured temperature profile can likely be explained by measurement uncertainties, presented in Section 4.3.

Regarding the total temperature increase from inlet to outlet, the measurements differ from the theoretical results, exhibiting both higher and lower temperatures. However, this phenomenon can be explained by the measured temperatures on the bottom surface being either higher or lower than what it would have been in a steady-state condition. This is due to the experimental procedure, as explained in Section 4.1.3, not awaiting the temperatures on the bottom surface to stabilise (only the ones on the top surface) before starting the measurements. Of note is also the fact that the measured temperature in position 1 shows higher values than the theoretical temperature in the same position, regardless of the difference in total temperature increase in the cavity. This may indicate an influence from radiation.

The results of T_0 from the complementary measurements, as shown in Figure 6.2, also indicate a lower effective temperature in the measurements than what is calculated from the reduction of the thermal network of the system. Hence, the temperature T_0 is likely to be lower for the experimental set-ups, considering 3-dimensional heat flow and efficiency for the heating foil.

This fact, along with the measured air velocities being likely to be overestimated, due to smoke buoyancy, could explain the difference between theoretical temperature profiles and measured air temperatures in the cavity, as presented in Figure 6.3. The shape of the theoretical temperature profile is dependent on the air velocity and a lower air velocity would give a faster temperature increase in the cavity, as the measured results show.

Figure 6.4 shows the simulated and measured temperature profiles in three positions along the cavity. Of note here is that the simulations are performed for steady-state conditions, while the measurements are not, thus having a lower bottom surface temperature. As shown in the simulation results, a large portion of the air in the centre of the cavity remains unaffected by heating, meaning a single air temperature measurement point near the centre of the cavity will be insufficient to gauge the average temperature in each section. Thus, T_a in the experiments may be either over- or underestimated depending on the position of measurement relative to the heated top and unheated bottom surfaces.

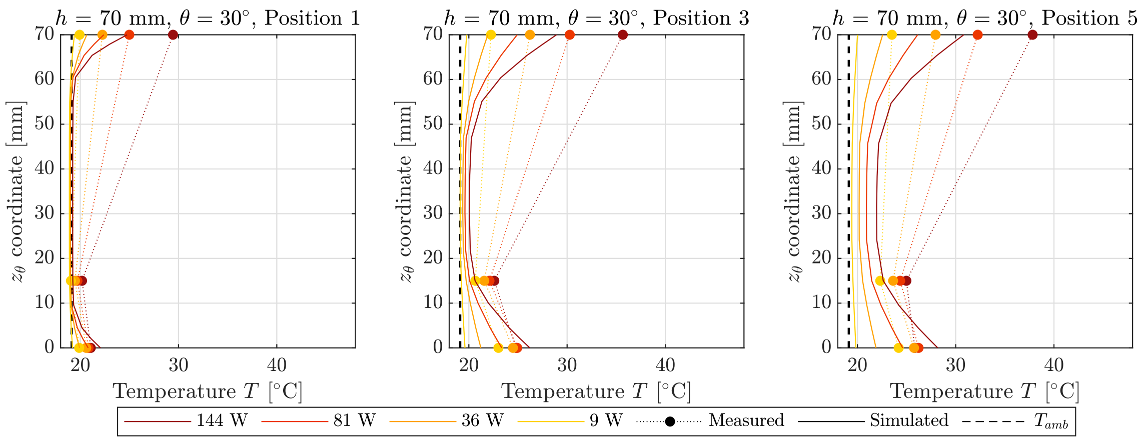

Figure 6.4. Measured and simulated air temperature profiles $T(z_\theta)$ in the three sections of measurement; 1, 3 and 5, along the cavity height z_θ for $h = 70$ mm and $\theta = 30°$.

6.2 Air flow and flow characteristics

To estimate if the air flow in the studied cases was laminar or turbulent, the Reynolds number Re was calculated using Equation 3.5. The result from the experimental and numerical study is presented in Figure 6.5. The grey area represents the transitional regime with $Re_{crit} = 2000$ (Kronvall, 1980). As seen in the figures, some of the measurement results are in the regime of transitional flow, while the majority is in the laminar regime. A similar fraction of the simulated results exceed Re_{crit}. Henceforth, tests with $Re > Re_{crit}$ are represented by a hollow symbol.

This result shows that the typical flow conditions caused by thermal buoyancy can be considered to be in the laminar regime, for the heat intensity applied, but that turbulence modelling may be relevant for cavities with higher h and θ, for high amounts of applied heat.

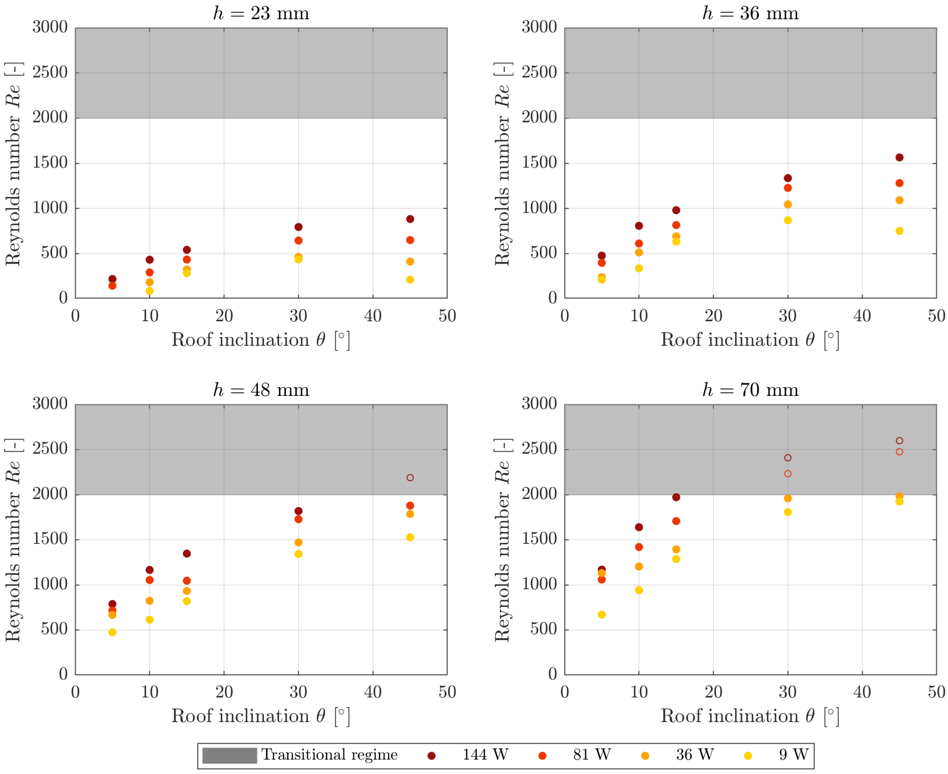

(a) Reynolds number *Re* calculated for all experimental tests.

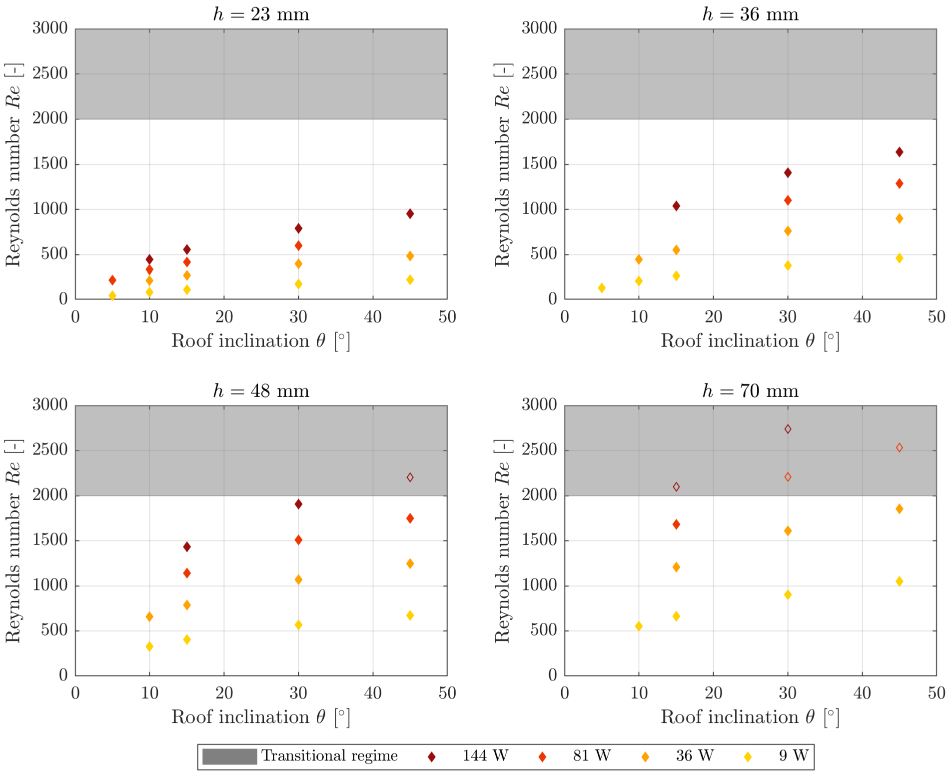

(b) Reynolds number *Re* calculated for all simulations.

Figure 6.5. Reynolds number *Re* calculated using Equation 3.5, for all measurements and simulations.

The air flow rate through the cavity in the experimental tests is calculated by Equation 3.4. Figure 6.6a shows the calculated air flow rate $\dot{V}$, from measured values, as a function of cavity height h and roof inclination θ. A clear linear relationship between the air flow and the cavity height can be seen, except for a slight decline for $h = 70\,\mathrm{mm}$. The relation between air flow and inclination is equally clear, however not linear.

Figure 6.6b shows the simulated air flow rate $\dot{V}$ as a function of cavity height h and roof inclination θ for different heat intensities Q, calculated through integration of the air velocity across the cavity outlet. The air flow rate is seen to increase with increasing heat intensity Q and roof inclination θ, while a near linear relationship is seen between air cavity height h and air flow.

To be able to compare the results from the experiments and the simulations, the simulation results, which were calculated for an assumed 1 m segment of an infinitely wide cavity, have been recalculated using $b = 0.49\,\mathrm{m}$ as used in the experimental study.

As mentioned previously, some of the measurement were estimated to be in the transitional flow regime. However, no drastic changes to the flow conditions can be noted from the measured air flow rates.

From considering the magnitudes of the measured and simulated air flow rate, the agreement is excellent for high heat intensity Q, but more and more overestimated in the measurements for lower Q. This may be explained by the intrinsic buoyancy of the smoke as discussed in Section 4.3 - for a higher heat intensity Q the heating of air by the heating foil should be the dominating driving force for buoyant air flow, while the buoyancy of the smoke may have a large impact for lower heat intensities Q.

Figure 6.7 shows the pipe factor f_p, calculated from the simulated maximum and mean air velocities, according to Equation 3.7. The results show a larger pipe factor for increased supplied heat Q, as well as a slight increase with increased θ and h. The changed velocity profile may be explained through the fact that the air closest to the surface is heated the most quickly. In general, the simulated values exceed the assumed value of 0.67 as used for the calculation of mean velocities for the experimental results, suggesting that a parabolic velocity profile cannot be assumed.

A parabolic flow profile was observed visually, as presented in Section 4.2.3. Thus the assumption is made that the mean velocity used for calculation of Reynolds number Re, Air flow rate $\dot{V}$ and other parameters that are based on measurements can be calculated through Equation 3.7. However, the results of the numerical study indicate that different flow profiles may be appropriate (see Figure 5.10), and that a higher factor f_p for the average velocity should be used. On the other hand, the assumption of a wide rectangular cross-section for the cavity is less valid for higher cavities, meaning f_p is likely to be overestimated in the simulations.

Ultimately, the human factors involved in velocity measurements, as presented in Section 4.3, are likely to cause larger errors than these assumptions. A different method, with multiple sensitive velocity measurement devices fixed in the cavity, would be required to experimentally study the actual flow profile of thermally driven flow in cavities heated from the top, and thus the assumption of $f_p = 0.67$ is deemed to be an acceptable approximation of the relationship between maximum and average air velocity.

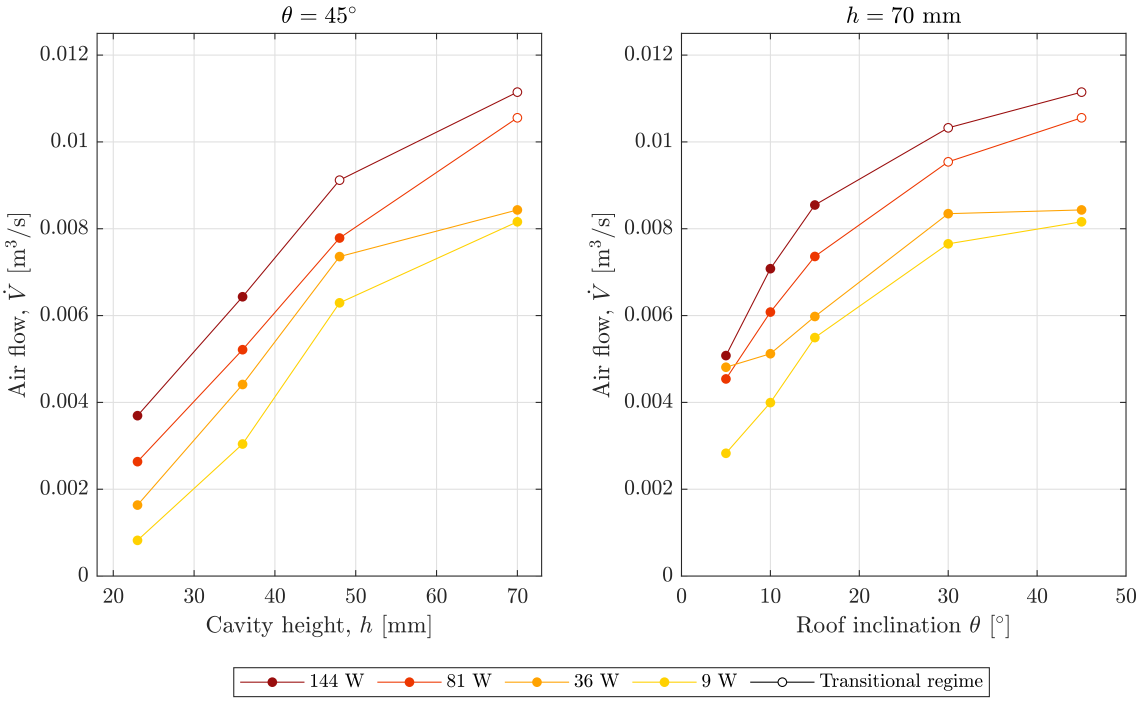

(a) Air flow rate $\dot{V}$ through the cavity, calculated from measured velocity results, as a function of air cavity height h and roof inclination θ.

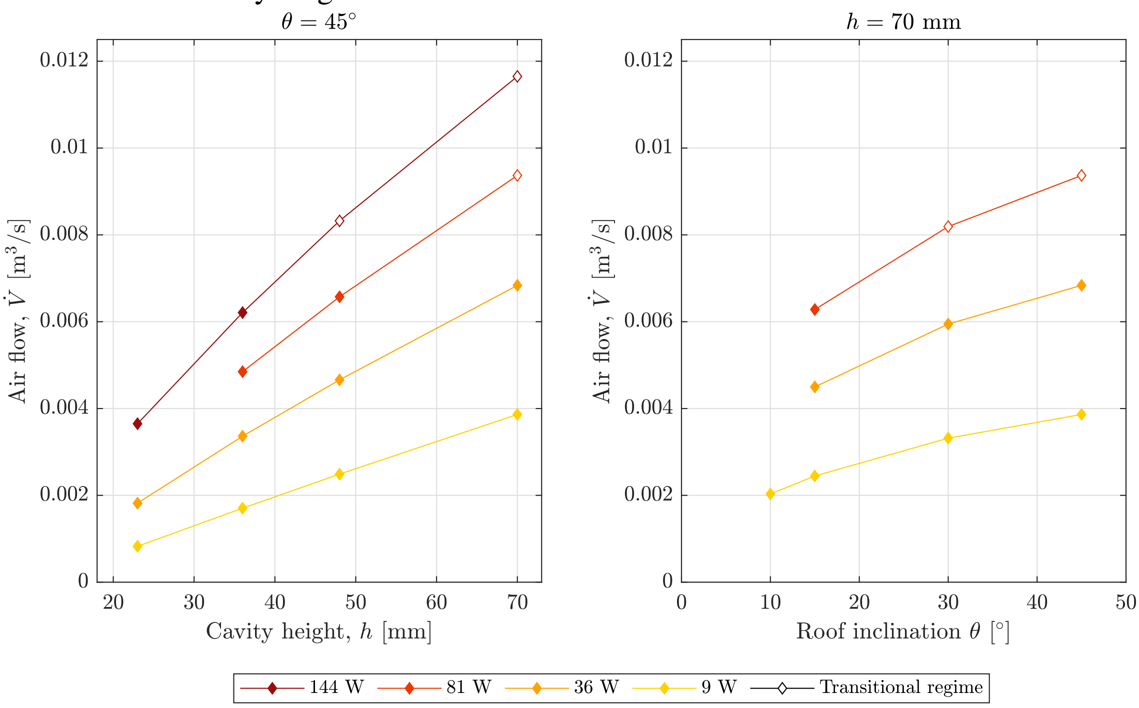

(b) Simulated air flow rate $\dot{V}$ as a function of air cavity height h and roof inclination θ.

Figure 6.6. Air flow rate $\dot{V}$ through the cavity as a function of air cavity height h and roof inclination θ.

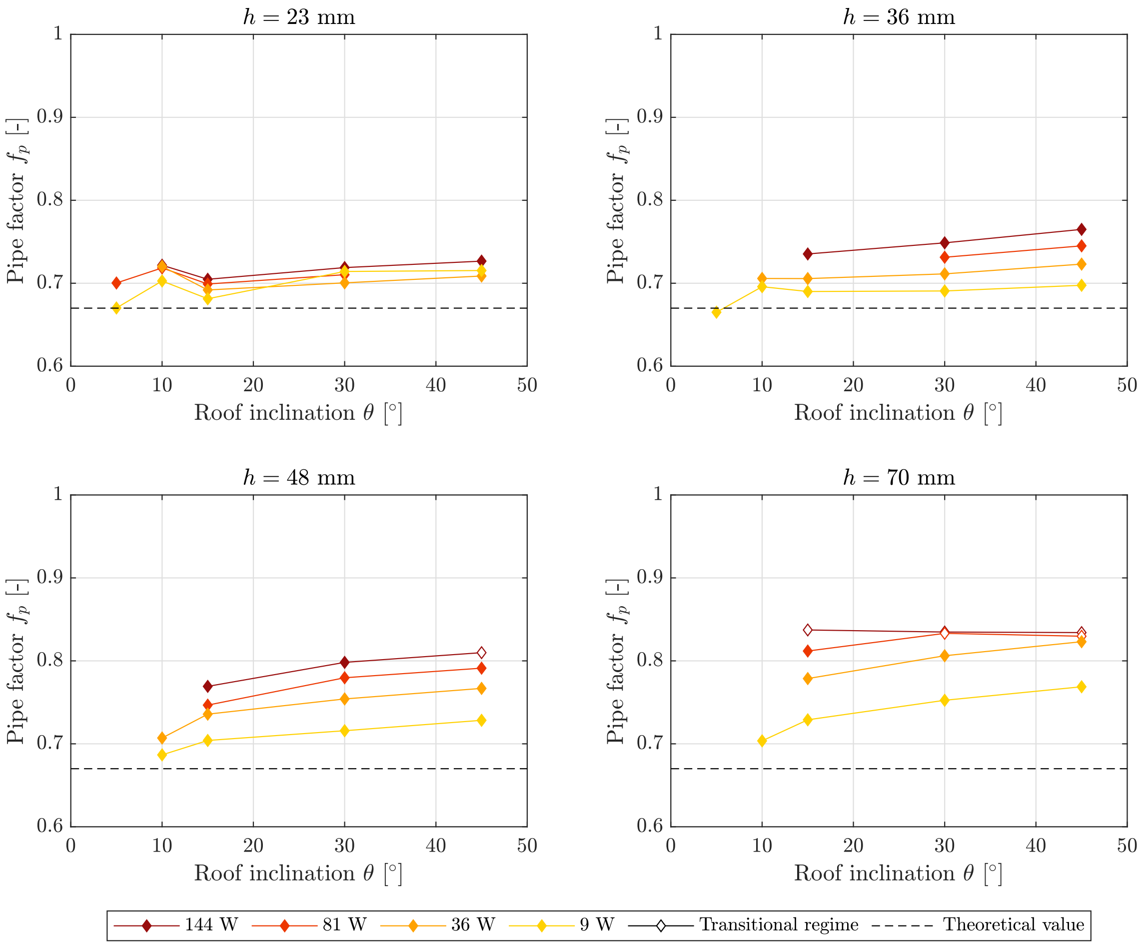

Figure 6.7. Pipe factor f_p calculated according to Equation 3.7 for all simulations, along with theoretical value 0.67 as defined in ASHRAE (2013).

6.3 Thermal driving force

As presented in Section 3.2.2, the thermal driving force for cavity air flow is dependent on the temperature conditions in the cavity along with total roof height, i.e. the height difference between inlet and outlet. The increase of air temperature in the cavity from inlet to outlet for the experimental tests is presented in Figure 6.8, calculated according to Equation 6.1, while the full driving force, calculated according to Equation 3.14b, is presented in Figure 6.9.

$$\Delta T = T_{a5} - T_{amb} \tag{6.1}$$

where

T_{a5} is the temperature measured in position 5, see Figure 4.5 [°C]

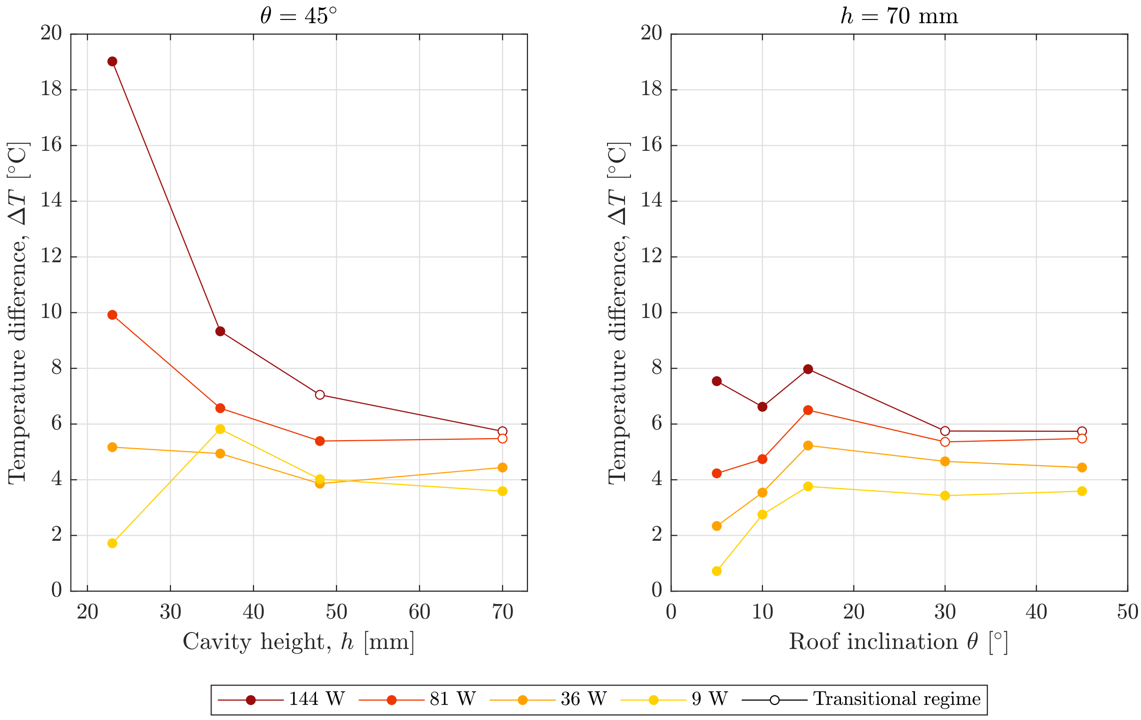

Figure 6.8. Measured air temperature difference in the experimental tests, for varying cavity heights, *h*, and varying inclinations, θ.

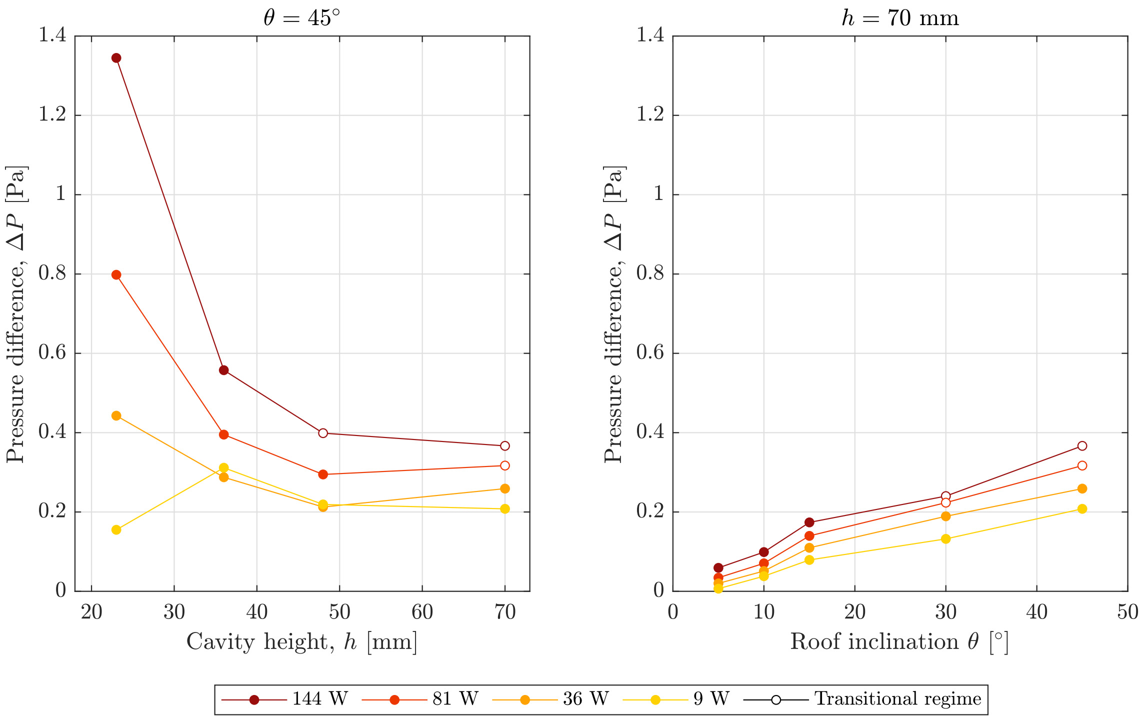

Figure 6.9. Thermal driving force ΔP, calculated from measured temperatures with Equation 3.14b, for varying cavity heights and varying inclinations.

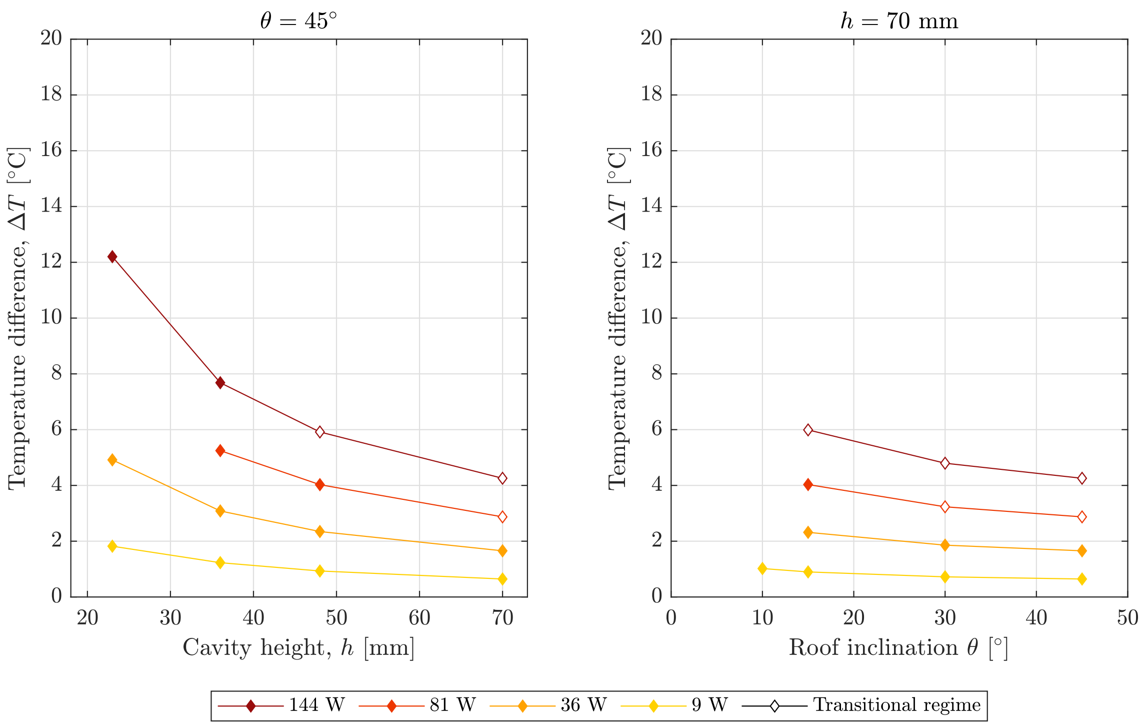

Figure 6.10. Simulated air temperature difference ΔT, for varying cavity heights, h, and varying inclinations, θ.

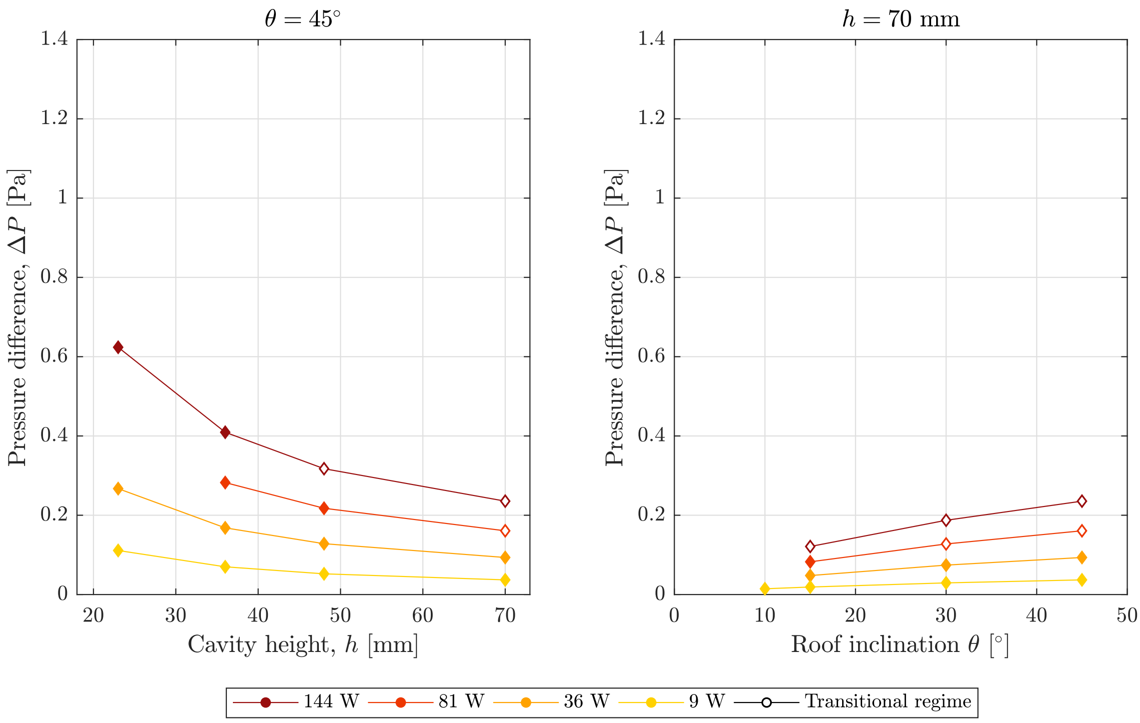

Figure 6.11. Simulated thermal driving force ΔP, calculated by Equation 3.14a, for varying cavity heights h and varying inclinations θ.

When calculating the driving force, the assumption is made that the air temperature is constant in each section of the cavity, which is a gross simplification as shown by CFD results (see Figure 5.8a and 5.8b). Figure 5.8a and 5.8b indicate that the temperature profile across the cavity height $T(z_\theta)$ varies with several degrees for the high heat intensities Q. The error grows along the cavity length and varies with increased cavity height.

The experimental results depicted in Figure 6.8 and 6.9 show no relation between temperature difference in the cavity and the inclination, but when considering the total driving force as a function of roof inclination, a rather linear relationship can be seen between θ and ΔP. This indicates that the total roof height H, as defined in Figure 0.1, is a key factor in controlling the driving force for cavity air flow.

The experimental results show a clear relationship between increased heat intensity Q and increased temperature difference ΔT and thermal driving force ΔP. When increasing the air cavity height h from 23 mm to 36 mm the results show a drastic reduction in both ΔT and ΔP , while both ΔT and ΔP seems to stabilise for $h \geq 48$mm. Reducing the cavity height reduces the air flow resistance S, causing a higher resulting air flow rate $\dot{V}$. As the air moves more quickly through the cavity, it has less time to be heated, which in turn causes a smaller ΔT and consequently a smaller driving force ΔP. For large h, the effect of increasing h on the temperature difference is smaller, as L_0 is becoming larger than the cavity length.

The driving force, for the experimental results, is calculated using the measured air temperatures in each position. Note that the air temperature was measured at a distance of 15 mm from the bottom surface in the experimental study for all cavity heights, and according to the CFD results (Figure 5.8a and 5.8b) the temperature at these positions represents the lower temperature range in the section. This would mean that the driving force calculated from the measured results is underestimated, as the mean temperature in each section is likely to be higher than the one measured. However, the simulations are run in steady-state conditions, meaning that the temperature of the bottom surface of the cavity is higher than of the air in the section, for all tests, which is not the case for the experiments. Hence, for the experimental tests where the bottom surface of the cavity has a lower temperature than the air, the measured air temperature might be more similar to the mean temperature in the section.

The simulated air temperature difference in the cavity is presented as a function of roof inclination and cavity height in Figure 6.10. A higher heat intensity Q gives a higher temperature difference between inlet and outlet, as expected. Similarly to the experimental results, the temperature increase is higher for lower cavity heights, explained by a lower flow rate which on the one hand leads to a higher thermal surface resistance, but on the other hand a longer time for the air to be heated and a smaller volume of air to be heated in each cavity cross-section.

The trend of a reduced ΔT with increasing h and θ is similar, albeit not quite showing the same quick tendency towards a state where $L_0 \gg L$.

The simulated driving force is presented in Figure 6.11, calculated using Equation 3.14a. The driving force is clearly dominated firstly by increased Q, secondly by the increasing total cavity height H with increasing θ, and thirdly by a higher ΔT caused by a decreased cavity height.

6.4 Air flow resistance

As presented in Section 3.2, the relation between air flow and driving force in the cavity is the air flow resistance S, described by Equation 3.3. Figure 6.12 presents the air flow $\dot{V}$ from measured and simulated values as a function of the calculated driving force ΔP for the same tests. The figure shows that an increased ΔP also causes a larger $\dot{V}$ and that the relation is dependent on the cavity height.

As presented in Section 3.2.3, the flow resistances are dependent on geometry as well as the air flow. The geometry dependency is clearly shown in Figure 6.12, as just mentioned, where the higher cavity heights h get a higher air flow for a constant driving force; indicating a lower flow resistance S for high air cavities compared to low.

In Figure 6.12, fitted curves of the measured data are also plotted, which provides the function $\dot{V}(\Delta P)$. From the inclination of the function, $\sum S(h)$ can be estimated. The fitted curves show a non-linear relation, indicating the flow dependency of the flow resistances.

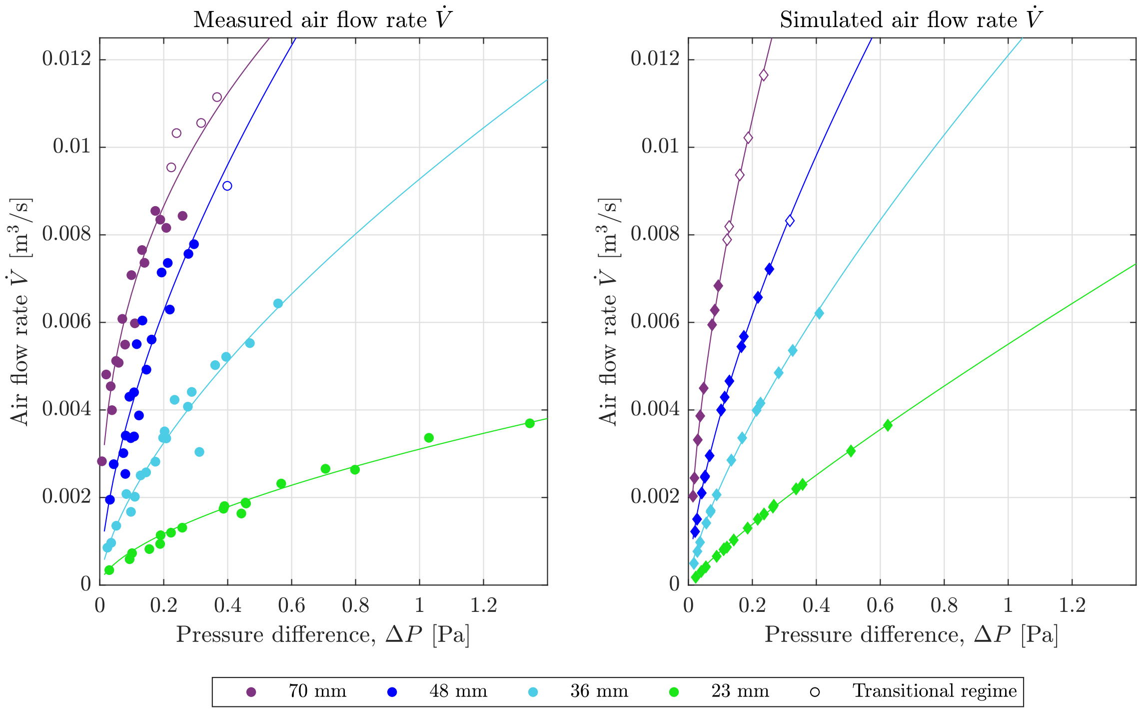

Figure 6.12. Measured and simulated air flow rate $\dot{V}$, as a function of calculated thermal driving force ΔP.

The measured and simulated air velocities as a function of driving pressure are shown in Figure 6.13. The simulations show an increased u with increasing cavity height. However, the measurements appear to reach a maximum value for the velocity at $h = 48$ mm, as already seen in Section 4.2.2. This indicates that the flow resistance $S(h)$ is proportional to $\dot{V}$ rather than to u.

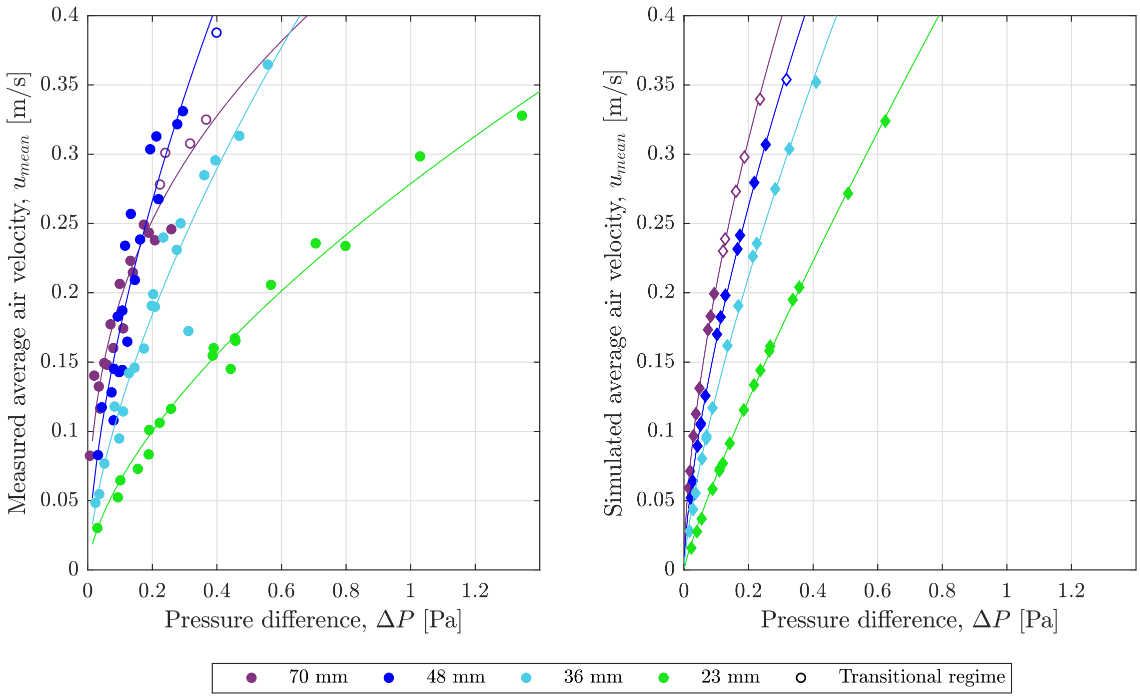

Figure 6.13. Measured and simulated average air velocity u_{mean} as a function of calculated thermal driving force ΔP.

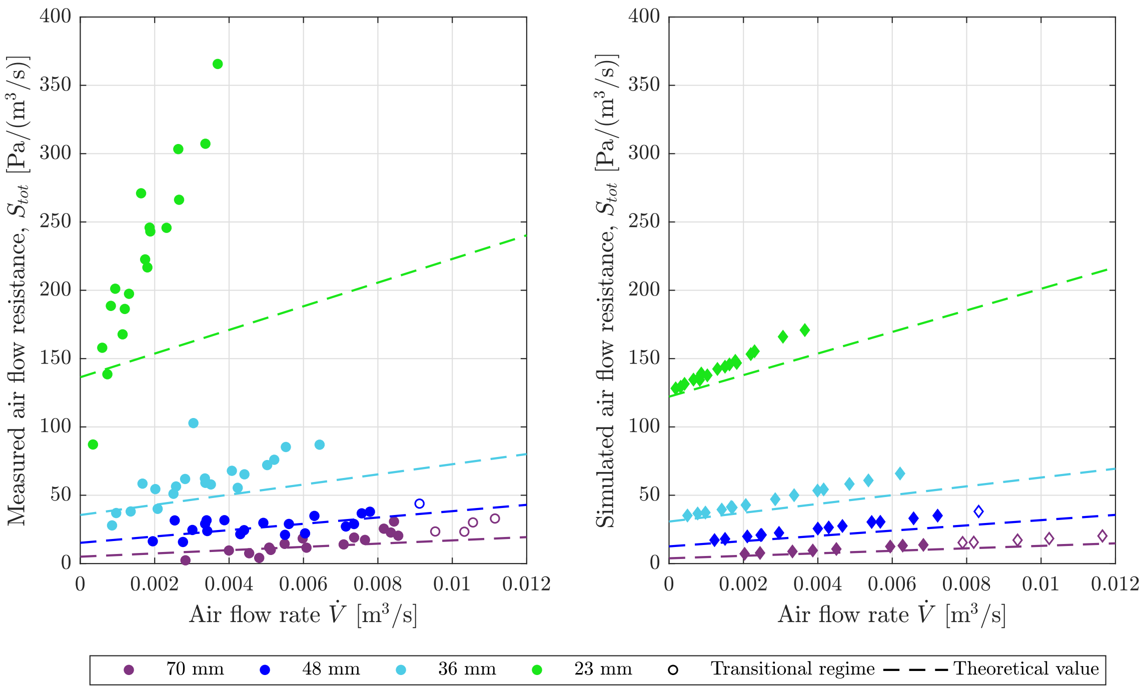

Figure 6.14. Calculated air flow resistance S_{tot} for measurements and simulations, as a function of air flow rate $\dot{V}$, along with theoretical values for $\sum S$.

Figure 6.14 presents the total flow resistance $\sum S$ as a function of flow rate, calculated both from the measurements and simulations using Equation 3.3, as well as from theory using Equation 3.17b and 3.17a. The theoretical pressure losses due to frictional pressure loss is calculated with Equation 3.18 while the flow resistances from local pressure losses are calculated according to Equation 3.23, including the pressure loss at inlet and outlet.

The results from both measurements and simulations show a rather linear relation of $S(\dot{V})$ dependent on cavity height, in accordance with theory. However, the measurements show higher flow resistances for the lower cavities compared to the theory and the inclination of the linear relation also seems to be higher for all h. This may be explained both by additional resistances being introduced by measurement equipment in the channel, as well as a potentially overestimated driving force because of radiative effects, further described in Section 4.3.

The simulations show similar magnitudes of flow resistance to theoretical values, but the air flow rate dependency and frictional flow resistance differ slightly. This indicates that the flow resistance due to frictional pressure loss S_f is smaller in the simulations than for the theoretical expression. This may be explained by the two-dimensional representation of the cavity, where the sides of the cavity are not affecting the frictional loss, hence the hydraulic diameter D_h and the dimensional factor ϕ differ. Meanwhile, the flow resistance due to local pressure losses, S_ξ, is somewhat larger in the simulations than for the theoretical expression.

The analysis performed in this study has assumed fully developed flow. However, the entrance length for the studied cavity, as calculated through Equation 3.8, exceeds the cavity length for most of the measurements, meaning fully developed flow cannot be assumed. As the flow is still disturbed by the influence of the entrance, the friction losses S_f are likely to be underestimated in the analytical solution for frictional air flow resistance.

Furthermore, the theoretical value for the air flow resistance S_ξ caused by local losses is assumed to only include the influence of entrance and exit contraction of the air. This should be a good approximation for larger cavity heights, but may be a large simplification for smaller cavity heights, where even a small obstacle such as a cable, surface defect or measurement device represents a large contraction of the air flow. This means the local losses are likely to be underestimated, especially for low cavity heights.

In the calculation of $\sum S$, full air tightness of the model is assumed meaning all of the driving force is converted into air cavity air flow. As the magnitudes of pressure are low, and the model was carefully taped to improve air tightness, the impact of this factor should be small, but it may cause a slight overestimation of the driving force available for air flow, and this a slight overestimation of $\sum S$.

6.5 Dimensionless relations

The dimensionless relation between driving force and flow resistances for a cavity, Grashof number Gr_c, can be calculated theoretically for each test set-up according to Equation 3.26. For each test set-up, the effective temperature T_0 is calculated as described in Appendix D.2 and the flow resistances are theoretically calculated according to Section 3.2.3, with Equation 3.23 for resistance due to the local pressure losses.

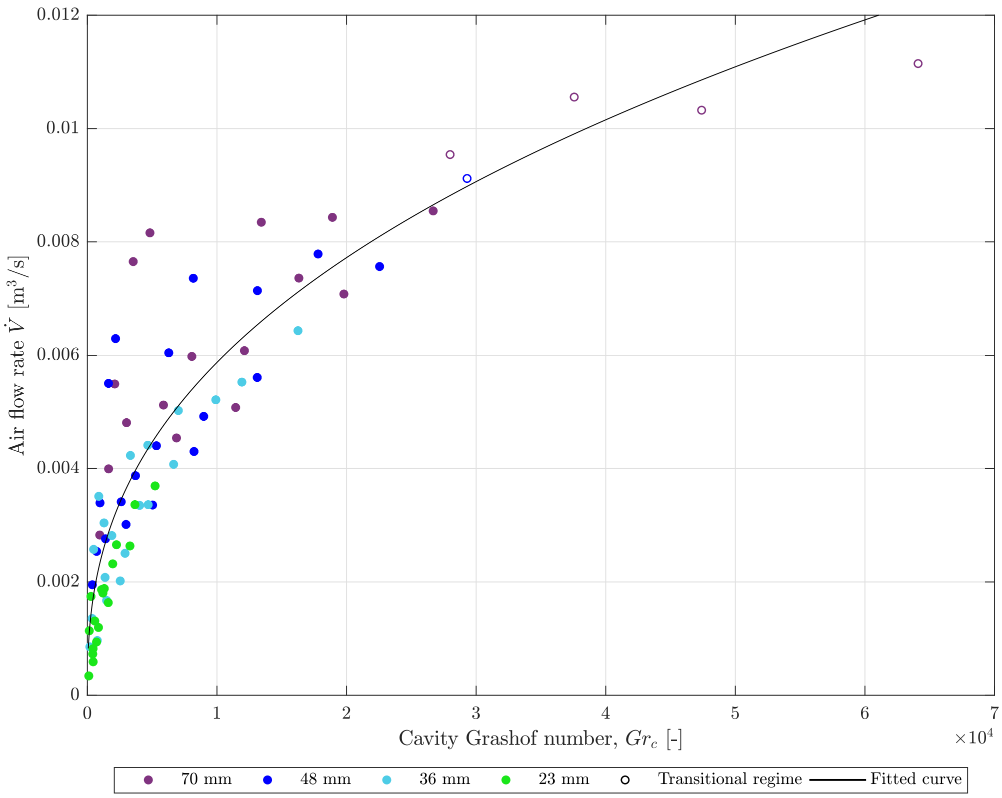

(a) Experimental $\dot{V}(Gr_c)$, for all tests.

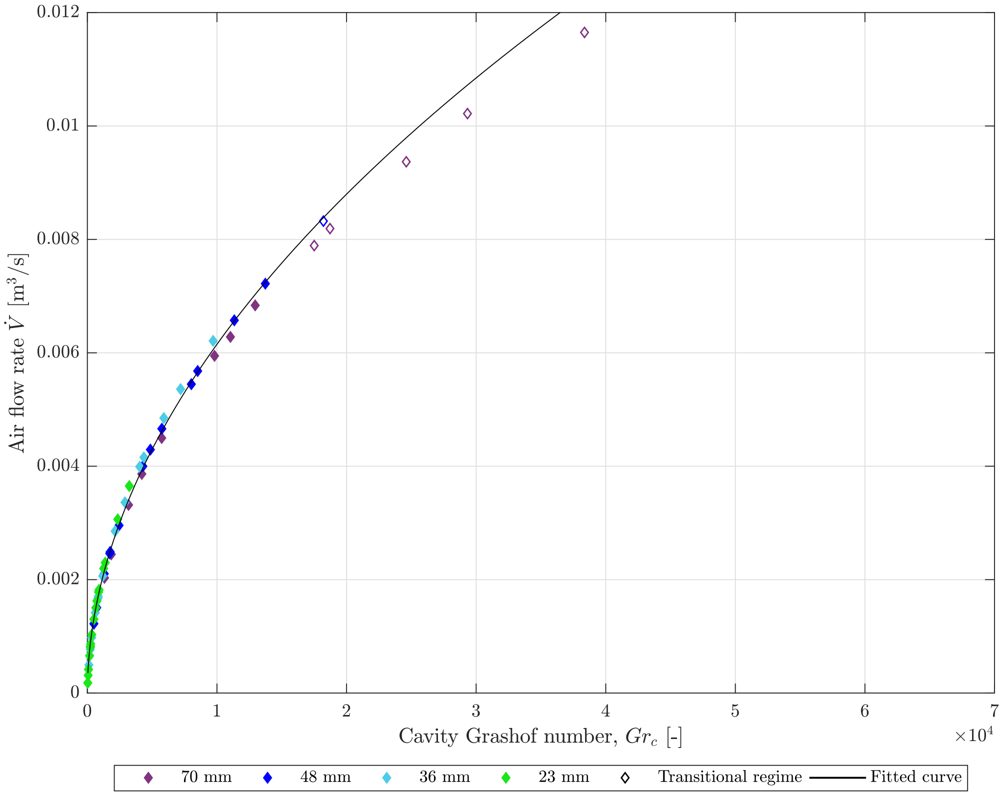

(b) Simulated $\dot{V}(Gr_c)$ for all tests.

Figure 6.15. Measured and simulated air flow rate $\dot{V}$ versus calculated Grashof number Gr_c, for all tests.

Figure 6.15 presents the theoretically calculated Grashof number Gr_c, for each test set-up, versus calculated air flow rates $\dot{V}$ from measured and simulated results, respectively. The fitted curves have the formulas:

$$\dot{V}_{Gr.measurements} = 15.46 \cdot 10^{-5} \cdot Gr_c^{0.3949}, \tag{6.2}$$

with a coefficient of determination $R^2 = 0.7381$.

$$\dot{V}_{Gr.simulations} = 5.3 \cdot 10^{-5} \cdot Gr_c^{0.52}, \tag{6.3}$$

with a coefficient of determination $R^2 = 0.9973$.

While the Grashof number characterises the relationship between driving forces for buoyancy and air flow resistances, the Rayleigh number $Ra_c = Gr_c \cdot Pr_c$ (Equation 3.28) also includes the material properties of the materials in the air cavity by introducing the Prandtl number Pr_c. Hence, the Rayleigh number Ra_c can be used to predict the air flow rate for any given roof construction. The Rayleigh number Ra_c is therefore calculated from the results of measurements and simulations in order to compare the result with an analytical solution.

Figure 6.16 presents the fitted curves from both measurements and simulations representing air flow as a function of Rayleigh number, as well as the analytically calculated $\dot{V}(Ra)$, the calculation of which is described in detail in Appendix E.

As can be seen, the analytically calculated curve estimates a slightly higher air flow rate than the fit curves for simulated and experimentally measured results. This may be explained by the fact that the theoretical value assumes completely undisturbed flow, while the actual flow profile in simulations shows a tendency to change along the cavity length. The experimentally measured values yields a smaller air flow rate for the same Rayleigh number, compared to the analytically calculated relation and the simulated curve, which can be explained by measurement uncertainties, as presented earlier, and the assumption regarding the pipe factor f_p being equal to 0.67.

However, the similarity of the results indicates that the Rayleigh number has a rather good correlation with the flow rate for any given roof construction. The application of this is further discussed in Section 8.1. This result indicates that the Rayleigh number provides a useful prediction for the air flow rate in the air cavity. Hence, the cavity air flow model described further in Chapter 8 calculates the Rayleigh number for a given construction and climate conditions, which enables a prediction of the air flow rate, using the analytical calculation described in Appendix E.

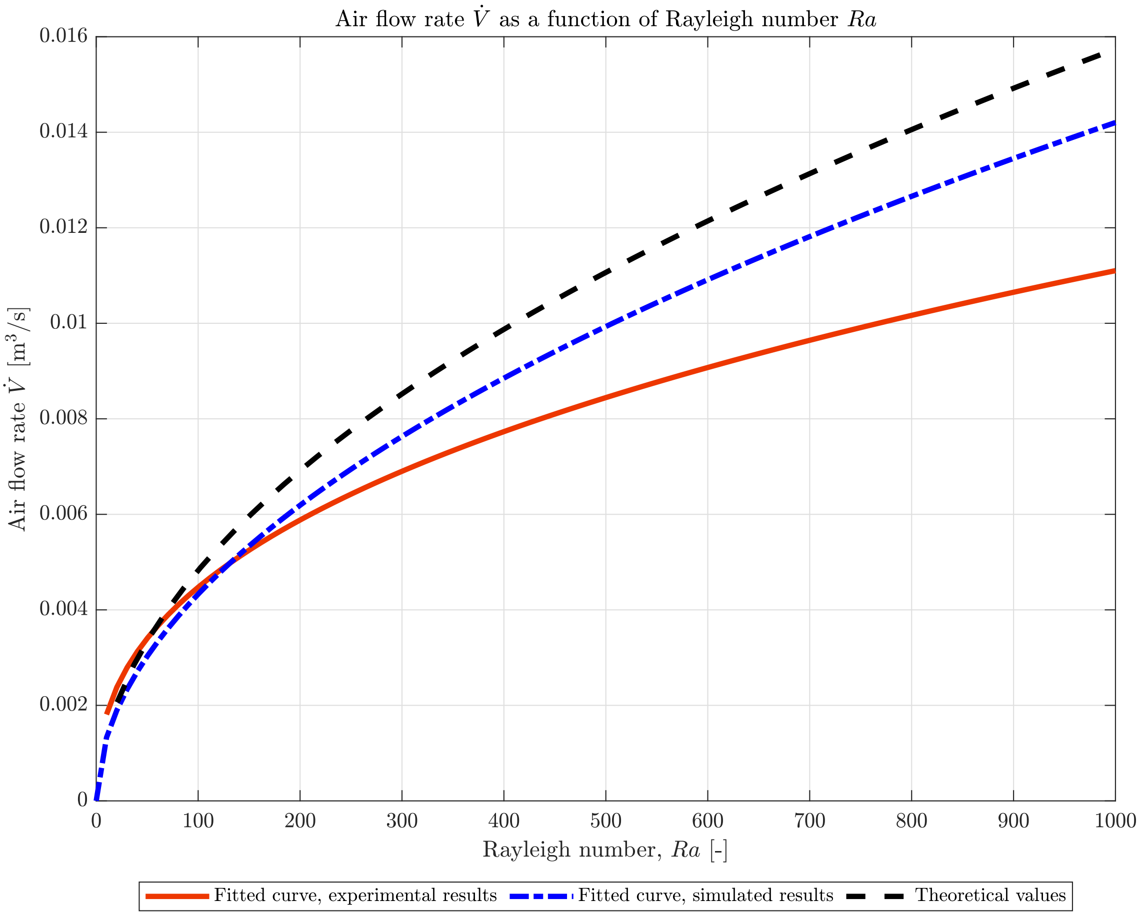

Figure 6.16. Fitted curves from both measurements and simulations representing air flow rate as a function of Rayleigh number, as well as the theoretically calculated relationship.

6.6 Comparison with previous studies

Biwole et al. (2008) studied the air flow and thermal conditions in air cavities of varying height and inclination for different amounts of heating by solar radiation, in a numerical study. The simulated air velocity profile across the cavity height shows a similar pattern as the results of this study, with a higher air velocity closer to the heated surface.

Bunnag et al. (2004) performed an experimental study, investigating convection in an open-ended rectangular inclined channel heated from the top, for different air cavity heights h and roof inclinations θ. The results are in agreement with the present study, showing decreasing air temperatures but higher air velocities for increasing inclination θ. The measured velocity is in a similar range as the present study, ranging between $0.2-0.4\,\mathrm{m/s}$. The study also found a similar logarithmic temperature profile along the cavity length but the difference in cavity heights studied, compared to the cavity heights studied in the present work, make a quantitative comparison of the temperature conditions difficult.

Susanti et al. (2008) also studied the air flow and thermal conditions experimentally. The study found a similar temperature profile along the cavity length. One of the cases studied is comparable to the results of the present study. For a cavity with air cavity height $h = 78\,\mathrm{mm}$, roof inclination $\theta = 30°$, and for heat intensity $q = 100\,\mathrm{W/m^2}$ the total temperature increase ΔT along the cavity was measured to be $4-5\,°\mathrm{C}$, whereas the present study estimated $\Delta T = 5-6\,°\mathrm{C}$ in the measurements, and $\Delta T = 5\,°\mathrm{C}$ in the simulations, for similar conditions. The measured maximum velocity u_{max} in the study was $0.33\,\mathrm{m/s}$, while the present study estimated $u_{max} = 0.44\,\mathrm{m/s}$ in the measurements, and $u_{max} = 0.30\,\mathrm{m/s}$ in the simulations, for similar conditions.

Another experimental study of the temperature conditions in ventilated air channels was performed by Chami and Zoughaib (2010). For a a cavity with air cavity height $h = 30\,\mathrm{mm}$, roof inclination $\theta = 30°$, and for a temperature difference between the heated surface and the ambient air of $25\,°\mathrm{C}$, the total temperature increase of the air ΔT was measured to be $13\,°\mathrm{C}$, whereas the present study estimated $\Delta T = 11\,°\mathrm{C}$ in the measurements, and $\Delta T = 9\,°\mathrm{C}$ in the simulations, for similar conditions. For the same set-up, the measured average velocity u_{mean} in the study was $0.44\,\mathrm{m/s}$, while the present study estimated $u_{mean} = 0.31\,\mathrm{m/s}$ in the measurements, and $u_{mean} = 0.41\,\mathrm{m/s}$ in the simulations for similar conditions.

Thermal buoyancy driven airflow in the cavity of low-pitched roofs in particular was examined experimentally by Nusser and Teibinger (2013). The study does not provide temperature measurement data, but measurements were performed to similar conditions as some of the tests in the present study. For a a cavity with air cavity height $h = 50\,\mathrm{mm}$, roof inclination $\theta = 5°$, and for a temperature difference between the heated surface and the ambient air of $5\,°\mathrm{C}$ and $25\,°\mathrm{C}$ respectively, the measured average velocity u_{mean} in the study was $0.07\,\mathrm{m/s}$ and $0.38\,\mathrm{m/s}$, while the present study estimated $u_{mean} = 0.11\,\mathrm{m/s}$ and $0.14\,\mathrm{m/s}$ respectively in the measurements for similar conditions. The large difference may be explained by a much longer cavity used in this study.

7
Discussion

This chapter contains the interpretation of the measured and simulated results, providing an assessment of the most important factors governing the air flow and thermal conditions in the air cavity. Further, the contributing factors to removal of excess moisture are discussed, as well as the relevance of the present study in the design of ventilated air cavities. Finally, the fundamental differences between the simulated and measured results are discussed.

7.1 Interpretation of results

In general, the numerical study shows good correspondence with the trends in the experimental study. Many uncertainties inherent in the experimental study can be avoided in numerical modelling. However, the simulations also include a large number of simplifications and input data. Thus, neither method can be seen as an adequate representation of reality on its own, but must be studied critically and should preferrably be compared to field studies.

However, the similarity in the results of this study, as well as the large agreement with other studies performed on thermal buoyancy in inclined air cavities, suggests that the results of the two methods used in the present work together are useful to facilitate understanding for the physics of the air cavity in ventilated roof constructions.

Parameters affecting the air flow

The results clearly show that for a constant inclination, a larger supplied heat Q will cause a larger air flow $\dot{V}$ as the thermal driving force is increased. The simulations show a near linear relationship between the Q and $\dot{V}$, while the measurements show a less consistent but clear relationship. Hence, solar radiation on a roof construction will cause an air flow upwards in the cavity.

An increased cavity height, h, also causes an increased air flow rate $\dot{V}$. This may be explained by reduced air flow resistances, S, caused by reduced frictional losses, since S clearly has a strong relationship with h. However, the increased cavity height h also causes lower average air temperatures. This can be explained through a larger air volume to be heated, and shorter time for heating in the cavity, due to higher air velocity and longer characteristic length L_0. This will decrease the thermal driving force, slightly counteracting the benefits of a reduced air flow resistance, however not fully since the air flow continues to increase with increased h.

The measured and simulated air velocity reaches its maximum value for air cavity height $h = 48$ mm and $h = 36$ mm, respectively, then declining for higher h. This suggests that the effect of a reduced air flow resistance S is dominating for low flow rates, while a reduced thermal driving force ΔP dominates for higher flow rates.

An increased roof inclination θ will have its main influence through an increased total roof height H, improving the driving force through the stack effect. There is also a minor reduction in the thermal driving force caused by an increased air flow, as outlined above. However, this effect appears to be negligible in comparison with the increased potential height.

To summarise; the supplied heat intensity Q appears to be the main influencing factor for air cavity air flow by thermal buoyancy. The roof inclination θ and by extension the total roof height H also play a major role in improving the driving force. The effect of a reduced air flow resistance, S, caused by an increased cavity height, h, were shown to increase the air flow rate $\dot{V}$. However, the effect is partially counteracted by a consequent decrease in the thermal driving force, ΔP_s, for larger air flows, thus limiting the maximum air velocity u. This phenomenon makes the question of the critical factor for moisture removal of great interest. If a high air flow rate is of the highest importance, an increased h would be beneficial to the moisture safety of air cavities. However, if increased temperature, or increased air velocity u is critical, an increased h may have a limited or even negative effect on the moisture safety of the roof construction, which will be further discussed in Section 7.2. A schematic summary of the studied parameters and their influence on the air flow and air velocity, is presented in Figure 7.1.

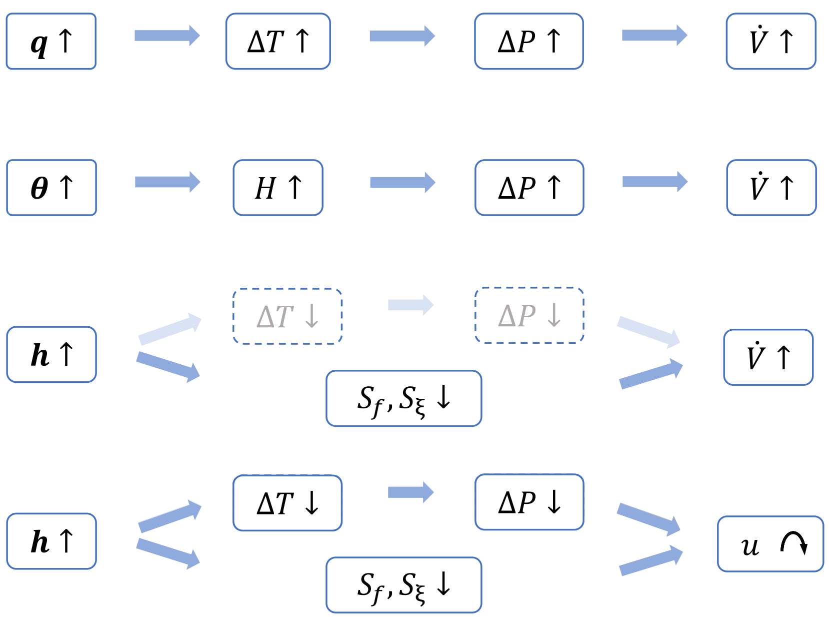

Figure 7.1. Schematic representation of the studied parameters and their influence on the air flow and air velocity.

Thermal conditions

The simulations show a good correspondence between the measured air temperature T_a and the theoretical values as calculated using T_0, with small discrepancies likely explained by different assumptions regarding the convective heat transfer coefficient α_c. This indicates that the theoretically calculated profile holds true and that the assumed α_c $= 3\,\mathrm{W/(m^2K)}$ can be used for calculations of the temperature profile for velocities and thermal conditions similar to the set-up in this study.

The simulated temperature profiles across the cavity height shows a slightly higher air temperature near the heated cavity wall. In real conditions this effect may be even greater due to variations in external temperature and solar heat load. These temperature gradients may affect the channel flow, causing turbulence to occur at even lower Re than the assumed $Re_{crit} = 2000$, leading to increased flow resistance S. Numerical studies including turbulence modelling would be needed to further study this effect.

Time dependency

Transient effects were not covered in this study. However, from the experimental study, the influence of the thermal inertia of the air cavity building components were evident. The theoretically calculated temperatures is seen to be overestimated for some tests, and underestimated for some. For practical reasons, the temperatures of all surfaces in the cavity could not be allowed to stabilise during the experimental tests, meaning the measurements were performed with bottom surface temperatures different from the theoretical steady-state conditions, which was seen to have a large effect on the air temperatures. The time that passed from turning the heat intensity on to the heating foil and to the start of the measurements, was approximately 20 minutes. Even for the complementary measurements running for 8 hours, steady-state was not completely reached. This indicates that the simplification of steady-state conditions, when calculating the temperature conditions in an air cavity, is an oversimplification, as real climatic conditions include both daily periodic fluctuations as well as rapid changes in thermal conditions, such as changes in solar radiation on the roofing.

Turbulence and flow profile

The calculation of the Reynolds number, for both measured and simulated results, show that some of the tests have air velocities in the transitional regime where laminar flow can no longer be assumed. This corresponds well with the fact that some tendencies toward turbulence were visually noted for the highest cavities. However, no drastic changes due to flow characteristics can be noted in the data. This indicates that the assumption of laminar flow is an adequate approximation for this study and that the significance of the parameters affected by the flow characteristic is low, in comparison with other uncertainties. However, for a case with a significantly larger driving force, the flow characteristics may be of importance when assessing the flow resistance.

Further, the theory which is assuming a laminar flow is based on a parabolic velocity profile as typical of pipe flow. The simulation results show a more flattened air velocity profile, where the relationship between max velocity, u_{max}, and average velocity, u_{mean}, defined as the pipe factor, f_p, does not correspond to the theoretical values for air flow in rectangular cavities. This is because fully developed flow is not reached, as the entrance length, L_e, is longer than the studied cavity in the majority of the tests. It is not clear if a flow within the entrance length of a cavity indicates that turbulent flow is present, or if the flow can still be described as laminar despite a distorted velocity profile. Especially higher velocities near the top surface of the cavity indicate the potential for more complex back-flow phenomena than would typically be assumed for pipe flow.

Flow resistance

When estimating the flow resistance, S, of the test set-up used for the experiments, the air flow rate, $\dot{V}$, and driving force, ΔP_s, calculated from the measured air velocity, u, and measured air temperature, ΔT_a, were used. However, these parameters include a number of assumptions, measurement uncertainties and simplifications in the analysis. For large cavity heights, h, air temperature, T_a, was measured closer to the bottom surface of the cavity, than from to the top surface of the cavity, likely underestimating the average air temperature in the cavity; thus underestimating the driving force, ΔP_s. For small cavity heights, h, the measured air temperature, T_a, is assumed to be influenced by radiation from the high temperatures of the bottom surface of the cavity, likely overestimating the average air temperature in the cavity; thus overestimating ΔP. Adding to this effect, the complementary measurements indicate that the smoke used for measurements has a buoyancy force of its own, likely overestimating $\dot{V}$. On the other hand, the simulations indicate that the pipe factor, f_p, is underestimated, thus underestimating the average air velocity, u_{mean}, as calculated from the measured maximum velocity, u_{max}. These contributing factors mean the exact magnitude of flow resistance, S, is difficult to determine from the experimental results. To find the flow resistance from the experimental tests, a different method would be required, preferably measurements on the pressure loss for different parts of the cavity. However, as noted by Gullbrekken et al. (2017a), local pressure losses are difficult to estimate and measure for low flow rates, which is the case for this study.

Despite the uncertainties in the calculations of flow resistances, S, the trend is clear and the simulated results corroborate that the flow resistance, S, as calculated using the available theory is a good estimate of the air flow resistance. Additionally, this indicates that using a constant quadratic loss coefficient, qlc, and the Grille boundary condition to model the entrance and pressure losses corresponds to the theoretical behaviour of the entrance and exit. The results also show that entry and exit pressure losses have a similar order of magnitude to the frictional losses for the tested cavity geometries, and that both must be considered. For real cavities where fire protection vents, insect nets and generally more complex geometries for inlets and outlets, will most likely have an even higher impact which must be studied further.

Grashof and Rayleigh number

The main result of this study is the relationship between the flow rate $\dot{V}$ and the cavity Grashof number Gr_c, calculated from each test set-up. As evident in Figure 6.15a and 6.15b, there is a clear relationship for the set-up and the results correlates between the two methods used. When taking the results from Figure 6.15a and 6.15b further to the Rayleigh number Ra_c, the results can be used to predict the air flow rate based on specific geometric and climatic conditions.

As further described in Chapter 8, the calculation of Ra_c requires a number of assumptions. However, the results of this study indicate that the assumptions involved in calculating the theoretical temperature T_0, based on climatic conditions, and the theoretical air flow resistance S, based on the air cavity geometry, are good enough to provide a quantitative prediction of the air flow rate in a typical air cavity without major obstructions, subjected to heating from the top. However, there is a risk for over-estimations of the air flow when using the analytical calculation of Ra_c, as evident in Figure 6.16, due to the fact that fully developed flow cannot be assumed along the full cavity length.

7.2 Drying potential

This study has not included any analysis on the drying potential in the cavity, or how the relation between air flow rate in the cavity and drying of the cavity correlates. As presented in Section 2.1, while efficient ventilation of the cavity is necessary for adequate drying in summer conditions, it also means larger amounts of moisture can be introduced in the cavity under colder conditions. As presented in Section 3.3 the temperature conditions in the cavity may be equally, or more, important for the drying potential. Hence, the thermal buoyancy effect in the cavity, from an over-heated roofing, could play an important role for the drying of the cavity since the effect increases both the temperature and the air flow. However, the thermal buoyancy effect can also occur from an under-cooled roofing, e.g. from long-wave radiation to the sky, which lowers the temperature in the cavity alongside increased air flow in opposite direction.

The temperature profile along the cavity is also relevant from a moisture perspective, as air of higher temperature can hold more moisture. From the results, the air temperature is seen to increase rapidly near the inlet of the cavity, then reaching a more stable temperature depending on the characteristic length L_0, which is in turn dependent on the air velocity u. Hence, a cavity with a shorter L_0 is not very efficient from the perspective of cooling. From a drying perspective, however, higher temperatures are beneficial. Thus, a lower cavity where the air entering the cavity is heated faster might be beneficial for the moisture transport potential. A longer cavity will also get a higher average temperature, which could improve moisture conditions regarding condensation. This means that the main objective of the air cavity in any specific roof construction design must be clearly established to be able to optimise the air cavity design.

Arfvidsson et al. (2017) suggests that the air flow rate along with the difference in moisture content from the air inlet to the outlet, largely influenced by thermal conditions, governs the rate of drying in the air cavity. This suggests that any model which evaluates the moisture safety of ventilated roof constructions must take climatic conditions, air flow conditions, and thermal conditions into account. The model must also be transient, as the moisture conditions are greatly dependent on the potential of materials in the air cavity to buffer moisture in periods of excessive moisture.

This study provides the means to predict the air flow and thermal conditions caused by the thermal buoyancy effect. However, further studies are needed to ascertain the implications for the moisture safety of roof constructions. Specifically, the temporal aspect is important - does the critical drying occur during daytime in winters, when high overtemperatures can occur and thermal buoyancy come into effect; or is the most important drying period the summertime?

One further aspect to consider is what flow conditions achieve the most efficient drying. Turbulent flow may cause a reduced resistance to moisture exchange between the moist surface and the flowing air. However, further numerical and experimental studies are needed to investigate this aspect.

The large number of occurrences of mould growth in roof constructions can be considered a motivation for this study. However, almost all of such damage cases have been found in cold attic constructions. Such constructions are easier to inspect, and are also clearly a risk construction from the perspective of moisture safety. However, further research is needed to establish if parallel roof constructions generally suffer from the same issues. This would provide crucial information in developing a tool for the design of ventilated roof constructions.

8
Practical applications

In order to find relevance in the results of this study, this chapter describes how the findings can be interpreted and used. It also puts the results in a context applicable for the reference roof construction described in Section 2.3. Still, only overheating of the roofing compared to ambient temperature is considered and not the effect of a cooled surface. The weather data used in this chapter is a representative year for Gothenburg, from SMHI (2019).

8.1 Interpretation and application of $\dot{V}(Ra)$

As presented in Section 3.2.4, the dimensionless Rayleigh number Ra_c can describe the air flow rate, $\dot{V}$, caused by thermal buoyancy in a cavity. However, the relation between Ra_c and $\dot{V}$ is dependent on the characteristic length, L_0, which in turn is dependent on the effective heat transfer coefficient, α_0, as described in Appendix E. This means that the curve presented in Figure 6.16 represents only the roof constructions with the same effective heat transfer coefficient, α_0, as the model used in this study. However, for each unique roof construction, α_0 can be calculated and the relation between Ra_c and $\dot{V}$ can be derived in the same way as presented in Appendix E. Figure 8.1 presents the $\dot{V}$-Ra_c-curve derived for two different α_0.

As seen in Figure 8.1, the impact of changed effective heat transfer coefficient, α_0, is small on the relation between Ra_c and $\dot{V}$. Hence, the air flow rate is mainly dependent on the Rayleigh number Ra_c. This naturally leads to the question on how design changes affect the Rayleigh number and what impact different design changes have. Figure 8.2 provides an overview of what parameters are included in the Rayleigh number and their dependencies.

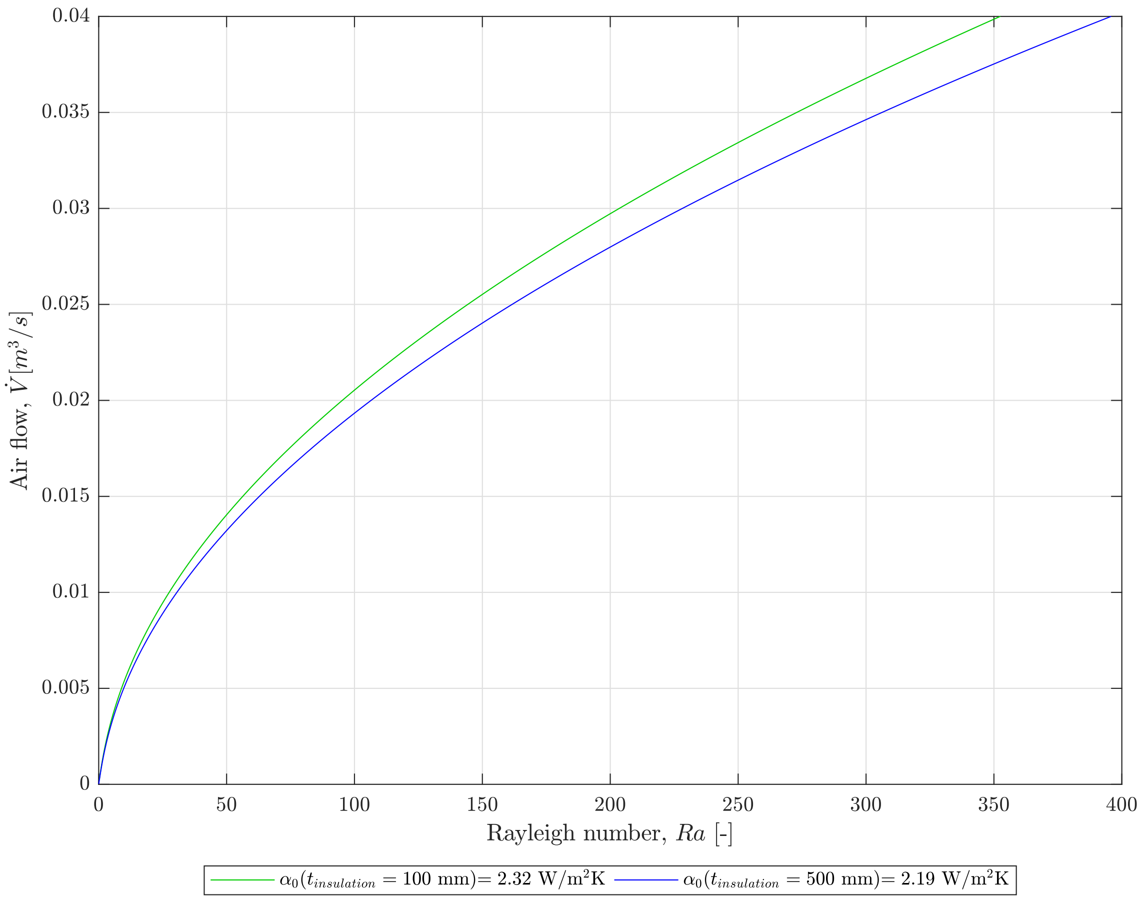

Figure 8.1. Relation between Rayleigh number Ra_c and air flow rate $\dot{V}$ for different effective heat transfer coefficients α_0 due to different insulation thickness.

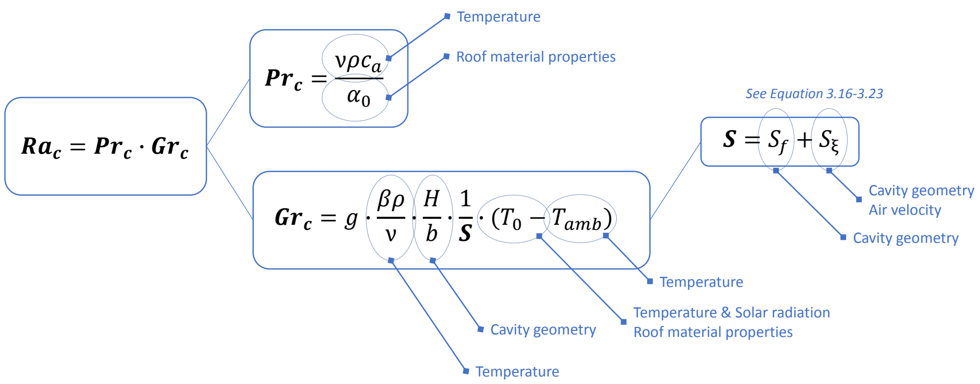

Figure 8.2. Presentation of Rayleigh number and the dependencies of the parameters included.

As can be seen in Figure 8.2, some parameters are only temperature dependent, hence not possible to affect by design or roof materials. However, the effect of change in the cavity geometry is clearly seen through changes in the parameters H, b and S.

The effect of an increased cavity height, h, is a decreased flow resistance, S (see Section 3.2.3), hence an increased Rayleigh number, Ra_c. The effect of a larger roof inclination, θ, (assuming a constant roof length, L) is an increased total roof height, H, hence an increased Rayleigh number, Ra_c. Further, the effect of a longer roof, L, is an increased total roof height, H, (assuming a constant inclination, θ) and an increased frictional flow resistance, S_f (see Equation 3.18). As can be seen in Figure 8.2 the Rayleigh number, Ra_c, is proportional to the total cavity height, H, but not inversely proportional to the frictional flow resistance, S_f, hence, the Rayleigh number, Ra_c will increase with an increased roof length, L.

The effect of changes to the roof construction or the material properties, such as an increased insulation thickness on the internal side of the cavity, is clearly seen through a changing effective heat transfer coefficient, α_0, and effective temperature, T_0. An increased insulation thickness yields decreased α_0 (see Equation D.8a) and increased T_0 (see Equation D.7c), hence the Ra_c will increase. This means that the effective heat transfer coefficient α_0 does have an impact on the air flow, since Ra_c is inversely proportional to α_0, despite the small dependency of α_0 for the relation between the Rayleigh number, Ra_c, and air flow rate, $\dot{V}$, as just explained.

8.2 Solar heat load corresponding to the test set-up

The thermal conditions affecting the air in the cavity in the experimental and numerical study could correspond to real weather conditions for the reference roof construction described in Section 2.3.

The first level of comparison is to assign the effective temperature T_0 to be equal for the two cases. The effective temperature T_0 is calculated from the reduction of the thermal networks, described in Appendix D.1 and D.2. From this, a solar heat load I_{sol} acting on the roof surface, corresponding to the heat intensity added to the experimental set-ups, can be found. The internal as well as external air temperature were assumed to be $= 20\,°\mathrm{C}$, for the case with the reference roof construction, and the wind speed was assumed to be $U_{10} = 0$ m/s, not to include the effect of combined driving forces. Table 8.1 presents the solar heat load, acting normal to the roof surface, corresponding to the various heat intensity on the heating foil in the test set-up.

Table 8.1. Weather cases corresponding to the experimental set-ups and heat intensities.

Q [W]	I_{sol} [W/m^2]
9	$\simeq 120$
36	$\simeq 300$
81	$\simeq 590$
144	$\simeq 1000$

The results show that the heat intensities applied in the experimental tests and simulations, correspond to a solar heat load in the range of 100-1000 W/m^2. In Gothenburg, these weather cases could occur many times over the year. Solar heat load by mid day normally reaches values in the range of 500-1000 $\mathrm{W/m^2}$ during summer, and 100-500 $\mathrm{W/m^2}$ during winter (SMHI, 2019). Hence, the heat intensities applied in the experimental tests and simulations correspond to a realistic solar heat load.

However, one must be aware that equal effective temperatures, T_0, for the reference roof construction and the test set-ups in this study, do not mean that same thermal conditions will be reached in the reference roof as in this study. Thermal conditions reached in the cavity are dependent on the characteristic length, L_0 (see Equation 3.2), which is dependent on the air flow rate, $\dot{V}$, as well as the effective heat transfer coefficient, α_0. To predict the thermal conditions in the reference roof construction, the air flow is required, meaning that the Rayleigh number Ra_c has to be calculated for the specific case.

8.3 Application to reference roof construction

As presented in Section 8.1, the Rayleigh number can be calculated for a specific roof construction and climate condition. In this section, the reference roof construction is analysed. Geometries and material properties of the construction are presented in Section 2.3.

The flow resistances S for the reference roof are calculated according to Equation 8.1, where S_f is calculated according to Equation 3.16 and 3.18, S_ξ according to Equation 3.23 and S_{vent} according to Equation 3.16 and 3.24. The flow resistance from the vent is multiplied by two to include the pressure loss for the outlet. However, the vents are also assumed to handle twice the air flow of the rest of the cavity, covering the fact that vents are placed with some spacing, approximately one vent for every second cavity width.

$$S_{tot} = S_f + S_\xi + 2 \cdot S_{vent}(2 \cdot \dot{V}) \tag{8.1}$$

In Figure 8.3, the Rayleigh number Ra_c for the reference roof construction is calculated for various climate conditions. The wind speed is assumed to be U_{10} = 0 m/s and the relative humidity is assumed to be RH = 50 %.

From Figure 8.3, the air flow rate caused by thermal buoyancy for the reference roof construction can be estimated, for different climate conditions. The result shows that air flow rates up to 0.04 $\mathrm{m^3/s}$ could be expected from thermal buoyancy in a roof like the reference roof. Note, however, that the model is limited to steady-state conditions and the roof material properties might have an impact on the thermally driven air flow when transient phenomenons are considered. The model is also based on the assumption of a laminar flow in the cavity.

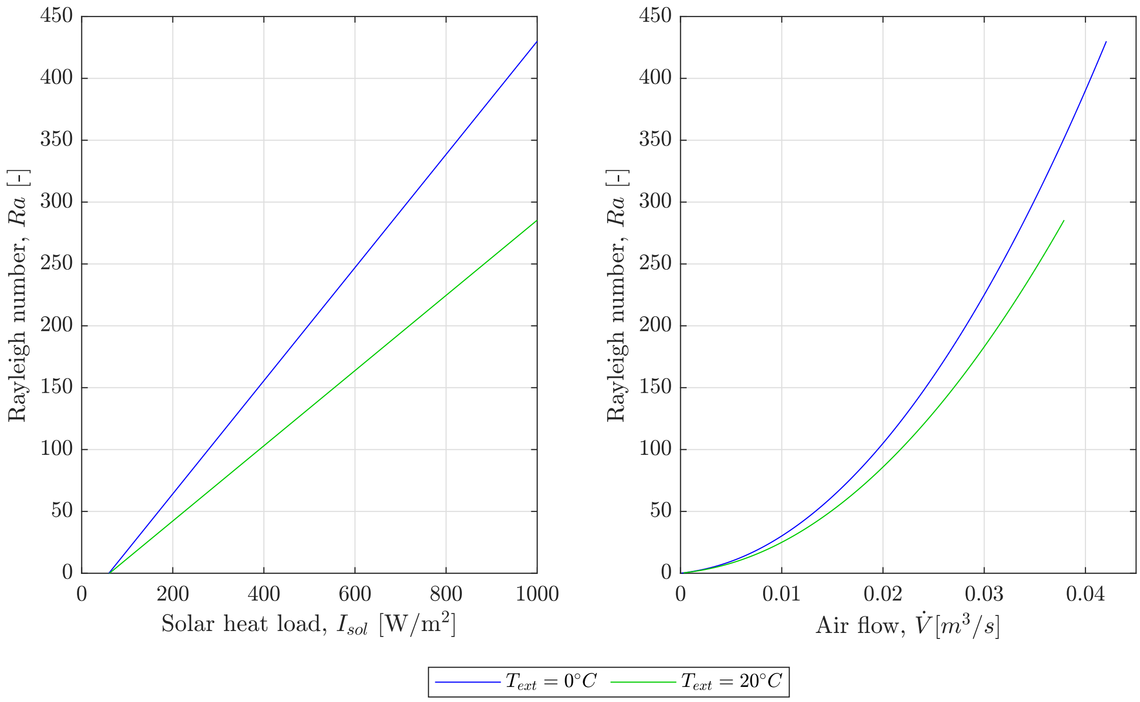

Figure 8.3. Rayleigh number Ra_c for varying solar heat load I_{sol} and resulting air flow $\dot{V}$, for different external temperatures, for the reference roof construction.

Further, as can be seen from Figure 8.3, for the same solar heat load, the Rayleigh number becomes higher for a colder external temperature. Hence, the thermal driving force becomes larger during winter than summer, for the same solar heat load. However, the solar heat load is generally lower during winter, as presented in Section 8.2. Solar heat loads below 70 W/m^2 are excluded from the plot due to the long wave radiation to the sky, counteracting the solar heat load on the roof for the low heat intensities.

8.4 Buoyant air flow model

As described above, the Rayleigh number can be calculated based on air cavity geometry, thermal properties and climatic conditions. Based on the Rayleigh number, the air flow rate can be predicted. This process, outlined above for a given case, has been generalised into a model implemented in MATLAB, provided in Appendix F. An overview of the input data for the model is provided in Figure 8.4. The output of the model is a graph which relates selected relevant outdoor air temperatures to the Rayleigh number of the construction, and a graph which relates this Rayleigh number to an air flow rate prediction, see Figure 8.3.

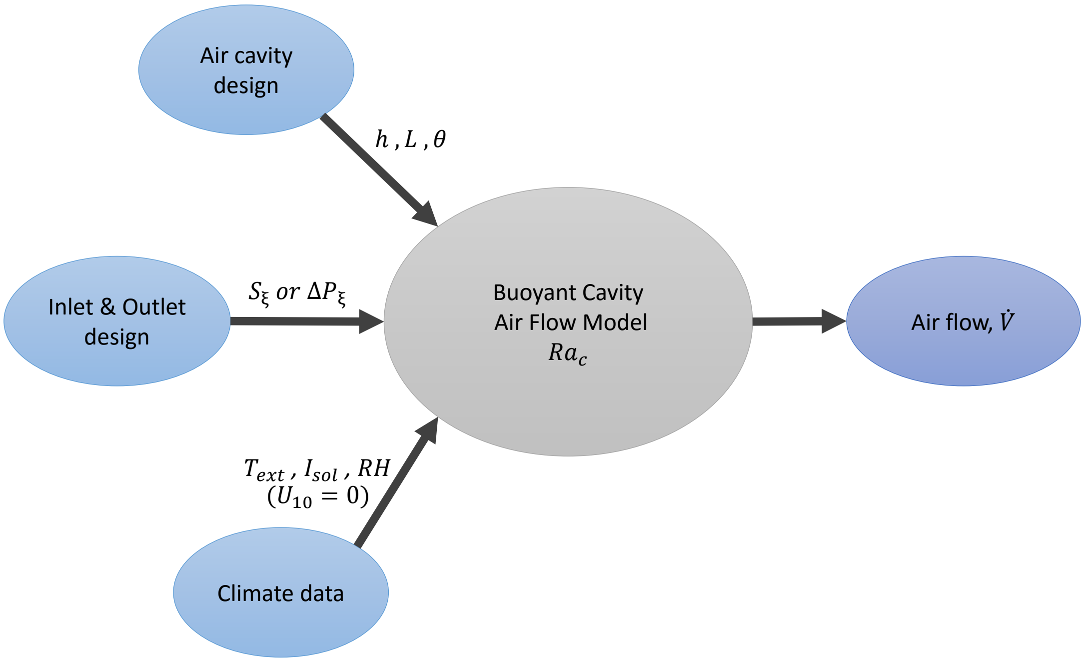

Figure 8.4. Required input data for buoyant air flow model implemented in MATLAB.

When using this model the assumptions and simplifications outlined throughout this thesis need to be considered, and the model output should be considered an idealised version of reality. Assumptions such as steady-state conditions and one-dimensional heat flux through the roof construction might be an oversimplification for certain conditions. This must be taken into account when applying the air flow model for e.g. moisture risk assessment. Additionally, the model is limited to roof constructions with inlet and outlet designs studied in previous research, as the local pressure losses are input data. The model also assumes a wind speed of $U_{10} = 0\,\mathrm{m/s}$, meaning that for times when the wind pressure is the governing driving force on the system, the model is not applicable.

8.5 Thermal buoyancy compared to wind pressure

The air flow in the cavity is driven by a difference in pressure between inlet and outlet, as presented in Section 3.2.2, and caused by either thermal buoyancy effects or wind pressure. In order to know if the thermal buoyancy is of relevance for the cavity ventilation in a roof, this driving force has to be compared with the driving force caused by wind.

According to Equation 3.9, the two driving forces can be combined by addition, meaning effects from mixed convection are neglected, making the pressure difference from the two driving forces comparable with each other. Based on this assumption, a wind speed corresponding to the pressure differences caused by thermal buoyancy can be calculated.

In the experimental study, the driving force caused by thermal buoyancy was in the range between 0 and 1.4 Pa while highest driving force found in the simulations was 0.8 Pa (see the driving force from all tests in Appendix C). Further, as presented in Section 8.2, the pressure differences which occurred in this study could be comparable with real weather cases, which means that the driving force from thermal buoyancy most likely is in the range up to 1 Pa.

The driving force from wind pressure is calculated according to Equation 3.10a. By assuming a Δc_p of 0.7 (see Section 3.2.2.1) and the reference weather case used in Section 8.3 (T_{ext} = 0 °C, RH = 50 %), the wind speed correlating to pressure difference up to 1 Pa can be calculated and the results are presented in Figure 8.5.

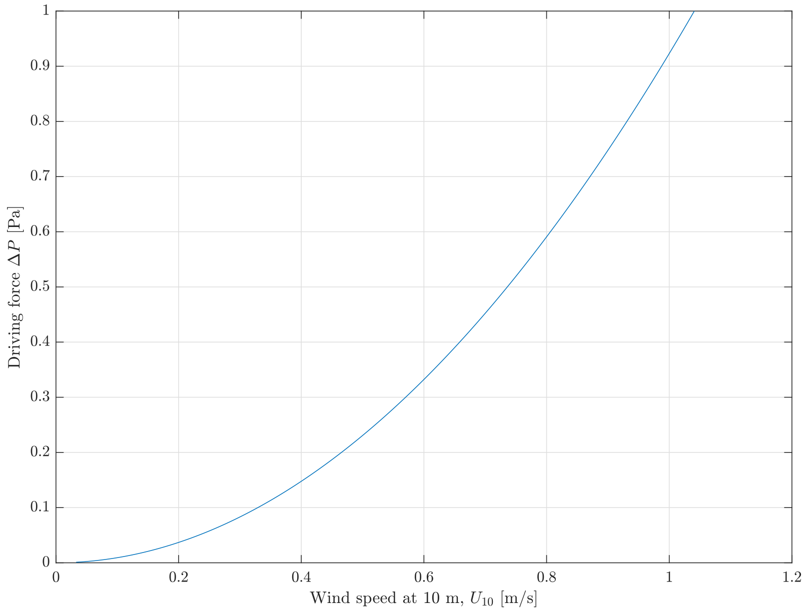

Figure 8.5. Wind speed perpendicular to the air cavity at 10 m height, U_{10} and corresponding driving force ΔP_w for T_{ext} = 0 °C and RH = 50 %.

As can be seen, pressure difference up to 1 Pa corresponds to a wind speed up to approximately 1 m/s. Hence, the thermal buoyancy effect may be dominating for wind speeds below 1 m/s while the driving force from wind most likely is dominating over the thermal buoyancy effect for higher wind speeds. However, this calculation assumes the wind to act perpendicularly to the roof side where the cavity inlet is. As Equation 3.10c states, the wind pressure coefficient Δc_p is dependent on the wind direction, which means that the driving force from thermal buoyancy can be of the same magnitude as from wind with a higher wind speed U_{10} than 1 m/s.

In order to estimate the relative importance of the wind driven and the thermally driven air flow, climate data for a year has to be studied. Also, the wind direction compared to the orientation of the building as well as the direction of solar radiation compared to the orientation of the building and the roof inclination have to be taken into account. Additionally, the impact of topography and surroundings of the building might play an important role for the relation between wind driven air flow and the air flow from thermal buoyancy. Hence, the modelling of the cavity air flow dependent on both of the two driving forces, for yearly variations, is complex and makes the analysis regarding the relative importance of the two driving forces excluded from this study.

9
Conclusions

This study has investigated the relationship between air cavity design in parallel roofs, and the thermal and air flow conditions for air cavity ventilation driven by thermal buoyancy. The study includes experimental tests and a numerical study in COMSOL Multiphysics on a roof model with length 3.5 m. The tests were made for a roofing overheated compared to the inlet air temperature, which in reality would correspond to a roof heated by solar radiation. Cavity heights of $23-70$ mm, and roof inclinations of $5-45°$ were studied.

The study found that for a roof with constant length, both cavity height and roof inclination have a large influence on the air flow caused by thermal buoyancy. An increased cavity height or increased inclination leads to a higher air flow rate in the cavity. However, the air velocity in the cavity is not as dependent on the cavity height and appears to have a maximum value for a given heat intensity and roof inclination.

Regarding the experimental study, the measurement uncertainties are many, both for temperature measurements and velocity measurements. The thermocouples could have been shielded from radiation in a more robust way and the air temperature measurements could have been performed in more locations across the cavity height for more useful results. Further, the types of smoke used for velocity measurements were not suitable for studying thermal buoyancy, due to the buoyancy of the smoke itself.

However, the trends shown from the numerical and experimental results were generally in agreement, showing that with increasing roof inclination, cavity height, and heat production being shown to cause a higher flow rate. The results from simulations were compared to analytical models, and were estimated to provide a good representation of reality. This shows that CFD simulations are useful to study coupled heat transfer and air flow in cavities in building components.

Most of the studied cases, both experimental and numerical, show Reynolds numbers within the laminar regime, meaning laminar flow can be assumed for most cases of thermal buoyancy driven convection in air cavities of typical dimensions.

The study found that it is possible to create an analytical calculation model for estimations of the air flow in a cavity from given geometries and climate data. The cavity Rayleigh number Ra_c was shown to provide a useful prediction of the impact of buoyancy when determining the driving forces for air movement in an air cavity. The theoretical models for calculating the thermal conditions and the air flow resistance caused by frictional and local losses, used for determining the air cavity Rayleigh number, were shown to correlate well with measured and simulated results.

However, the impact from time dependent thermal effects was found to influence the measurement results greatly. This means that transient effects, depending on the materials in the cavity, has to be considered in a calculation model in order for it to be correct.

The magnitude of the driving force from thermal buoyancy was shown to reach similar values to the driving force caused by a wind speed of $1\,\mathrm{m/s}$, acting perpendicular to the cavity inlet. This indicates that thermal buoyancy as a driving force for convection in air cavities could be relevant for a large portion of the year.

9.1 Further studies

In order to fully understand the impact of thermal buoyancy effects in the air cavity in a roof construction, further research is required. The effect of turbulence or other disturbances against laminar flow should be investigated, e.g. bends in the cavity flow, contraction due to battens, or horizontal flow paths. In addition, further research should study the effect of under-cooling of the cavity air, e.g. due to long-wave radiation during night.

The results for thermal conditions in this study could be used to estimate the convective heat transfer coefficient α_c for inclined cavities which would develop the model derived in this study further.

Additionally, moisture simulations is required to predict the risk of condensation and moisture damages to the construction. Since moisture conditions are highly correlated with both thermal conditions and air movements as well as time, the problem regarding cavity ventilation is complex and requires simulations which consider yearly and daily variations.

The relation between air flow and drying also remains unknown and in order to fully address the challenges of roof ventilation in the Nordic climate, the drying effect of varied ventilation, both in magnitude, flow profiles and flow characteristics, should be studied. Furthermore, field studies could be conducted both to ascertain the prevalence of moisture damage in Nordic parallel roof constructions, and the risk associated with such damage for the health of building users.

Finally, further studies are needed to quantify the relative importance of the driving forces, especially for the purpose of removing excess moisture. The understanding of influence of forced convection on the hygrothermal and air flow conditions in the air cavity, regarding moisture safety of roof constructions, can in general be developed. Further studies on the thermal buoyancy effect in combination with driving forces from wind pressure are also needed, including yearly variations.

Bibliography

Arfvidsson, J., Harderup, L.-E. & Samuelson, I. (2017). *Fukthandbok: praktik och teori* (4th ed.). Stockholm: AB Svensk Byggtjänst.

ASHRAE. (2013). *2013 ASHRAE Handbook: Fundamentals*. Atlanta: ASHRAE.

Åström, A. (2017). *Täta tak - en guide till skadefria takpannetak* (Master's thesis, KTH, Stockholm).

Autodesk. (2019). Finite Element vs Finite Volume. Retrieved June 3, 2019, from https://knowledge.autodesk.com/support/cfd/learn-explore/caas/CloudHelp/cloudhelp/2019/ENU/SimCFD-Learning/files/GUID-12A9AED8-2047-4D3A-BC80-82BE9CF47517-htm.html

Bejan, A. (2004). *Convection heat transfer*. New Jersey: Wiley.

Bengtson, A. & Fransson, V. (2014). *The Influence of Natural and Forced Convection in Attics-A CFD Analysis* (Master's thesis, Chalmers University of Technology, Gothenburg).

Biwole, P. H., Woloszyn, M. & Pompeo, C. (2008). Heat transfers in a double-skin roof ventilated by natural convection in summer time. *Energy and Buildings*.

Björk, C., Nordling, L. & Reppen, L. (2009). *Så byggdes villan - Svensk villaarkitektur från 1890 till 2010*. Stockholm: Formas.

Blom, P. (1991). *Lufting av isolerte, skrå tak* (Doctoral dissertation, NTH, Trondheim).

Blom, P. (2001). Venting of Attics and Pitched, Insulated Roofs. *Journal of Thermal Envelope and Building Science*, *25*(1), 32–50.

Bornehag, C.-G., Blomquist, G., Gyntelberg, F., Jarvholm, B., Malmberg, P., Nordvall, L., … Sundell, J. (2001). Dampness in Buildings and Health. *Indoor Air*, *11*(2), 72–86.

Boverket. (1988). Nybyggnadsregler.

Boverket. (2018). Boverkets byggregler - föreskrifter och allmänna råd.

Bunkholt, N. S., Säwén, T., Svantesson, M., Kvande, T., Gullbrekken, L., Wahlgren, P. & Lohne, J. (2019). Experimental study of thermal buoyancy in the cavity of ventilated roofs. *Submitted to Journal of Building Physics*.

Bunnag, T., Khedari, J., Hirunlabh, J. & Zeghmati, B. (2004). Experimental investigation of free convection in an open-ended inclined rectangular channel heated from the top. *International Journal of Ambient Energy*, *25*(3), 151–162.

Chami, N. & Zoughaib, A. (2010). Modeling natural convection in a pitched thermosyphon system in building roofs and experimental validation using particle image velocimetry. *Energy and Buildings*, *42*(8), 1267–1274.

COMSOL. (2017). *Introduction to COMSOL Multiphysics*.

COMSOL Inc. (2018). COMSOL Multiphysics Reference Manual (version 5.3a). *Comsol*.

Edvardsen, K. I. & Torjussen, L. (2000). Håndbok 45-TREHUS. *Oslo, NBI*.

Eggen, M. G. & Røer, O. V. (2018). *Lufting av skrå tretak-Trykktap ved ulike luftespalteutforminger* (Master's thesis, NTNU, Trondheim).

Eriksson, O. (2017). *Fuktsäkra parallelltak - En studie av risken för mögelpåväxt i parallelltak med variabel ångbroms* (Master's thesis, Linnéuniversitetet, Växjö).

Falk, J. (2014). *Rendered rainscreen walls Cavity ventilation rates, ventilation drying and moisture-induced cladding deformation* (Doctoral dissertation, Lund).

Flexwatt. (2019). Flexwatt varmefolie.

Gullbrekken, L. (2018). *Climate adaptation of pitched wooden roofs* (Doctoral thesis, NTNU, Trondheim).

Gullbrekken, L., Kvande, T. & Time, B. (2017a). Ventilated wooden roofs: Influence of local weather conditions-measurements. In *Energy procedia*.

Gullbrekken, L., Uvsløkk, S., Geving, S. & Kvande, T. (2017b). Local loss coefficients inside air cavity of ventilated pitched roofs. *Journal of Building Physics*.

Gullbrekken, L., Uvsløkk, S. & Kvande, T. (2018). Wind pressure coefficients for roof ventilation purposes. *Journal of Wind Engineering and Industrial Aerodynamics*, *175*, 144–152.

Hagentoft, C.-E. (1991). Air convection coupled with heat conduction in a wall. A thermal analysis. *Notes on Heat Transfer*, *7*.

Hagentoft, C.-E. (2001). *Introduction to Building Physics*. Lund: Studentlitteratur AB.

Hansen, E. (2016). *Luftstrømning i skrå tretak-Eksperimentelle undersøkelser og numeriske beregninger* (Master's thesis, NTNU, Trondheim).

Hansen, H., Stampe, O. & Kjerulf-Jensen, P. (1992). Varme-og klimateknik: grundbog.

Hellsvik, R. (2015). *Transient Simulation of Ventilation Rate and Moisture load for Cold Attic Constructions-A CFD Analysis* (Master's thesis, Chalmers University of Technology, Gothenburg).

Hofseth, V. (2004). *Lufting av skrå isolerte tak* (Master's thesis, NTNU, Trondheim).

Incropera, F., DeWitt, D., Bergman, T. & Lavine, A. (2007). *Fundamentals of Heat and Mass Transfer* (6th ed.). New Jersey: Wiley.

Johansson, A. & Larsson, A. (2016). *Riskbedömning för mikrobiell påväxt i ett välisolerat parallelltak* (Master's thesis, Högskolan i Halmstad).

Kjellström, E., Bärring, L., Jacob, D., Jones, R., Lenderink, G. & Schär, C. (2007). Modelling daily temperature extremes: recent climate and future changes over Europe. *Climatic Change*, *81*(S1), 249–265.

Korsgaard, V., Christensen, G., Prebensen, K. & Bunch-Nielsen, T. (1985). Ventilation of Timber Flat Roofs.

Kronvall, J. (1980). *Air flows in building components* (Doctoral dissertation, LTH, Lund).

Latif, H. A. & Ehsani, S. (2013). *Analys av fuktomlagring i välisolerade parallelltak* (Master's thesis, KTH, Stockholm).

Lee, S., Park, S. H., Yeo, M. S. & Kim, K. W. (2009). An experimental study on airflow in the cavity of a ventilated roof. *Building and Environment*.

Liersch, K. W. (1986). *Belüftete Dach- und Wandkonstruktionen, Band 3: Dächer*. Berlin: Bauverlag.

Lindgren, T. (2017). *Parameterstudie i WUFI om fuktsäkra parallelltak* (Master's thesis).

Manca, O., Mangiacapra, A., Marino, S. & Nardini, S. (2014). Numerical Investigation on Thermal Behaviors of an Inclined Ventilated Roof. In *Volume 2: Dynamics, vibration and control; energy; fluids engineering; micro and nano manufacturing* (V002T09A017). ASME.

Nikulin, G., Kjellström, E., Hansson, U., Strandberg, G. & Ullerstig, A. (2011). Evaluation and future projections of temperature, precipitation and wind extremes over Europe in an ensemble of regional climate simulations. *Tellus A: Dynamic Meteorology and Oceanography*, *63*(1), 41–55.

Nusser, B. & Teibinger, M. (2013). Experimental investigations about the air flow in the ventilation layer of low pitched roofs.

Petersson, B.-Å. (1983). Tilläggsisolering av tak: problem, erfarenheter och möjligheter.

Petersson, B.-Å. (2009). *Byggnaders klimatskärm: fuktsäkerhet, energieffektivitet, beständighet*. Lund: Studentlitteratur.

Pozrikidis, C. (2016). Fluid dynamics: theory, computation, and numerical simulation.

Rada, D. & Beto, E. R. (2016). Isolerat parallelltak ur fuktperspektiv.

Rikner, V. & von Platen, H. (2015). *Mätningar och simuleringar av fukt i tak*.

Samuelson, I. (2000). Tak utan ventilationsspalt–en riskkonstruktion? *Bygg & teknik*, (2).

SMHI. (2019). Utforskaren - Öppna data. Retrieved April 24, 2019, from https://www.smhi.se/klimatdata/utforskaren-oppna-data/

Susanti, L., Homma, H., Matsumoto, H., Suzuki, Y. & Shimizu, M. (2008). A laboratory experiment on natural ventilation through a roof cavity for reduction of solar heat gain. *Energy and Buildings*.

Svensk Byggtjänst. (2018). *RA Hus 18*. Stockholm.

Tobin, L. (2016). *Med eller utan luftspalt i parallelltak?*

Träguiden. (2019). Konstruktionsexempel tak. Retrieved May 24, 2019, from https://www.traguiden.se/konstruktion/konstruktionsexempel/tak/

A

Experimental results

A.1 Temperature

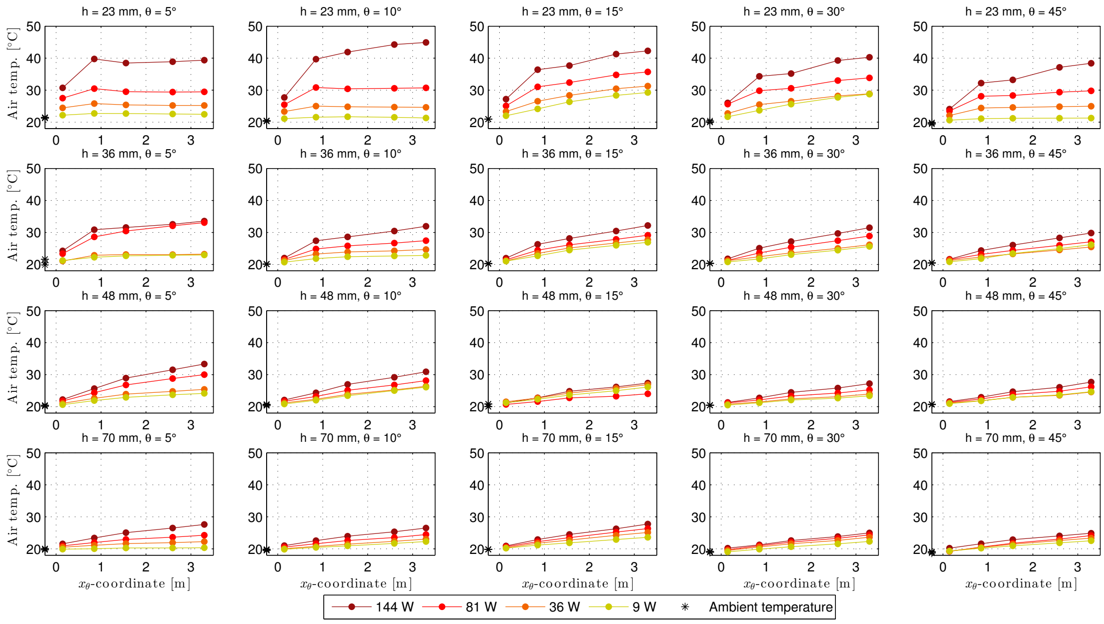

Figure A.1. Measured air temperatures along the cavity length

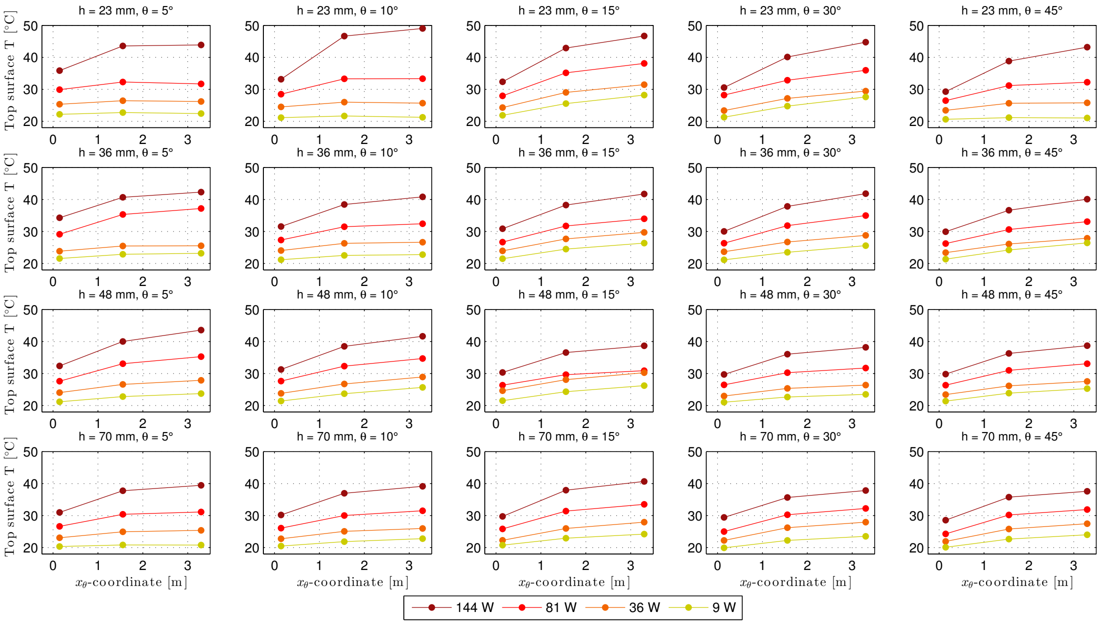

Figure A.2. Measured top surface temperatures along the cavity length

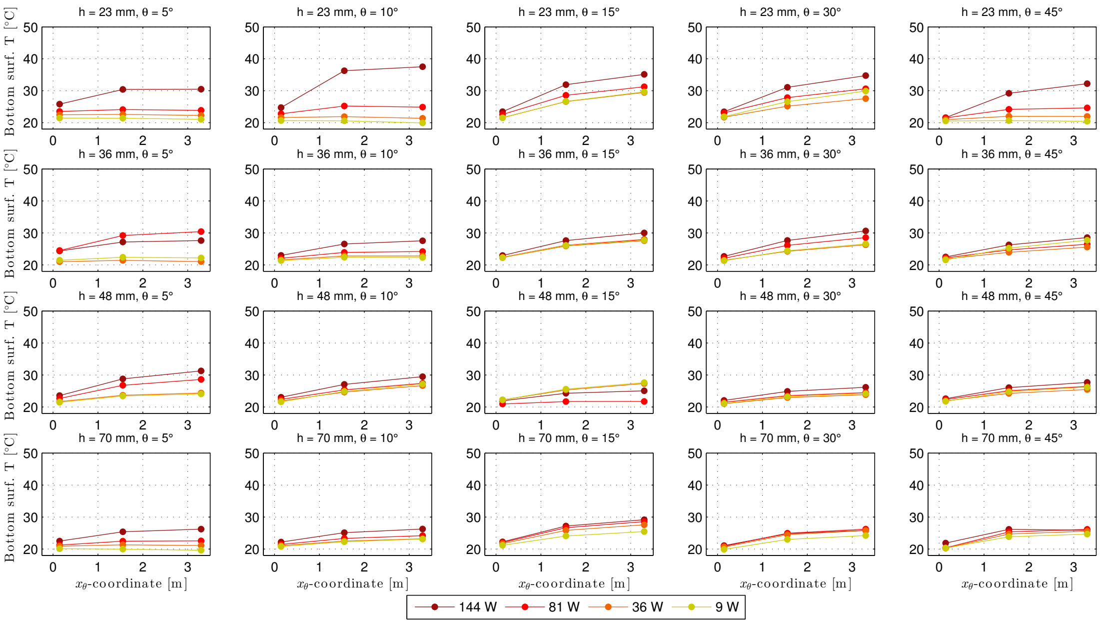

Figure A.3. Measured bottom surface temperatures along the cavity length

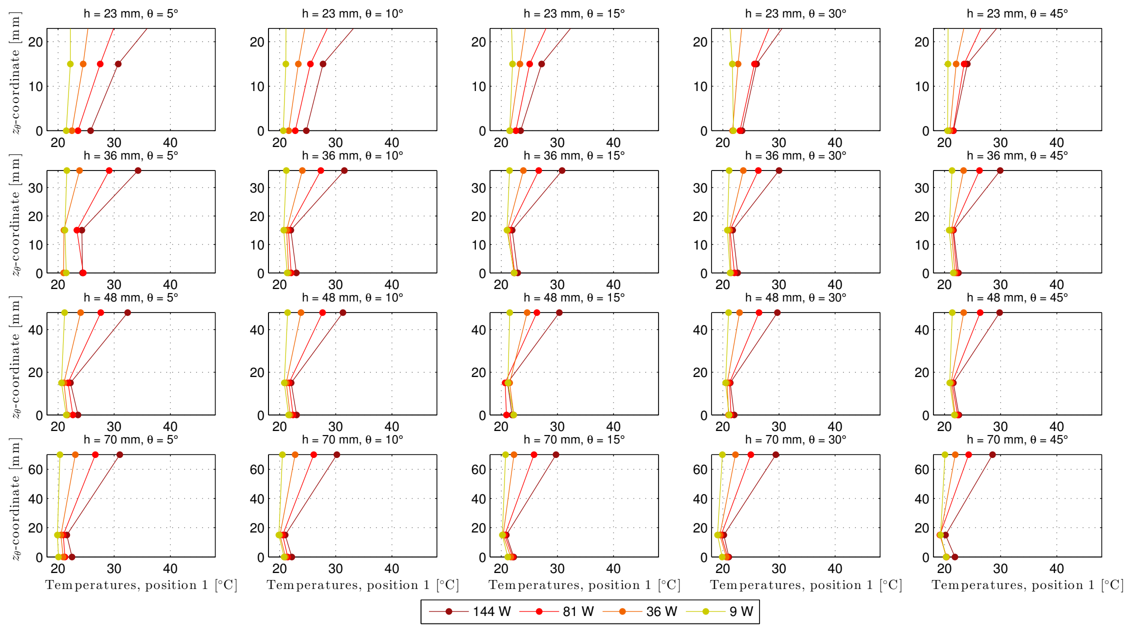

Figure A.4. Measured air and surface temperatures along the cavity height, z_θ, in measurement position 1.

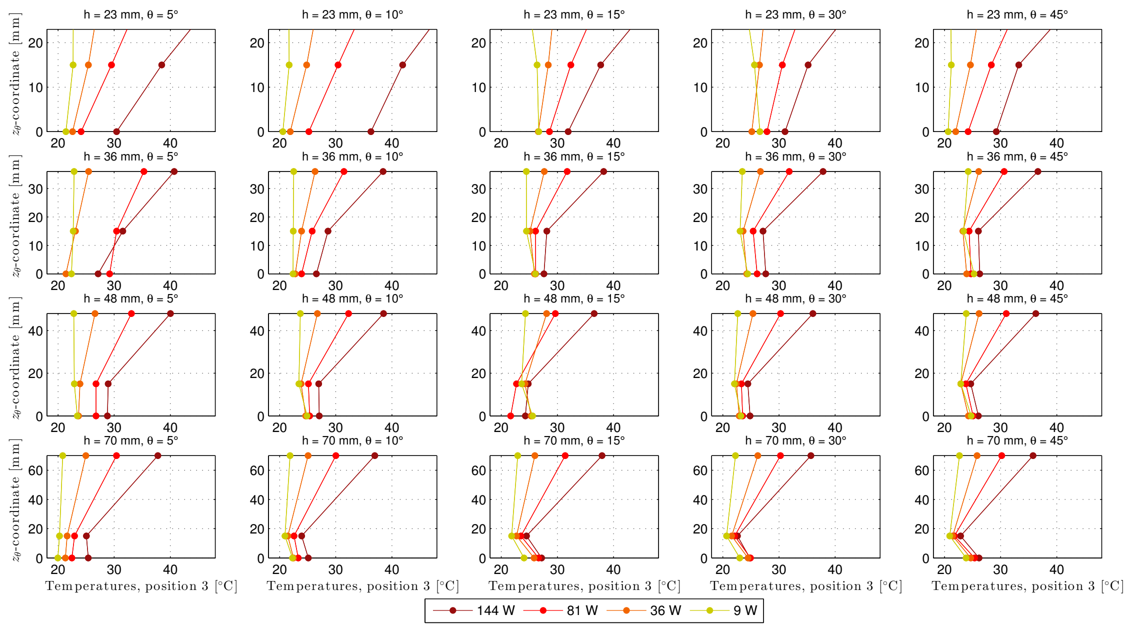

Figure A.5. Measured air and surface temperatures along the cavity height, z_θ, in measurement position 3.

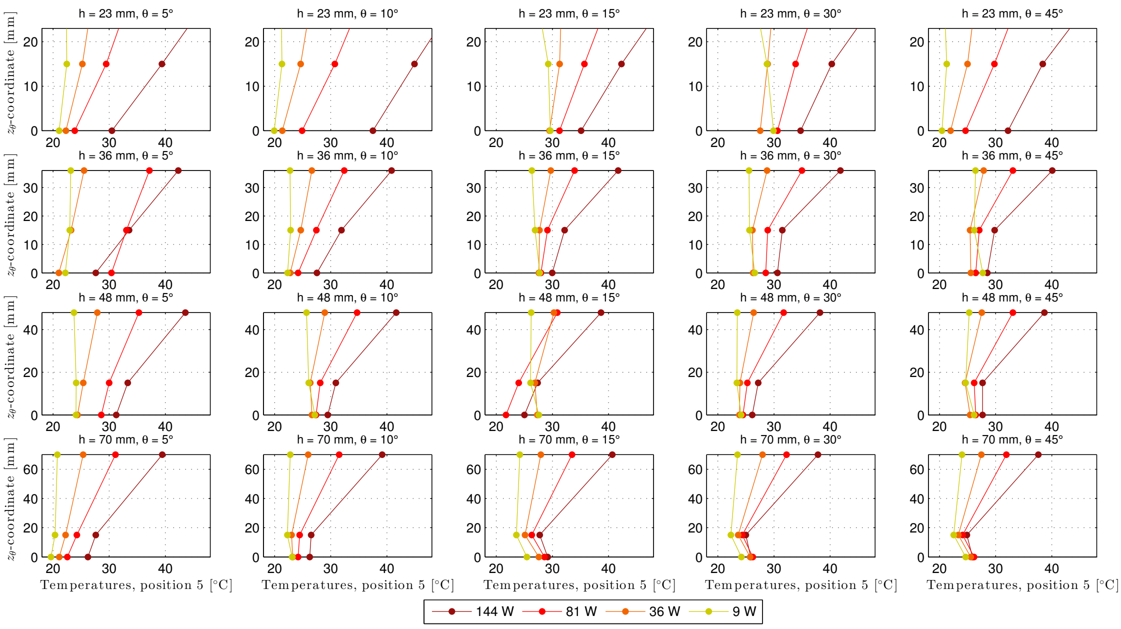

Figure A.6. Measured air and surface temperatures along the cavity height, z_θ, in measurement position 5.

A.2 Air velocity

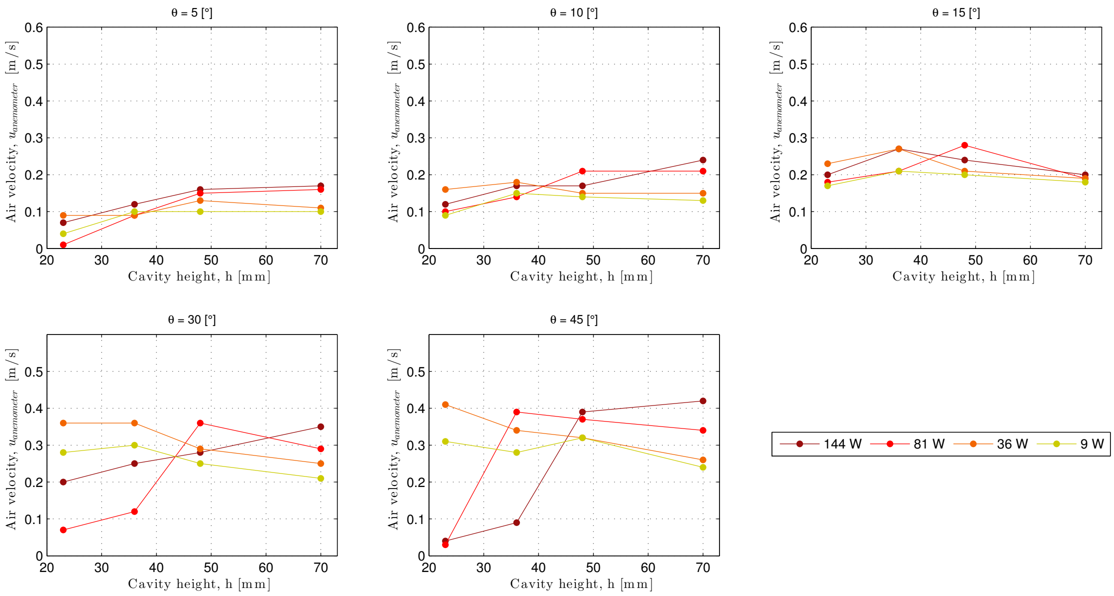

Figure A.7. Air velocity measured by anemometer, for varying cavity heights.

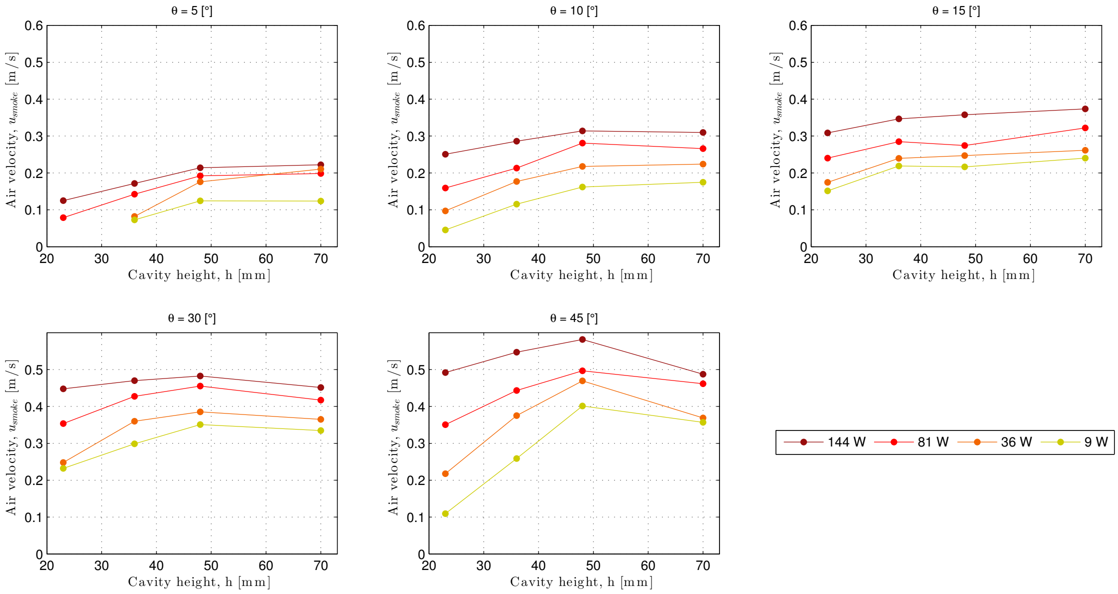

Figure A.8. Air velocity measured by smoke tests, for varying cavity heights.

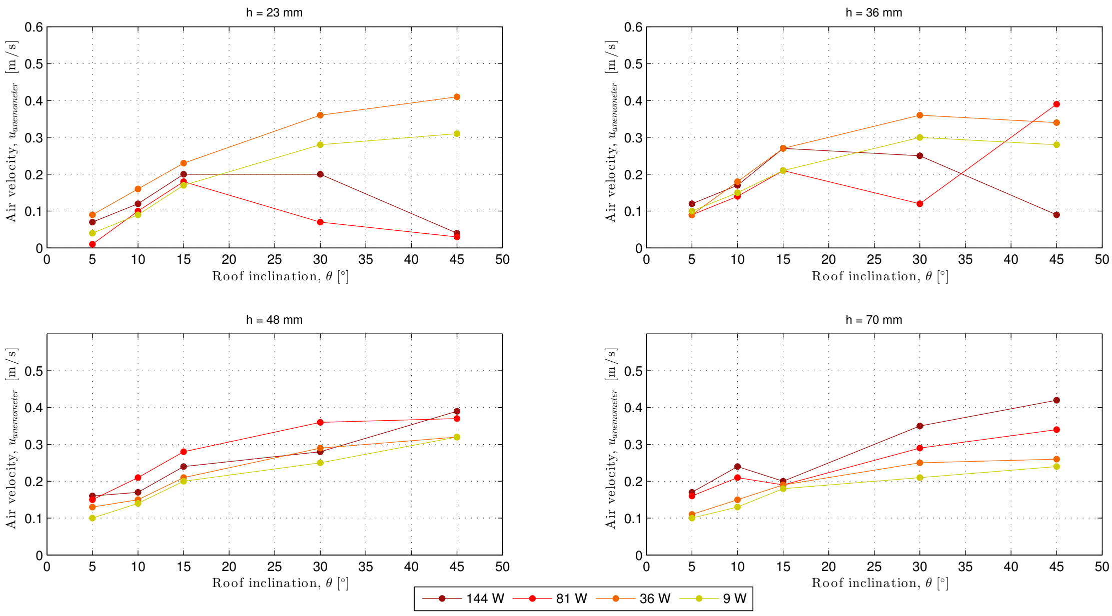

Figure A.9. Air velocity measured by anemometer, for varying roof inclination.

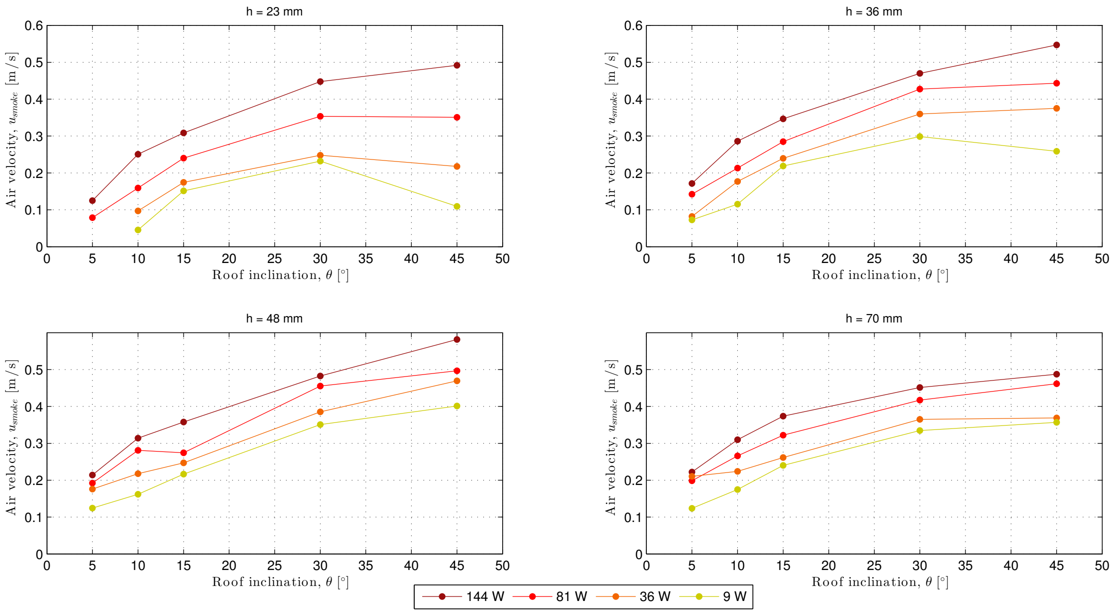

Figure A.10. Air velocity measured by smoke tests, for varying roof inclination.

B

Simulated results

B.1 Temperature

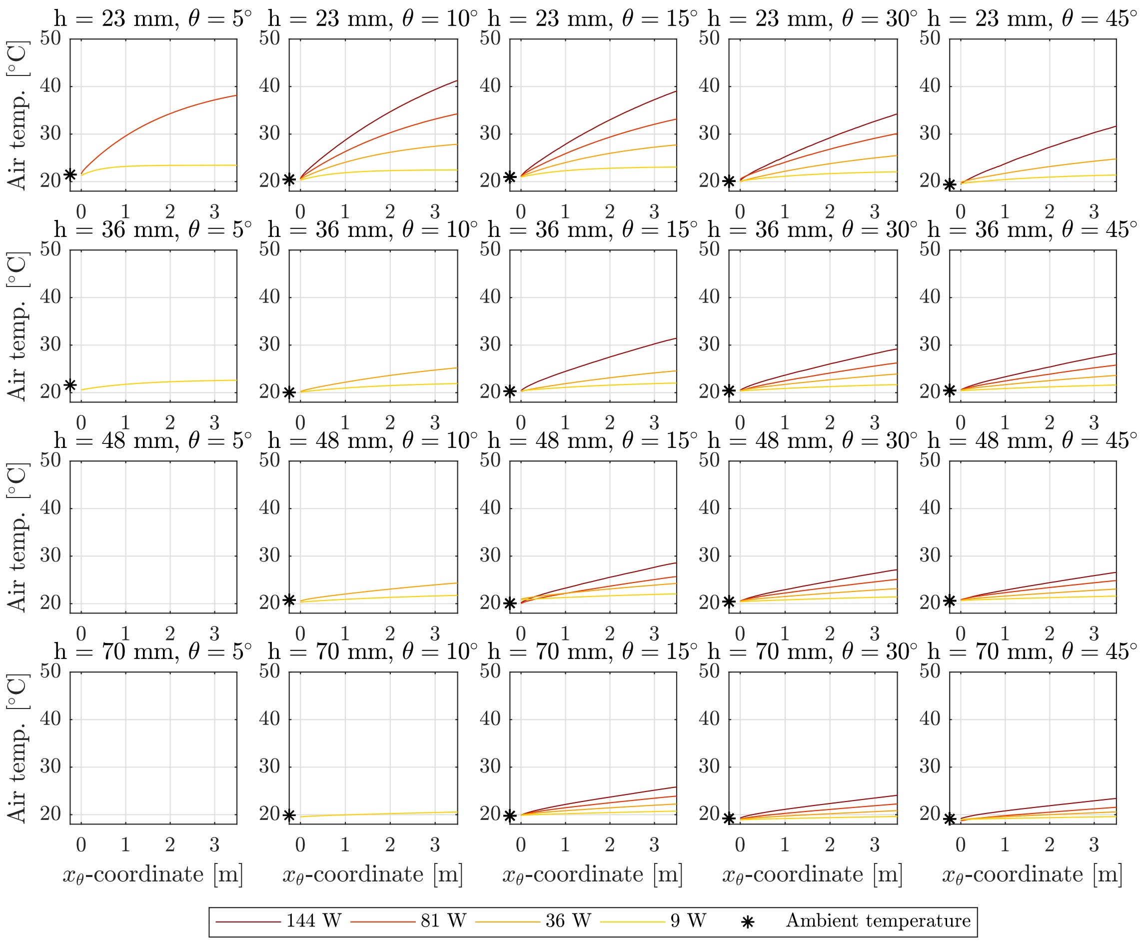

Figure B.1. Simulated air temperatures along the cavity length, x_θ.

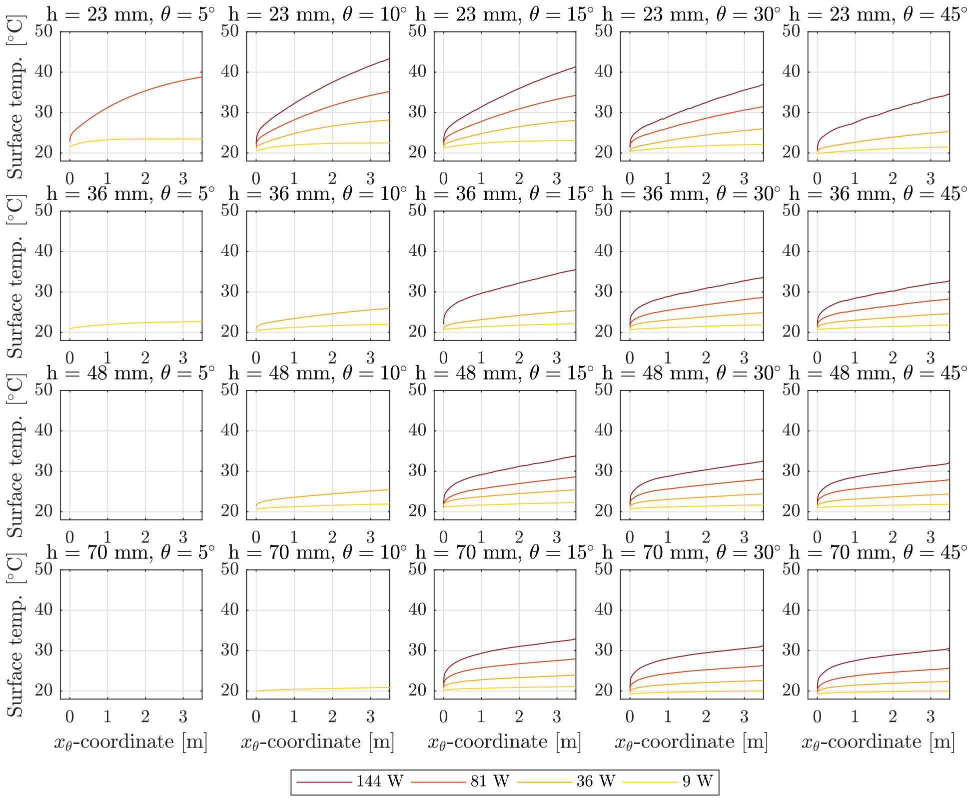

Figure B.2. Simulated top surface temperatures along the cavity length, x_θ.

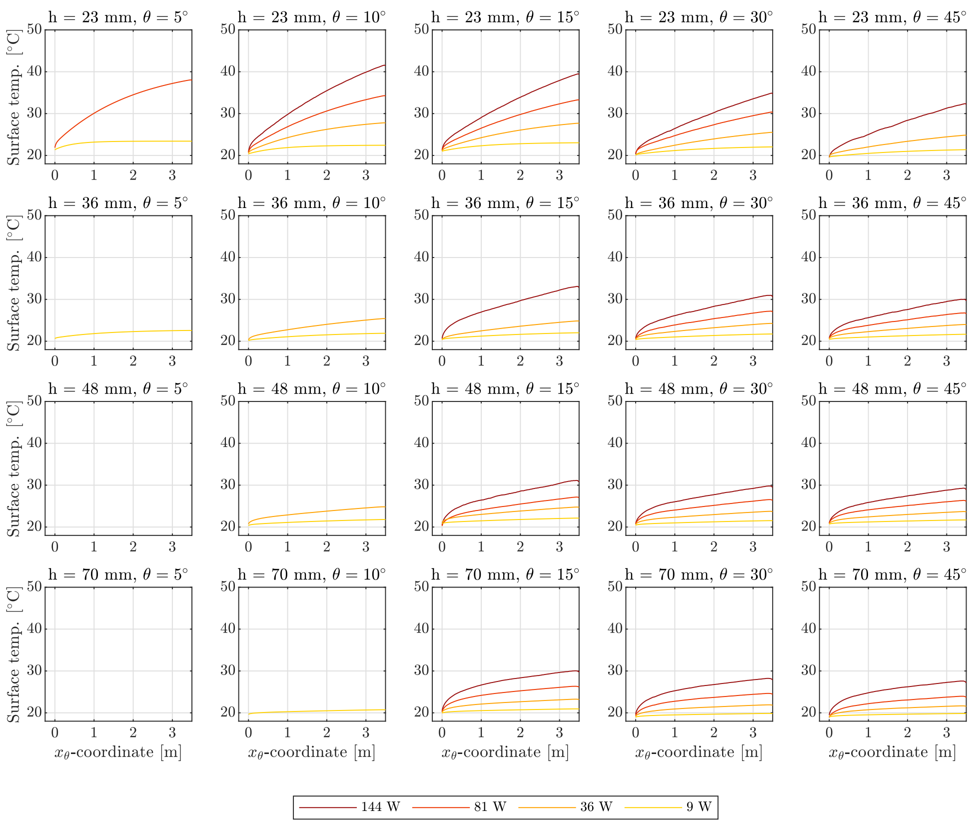

Figure B.3. Simulated bottom surface temperatures along the cavity length, x_θ.

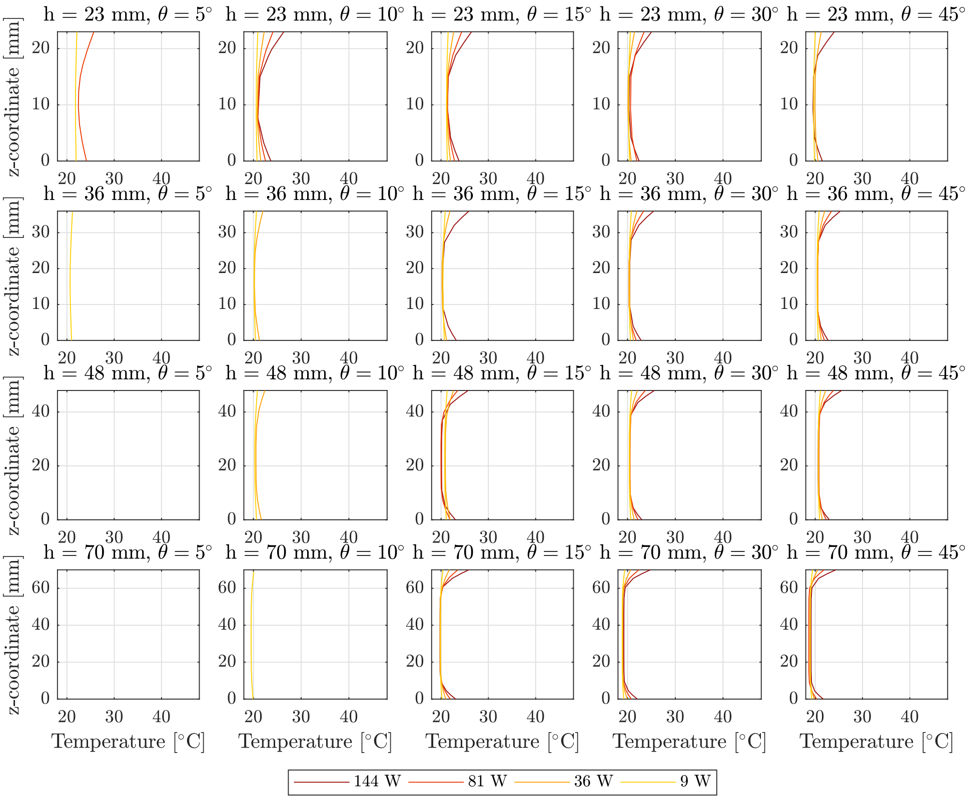

Figure B.4. Simulated air temperatures along the cavity height, z_θ, in position 1.

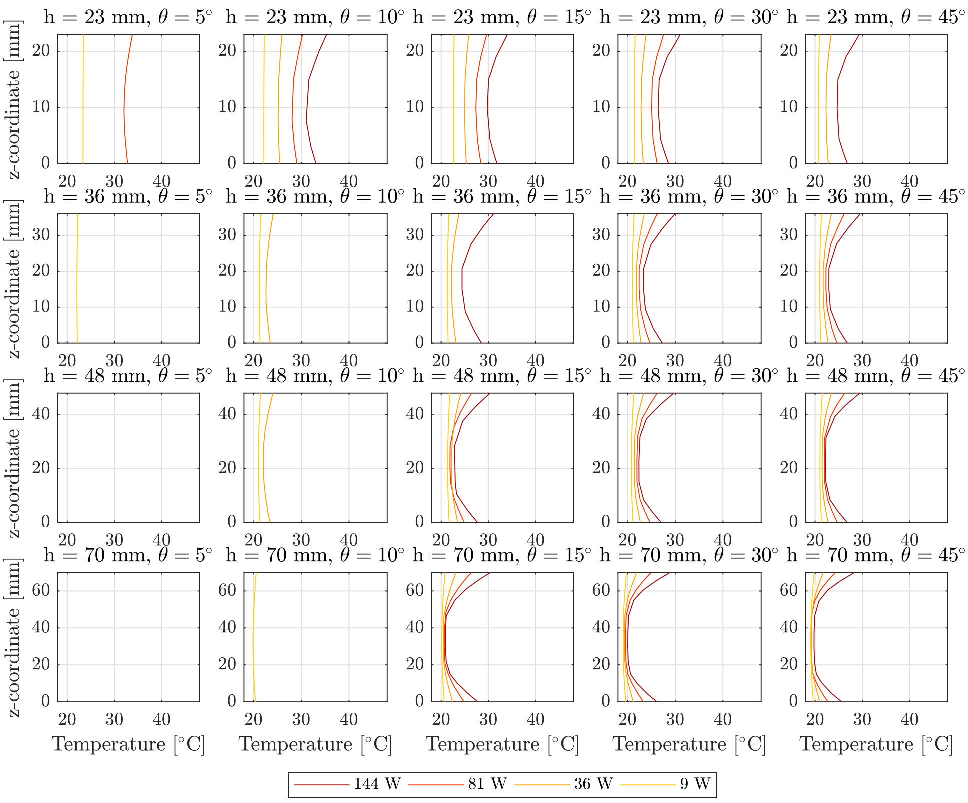

Figure B.5. Simulated air temperatures along the cavity height, z_θ, in position 3.

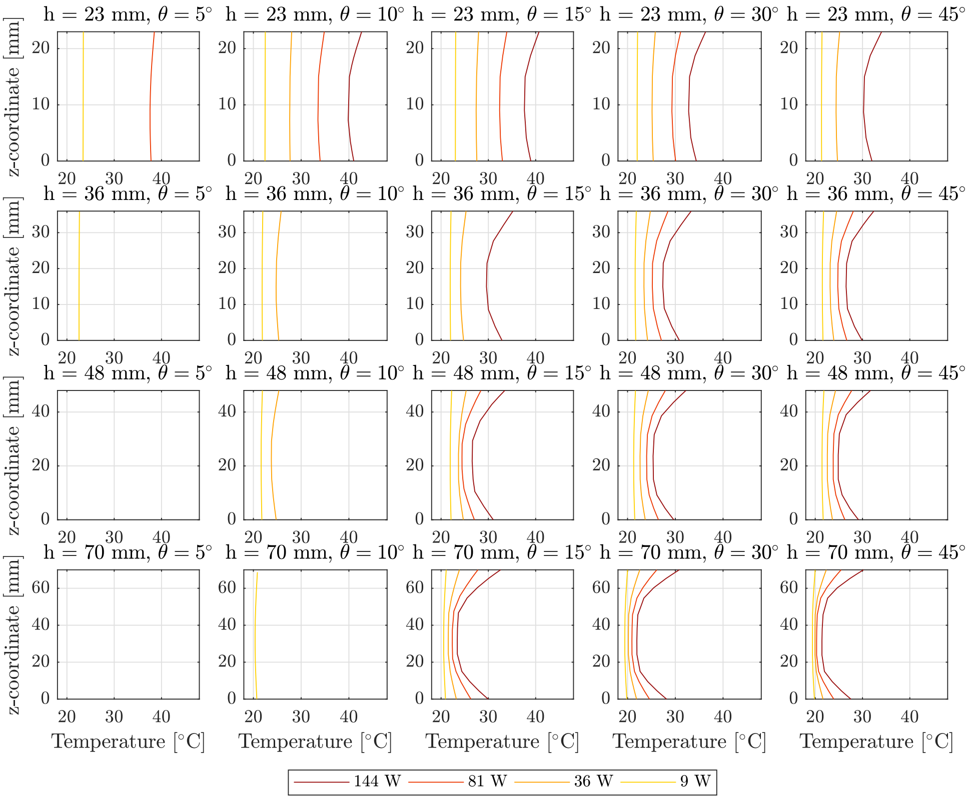

Figure B.6. Simulated air temperatures along the cavity height, z_{θ}, in position 5.

B.2 Air velocity

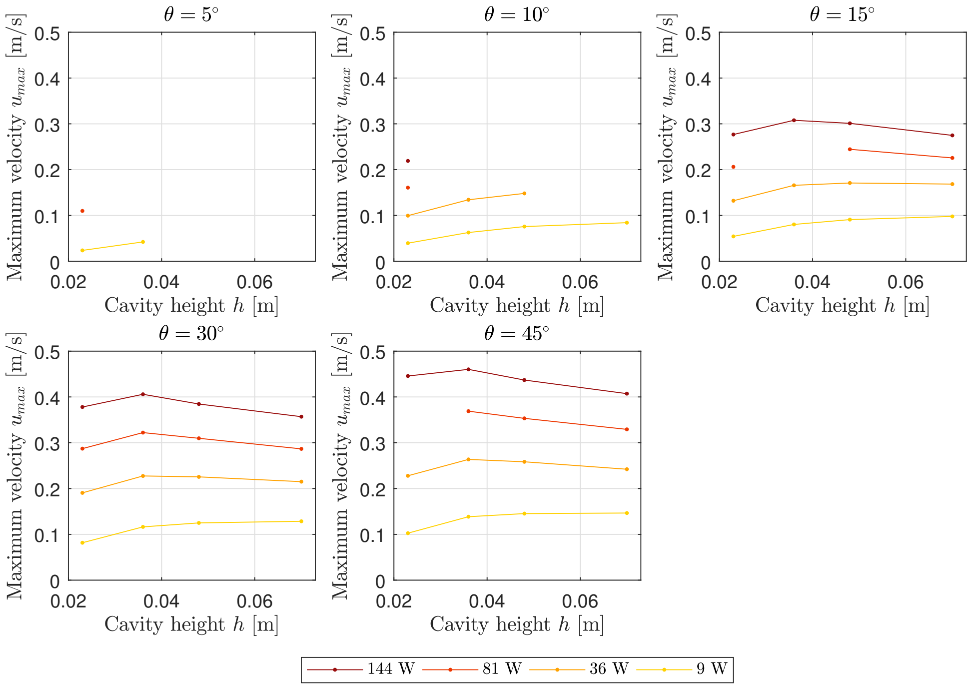

Figure B.7. Simulated maximum air velocity, as a function of cavity height, h.

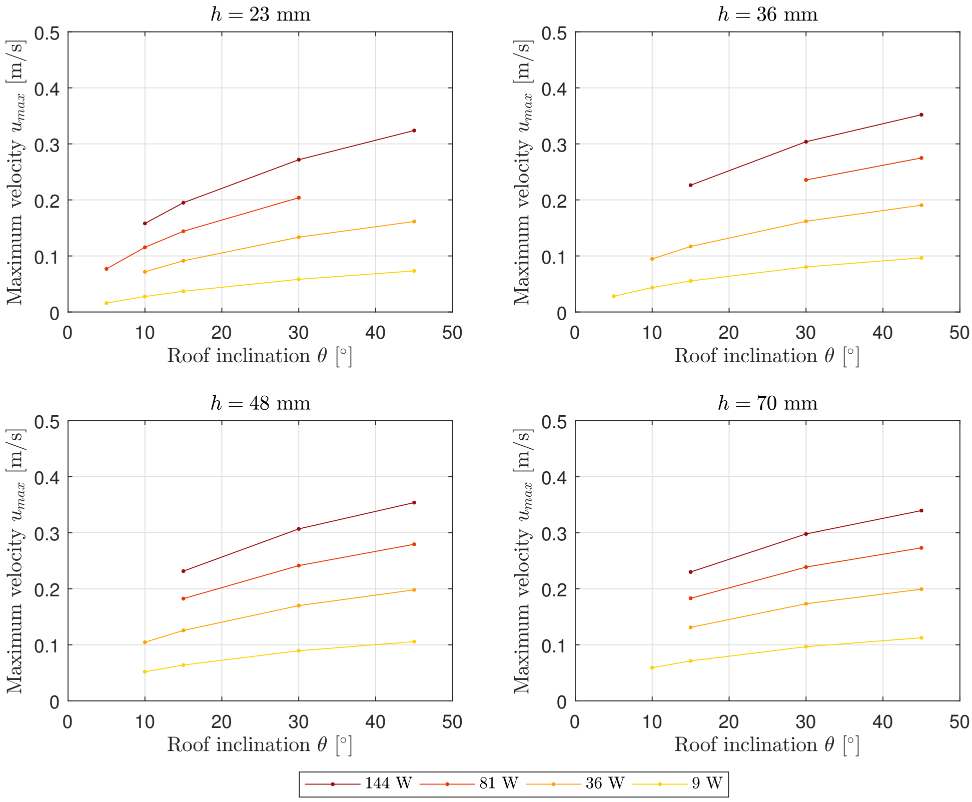

Figure B.8. Simulated maximum air velocity as a function of inclination, θ.

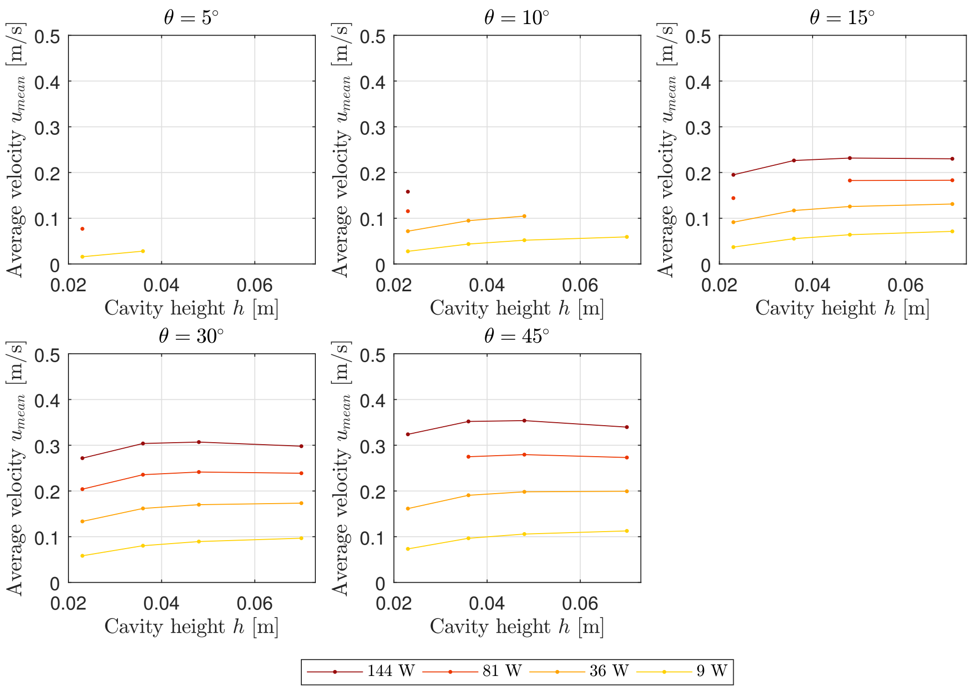

Figure B.9. Simulated mean air velocity as a function of cavity height, *h*.

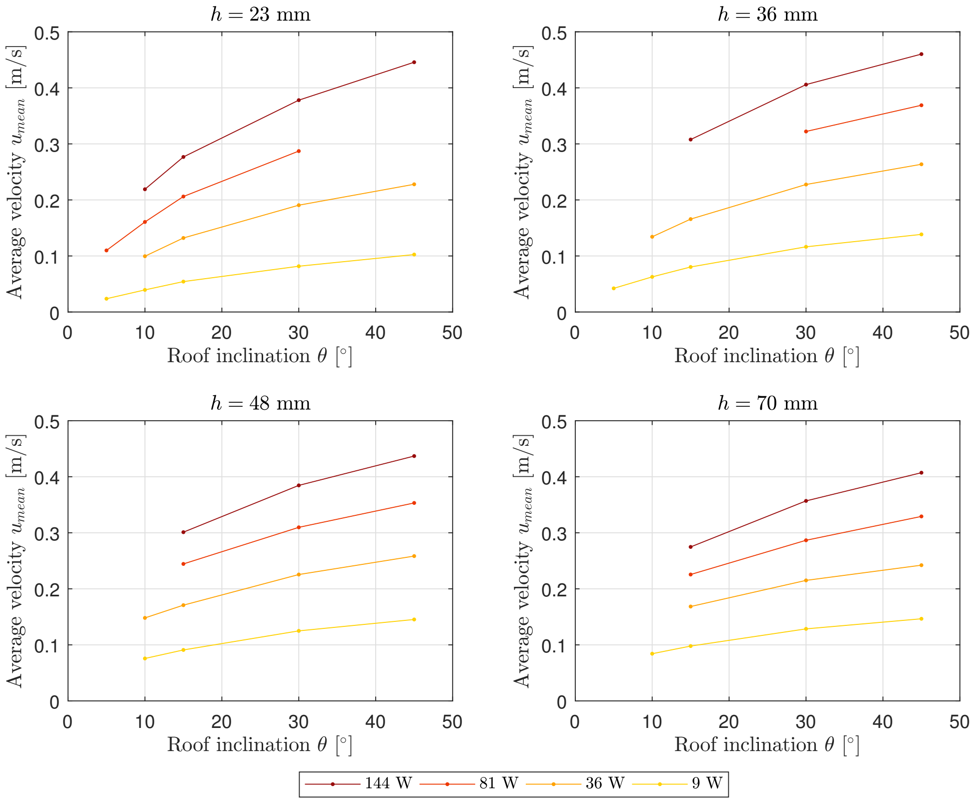

Figure B.10. Simulated mean air velocity as a function of inclination, θ.

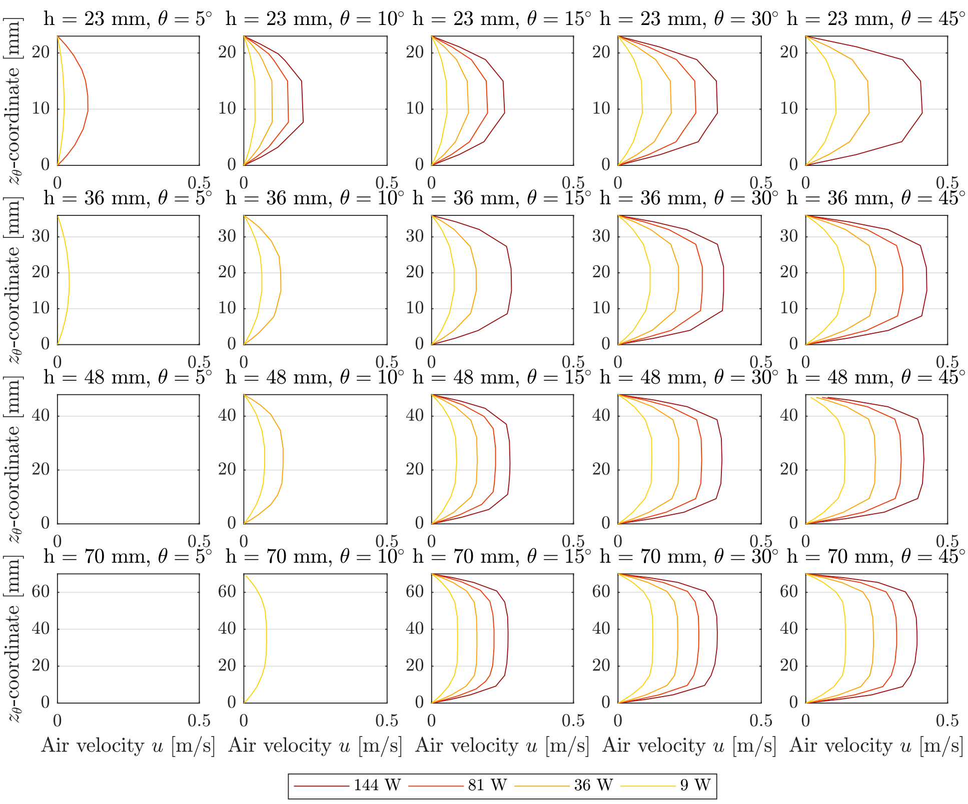

Figure B.11. Simulated air velocity along the cavity height, z_θ, in position 1.

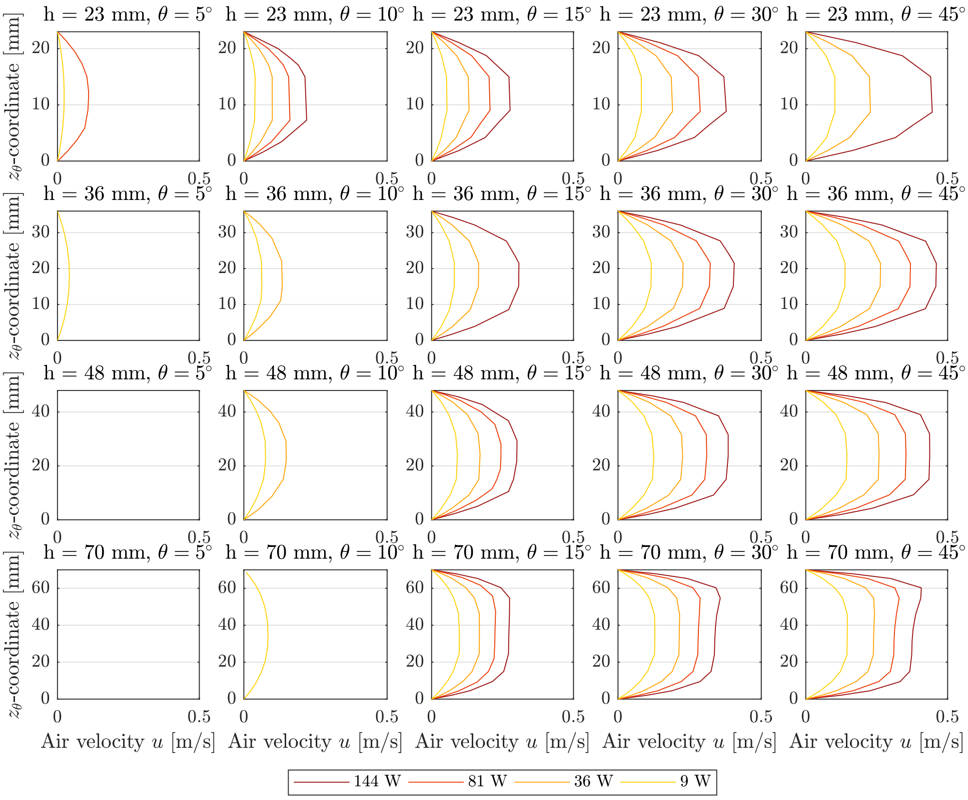

Figure B.12. Simulated air velocity along the cavity height, z_θ, in position 5.

B.3 Air flow

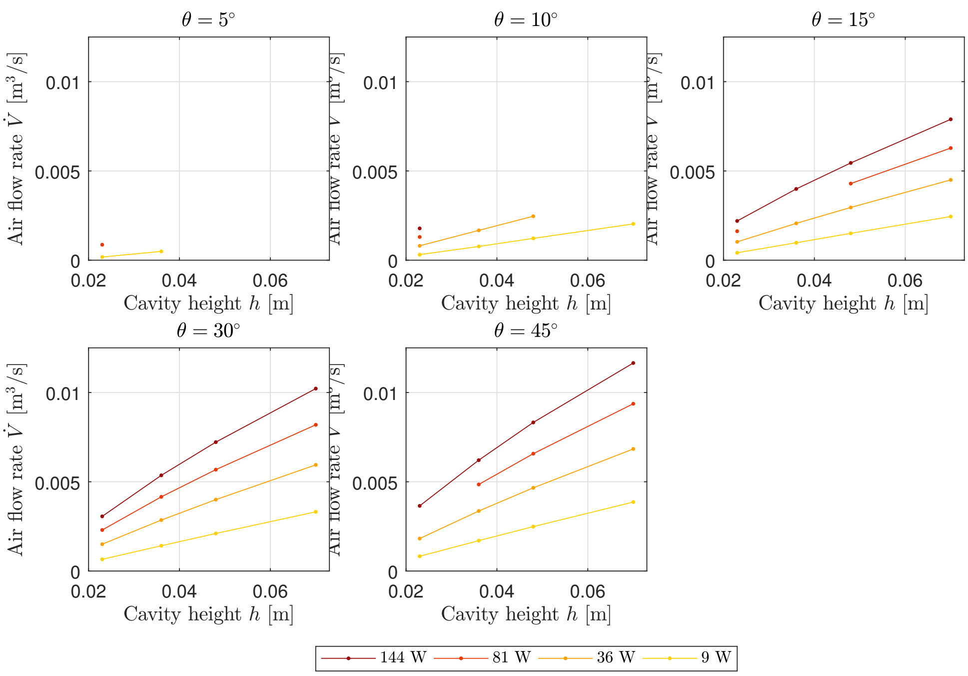

Figure B.13. Simulated air flow rate as a function of cavity height, h.

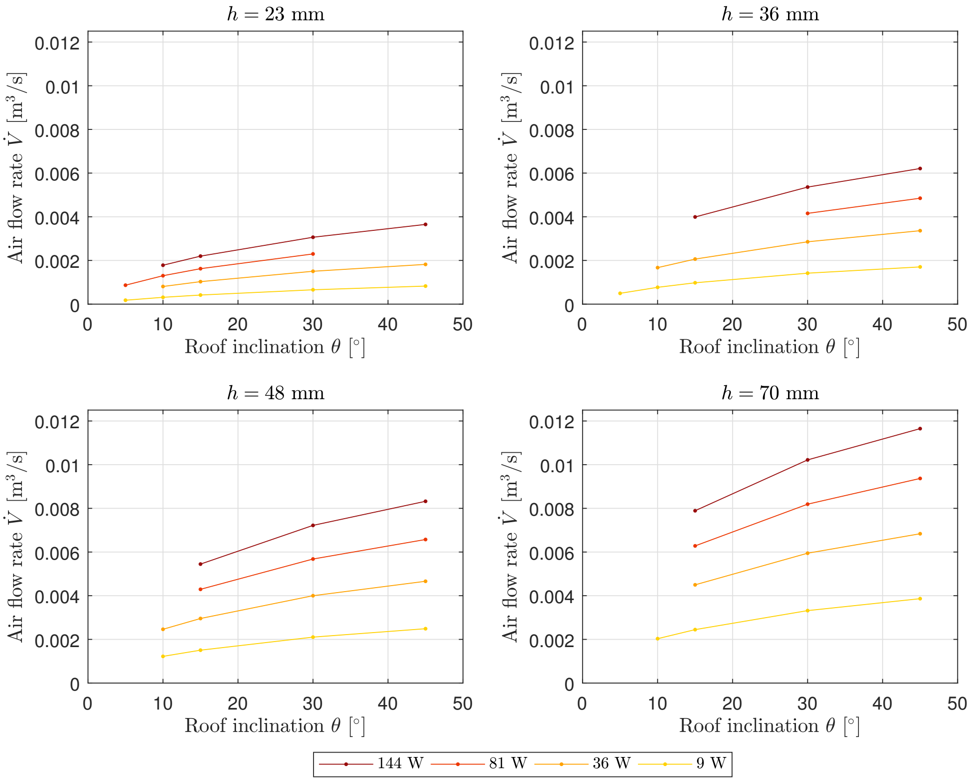

Figure B.14. Simulated air flow rate as a function of inclination, θ.

C

Analysis of results

C.1 Temperature

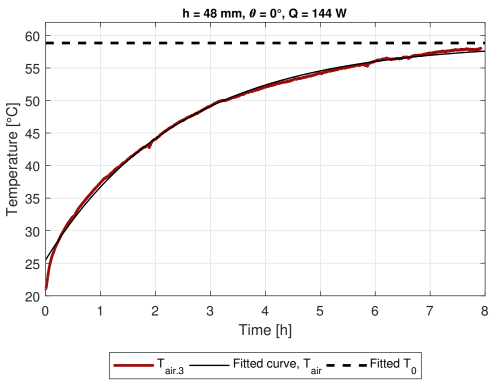

(a) $Q = 144W$

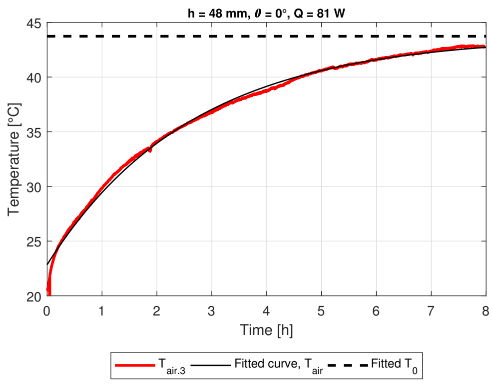

(b) $Q = 81W$

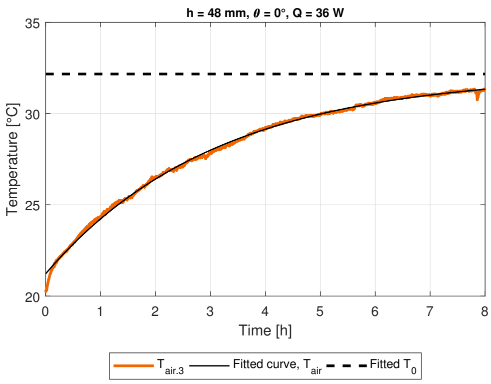

(c) $Q = 36W$

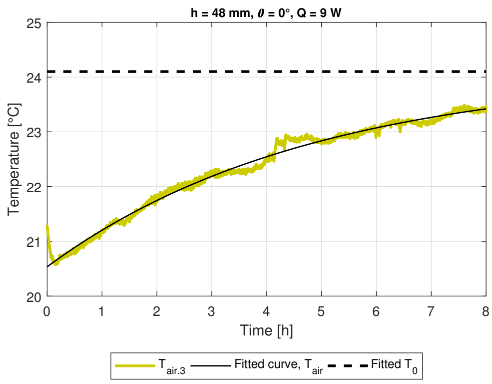

(d) $Q = 9W$

Figure C.1. Measured air temperatures in position 3 during 8 hour measurements, along with fitted curves and estimated effective temperatures, T_0. Note the different temperature scale on the y-axis.

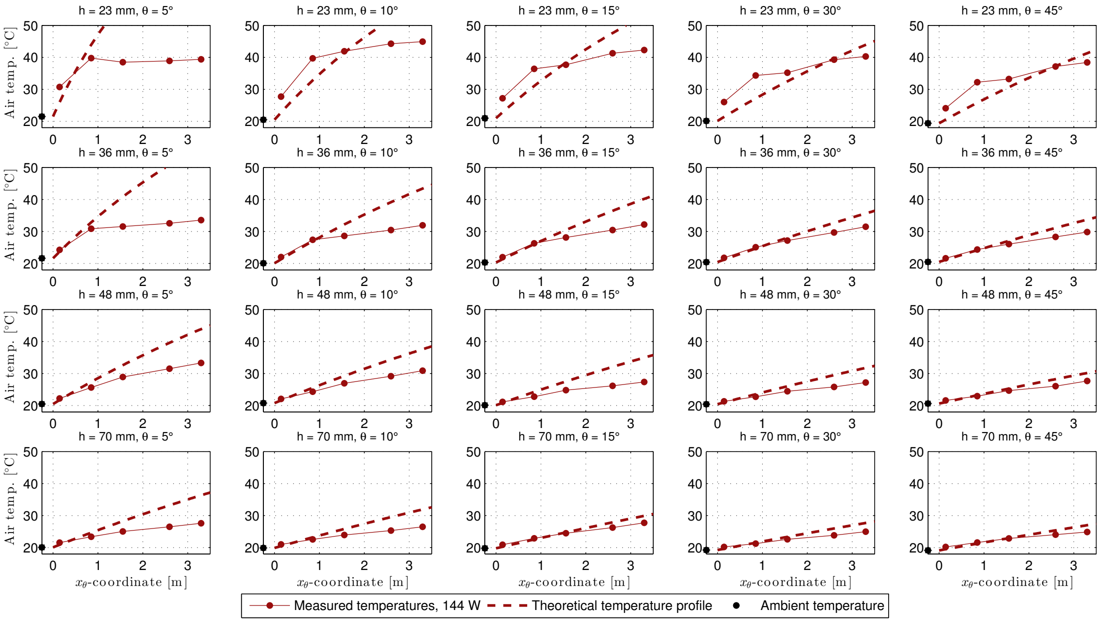
h = 23 mm, θ = 5°
h = 23 mm, θ = 10°
h = 23 mm, θ = 15°
h = 23 mm, θ = 30°
h = 23 mm, θ = 45°
h = 36 mm, θ = 5°
h = 36 mm, θ = 10°
h = 36 mm, θ = 15°
h = 36 mm, θ = 30°
h = 36 mm, θ = 45°
h = 48 mm, θ = 5°
h = 48 mm, θ = 10°
h = 48 mm, θ = 15°
h = 48 mm, θ = 30°
h = 48 mm, θ = 45°
h = 70 mm, θ = 5°
h = 70 mm, θ = 10°
h = 70 mm, θ = 15°
h = 70 mm, θ = 30°
h = 70 mm, θ = 45°
Air temp. [°C]
x_θ-coordinate [m]
Measured temperatures, 144 W
Theoretical temperature profile
Ambient temperature

(a)

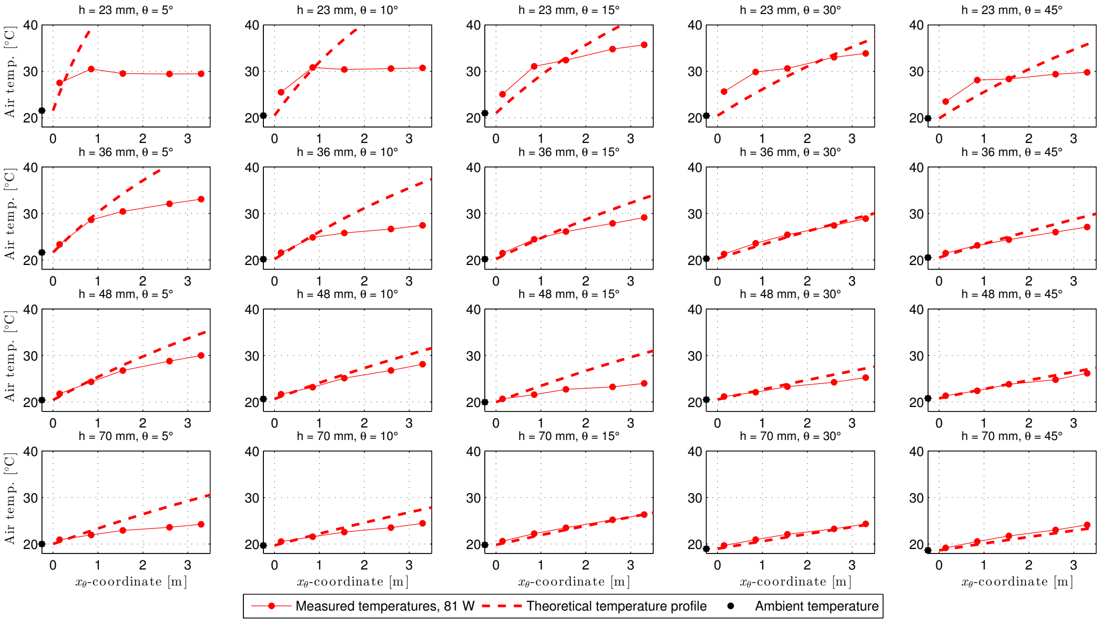
h = 23 mm, θ = 5°
h = 23 mm, θ = 10°
h = 23 mm, θ = 15°
h = 23 mm, θ = 30°
h = 23 mm, θ = 45°
h = 36 mm, θ = 5°
h = 36 mm, θ = 10°
h = 36 mm, θ = 15°
h = 36 mm, θ = 30°
h = 36 mm, θ = 45°
h = 48 mm, θ = 5°
h = 48 mm, θ = 10°
h = 48 mm, θ = 15°
h = 48 mm, θ = 30°
h = 48 mm, θ = 45°
h = 70 mm, θ = 5°
h = 70 mm, θ = 10°
h = 70 mm, θ = 15°
h = 70 mm, θ = 30°
h = 70 mm, θ = 45°
Air temp. [°C]
x_θ-coordinate [m]
Measured temperatures, 81 W
Theoretical temperature profile
Ambient temperature

(b)

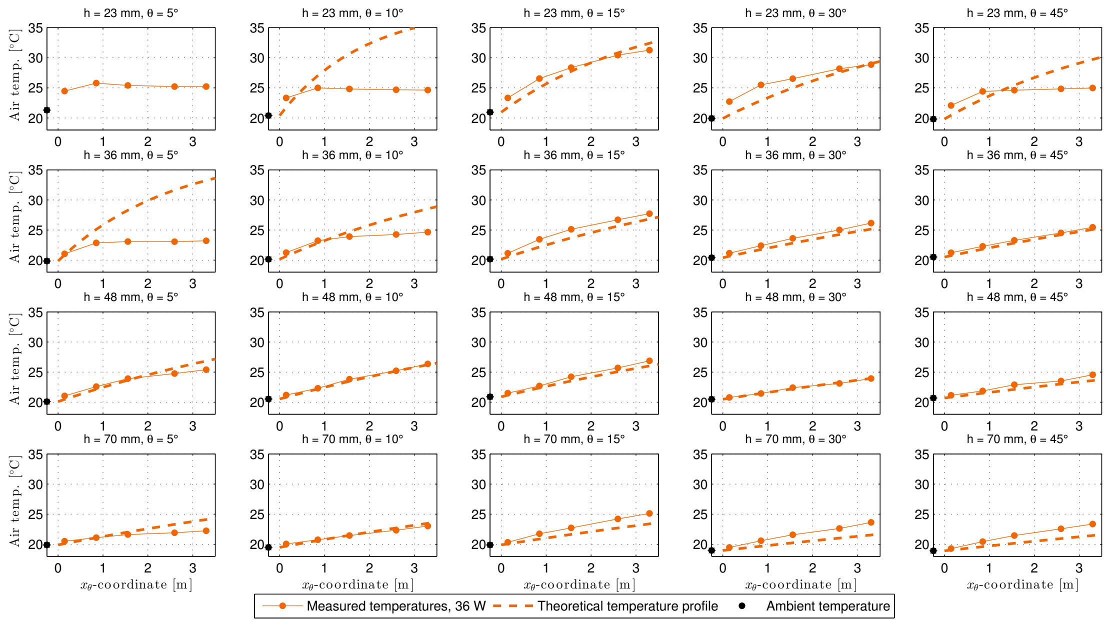

(c)

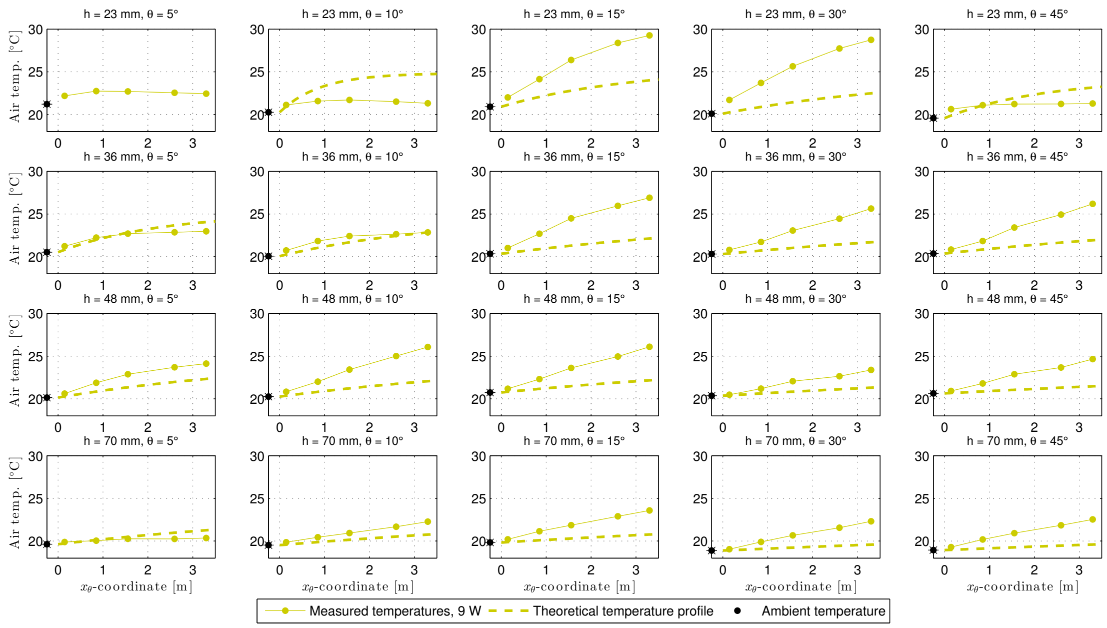

(d)

Figure C.2. Measured and theoretically calculated air temperature profiles.

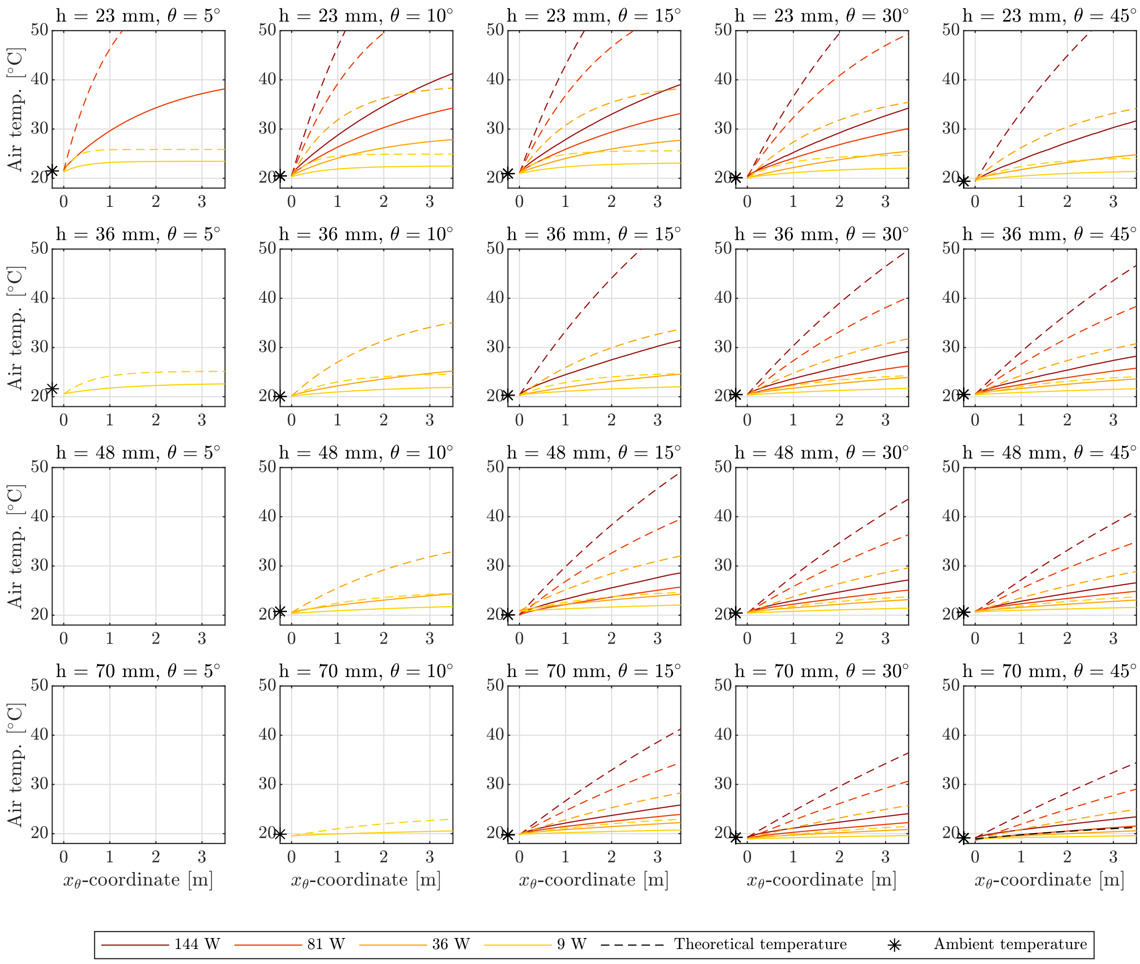

Figure C.3. Simulated and theoretically calculated air temperature profiles.

C.2 Air flow

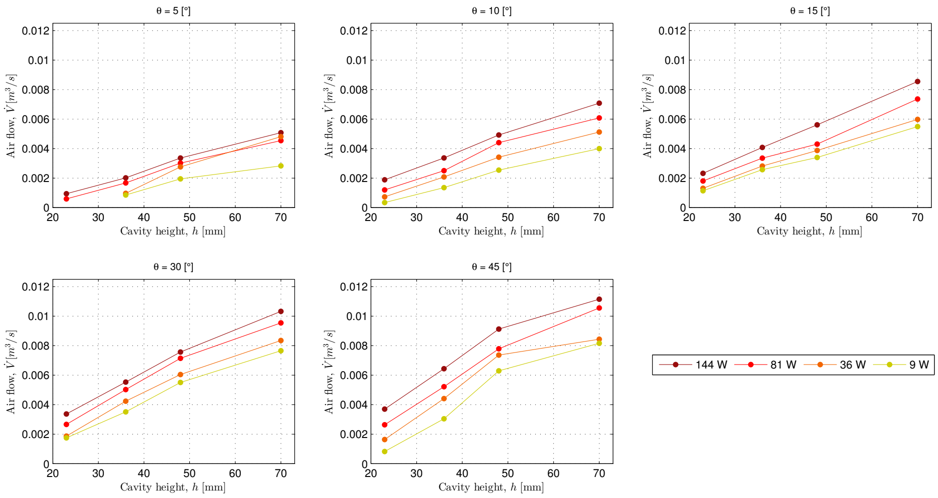

Figure C.4. Air flow, calculated from smoke test results, for varying cavity heights.

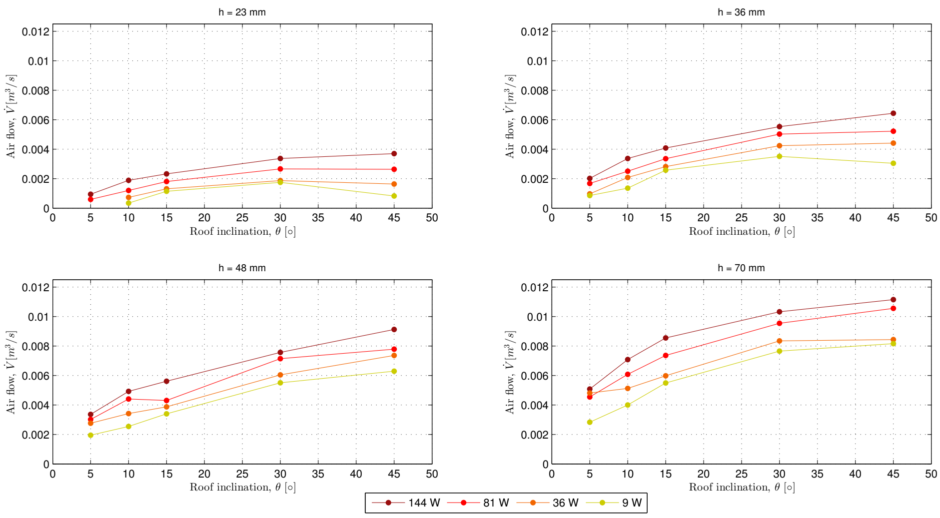

Figure C.5. Air flow, calculated from smoke test results, for varying roof inclination.

C.3 Driving force

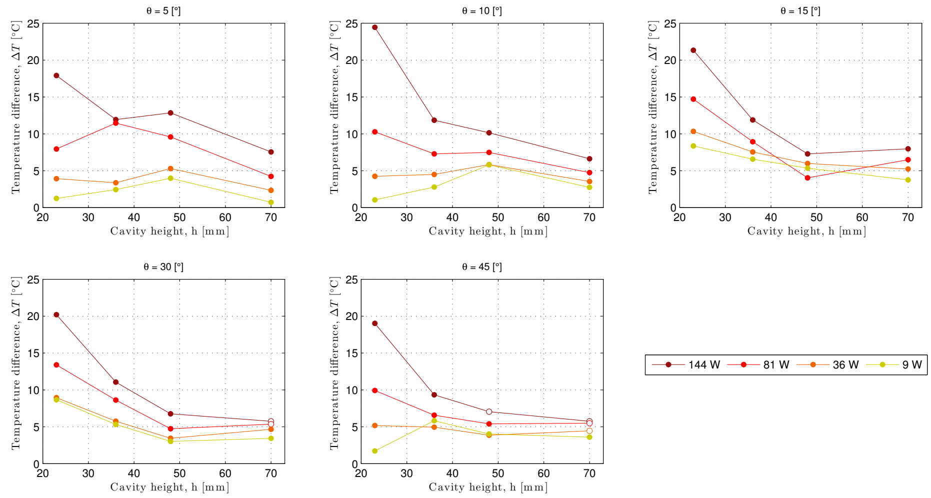

Figure C.6. Measured air temperature difference $T_{a5} - T_{amb}$, as a function of h.

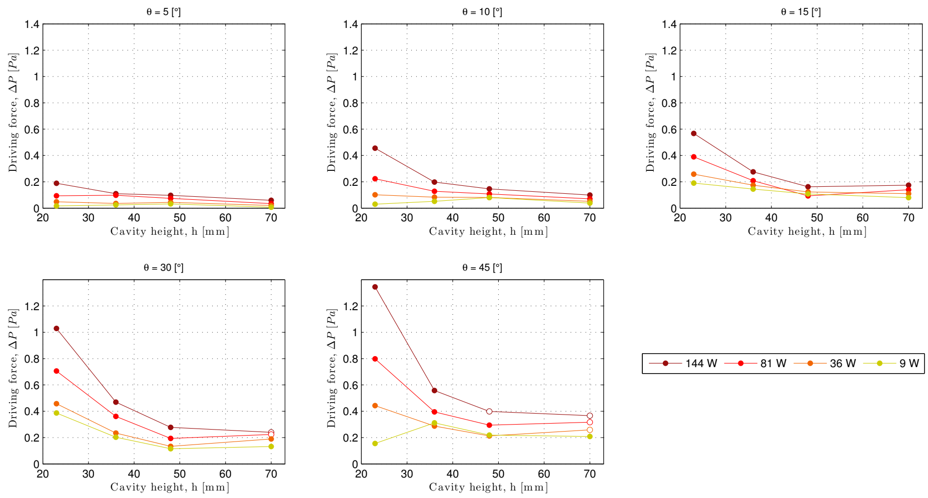

Figure C.7. Thermal driving force calculated from temperature results of the experimental tests, as a function of h. $\Delta P(h)$

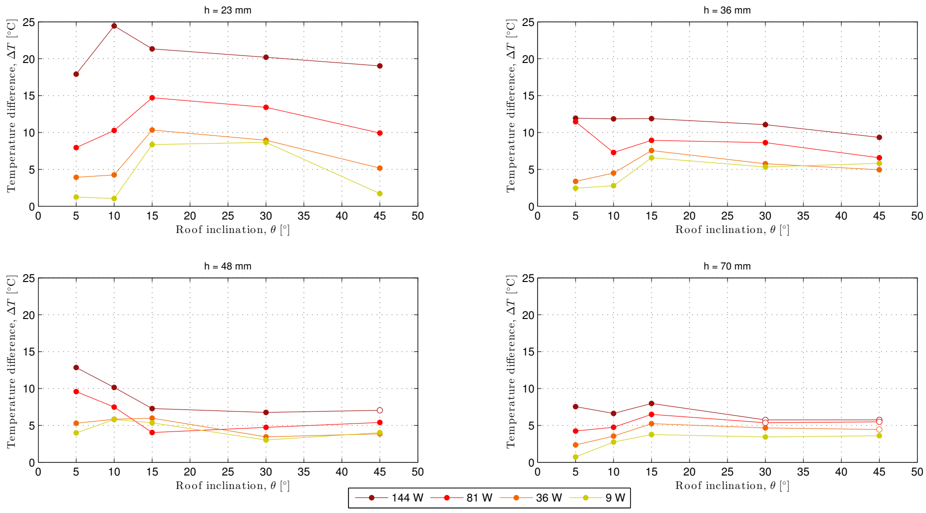

Figure C.8. Measured air temperature difference $T_{a5} - T_{amb}$ in experimental tests, as a function of θ. $\Delta T(\theta)$

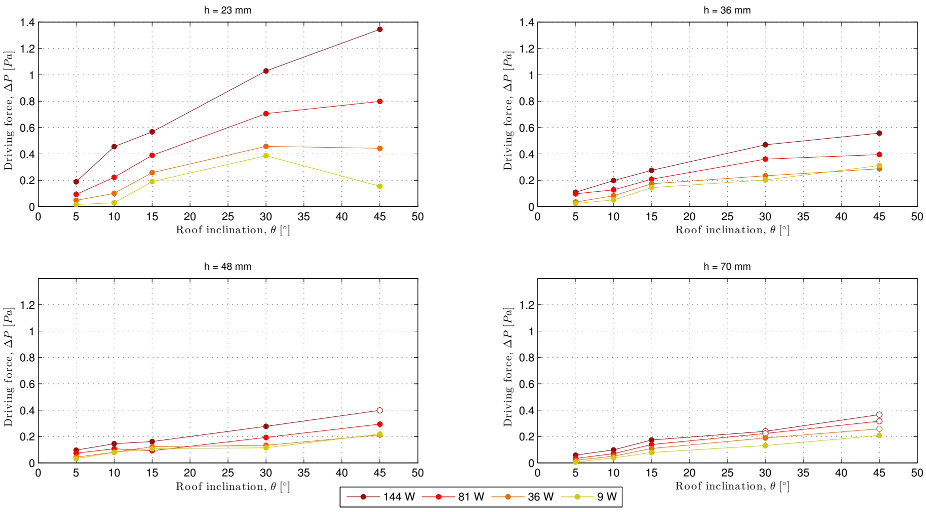

Figure C.9. Thermal driving force calculated from temperature results of the experimental tests, as a function of θ.

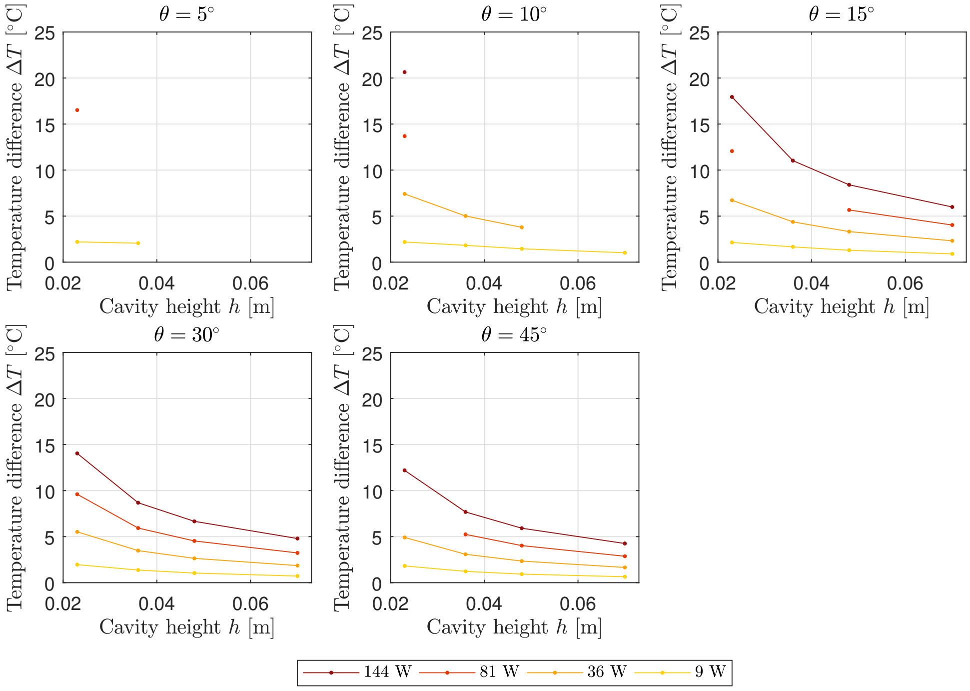

Figure C.10. Simulated air temperature difference $T_{a5} - T_{amb}$, as a function of θ.

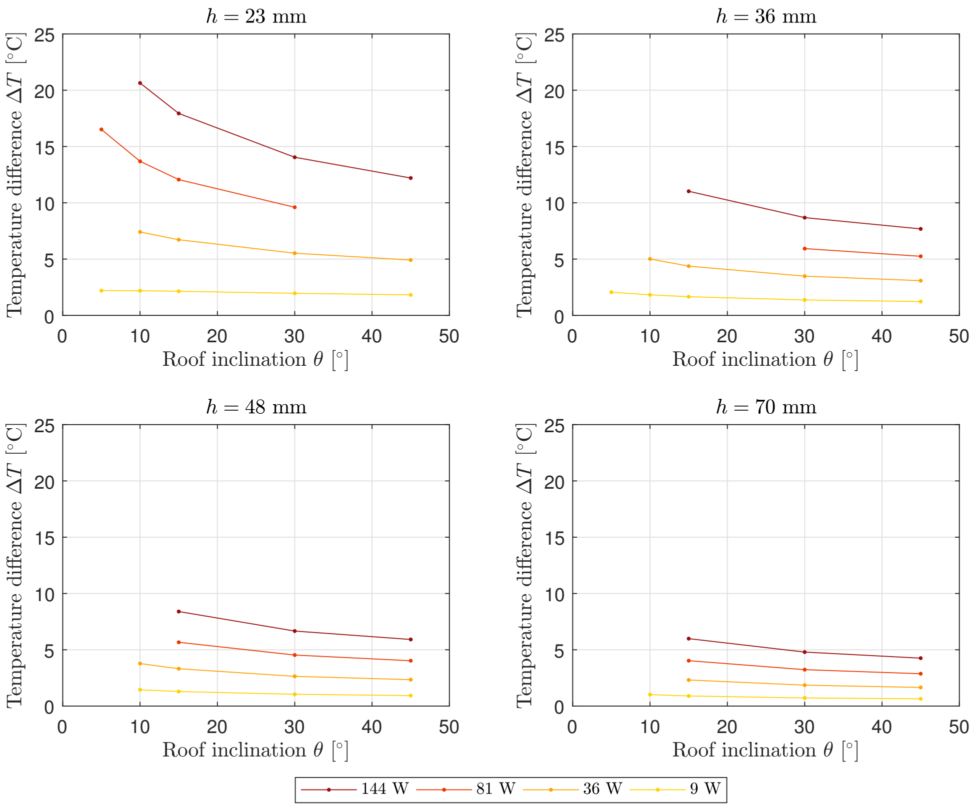

Figure C.11. Simulated air temperature difference $T_{a5} - T_{amb}$, as a function of θ.

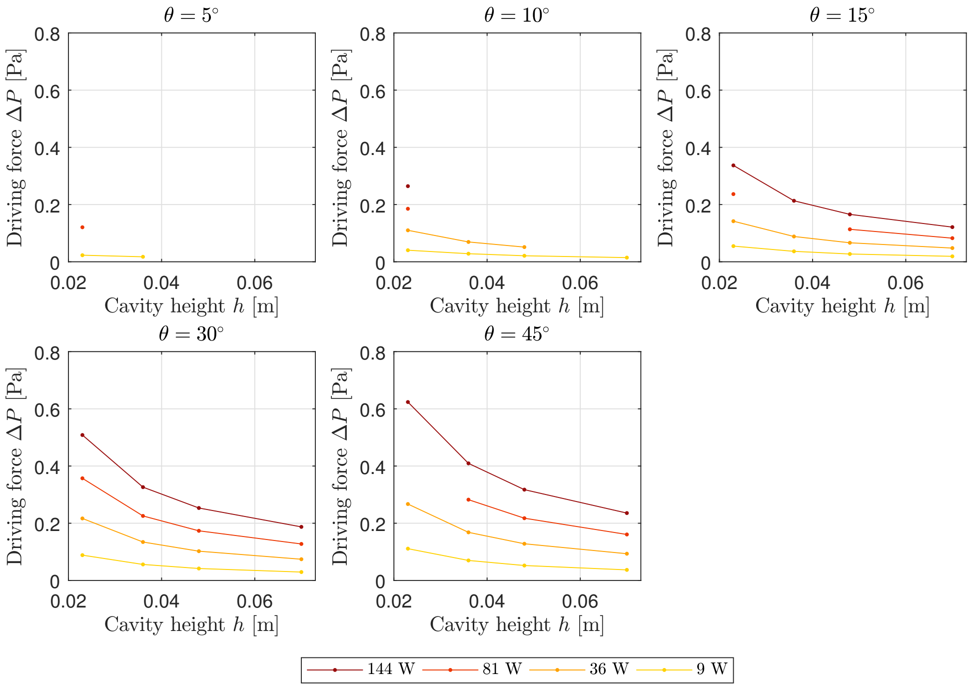

Figure C.12. Thermal driving force calculated from temperature results of the simulations, as a function of h.

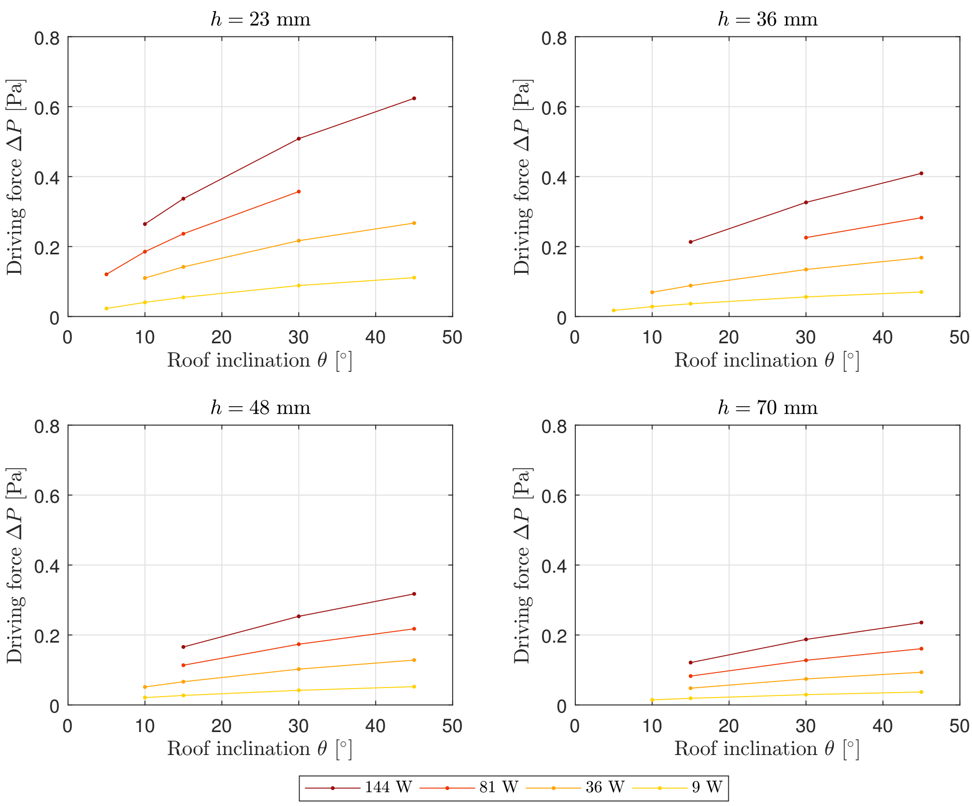

Figure C.13. Thermal driving force calculated from temperature results of the simulations, as a function of θ.

D

Thermal network calculations

D.1 Reduction of thermal network, and calculation of the temperature T_0, for the reference roof construction.

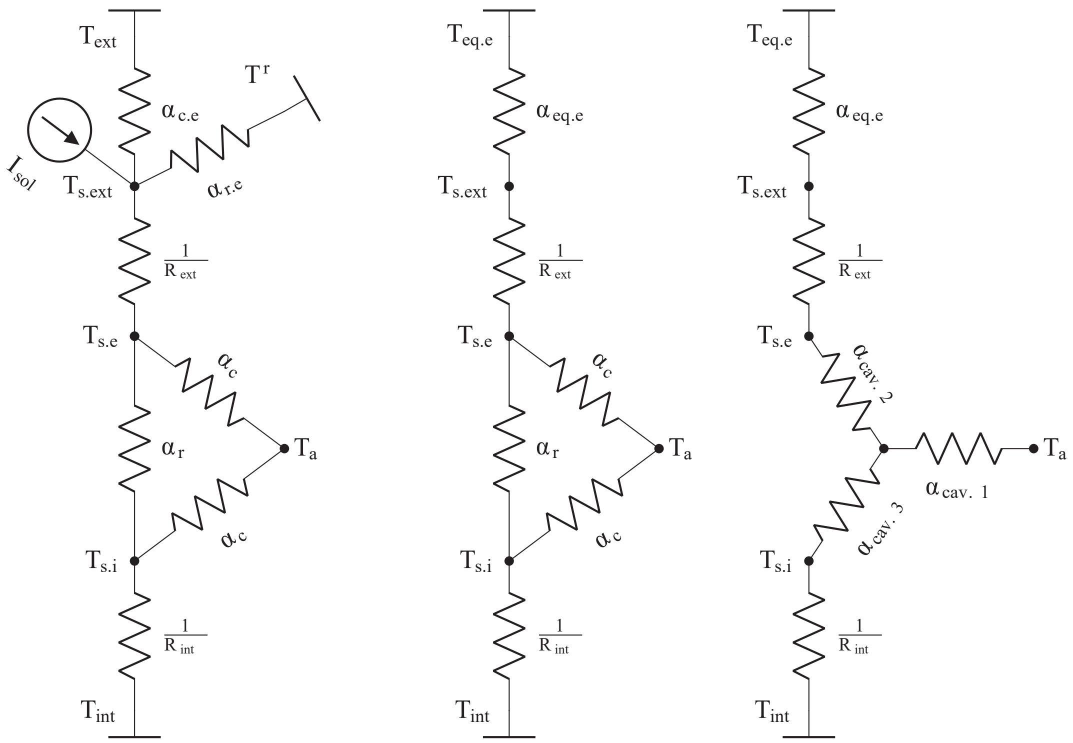

Figure D.1. Reduction of the thermal network of the roof construction, step 1 and 2. The network to the left is the same as in Figure 3.2.

As presented in Figure D.1, the first step of reduction is to reduce the network for the external surface into the equivalent exterior temperature $T_{eq.e}$ according to Equation D.1 (Hagentoft, 2001). The convective heat transfer coefficient for the external roof surface

$\alpha_{c.e}$ is calculated by Equation D.2 (Hagentoft, 2001) where U_{10} is the wind speed [m/s].

$$T_{eq.e} = T_{ext} + \frac{I_{sol} \cdot \alpha_{sol} + \alpha_{r.e} \cdot (T^r - T_{ext})}{\alpha_{eq.e}} \tag{D.1a}$$

$$\alpha_{eq.e} = \alpha_{r.e} + \alpha_{c.e} \tag{D.1b}$$

$$\alpha_{c.e} = 5 + 4.5 \cdot U_{10} - 0.14 \cdot U_{10}^2 [°C] \tag{D.2}$$

A flat roof has only a radiation exchange with the sky and the temperature T^r is assumed to be equal to the sky temperature. The sky temperature is approximated by Equation D.3a for a clear sky, or by Equation D.3b for a cloudy sky (Hagentoft, 2001). The radiant surface heat transfer coefficient for the roof can be calculated by Equation D.4, where T_{12} is the mean of the surface temperature of the roof $T_{s,ext}$ [°C] and the temperature of the sky T^r [°C] (Hagentoft, 2001). The surface temperature of the roof is assumed to be equal to the external temperature T_{ext}.

$$T^r = 1.2 \cdot T_{ext} - 14 \tag{D.3a}$$

$$T^r = T_{ext} \tag{D.3b}$$

$$\begin{aligned} \alpha_r &= 4 \cdot \sigma \cdot \varepsilon_{12} \cdot T_{12}^3 \\ \frac{1}{\varepsilon_{12}} &= \frac{1}{\varepsilon_1} + \frac{1}{\varepsilon_2} - 1 \end{aligned} \tag{D.4}$$

The second step of reduction (also presented in Figure D.1) is to reduce the network in the cavity from a Δ-network to a Y-network, according to Equation D.5 (Hagentoft, 2001).

$$\alpha_{cav.0} = \frac{1}{\frac{1}{\alpha_c} + \frac{1}{\alpha_c} + \frac{1}{\alpha_r}} \tag{D.5a}$$

$$\alpha_{cav.1} = \frac{\alpha_c \cdot \alpha_c}{\alpha_{cav.0}} \tag{D.5b}$$

$$\alpha_{cav.2} = \frac{\alpha_r \cdot \alpha_c}{\alpha_{cav.0}} \tag{D.5c}$$

$$\alpha_{cav.3} = \frac{\alpha_r \cdot \alpha_c}{\alpha_{cav.0}} \tag{D.5d}$$

The convective heat transfer coefficient in the cavity α_c can be estimated by the expression in Equation D.6 (Hagentoft, 2001). However, as a simplification in this study, α_c is assumed to be constant $= 3$ W/(m^{2}K) along the cavity length, corresponding to a difference between the surface temperature T_s and air temperature T_a of 5 °C.

$$\alpha_c = 2 \cdot |T_a - T_s|^{1/4} \tag{D.6}$$

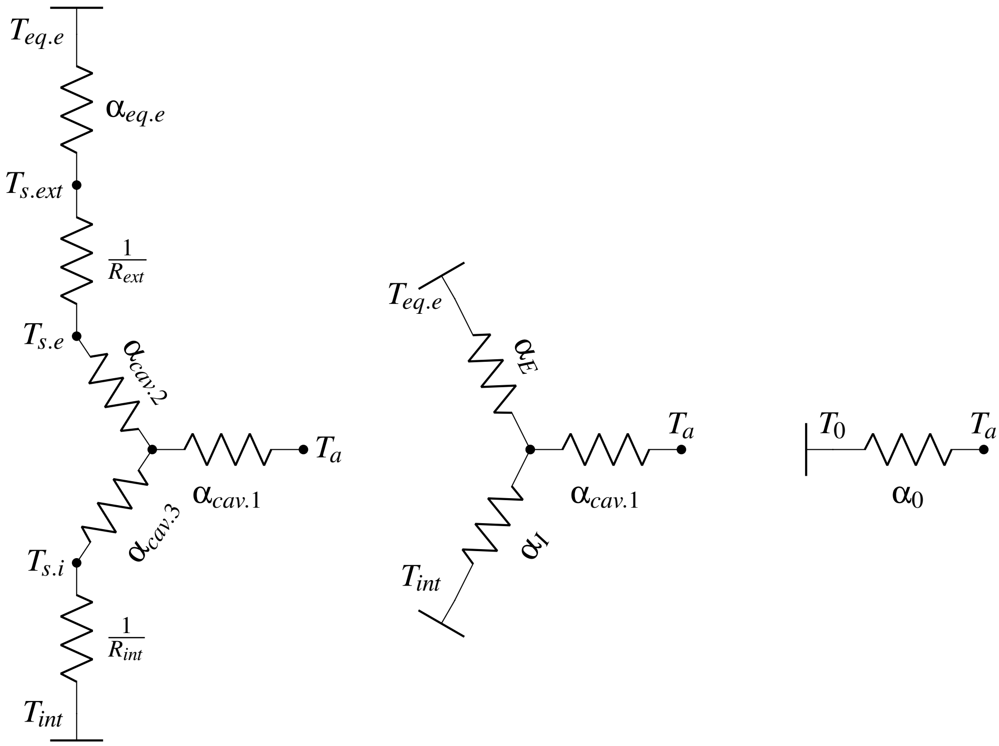

Figure D.2. Reduction of the thermal network of the roof construction, step 3 and 4.

The final steps of the reduction of the network, as presented in Figure D.2, is covered by Equation D.7 and effective temperature T_0 is calculated according to Equation D.7c. The effective heat transfer coefficient α_0 and the heat flux q W/m^2 to the cavity is calculated by Equation D.8.

$$\alpha_I = \frac{1}{\frac{1}{\alpha_{cav.3}} + R_{int}} \tag{D.7a}$$

$$\alpha_E = \frac{1}{\frac{1}{\alpha_{cav.2}} + R_{ext} + \frac{1}{\alpha_{eq.e}}} \tag{D.7b}$$

$$T_0 = \frac{T_{eq.e} \cdot \alpha_E + T_{int} \cdot \alpha_I}{\alpha_E + \alpha_I} \tag{D.7c}$$

$$\alpha_0 = \frac{1}{\frac{1}{\alpha_{cav.1}} + \frac{1}{\alpha_E + \alpha_I}} \tag{D.8a}$$

$$q = \alpha_0 \cdot (T_0 - T_a) \tag{D.8b}$$

D.2 Reduction of thermal network, and calculation of the effective temperature T_0, for the experimental rig and set-up.

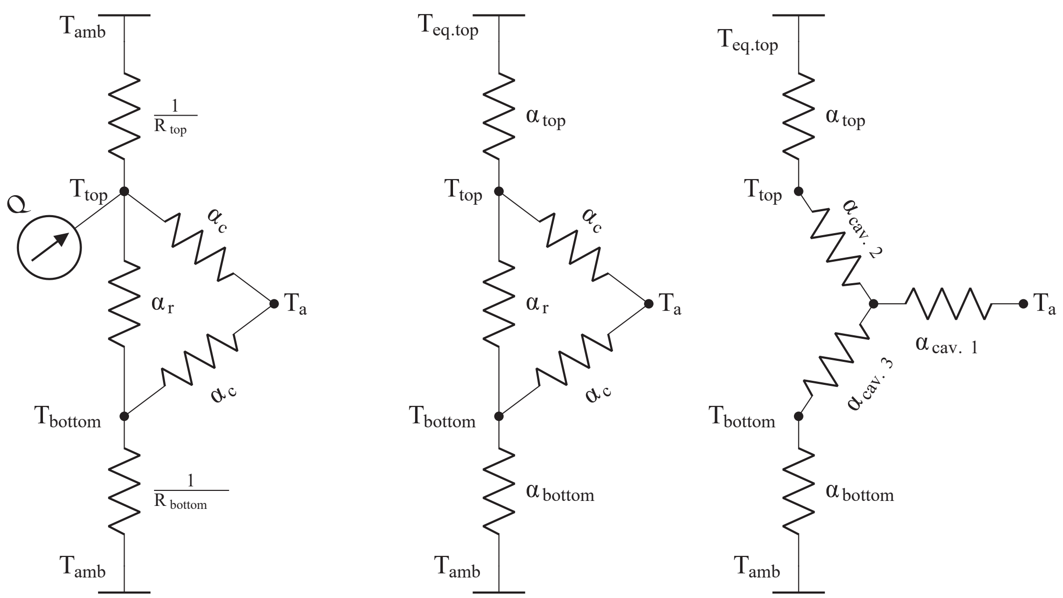

Figure D.3. Reduction of the thermal network of the experimental rig and set-up, step 1 and 2. The network to the left is the same as in Figure 4.4.

As presented in Figure D.3, the network for the top part of the rig can be reduced into the equivalent ambient temperature $T_{eq.top}$ according to Equation D.9. The surface heat resistances of the outer surfaces of the model (not the surfaces in the cavity) are assumed to $R_{si} = 0.13\ \mathrm{m^2 K/W}$.

$$T_{eq.top} = T_{amb} + Q_{eq} \cdot R_{top} \tag{D.9a}$$

$$Q_{eq} = \frac{Q}{L \cdot b} \tag{D.9b}$$

As the second step of reduction, the network in the cavity can be reduced from a

Δ-network to a Y-network according to Equation D.10 (Hagentoft, 2001).

$$\alpha_{cav.0} = \frac{1}{\frac{1}{\alpha_c} + \frac{1}{\alpha_c} + \frac{1}{\alpha_r}} \tag{D.10a}$$

$$\alpha_{cav.1} = \frac{\alpha_c \cdot \alpha_c}{\alpha_{cav.0}} \tag{D.10b}$$

$$\alpha_{cav.2} = \frac{\alpha_r \cdot \alpha_c}{\alpha_{cav.0}} \tag{D.10c}$$

$$\alpha_{cav.3} = \frac{\alpha_r \cdot \alpha_c}{\alpha_{cav.0}} \tag{D.10d}$$

The convective heat transfer coefficient in the cavity α_c can be estimated by the expression in Equation D.11. However, in this study α_c is simplified and assumed to be constant $= 3$ W/(m^{2}K) along the cavity length, corresponding to a difference between the surface temperature T_s and air temperature T_a of 5 °C.

$$\alpha_c = 2 \cdot |T_a - T_s|^{1/4} \tag{D.11}$$

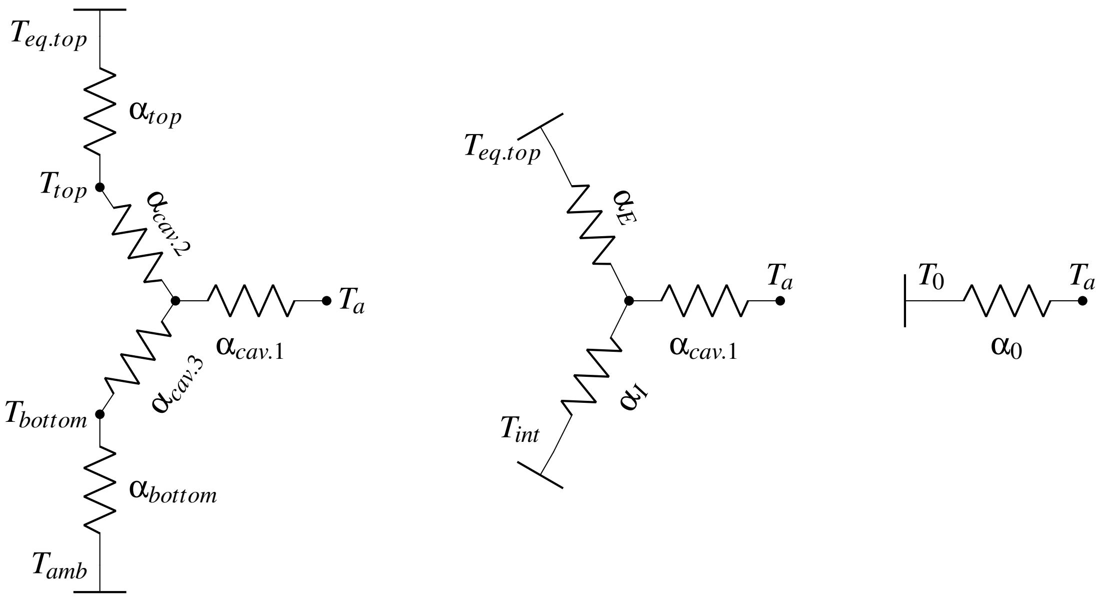

Figure D.4. Reduction of the thermal network of the experimental rig and set-up, step 3 and 4.

The final two steps of reduction are presented in Figure D.4, and the reduction is covered by Equation D.12. The effective temperature T_0 is calculated according to Equation D.12c, the effective heat transfer coefficient α_0 according to Equation D.13a, and the heat flux q W/m^2 to the cavity is calculated by Equation D.13.

$$\alpha_I = \frac{1}{\frac{1}{\alpha_{cav.3}} + R_{bottom}} \tag{D.12a}$$

$$\alpha_E = \frac{1}{\frac{1}{\alpha_{cav.2}} + R_{top}} \tag{D.12b}$$

$$T_0 = \frac{T_{eq.top} \cdot \alpha_E + T_{amb} \cdot \alpha_I}{\alpha_E + \alpha_I} \tag{D.12c}$$

$$\alpha_0 = \frac{1}{\frac{1}{\alpha_{cav.1}} + \frac{1}{\alpha_E + \alpha_I}} \tag{D.13a}$$

$$q = \alpha_0 \cdot (T_0 - T_a) \tag{D.13b}$$

(D.13c)

D.3 Effect of radiation, on air temperature measurements

The emissivity of the measuring point of the thermocouples, as well as the emissivity of the surroundings facing the measuring point of the thermocouple, is conservatively assumed to be 0.9. Further, the convective surface heat transfer coefficient of the thermocouple is assumed to be equal to 3 W/m$^2 \cdot$K. From these assumptions, the addition in measured air temperature, due to radiation from the bottom surface, can be calculated using Equation D.14 and D.15.

$$T_{rad.addition} = \frac{\alpha_{r.i} \cdot (T_{b.i} - T_{a.i})}{\alpha_{r.i} + \alpha_c} \tag{D.14}$$

$$\begin{gathered} \alpha_{r.i} = 4 \cdot \sigma \cdot \varepsilon_{12} \cdot T_{12}^3 \\ \frac{1}{\varepsilon_{12}} = \frac{1}{\varepsilon_1} + \frac{1}{\varepsilon_2} - 1 \end{gathered} \tag{D.15}$$

$T_{a.i}$ measured air temperature in position i [°C]
$T_{b.i}$ measured bottom surface temperature in position i [°C]
σ Stefan-Boltzmanns' constant, $5.67 \cdot 10^{-8}$W/m$^2 \cdot$K
T_{12} mean absolute temperature of the surfaces [K]

E

Derivation of air flow rate dependent on Rayleigh number

The air flow rate caused by thermal buoyancy as a driving force can be calculated according to Equation E.1 (same as Equation 3.3) where the driving force is calculated according to Equation E.2 (same as Equation 3.13).

$$\dot{V} = \frac{\Delta P_s}{\sum S} \tag{E.1}$$

$$\Delta P_s = \sin\theta \cdot g\beta\rho_{amb} \int_0^L (T_0 - (T_0 - T_{amb}) \cdot e^{-x_\theta/L_0} - T_{amb}) dx_\theta \tag{E.2}$$

Combining Equation E.1 with E.2 yields:

$$\begin{aligned}
\dot{V} &= \frac{g\beta\rho_{amb} \cdot \sin\theta}{\sum S} \int_0^L (T_0 - (T_0 - T_{amb}) \cdot e^{-x_\theta/L_0} - T_{amb}) dx_\theta \\
&= \frac{g\beta\rho_{amb} \cdot \sin\theta \cdot L(T_0 - T_{amb})}{\sum S} \left(1 - \frac{L_0}{L} + \frac{L_0}{L} e^{-L/L_0}\right) \\
&= \frac{g\beta\rho_{amb} H(T_0 - T_{amb})}{\sum S} \left(1 - \frac{L_0}{L} + \frac{L_0}{L} e^{-L/L_0}\right)
\end{aligned} \tag{E.3}$$

Combining Equation 3.2 and 3.27 with Equation E.3 yields:

$$\begin{aligned}
L_0 &= \frac{\rho c_a \cdot h \cdot u}{\alpha_0} \\
&= Pr_c \frac{\dot{V}}{\nu b} \\
&= Pr_c \frac{g\beta\rho_{amb} H(T_0 - T_{amb})}{\nu b \sum S} \left(1 - \frac{L_0}{L} + \frac{L_0}{L} e^{-L/L_0}\right) \\
&= Pr_c \, Gr_c \left(1 - \frac{L_0}{L} + \frac{L_0}{L} e^{-L/L_0}\right) \\
&= Ra_c \left(1 - \frac{L_0}{L} + \frac{L_0}{L} e^{-L/L_0}\right)
\end{aligned} \tag{E.4}$$

Hence, Equation E.4 is reduced into only being dependent on Ra_c, L and L_0 where L_0 includes the air flow rate $\dot{V}$ and Ra_c characterise the thermal conditions as well as geometry of the roof. Ra_c is slightly dependent on $\dot{V}$ as well, from the local pressure losses S_ξ included in $\sum S$, but by solving from Equation E.5 in an iterative way, the air flow rate is found for given conditions.

$$0 = Ra_c \left(1 - \frac{L_0}{L} + \frac{L_0}{L} e^{-L/L_0}\right) - L_0 \tag{E.5}$$

F

Buoyant air flow model

This appendix presents the functional code for predicting the air flow based on calculation of the Rayleigh number of a roof construction. The assumptions outlined throughout this thesis need to be considered when using this model, and the model output should be considered an idealised version of reality.

For any given case, the input data is entered in the first section of the MATLAB code.

The output of the model is a graph which relates selected relevant solar heat load and external air temperatures to the Rayleigh number of the construction, and a graph which relates this Rayleigh number to an air flow rate prediction.

The file provided includes a function and the input data for the construction used for this study as a reference case. The model including thermal network must be modified to be able to be used with any given construction, but the provided data can be used as a first rough estimate.

The input parameters for the model are the following:

- Outdoor air temperature, T_{ext}
- Relative humidity of outdoor air, RH
- Indoor air temperature T_{int}
- Roof inclination θ
- Cavity length L
- Cavity width b
- Cavity height h
- Layer thickness and thermal conductivity of:
  - Roof cladding
  - Roofing underlay
  - Wind barrier
  - Thermal insulation

The output of the model is the following, for each solar heat load:

- Rayleigh number
- Air flow rate
- Solar heat load

```
%%%%%%%%%%%%%%%%%%%%%%%%%%%%%%%%%%%%%%%%%%%%%%%%%%%%%
% Buoyant Cavity Air Flow Model                     %
% Created by Martina Svantesson and Toivo Sawen,    %
% 2019-06-13                                        %
% Chalmers University of Technology,                %
% Department of Architecture and Civil Engineering  %
% Division of Building Technology                   %
%                                                   %
% Calculates the cavity Rayleigh number for a given %
% roof construction and specific weather data       %
% and estimates the air flow rate through the air   %
% cavity in a plot.                                 %
%%%%%%%%%%%%%%%%%%%%%%%%%%%%%%%%%%%%%%%%%%%%%%%%%%%%%

%%% Input data
% Weather data:
% Outdoor temperature
T_ext = 20;                         % [C]

% Relative humidity
RH = 0.50;                          % [%]

% Internal air temperature:
T_int = 20;                         % [C]

% Geometrical parameters:
% Roof inclination
theta = 30;                         % [deg]
% Cavity length
L = 10;                             % [m]

% Cavity width
b = 0.552;                          % [m]

% Cavity height
h = 0.045;                          % [m]

% Roof construction:
% The roof construction has an external
% metal cladding, a roofing underlay,
% an air cavity, a wind barrier of wooden
% board, and thermal insulation.

% External cladding
t_int_cladding = 0.013;             % [m]
```

```
lambda_int_cladding = 0.25;         % [W/m*K]

% Insulation thickness
t_insulation = 0.35;                % [m]
lambda_insulation = 0.036;          % [W/m*K]

% Wind barrier
t_wind_barrier = 0.003;             % [m]
lambda_wind_barrier = 0.13;         % [W/m*K]

% Roofing underlay
t_roofing_underlay = 0.018;         % [m]
lambda_roofing_underlay = 0.13;     % [W/m*K]

% Calculate Rayleigh number, air flow rate, and
% solar heat load, for I between 0 and 1000 W/m^2K
[Ra_plot, V_dot, I_sol_plot] = ...
    buoyant_air_flow(...
        T_ext,...
        RH,...
        T_int,...
        theta,...
        L,...
        b,...
        h,...
        t_insulation,...
        t_int_cladding,...
        lambda_int_cladding,...
        lambda_insulation,...
        t_wind_barrier,...
        lambda_wind_barrier,...
        t_roofing_underlay,...
        lambda_roofing_underlay);

function [Ra_plot, V_dot, I_sol_plot] = ...
    buoyant_air_flow(...
        T_ext,...
        RH,...
        T_int,...
        theta,...
        L,...
        b,...
        h,...
        t_insulation,...
        t_int_cladding,...
        lambda_int_cladding,...
```

```
        lambda_insulation,...
        t_wind_barrier,...
        lambda_wind_barrier,...
        t_roofing_underlay,...
        lambda_roofing_underlay)

    %%% Constants and assumptions
    % Wind speed
    U_10 = 0;                            % [m/s]

    % Gravity constant
    g = 9.82;                            % [m/s^2]

    % Specific heat capacity:
    c_pa = 1006;                         % [J/kg*K]

    % Stefan-Boltzmanns constant:
    sigma = 5.67*10^(-8);

    % Emissivity of roof cladding:
    epsilon_roof = 0.9;

    % Solar absorptivity of roof cladding:
    alpha_sol = 0.8;


    %%% Data processing
    % Air temperature
    T_ext_K = T_ext + 273.15;                     % [K]

    % Air density:
    rho = density_a(T_ext, RH);                   % [kg/m^3]

    % Coefficient of thermal expansion:
    beta = 1/T_ext_K;                                % [1/K]

    % Dynamic viscosity [Pa*s]:
    C1 = 1.458e-6;
    C2 = 110.4;
    mu = C1 * T_ext_K^(3/2) / (T_ext_K + C2);

    % Kinematic viscosity:
    nu = mu/rho;                                     % [m^2/s]


    %%% Data processing, Geometry
```

```
    % Total roof height:
    H = sin(theta*pi/180)*L;                          % [m]

    % Hydraulic diameter:
    D_h = 2*h*b / (h+b);                              % [m]

    % Roof construction: R - thermal resistance [m^2*K]
    R_int_cladding = t_int_cladding/lambda_int_cladding;
    R_insulation = t_insulation/lambda_insulation;
    R_wind_barrier = t_wind_barrier/lambda_wind_barrier;
    R_roofing_underlay = ...
       t_roofing_underlay/lambda_roofing_underlay;

    %%% Thermal network internal side

    % Internal thermal surface resistance:
    R_si = 0.13;

    R_int = R_si + R_int_cladding + R_insulation + R_wind_barrier;


    %%% Thermal network external side
    % Radiation:
    % Assume a horisontal surface (Hagentoft 2001)
    T_r =1.2*T_ext-14;                             % [K]
    T_mean_roof = (T_r + T_ext)/2+273.15;
    alpha_r_ext =...
        4 * epsilon_roof * sigma * T_mean_roof.^3;  % [W/K*m2]

    % Convection:
    alpha_c_ext = 5+4.5*U_10-0.14*U_10^2;             % [W/K*m2]

    % Equivalent heat transfer coeff. external side
    alpha_eq_ext = alpha_c_ext+alpha_r_ext;           % [W/K*m2]

    % External roof construction:
    R_ext = R_roofing_underlay;                       % [m2*K/W]


    %%% Thermal network inside the cavity
    % Radiation:
    % Emissivity of cavity surfaces assumed to = 0.9
    epsilon_cavity = 1/(1/0.9 + 1/0.9 - 1);

    % Assume cavity temperature:
    T_s_avg_roof = T_ext+273.15; % [K]
```

```

% Convection:
alpha_c_cav = 3;

% Assume two infinity large parallel planes
alpha_r_cav = 4*epsilon_cavity*sigma*T_s_avg_roof^3;


%%% Reduction of thermal network
% Reduction of the network:
alpha_cav0 = 1/(2/alpha_c_cav + 1/alpha_r_cav);      %[W/K*m2]
alpha_cav1 = alpha_c_cav*alpha_c_cav/alpha_cav0;     %[W/K*m2]
alpha_cav2 = alpha_r_cav*alpha_c_cav/alpha_cav0;     %[W/K*m2]
alpha_cav3 = alpha_cav2;                             %[W/K*m2]
alpha_E = 1/(1/alpha_cav2 + R_ext + 1/alpha_eq_ext); %[W/K*m2]
alpha_I = 1/(1/alpha_cav3 + R_int);                  %[W/K*m2]

% Effective heat transfer coefficient:
alpha_0 =...
    1/(1/alpha_cav1 + 1/(alpha_E + alpha_I));        %[W/K*m2]
R_0 = 1/alpha_0;

% Containers for output data
Ra_plot = zeros(1000,1);
V_dot = zeros(1000,1);
I_sol_plot = zeros(1000,1);
% Loop for different solar heat load
for i=1:1000
    I_sol = i;                           % [W/m^2]

    %Initial guess of air velocity in the cavity:
    u_guess = 0.01;

    % Equivalent temperature, external side:
    T_eq_ext = T_ext + ...
        (I_sol*alpha_sol + (T_r-T_ext)*alpha_r_ext)/ ...
        alpha_eq_ext;                                % [K]

    % Effective temperature:
    T_0 =...
        (T_eq_ext*alpha_E + T_int*alpha_I)/...
        (alpha_E + alpha_I);                              % [C]

    % Characteristic length:
    L_0 = rho * c_pa * h * u_guess / alpha_0;          % [m]

```

```
%%% Flow resistance
    % Reynolds number:
    Re = rho * u_guess * D_h / mu;

    % Frictional flow resistance
    % Formula modified from Kronvall (1980)
    phi = 2/3 + 11/24 * h/b * (2 - h/b);          % Dimensional factor
    S_f = 32 * mu * L / (phi * D_h^2 * b * h);    % [Pa/(m^3/s)]

    % Flow resistance at inlet and outlet
    % Formula modified from Hagentoft (1991)
    if Re<1000
        K_c = 0.98*Re^(-0.03);
    else
        K_c = 10.59*Re^(-0.374);
    end
    S_xi = rho * u_guess * (1 + K_c) / (D_h * b); % [Pa/(m^3/s)]

    % Flow resistance from inlet vent at inlet and outlet
    S_vent = 1500 * (2 * u_guess * b * h)^0.8;     % [Pa/(m^3/s)]

    % Total flow resistance:
    S = S_f + S_xi + 2*S_vent;                     % [Pa/(m^3/s)]


%%% Dimensionless numbers
    % Grashof number
    Gr_c=g*beta*rho*H*(T_0-T_ext)/(nu*b*S);

    % Prandtl number
    Pr_c = nu*rho*c_pa/alpha_0;

    % Rayleigh number
    Ra_c = Gr_c*Pr_c;


%%% Iterative solution of air flow rate
    diff = 1;
    tol = 0.001;
    while diff > tol
        L_0 = Ra_c * (1 - L_0/L + L_0/L * exp(-L/L_0));
        u = L_0 * alpha_0/(rho * c_pa * h);

        Re = rho * u * D_h / mu;
```

```
            if Re<1000
                K_c = 0.98*Re^(-0.03);
            else
                K_c = 10.59*Re^(-0.374);
            end
            S_xi = rho * u * (1+K_c) / (D_h * b);
            S_vent = 1500 * (2*u*b*h)^0.8;
            S = S_f + S_xi + 2*S_vent;

            Gr = g * beta * rho * H * (T_0 - T_ext) / (nu * S * b);
            Pr_c = nu * rho * c_pa / alpha_0;
            Ra_c = Gr_c * Pr_c;

            diff = abs(u - u_guess);
            u_guess = u;
        end

        % Output data
        Ra_plot(i) = Ra_c;
        V_dot(i) = u * h * b;
        I_sol_plot(i) = I_sol;
    end


    %%% Plot of results

    def_ax_pos = [0.1, 0.14*600/450, 0.8, 0.75];
    figure('DefaultAxesPosition', def_ax_pos)

    subplot(1,2,1,'align');
    plot(I_sol_plot(:),Ra_plot(:),'Color','b')
    hold on
    axis([0 1000 0 450])
    xlabel('Solar heat load, $I_{sol}$ [W/m$^2$]', 'Interpreter','
        latex')
    ylabel('Rayleigh number, $Ra_c$ [-]', 'Interpreter','latex')
    grid on

    subplot(1,2,2,'align');
    plot(V_dot(:),Ra_plot(:),'Color','b')
    hold on
    axis([0 0.045 0 450])
    xlabel('Air flow $\dot V$ [m$^3$/s]', 'Interpreter','latex')
    ylabel('Rayleigh number, $Ra_c$ [-]','Interpreter','latex')
    grid on
```

```
    bot_offset = 0.04;
    fz = [100 100 800 450];
    set(gcf, 'Position', fz);
    lgd = legend(sprintf('$T_{ext} = %d ^\\circ$C',T_ext),...
        'Interpreter','latex');
    set(lgd, 'Position',[0.5 bot_offset 0 0],'Orientation','horizontal')
end

% Calculates density of moist air
% Input: Air temperature [degC], RH 0.0-1.0 [-]
function rho_a = density_a(T_a, RH)
    T_a_K = T_a+273.15;                    % Temperature [K]

    p_d = 101325;                          % Partial pressure of dry air
    R_d = 287.058;                         % Specific gas constant of dry air

    p_sat = 6.1078*10^(7.5*T_a/T_a_K); % Saturation vapor pressure
    p_v = RH*p_sat;                        % Vapor pressure
    R_v = 461.495;                         % Specific gas constant for water vapor

    rho_a = p_d./(R_d*T_a_K)+p_v./(R_v*T_a_K); % Air density of inlet air
end
```